

Mono- and Dinuclear Nonheme Iron Model Complexes: O-O Bond Activation,  
Structural Characterization and Reactivity Study

A DISSERTATION  
SUBMITTED TO THE FACULTY OF  
UNIVERSITY OF MINNESOTA  
BY

Gregory Todd Rohde

IN PARTIAL FULFILLMENT OF THE REQUIREMENTS  
FOR THE DEGREE OF  
DOCTOR OF PHILOSOPHY

Professor Lawrence Que, Jr., Advisor

May, 2015

© Gregory Todd Rohde 2015

## Acknowledgements

I want to acknowledge the National Science Foundation, National Institute of Health and the UMN Doctoral Dissertation Fellowship for funding.

I thank my advisor Lawrence Que, Jr. for giving me the space and resources to explore ideas and helping me develop as a scientist. I appreciate his attention to detail about how to present information in both the scientific arena and in the classroom, not to mention all of the grammar lessons during the final stages. Lastly, I want to thank him for his patience throughout.

Dr. Victor Young, Jr. showed me a glimpse of the world of crystallography, and I refined my skills as a crystallographer under his tutelage. Without Victor's hands-on help and advice mounting temperature sensitive crystals, the most interesting structures in this dissertation would not have been collected and I am grateful for his contribution.

I have to thank a cadre of post docs throughout my time at the UMN. Chapters 2 and 3 would not be possible without Dr. Genqiang Xue. He did many of the experiments and taught me how to do the rest- I cannot thank him enough. Dr. Jai Prakash supplied the crystals for Chapter 4. It was very fulfilling working with Dr. Prakash while we designed and performed X-ray diffraction experiments for the TMC project. It was a true symbiotic relationship. I want to acknowledge Dr. Jason England for creating the  $S = 2$  high-valent nonheme iron complexes and providing the framework for the study in Chapter 5. His insight gave the project momentum from the beginning.

Professor Eckard Münck and Dr. Katlyn Meier of Carnegie Mellon University provided in-depth Mössbauer studies that gave us critical insight into our systems and we are indebted for it.

Finally, I thank all of the lab members I have worked with over the years. Sometimes I am surprised I made it and you all helped get me through.

Greg,  
May 2015

## Abstract

The structures and reactivities of mono- and dinuclear nonheme iron model complexes were investigated. In Chapters 2 and 3, O-O bond activation of H<sub>2</sub>O<sub>2</sub> by the dinuclear complexes [(Fe<sup>III</sup>)<sub>2</sub>(μ-O)(μ-OH)L<sub>2</sub>]<sup>3+</sup> (**1A**) and [(Fe<sup>III</sup>)<sub>2</sub>(μ-OH)<sub>2</sub>L<sub>2</sub>]<sup>4+</sup> (**2A**), L = tris(3,5-di-methyl-4-methoxypyridyl-2-methyl)amine, to form the high-valent [(Fe<sup>IV</sup>)<sub>2</sub>(μ-O)(OH)(O)L<sub>2</sub>]<sup>3+</sup> (**3A**) and [(Fe<sup>IV</sup>)<sub>2</sub>(μ-O)<sub>2</sub>L<sub>2</sub>]<sup>4+</sup> (**4A**) was studied. H<sub>2</sub>O<sub>2</sub> and H<sub>2</sub>O competed for binding to the Fe centers of **1A** and **2A**, and [H<sub>2</sub>O<sub>2</sub>] was rate limiting under the concentrations studied. The presence of base increased the H<sub>2</sub>O<sub>2</sub> activation rate for **2A**, but not for **1A**. The H<sub>2</sub>O<sub>2</sub> activation rates by **1A** and **2A** were comparable to that of the mononuclear nonheme iron complex [Fe<sup>II</sup>(TMC)]<sup>2+</sup> (TMC = tetramethylcyclam) (*J. Am. Chem. Soc.* **2010**, 2134-2135) after accounting for water inhibition. A crystal structure of [(Fe<sup>IV</sup>)<sub>2</sub>(μ-O)<sub>2</sub>L<sub>2</sub>]<sup>4+</sup> (**4A**), or diamond core, was solved and described the Fe<sub>2</sub>O<sub>2</sub> core in more detail than the original EXAFS structural assignment. In addition, structures of other complexes with Fe<sub>2</sub>O<sub>2</sub>L<sub>2</sub> cores in different oxidation and protonation states were also studied and compared to the Fe<sub>2</sub>O<sub>2</sub> cores of the high-valent enzymes intermediates RNR-X and sMMO-Q.

In Chapter 4, iron complexes supported by the TMC ligand were studied by X-ray crystallography. A second isomer of the [Fe<sup>IV</sup>(O)(TMC)]<sup>2+</sup> complex was found, and the mechanism of conversion to the original isomer was explored. Additionally, the crystal structure of (TMC)Fe<sup>III</sup>(μ-O)Sc(NCCH<sub>3</sub>)(OTf)<sub>4</sub> complex

was obtained and used to reassign the Fe oxidation state of the originally reported (TMC)Fe<sup>IV</sup>( $\mu$ -O)Sc(OH)(OTf)<sub>4</sub> complex. (*Nat. Chem.* **2010**, 756-759)

In Chapter 5, the hydrogen atom transfer (HAT) rates of a series of *S* = 2 mononuclear nonheme iron complexes, [Fe<sup>IV</sup>(O)TMG<sub>2</sub>dien(X)]<sup>2+,+</sup> (X = CH<sub>3</sub>CN, Cl<sup>-</sup>, Br<sup>-</sup>, N<sub>3</sub><sup>-</sup>, CH<sub>3</sub>CO<sub>2</sub><sup>-</sup> and CF<sub>3</sub>CO<sub>2</sub><sup>-</sup>; TMG<sub>2</sub>dien = 1,1-bis{2-[N<sup>2</sup>-(1,1,3,3-tetramethylguanidino)]ethyl}amine), were reported. Substitution of CH<sub>3</sub>CN with carboxylate and halide anions *cis* to the oxo ligand increased the HAT oxidation rate by as much as 15 times. A series of *S* = 1 nonheme iron complexes, [Fe<sup>IV</sup>(O)TPA(Y)]<sup>2+,+</sup> (Y = CH<sub>3</sub>CN, Cl<sup>-</sup>, CH<sub>3</sub>CO<sub>2</sub><sup>-</sup> and CF<sub>3</sub>CO<sub>2</sub><sup>-</sup>; TPA = tris(pyridyl-2-methyl)amine), was also investigated to explore what effect spin state has on reactivity. The HAT rates were similar for the [Fe<sup>IV</sup>(O)TPA(Y)]<sup>2+,+</sup> series, while OAT rates were much faster for the [Fe<sup>IV</sup>(O)TPA(CH<sub>3</sub>CN)]<sup>2+</sup> species.

## Table of Contents

Acknowledgements	i	
Abstract	ii	
List of Tables	vi	
List of Figures	viii	
List of Schemes	xxiii	
List of Equations	xxv	
Chapter 1	1	
<i>Nonheme Iron Enzymes and High-Valent Diiron Models</i>		
1.1	Scope and Aim of Dissertation	2
1.2	Introduction	3
1.2.1	Nonheme Iron Enzymes	3
1.2.2	High-Valent Diiron Model Complexes	5
Chapter 2:		37
<i>Activating the O-O Bond to Form High-Valent Diiron Model Complexes</i>		
2.1	Introduction	38
2.2	Results	42
2.3	Discussion	70
2.4	Conclusion	76
2.5	Experimental	77

Chapter 3:		81
	<i>Structural Investigation of the Diamond Core Motif in Nonheme Iron Chemistry.</i>	
3.1	Introduction	82
3.2	Results and Discussion	84
3.3	Experimental	101
Chapter 4:		113
	<i>X-ray Crystallographic Investigation of Ferryl, Ferric and Ferrous Complexes Supported by the TMC Ligand</i>	
4.1	Introduction	114
4.2	Results	116
4.3	Discussion	129
3.3	Experimental	139
Chapter 5:		157
	<i>The cis- Substitution Effect on Reactivity of S = 2 and S = 1 Ferryl Complexes</i>	
4.1	Introduction	158
4.2	Results and Discussion	161
4.3	Conclusions	178
3.3	Experimental	178
Bibliography		180

## List of Tables

- Table 1.1:** p 6-14  
Spectroscopic Properties of High-Valent Nonheme Model Complexes
- Table 1.2:** p 33-34  
Rate constants of high-valent diiron model complexes supported by ligand L = SR<sub>3</sub>TPA (**A**).
- Table 2.1** p 47  
EXAFS fitting to unfiltered EXAFS data for **2A** solid [Fe<sup>III</sup><sub>2</sub>(μ-OH)<sub>2</sub>(SR<sub>3</sub>TPA)<sub>2</sub>]<sup>4+</sup> using Feff phase and amplitude parameters listed in (Å).
- Table 2.2.** p 50  
EXAFS fitting to unfiltered EXAFS data for **2A**, solution [Fe<sup>III</sup><sub>2</sub>(-μ-O)(OH)<sub>2</sub>(SR<sub>3</sub>TPA)<sub>2</sub>]<sup>4+</sup> using Feff phase and amplitude parameters listed in (Å).
- Table 2.3:** p 72  
Summary of rate constants for the activation of H<sub>2</sub>O<sub>2</sub> by diferric model complexes at -40° C in acetonitrile.
- Table 3.1:** p 87  
Select bond distances and angles for diamond core structures obtained from XRD and XAS.
- Table 3.2:** p 90  
EXAFS fitting to unfiltered EXAFS data of a 1:13 **1A**: BN crystalline sample using Feff phase and amplitude parameters listed in (Å).
- Table 3.3:** p 96  
EXAFS fitting to unfiltered EXAFS data of **5A** using Feff phase and amplitude parameters listed in (Å).



<b>Table 3.4:</b>	p 100
Number of scatterers and scatterer distances (Å) of reactive nonheme diiron enzyme intermediates from XAS	
<b>Table 3.5:</b>	p 103
Crystal structure collection and refinement information of diiron compounds	
<b>Table 4.1:</b>	p 117
Select bond lengths of Fe-O-Sc complexes, Å.	
<b>Table 4.2:</b>	p 132
Structural metrics of TMC supported Fe complexes	
<b>Table 4.3:</b>	p 140-141
Crystal structure collection and refinement information of TMC supported compounds	
<b>Table 5.1:</b>	p 163
Spectroscopic Parameters of Fe <sup>IV</sup> (O)L(X) Complexes and Second-Order Rate Constants for the Oxidation of Triphenylmethane	
<b>Table 5.2:</b>	p 169
Second-order rate constants of substrate oxidation by [Fe <sup>IV</sup> (O)TMG <sub>2</sub> dien(CH <sub>3</sub> CN)] <sup>2+</sup>	
<b>Table 5.3:</b>	p 174
Second-order rate constants for substrate oxidation rates by [Fe <sup>IV</sup> (O)TMG <sub>2</sub> dien(CH <sub>3</sub> CN)] <sup>2+</sup>	

## List of Figures

- Figure 1.1:** p 3  
Active site of nonheme iron enzymes. Left: mononuclear  $\alpha$ -ketoacid dependent dioxygenase <sup>1</sup> and right: diiron enzyme from a family of enzymes that contain a common four-helix bundle supporting the active site.<sup>2</sup>
- Figure 1.2:** p 4  
Reactive oxoiron(IV) species of the enzymes: left- mononuclear  $\alpha$ -ketoacid dependent taurine dioxygenase intermediate J <sup>1,3</sup> and right: soluble methane monooxygenase ( $\text{Fe}^{\text{IV}}\text{Fe}^{\text{IV}}$ ) and class Ia ribonucleotide reductase intermediate X ( $\text{Fe}^{\text{IV}}\text{Fe}^{\text{III}}$ ). Both diiron enzymes are from a family of enzymes that contain a common four-helix bundle supporting the active site.<sup>2</sup>
- Figure 1.3:** p 16  
Top: the first high-valent diiron crystal structure with ellipsoids drawn to the 50% probability level; hydrogen atoms are removed for clarity and atom colors are carbon- blue, nitrogen- lilac, oxygen- red, iron- orange.<sup>4</sup> Bottom left- ligands used in the initial model complexes of nonheme enzymes; bottom right- high-valent diiron core.
- Figure 1.4:** p 18  
Left: TPA variations that support high-valent high-spin diiron compounds; Right: proposed core structure of the  $S = \frac{1}{2}$   $\text{Fe}^{\text{IV}}\text{Fe}^{\text{III}}$  nonheme model complex.
- Figure 1.5:** p 19  
Proposed structure of an  $\text{Fe}^{\text{IV}}\text{Fe}^{\text{III}}$  complex supported by bulky carboxylates ( $\text{Ar}^{\text{Tol}}\text{CO}_2$ ) synthesized by the Lippard group.<sup>5</sup>
- Figure 1.6:** p 20  
Mixed-valent  $\text{Fe}^{\text{IV}}\text{Fe}^{\text{III}}$  species supported by symmetric and asymmetric ligand environments synthesized by the Wieghardt group.<sup>6</sup>

**Figure 1.7:** p 21

X-ray crystal structure and diagram of first diiron(IV) bis- $\mu$ -oxo.<sup>7</sup> The TAML ligand is tetraanionic and X = H or OMe, with X = H shown in the crystal structure. Ellipsoids are drawn to the 50% probability level, hydrogen atoms are removed for clarity and atom colors are: carbon-blue, nitrogen- lilac, oxygen- red and iron-orange.

**Figure 1.8:** p 22

Diiron(IV) cores. Left: First diiron(IV) diamond core model complex supported by ligand **A** (tris(4-methoxy-3,5-dimethylpyridylmethyl)amine or SR<sub>3</sub>TPA).<sup>8</sup> Right: Second diiron(IV) core supported by carboxamido bridging ligands (CXA).<sup>9</sup>

**Figure 1.9:** p 29

Top: di-nucleating ligands used by the Kodera group to support a diferryl model complex; Bottom: reversible O-O bond formation and formation of a diferryl species.<sup>10-12</sup>

**Figure 1.10:** p 32

Rate constants ( $M^{-1}s^{-1}$ ) displayed on the  $\log_{10}$  scale of the oxidation of 9,10-dihydroanthracene (DHA, black columns) and diphenyl(pentafluorophenyl)phosphine (PPh<sub>2</sub>(C<sub>6</sub>F<sub>5</sub>), red columns) by high-valent iron complexes supported by ligand **A** at -80° C. From references <sup>13-15</sup>.

**Figure 2.1:** p 38

Active site of soluble methane monooxygenase (sMMO) responsible for activating O<sub>2</sub>, with R representing the protein backbone.<sup>2</sup>

**Figure 2.2:** p 44

Formation of **4A** from the reaction of 0.3 mM **2A** and 1 eq H<sub>2</sub>O<sub>2</sub> in CH<sub>3</sub>CN at -40° C in 85% yield determined by UV-Vis spectroscopy.

**Figure 2.3:**

p 46

Fourier transform of the unfiltered EXAFS data (inset) of experimental data (dotted line) and best fit (solid line) of: Top- microcrystalline **2A** diluted 20:1 in BN. The best fit was accounted for by four shells at 1.91 Å (two O scatterers), 2.10 Å (four N scatterers), 2.95 Å (six C scatterers) and 3.04 Å (one Fe scatterer) and Bottom- 5 mM acetonitrile solution of **2A**. The best fit model contains five shells at 1.79 Å (one O scatterer), 2.12 Å (five N/O scatterers), 3.03 Å (six C scatterers), 3.42 Å (one Fe scatterer) and a 3.569 Å multiple scattering pathway modeled with a Fe-O-Fe moiety.

**Figure 2.4:**

p 52

Main window: rRaman spectra of **2A** in a CH<sub>3</sub>CN solution using a 413.1 nm excitation energy at 100mW power collected at liquid N<sub>2</sub> temperature. Main window-Top spectra: natural abundance isotopes, bottom spectra: <sup>18</sup>O isotopically labeled **2A** and Inset: CD<sub>3</sub>CN solvent was used with <sup>18</sup>O isotopically labeled **2A** to move solvent peak obstructing the <sup>18</sup>O vibration.

**Figure 2.5:**

p 54

Titration of 0.3 mM solution of **2A** in CH<sub>3</sub>CN with 3-bromopyridine to form the conjugate base **1A**. Monitoring the formation of **1A** (red circles) and **1B** (black squares) by the increase of the 550 nm band from the titration of **2A** and **2B** with of 3-bromopyridine (Inset).

**Figure 2.6:**

p 56

The oxidation of H<sub>2</sub>O<sub>2</sub> (under pseudo-first order conditions) by a 0.3 mM solution of **3A** in acetonitrile at -40° C (blue, dashed line) and the formation of the product **5A** (green, solid line). Inset: the rate of formation of **5A** from the reaction of **3A** and varying concentrations of H<sub>2</sub>O<sub>2</sub> (red) and D<sub>2</sub>O<sub>2</sub> (blue). The KIE was found to be 25.

**Figure 2.7:**

p 58

Formation of **5A** and 2,4,6-tri-*tert*-butylphenoxy radical from the reaction of 0.3 mM (**1<sup>WA</sup>**)<sup>16</sup> and 2,4,6-tri-*tert*-butylphenol (TTBP) and 100 mM H<sub>2</sub>O in acetonitrile at -40° C with 1 eq. mM H<sub>2</sub>O<sub>2</sub>. Kinetic traces of Formation of **5A** (620 nm) and 2,4,6-tri-*tert*-butylphenoxy radical (400 nm) from **1A**, H<sub>2</sub>O<sub>2</sub> and TTBP.

**Figure 2.8:**

p 58

Activation of H<sub>2</sub>O<sub>2</sub> in an acetonitrile solution at -40° C by 0.3 mM **1A** (black squares) 0.1 M H<sub>2</sub>O and 0.3 mM TTBP, and 0.5 mM **2A** (red circles) with H<sub>2</sub>O<sub>2</sub> in acetonitrile with 0.1 M H<sub>2</sub>O. The rate constants were determined to be 8 M<sup>-1</sup>s<sup>-1</sup> and 40 M<sup>-1</sup>s<sup>-1</sup> for **1A** and **2A** respectively. The concentration of water from the 70% H<sub>2</sub>O<sub>2</sub> was accounted in both reactions and was kept constant at 0.1 M H<sub>2</sub>O.

**Figure 2.9:**

p 60

Dependence of the concentration of H<sub>2</sub>O on the activation of a 2.5 mM H<sub>2</sub>O<sub>2</sub> acetonitrile solution at -40 °C by 0.3 mM **1A** (black squares) and 0.5 mM **2A** (red circles). Inset: plot of 1/k<sub>obs</sub> vs. H<sub>2</sub>O.

**Figure 2.10:**

p 63

Reaction of 0.25 mM **2A** and 2.7 mM 3-bromopyridine (black) with 1.3 mM H<sub>2</sub>O<sub>2</sub> and 1.1 mM H<sub>2</sub>O (from 70% H<sub>2</sub>O<sub>2</sub>) to form an intermediate (blue) and **4A** (red). The time traces at 705 and 875 nm are shown in the inset.

**Figure 2.11:**

p 64

Monitoring the initial rate of the growth of the 705 nm band with increasing concentration of 3-bromopyridine in a 0.25 mM **2A**, 1.3 mM H<sub>2</sub>O<sub>2</sub> and 1.1 mM H<sub>2</sub>O (from 70% H<sub>2</sub>O<sub>2</sub>) in CH<sub>3</sub>CN.

**Figure 2.12:** p 64  
Monitoring the rate of the growth of the 475 band (black squares) and the decay of the 705 nm band (red circles) with increasing concentration of 3-bromopyridine in a 0.25mM **2A**, 1.3 mM H<sub>2</sub>O<sub>2</sub> and 1.1 mM H<sub>2</sub>O (from 70% H<sub>2</sub>O<sub>2</sub>) in CH<sub>3</sub>CN.

**Figure 2.13:** p 65  
Difference spectrum of the spectrum of **4A** (inset red) from the spectrum at the maximum formation of the feature at ~705 nm (inset black) for the reaction of **2A** (0.25mM) and 3-bromopyridine (2.7 mM) with H<sub>2</sub>O<sub>2</sub> (1.3 mM).

**Figure 2.14:** p 66  
Reaction of 0.4 mM **2A** with 1 eq. H<sub>2</sub>O<sub>2</sub> in the presence of 1 eq. 2,4,6-tri-*tert*-butylphenol in CH<sub>3</sub>CN at -40° C to form **5A**.

**Figure 2.15:** p 69  
Reaction of 0.2 mM **2A**, 0.4 mM tri-*tert*-butylphenol and 3-bromopyridine with 2 mM H<sub>2</sub>O<sub>2</sub> in acetonitrile at -40° C.

**Figure 2.16:** p 69  
D<sub>2</sub>O (red circles) H<sub>2</sub>O (black squares) for the activation of H<sub>2</sub>O<sub>2</sub> or D<sub>2</sub>O<sub>2</sub> by a 0.5 mM solution of **2A** in acetonitrile at -40° C.

**Figure 2.17:** p 75  
Proposed structure of diferric-hydroxo-peroxo species (**III**, Scheme 2.5) with ligands trans to the peroxo highlighted in red.

**Figure 2.18:** p 76  
Top: di-nucleating ligands used by the Kodera group to support a diferryl model complex; Bottom: reversible O-O bond formation and formation of a diferryl species.<sup>10-12</sup>

**Figure 3.1:** p 83

Summary of diiron cores used in Chapter 3.

**Figure 3.2:** p 86

Structure of **4A** ( $[\text{Fe}^{\text{IV}}_2\text{-}\mu\text{-O}_2]^{4+}$ ), thermal ellipsoids drawn to the 50% probability level, with hydrogen atoms removed for clarity. An inversion center is present at the center of the  $\text{Fe}_2\text{O}_2$  core resulting in the one half of the molecule unique. Selected bond distances (Å) and angles (°): Fe1-O1, 1.787(6) ; Fe1-O1A, 1.810(9); Fe1-Fe1A, 2.711(4); Fe-N<sub>ave</sub>, 1.974; Fe1-O1-Fe1A, 97.8(4).

**Figure 3.3:** p 89

Fourier-transformed Fe K-edge EXAFS data obtained at 20 K of a 1:13 **1A**:BN solid state sample. (*Inset*)  $k^3\chi'(k)$  data. Fourier transform range 1-14 Å<sup>-1</sup>; experimental data (dotted line) and best fit solid line; scatterers consisting of 1 O at 1.80 Å, 1 O at 1.97 Å, 4 N at 2.14 Å, 1 Fe at 2.80 Å and an additional Fe-C shell at 3.01 Å.

**Figure 3.4:** p 92

Thermal ellipsoid plot of **2A** showing 50% probability ellipsoids. Non-oxygen bound hydrogen atoms, counterions and solvent molecules were removed for clarity. Colors of atoms: carbon- gray, oxygen- red, nitrogen- blue, iron- orange, hydrogen- green sphere. Selected bond distances (Å) and angles (°): Fe1-O1, 1.926(2) ; Fe1-O1A, 1.995(2); Fe1-Fe1A, 23.0224(10); Fe-N<sub>ave</sub>, 2.115; Fe1-O1-Fe1A, 100.86(11).

**Figure 3.5:** p 94

Structure of **5A** with hydrogen atoms, counterions and solvent molecules removed for clarity. Ellipsoids are displayed at 50% probability level. Atom colors: carbon- gray, oxygen- red, nitrogen- blue, iron-green. Selected bond distances (Å) and angles (°): Fe1-O1, 1.780(4) ; Fe1-O1A, 1.827(5); Fe1-Fe1A, 2.596(2); Fe-N<sub>ave</sub>, 1.995; Fe1-O1-Fe1A, 92.1(2).

**Figure 3.6:** p 95  
Fourier-transformed Fe K-edge EXAFS data obtained at 20 K of an 8 mM solution sample of **5A** in acetonitrile. (*Inset*)  $k^3\chi'(k)$  data. Fourier transform range 2-14 Å<sup>-1</sup>; experimental data (dotted line) and best fit solid line; scatterers consisting of 1 O at 1.75 Å, 3 N at 1.95 Å, 1 Fe at 2.57 Å and two additional Fe-C shells at 2.77 and 2.93 Å modeled with 4 and 6 scatterers respectively.

**Figure 3.7:** p 106  
Asymmetric unit of **4A** with thermal ellipsoids drawn to the 50% probability level and hydrogen atoms are removed for clarity.

**Figure 3.8:** p 107  
Packing diagram of **4A** looking down the a-axis. Hydrogen atoms are removed for clarity. The butyronitrile solvent molecules and the perchlorate counter ions form a channel surrounding the tetra-cationic compound of interest, likely buffering the large positive charged cations from their neighbors. Atom colors: carbon- gray, oxygen- small red, nitrogen- blue, iron- large red, chlorine- green.

**Figure 3.9:** p 109  
Asymmetric unit of **5A** with thermal ellipsoids drawn to the 50% probability level and hydrogen atoms are removed for clarity.

**Figure 3.10:** p 111  
Asymmetric unit of **2A** with thermal ellipsoids drawn to the 50% probability level and hydrogen atoms are removed for clarity.

**Figure 4.1:** p 114  
Crystal structure and cartoon of [Fe<sup>IV</sup>(O)TMC(CH<sub>3</sub>CN)]<sup>2+</sup> (**4.1**), the first well characterized Fe<sup>IV</sup>=O complex.<sup>17</sup>



**Figure 4.2:** p 115

Crystal structure of  $[(\text{OTf})_4(\text{OH})\text{Sc}^{\text{III}}(-\mu\text{-O})\text{Fe}^{\text{IV}}\text{TMC}]$ , **4.2**, reproduced from reference <sup>18</sup>. An independent computational study by Swart assigned the oxidation state of the iron atom to  $\text{Fe}^{3+}$  with a terminal aqua bound to the scandium atom.<sup>19</sup>

**Figure 4.3:** p 117

Crystal structure of **4.2a**. Thermal ellipsoids are drawn to the 50% probability level with hydrogen atoms and solvent molecules removed for clarity. Select bond distances (Å): Fe1-O1, 1.748(5); Fe-N<sub>Ave</sub>, 2.083; Sc1-O1, 1.888(5); Sc1-O<sub>OTf Ave</sub>, 2.083; Sc1-N<sub>CH<sub>3</sub>CN</sub>, 2.310(10); Fe1-Sc1, 3.6358(16).

**Figure 4.4:** p 118

Overlay of the Fe,  $\mu\text{-O}$ , Sc and all non-hydrogen atoms of the TMC ligand of **4.2** and **2a** resulting in a root-mean-square deviation of 0.0742 Å, as calculated by the OFIT command of SHELXP.<sup>20</sup> Atoms of **4.2a** are modeled as isotropic to the 25% probability level and atoms of **4.2** are displayed as small dots. Hydrogen atoms are removed for clarity.

**Figure 4.5:** p 119

H-bond acceptors of **4.2** located at standard donor-acceptor distances.<sup>21</sup> Figure 4.5 was create from the published crystal structure of **4.2** by the program Mercury CSD 3.31.<sup>18</sup>

**Figure 4.6:**

p 122

Top Left: XANES spectra of the **4.3** (black) and **4.1** (red) with the first derivative of the XANES spectra and pre-edge region displayed for comparison. The edge energies were found to be equal at 7123.8 eV and were determined by the maximum intensity of the first derivative in the rising edge. The pre-edge areas were found to be 42 a.u. for **4.3** and 32 a.u. for **4.1** when accounting for sample purity determined by Mössbauer spectroscopy. Top Right: functions used to model pre-edge transition for **4.3** (black) and **4.1** (red). Bottom: Fit of **4.3** (Left) and **4.1** (Right) with experimental data displayed with dots, rising edge modeled with the black line, pre-edge transition modeled with the blue line and over all fit displayed in red. The residuals of the data from the fit are displayed below.

**Figure 4.7:**

p 124

Thermal ellipsoids of the crystal structures of **4.4** and **4.5** are drawn at the 50% probability level with hydrogen atoms removed for clarity. **Left:** top- structure of **4.4** produced from the reaction of **4.1** and one equivalent  $[\text{Et}_4\text{N}][\text{FeCl}_4]$ . One acetonitrile molecule removed for clarity. Bottom Left- cartoon of **4.4**; **Right:** top- structure of **4.5** produced from the reaction between **4.3** and one equivalent  $[\text{Et}_4\text{N}][\text{FeCl}_4]$ . The OTf counter anion is included in the picture and two acetonitrile molecules were removed for clarity. Bottom right- cartoon of **4.5**. Select bond distances (Å) and angles (°): **4.4:** Fe1-O1, 1.8511(12); Fe1-N<sub>ave</sub>, 2.206; Fe1-Cl1, 2.3586(5); Fe2-O1, 1.7712(12); Fe1-O1-Fe2, 1.77.31(9); Fe1-Fe2 3.6213(5) **4.5:** Fe1-O1, 1.771(2); Fe1-N<sub>ave</sub>, 2.166; Fe2-O1, 1.771(2); Fe1-O1-Fe2, 171.21(14); Fe1-Fe2, 3.5056(7).

**Figure 4.8:**

p 126

Left : X-ray crystal structure of **4.3<sub>DCM</sub>** with thermal ellipsoids drawn to the 50% probability level. Hydrogen atoms, one OTf counterion and two dichloromethane solvent molecules were removed for clarity. Right: cartoon of **4.3<sub>DCM</sub>**. Select bond distances (Å): Fe1-O1, 1.626(4); Fe-N<sub>ave</sub>, 2.065; Fe-O<sub>OTf</sub>, 2.146(4).

**Figure 4.9:** p 127

Crystal structure and cartoon of **4.6** with ellipsoids drawn to the 50% probability level and hydrogen atoms, solvent molecules and OTf counter anions removed for clarity. Three molecules of **4.6** were located in the unit cell and only one is displayed for clarity. Select bond distances (Å), average of the two non-disordered molecules in the unit cell: Fe1-O1, 2.032(3); Fe-N<sub>ave</sub>, 2.181.

**Figure 4.10:** p 129

X-ray crystal structure of **4.8**. Thermal ellipsoids are drawn at the 50% probability level and hydrogen atoms and the counter cation [(Bu)<sub>4</sub>N]<sup>+</sup> are removed for clarity. The complex of interest is disordered over two positions and only one is displayed for clarity. Select bond distances (Å) and angles (°) from an average of two positions in disorder modeling: Fe1-O1, 1.931; Fe1-O2, 1.835; Fe2-O1, 1.763; Fe3-O2, 1.758; Fe-N<sub>ave</sub>, 2.211; Fe1-Fe2, 3.6705(32); Fe1-Fe3, 3.5738(32); Fe1-O1-Fe2, 166.5; Fe1-O2-Fe3, 169.1, O1-Fe1-O2, 172.8.

**Figure 4.11:** p 137

Resulting electronic absorption spectrum of adding 1 equivalent F<sup>-</sup> to 1 mM [Fe<sup>IV</sup>(O)TMC(OTf)](OTf) in dichloromethane at -40° C. The double-hump feature in the near-infra red region closely resembles the electronic absorption spectrum of the oxo-iron(IV) species reported in reference <sup>22</sup>.

**Figure 4.12:** p 138

Space filling models of the complexes **4.3<sub>DCM</sub>** (left) and **4.1** (right).

**Figure 4.13:** p 139

The solvent exposed areas of **4.3<sub>DCM</sub>** (left) **4.1** (right) illustrated by dots. Values of 7.5 and 6.7 Å<sup>2</sup> were calculated for **4.3<sub>DCM</sub>** and **4.1**, respectively by the program PyMOL v1.3r1.

**Figure 4.14:** p 143

The mirror bisecting the Fe-O-Sc axis and displaying the main-molecule disorder.

**Figure 4.15:** p 145

Disorder modeling of **4.2a**. Thermal ellipsoids are drawn to the 50% probability level and hydrogen atoms and solvent molecules are removed for clarity. Top: Four positions of the Sc-bound acetonitrile ligand. Middle: Pair of **4.2a** with crystallographically reasonable nonbonding distances between acetonitrile ligands; the pairs of  $\alpha$ -carbons are  $\sim 3.6$  Å apart. Bottom: Head-to-head packing diagram of **4.2a** looking down the c-axis.

**Figure 4.16:** p 147

Packing diagrams of **4.2a**. Thermal ellipsoids drawn to the 50% probability level and hydrogen atoms are removed for clarity. Top: Looking down the a-axis, layers of acetonitrile are visible surrounding a layer of **4.2a**. Bottom: Looking down the c-axis. Acetonitrile solvent molecules are colored green to highlight the solvent channels.

**Figure 4.17:** p 148

Asymmetric unit of **4.4** with thermal ellipsoids drawn to the 50% probability level and hydrogen atoms removed for clarity.

**Figure 4.18:** p 150

Asymmetric unit of **4.5** with thermal ellipsoids drawn to the 50% probability level and hydrogen atoms removed for clarity. The two positions of the OTf counter anion are displayed above.

**Figure 4.19:** p 152

Asymmetric unit of **4.3<sub>DCM</sub>** with thermal ellipsoids drawn to the 50% probability level and hydrogen atoms removed for clarity. The two positions of the Fe complex and one dichloromethane molecule are displayed above.

**Figure 4.20:** p 153

Asymmetric unit of **4.6** with thermal ellipsoids drawn to the 50% probability level and hydrogen atoms removed for clarity. The two positions one Fe complex, two OTf counter anions and one dichloromethane molecule are displayed above.

**Figure 4.21:** p 154

Unit cell of **4.6** displayed looking down the a-axis. A group of six Fe complexes are located around a pseudo rotation element at (0, 0, 0).

**Figure 4.22:** p 155

Asymmetric unit of **4.8** with thermal ellipsoids drawn to the 50% probability level and hydrogen atoms removed for clarity. The two positions of the Fe complex and [Bu<sub>4</sub>N]<sup>+</sup> are displayed above.

**Figure 5.1:** p 160

Nonheme ferryl complexes: left- [Fe<sup>IV</sup>(O)TMG<sub>3</sub>tren]<sup>2+</sup> (**5.1**); center- [Fe<sup>IV</sup>(O)TMG<sub>2</sub>dien(X)]<sup>2+,+</sup> (**5.2-X**), X = CH<sub>3</sub>CN, Cl<sup>-</sup>, Br<sup>-</sup>, CH<sub>3</sub>CO<sub>2</sub><sup>-</sup>, CF<sub>3</sub>CO<sub>2</sub><sup>-</sup> and N<sub>3</sub><sup>-</sup>; [Fe<sup>IV</sup>(O)TPA(X)]<sup>2+,+</sup> (**5.3-X**), X = CH<sub>3</sub>CN, Cl<sup>-</sup>, CH<sub>3</sub>CO<sub>2</sub><sup>-</sup>, CF<sub>3</sub>CO<sub>2</sub><sup>-</sup>. TMG<sub>3</sub>tren = 1,1,1-tris{2-[N<sub>2</sub>-(1,1,3,3- tetramethylguanidino)]ethyl}amine, TMG<sub>2</sub>dien = 1,1-bis{2-[N<sub>2</sub>-(1,1,3,3- tetramethylguanidino)]ethyl} methylamine, TPA = tris(2-pyridylmethyl)amine.

**Figure 5.2:** p 162

Electronic absorption spectra of **5.2** (black), **5.2-Cl** (red), **5.2-Br** (blue), **5.2-OAc** (magenta), **5.2-O<sub>2</sub>CCF<sub>3</sub>** (green) and **5.2-N<sub>3</sub>** (grey) in a 0.4 mM [Fe] CH<sub>3</sub>CN solution at -30° C.

**Figure 5.3:**

p 164

Decay of the spectrum of **5.2** in the presence of substrate. A single exponential function fit to the time traces at 550 and 820 nm resulted in the same observed rate constant ( $k_{obs}$ ). The spectra and time traces are representative of all kinetic experiments. The first ~10 seconds of the reaction were not modeled in the exponential fit to allow for the reactants to mix.

**Figure 5.4:**

p 165

Observed rate constants of **5.2-X** complexes plotted vs. substrate concentration to obtain second-order rate constants ( $k_2$ ). Triphenylmethane oxidation rate constants were determined for **5.2** (black squares), **5.2-Cl** (red circles), **5.2-Br** (blue diamonds), **5.2-OAc** (magenta down triangles), **5.2-O<sub>2</sub>CCF<sub>3</sub>** (green up triangles) and **5.2-N<sub>3</sub>** (grey left triangles) in a 1 mM [Fe] CH<sub>3</sub>CN solutions at -30° C.

**Figure 5.5:**

p 166

Electronic absorption spectra of **5.3** (black), **5.3-Cl** (red), **5.3-OAc** (magenta) and **5.3-CF<sub>3</sub>CO<sub>2</sub><sup>-</sup>** (green) in a 0.6 mM [Fe] acetonitrile solution.

**Figure 5.6:**

p 168

Observed rate constants of **5.3-X** complexes plotted vs. substrate concentration to obtain second-order rate constants ( $k_2$ ). Triphenylmethane oxidation rate constants were determined for **5.3** (black squares), **5.3-Cl** (red circles), **5.3-OAc** (magenta down triangles) and **5.3-O<sub>2</sub>CCF<sub>3</sub>** (green up triangles) in a 1 mM [Fe] CH<sub>3</sub>CN solutions at -30° C.

**Figure 5.7:** p 170  
Normalized second-order rate constants ( $k_2'$ ) of the oxidation of substrates by **5.2** plotted vs. the bond dissociation energy of the substrates.  $k_2'$  values are determined by dividing the  $k_2$  of a reaction by the number of C-H bonds available for oxidation. Reactions were conducted in CH<sub>3</sub>CN at -30° C under pseudo-first-order conditions.

**Figure 5.8:** p 172  
Gibbs Free energy of activation ( $\Delta G^\ddagger$ ) of triphenylmethane oxidation plotted vs. the energy of the near-infra red band of in the electronic absorption spectra of the ferryl complexes **5.2-X** (black squares) and **5.3-X** (red circles).

**Figure 5.9:** p 173  
Observed rate constants ( $k_{obs}$ ) of thioanisole oxidation by **5.2** plotted vs. thioanisole concentration to obtain second-order rate constants ( $k_2$ ). The reactions were in a 0.2-1.0 mM [Fe] acetonitrile solutions.

**Figure 5.10:** p 174  
Observed rate constants ( $k_{obs}$ ) of triphenylmethane oxidation by **5.2** plotted vs. triphenylmethane concentration to obtain second-order rate constants ( $k_2$ ). The reactions were in a 0.2-1.0 mM [Fe] acetonitrile solutions.

**Figure 5.11:** p 175  
Eyring plot of the oxidation of thioanisole (red circles) and triphenylmethane (black squares) by **5.2** in a 0.2-1 mM [Fe] acetonitrile solution between 233-273 K. Eyring Y axis is equal to  $R(\ln(k \cdot h \cdot k_B^{-1} \cdot T^{-1}))$  with the variables defined in equation 5.1.

**Figure 5.12:** p 175  
Oxidation of rates of thioanisole by **5.2** (red dots) and **3** (black squares) in a 1 mM [Fe] acetonitrile solution at -40° C.

**Figure 5.13:**

p 177

Cyclic voltamograms of an 1 mM  $[\text{Fe}^{\text{II}}\text{TMG}_2\text{dien}(\text{OTf})_2]$  in acetonitrile (1.0 mM  $[\text{Bu}_4\text{N}][\text{PF}_6]$  as supporting electrolyte) in a  $\text{N}_2(\text{g})$  environment using a glassy carbon working electrode with a Pt wire as the auxiliary and reference electrodes. Potential is referenced to ferrocenium/ferrocene couple.

**Figure 5.14:**

p 177

Plot of the  $\log k_2$  values for the oxidation of thioanisole by nonheme ferryl complexes at  $-10^\circ \text{C}$  vs. the  $E_{1/2}$  of the  $\text{Fe}^{\text{III}}/\text{Fe}^{\text{II}}$  of the Fe starting materials (vs. the ferrocenium/ferrocene couple). Red circles: compounds **5.2** and **5.3**; black squares: nonheme ferryl complexes supported by pentadentate ligands reported in reference <sup>23</sup>. The  $k_2$  value for thioanisole oxidation at  $-10^\circ \text{C}$  by species **5.3** was estimated by scaling the rate of thioanisole oxidation of **5.2** at  $-10^\circ \text{C}$  with the ratio of the thioanisole oxidation rates of **5.2** and **5.3** at  $-40^\circ \text{C}$ .



## List of Schemes

**Scheme 1.1:** p 23

Synthetic scheme of high-valent diiron complexes supported by ligand **A** (tris(4-methoxy-3,5-dimethylpyridylmethyl)amine).

**Scheme 2.1:** p 39

Activation of O<sub>2</sub> by sMMO and peroxide shunt pathway displayed in the center.<sup>24,25</sup> The protein backbone is removed for clarity.

**Scheme 2.2:** p41

Activation of H<sub>2</sub>O<sub>2</sub> by diiron complexes supported by the tris(4-methoxy-3,5-dimethylpyridylmethyl)amine ligand to form high-valent species.

**Scheme 2.3:** p 42

Activation of H<sub>2</sub>O<sub>2</sub> by the diiron(III) complex supported by ligand **A** to form the high valent diamond core **4A**.

**Scheme 2.4:** p 43

Possible core formulations of **2A** base on previous diferric species.<sup>26</sup>

**Scheme 2.5:** p 53

Structures of **2A** in the solid and solution state are shown in above. Acetonitrile may also play the role of the additional water molecule shown above.

**Scheme 2.6:** p 56

Activation of H<sub>2</sub>O<sub>2</sub> by **1A** and subsequent oxidation of H<sub>2</sub>O<sub>2</sub>.

- Scheme 2.7:** p 57  
Reaction of **1A** with H<sub>2</sub>O<sub>2</sub> in the presence of 2,4,6-tri-*tert*-butylphenol (TTBP).
- Scheme 2.8:** p 61  
Water inhibition of the activation of H<sub>2</sub>O<sub>2</sub> by **1A**, top and **2A** bottom.
- Scheme 2.9:** p 66  
H<sub>2</sub>O<sub>2</sub> activation by **2A** in the presence of 2,4,6-tri-*tert*-butylphenol (TTPB).
- Scheme 2.10:** p 70  
Proposed mechanism for the activation of H<sub>2</sub>O<sub>2</sub> by diiron compounds **1A** and **2A**. The amine N atom is *trans* to the oxo or (hydro)peroxo ligand when noted L' and the substituted pyridine is *trans* to the hydroxo or (hydro)peroxo ligand when noted L". Brackets indicate a proposed transient intermediate.
- Scheme 4.1:** p 134  
Proposed [Fe<sup>IV</sup>(O)TMC(CH<sub>3</sub>CN)]<sup>2=</sup> Inversion Mechanism
- Scheme 4.2:** p 135  
Proposed [Fe<sup>IV</sup>(O)TMC(CH<sub>3</sub>CN)]<sup>2+</sup> Synthesis Mechanism
- Scheme 4.3:** p 136  
Proposed Ferric-peroxo Precursor to Ferryl Complex Conversion. The crystal structure of the ferric-peroxo starting material is displayed on the left,<sup>116</sup> and the crystal structure of the ferryl product, **4.1**, is displayed on the right.<sup>17</sup>

## List of Equations

**Equation 2.1:** p 61  
Proposed model of the activation of  $\text{H}_2\text{O}_2$  by diiron compounds.

**Equation 5.1:** p 171  
Transition State Theory Equations



*Chapter 1: Nonheme Iron Enzymes and High-Valent Diron Models*

## 1.1 Scope and Aim of Dissertation

Chapter 1 introduces nonheme iron enzymes and reviews previously published high-valent diiron model compounds.

Chapter 2 investigates diiron compounds that activate the O-O bond of H<sub>2</sub>O<sub>2</sub> to form high-valent species.<sup>8,27</sup> Understanding how these systems activate H<sub>2</sub>O<sub>2</sub> will provide insight into the activation of an O-O bond by diiron systems.

Chapter 3 explores the diiron diamond core motif with X-ray crystallography and EXAFS analysis. The structural features observed in the synthetic model complexes are compared to the models of the high-valent enzyme intermediates derived from computational and EXAFS techniques.

Chapter 4 examines the X-ray crystallography of the tetramethylcyclam ligand (TMC) that supported the well-characterized first Fe<sup>IV</sup>=O species.<sup>17</sup> The crystal structures of geometric isomers of the TMC supported ferryl species are investigated. In addition, the crystal structure of the Sc<sup>3+</sup> adduct of the 2003 ferryl species<sup>18</sup> is reviewed and the oxidation state is re-assigned.

Chapter 5 probes the reactivity of the first well-characterized S = 2 family of mononuclear Fe<sup>IV</sup>=O complexes supported by the TMG<sub>2</sub>dien ligand.<sup>28</sup> In it, reactivities of the *cis* substituted complexes are investigated to gain insight into how a ligand *cis* to the oxo affects the substrate oxidation rate. Additionally, a parallel experiment on a series of S = 1 *cis* substituted ferryl species is completed and compared to the series of S = 2 complexes.

## 1.2 Introduction

### 1.2.1 Nonheme Iron Enzymes

Nonheme iron enzymes perform a wide variety of chemical transformations. These enzymes are categorized into mono- and di-nuclear active sites.<sup>1-3</sup> Both types of enzymes support their iron centers with histidine and carboxylate amino acids (Figure 1.1). The reactive intermediates of both mono and dinuclear enzymes are known to be oxoiron(IV) species (Figure 1.2), and are responsible for a deluge of life-sustaining and industrially important transformations.<sup>1-3</sup>

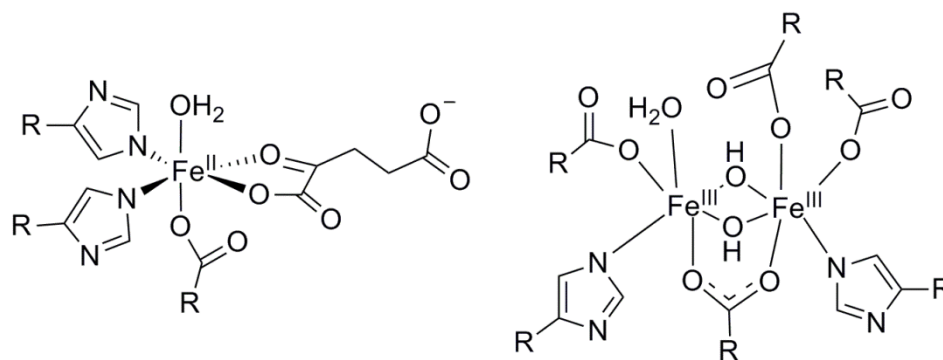


**Figure 1.1:** Active sites of nonheme iron enzymes. Left: a mononuclear  $\alpha$ -ketoacid dependent dioxygenase<sup>1</sup> and right: a diiron enzyme from a family of enzymes that contain a common four-helix bundle supporting the active site.<sup>2</sup>

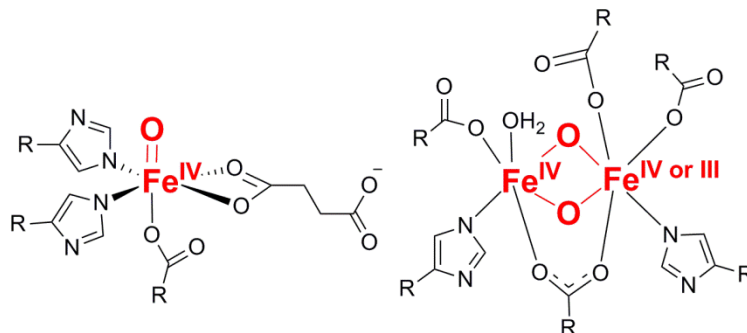


**Figure 1.2:** Reactive oxoiron(IV) species of the enzymes: left- mononuclear  $\alpha$ -ketoacid dependent taurine dioxygenase intermediate J<sup>1,3</sup> and right: soluble methane monooxygenase ( $\text{Fe}^{\text{IV}}\text{Fe}^{\text{IV}}$ ) and class Ia ribonucleotide reductase intermediate X ( $\text{Fe}^{\text{IV}}\text{Fe}^{\text{III}}$ ). Both diiron enzymes are from a family of enzymes that contain a common four-helix bundle supporting the active site.<sup>2</sup>

Mononuclear nonheme centers in biology catalyze many important reactions including the pterin-dependent hydroxylation with phenylalanine hydroxylase, antibiotic biosynthesis by isopenicillin *N*-synthase and clavamate synthase, selective halogenation of a C-H bond with the enzymes CytC3 and SyrB2, oxidation of taurine by the  $\alpha$ -ketoacid dependent taurine dioxygenase (TauD), anti-tumor activity of the cancer drug Bleomycin and the degradation of 2,4-D (2,4-dichlorophenoxyacetic acid) by the  $\alpha$ -ketoacid dependent enzyme TfdA.<sup>1,3,29–33</sup> 2,4-D is one of the most widely used herbicides in the world and an ingredient in Agent Orange. In all cases, a  $\text{Fe}^{\text{IV}}=\text{O}$ , or ferryl, moiety is accepted as the active oxidant (Figure 1.2).<sup>3</sup>

Dinuclear nonheme enzymes are involved in many diverse reactions and functions including fatty acid desaturation in  $\Delta^9$  stearoyl-acyl carrier protein desaturase ( $\Delta^9\text{D}$ ), regulation of cell proliferation in the biosynthesis of hypusine in human deoxyhypusine hydroxylase (hDOHH), biosynthesis of the antibiotic



chloramphenicol by the enzymes CmlP and CmlI and the production of fuel-length hydrocarbons from aldehyde precursors by aldehyde decarbonylase.<sup>2,34–36</sup> One subset of diiron enzymes contain a common four-helix bundle that supports a diiron center coordinated by a histidine and carboxylate-rich center.<sup>2</sup> Two well-studied members from the four-helix bundle family of enzymes are soluble methane monooxygenase (sMMO) and subunit R2 of class Ia ribonucleotide reductase (RNR). The enzyme sMMO selectively oxidizes methane to methanol and the enzyme RNR plays a vital role in the proliferation of eukaryotic cells by participating in the production of DNA from RNA. These two enzymes activate O<sub>2</sub> in a similar manner and form similar high-valent intermediates formulated as a {Fe<sup>IV</sup>-(μ-O)<sub>2</sub>Fe<sup>IV</sup>} and {Fe<sup>IV</sup>-(μ-O)<sub>2</sub>Fe<sup>III</sup>} species for sMMO and RNR, respectively (Figure 1.2).<sup>2</sup> Clearly, studying the mono and dinuclear high-valent species is of utmost interest to understand these important reactions.

### 1.2.2 High-Valent Diiron Model Complexes

Synthetic model compounds have made important contributions to understanding of many nonheme enzyme systems. The model systems have provided important spectroscopic and structural models that have helped identify important structural features for the enzyme systems. Additionally, the enzyme structure-function relationships controlling the difficult transformations have been investigated with the model systems. Detailed reviews of mono-iron high-valent nonheme model complexes exist,<sup>37,38</sup> but few are available for their diiron counterparts and the high-valent diiron species are summarized here with spectroscopic properties listed in Table 1.1.

**Table 1.1:** Spectroscopic Properties of High-Valent Nonheme Model Complexes

Complex:	$\lambda$ (nm), ( $\epsilon$ M <sup>-1</sup> , cm <sup>-1</sup> )	$S_{\text{(total)}}$ , g (G)	E/D	$\delta$ (mm/s)	$\Delta E_Q$ (mm/s)	$D$ (cm <sup>-1</sup> )	ref
[Fe <sup>IV</sup> -( $\mu$ -O) <sub>2</sub> Fe <sup>III</sup> (TPA) <sub>2</sub> ] <sup>3+</sup>	614 (3500)	3/2, 4.40, 3.95, 2.00	0.04	0.11	0.53	-	39,40
[Fe <sup>IV</sup> -( $\mu$ -O) <sub>2</sub> Fe <sup>III</sup> (5-Me <sub>3</sub> TPA) <sub>2</sub> ] <sup>3+</sup>	370 (8000) 615 (5000)	3/2, 4.45, 3.90, 2.01	0.04	0.12	0.49	30	40
[Fe <sup>IV</sup> -( $\mu$ -O) <sub>2</sub> Fe <sup>III</sup> (5-Et <sub>3</sub> TPA) <sub>2</sub> ] <sup>3+</sup>	614 (3200)	3/2 4.45, 390, 2.01	0.041	-	-	37.9	4,41,42
[Fe <sup>IV</sup> -( $\mu$ -O) <sub>2</sub> Fe <sup>III</sup> (SR <sub>3</sub> TPA) <sub>2</sub> ] <sup>3+</sup> , <b>5A</b>	350 (10000)sh 620 (5300)	3/2	-	0.12	0.44	-	8
[O=Fe <sup>IV</sup> - $\mu$ -O-Fe <sup>III</sup> (6-MeTPA) <sub>2</sub> ] <sup>3+</sup>	~350 (8000)	1/2, 2.00 ( <sup>57</sup> Fe and <sup>17</sup> O broadening)	-	Fe <sup>III</sup> 0.48 Fe <sup>IV</sup> 0.08	Fe <sup>III</sup> 1.6 Fe <sup>IV</sup> 0.5	-	43
[O=Fe <sup>IV</sup> - $\mu$ -O-Fe <sup>III</sup> -(OH <sub>2</sub> )(6-Me <sub>3</sub> TPA) <sub>2</sub> ] <sup>3+</sup>	-	1/2, 1.999	-	Fe <sup>III</sup> 0.50 Fe <sup>IV</sup> 0.10	Fe <sup>III</sup> 1.3 Fe <sup>IV</sup> 1.14	-	44,45

Table 1.1: Continued Complex:	$\lambda$ (nm), ( $\epsilon$ M <sup>-1</sup> , cm <sup>-1</sup> )	$S_{\text{(total)}}$ , g (G)	E/D	$\delta$ (mm/s)	$\Delta E_Q$ (mm/s)	$D$ (cm <sup>-1</sup> )	ref
{Fe <sup>IV</sup> Fe <sup>III</sup> (Ar <sup>Tol</sup> CO <sub>2</sub> ) <sub>4</sub> }	~670 (1700)	1/2,	-	Fe <sup>III</sup> 0.55	Fe <sup>III</sup> 0.80	-	5,46
		1.986, 1.997, 2.011		Fe <sup>IV</sup> 0.12	Fe <sup>IV</sup> 0.90		
[Fe <sup>IV</sup> -( $\mu$ -O)-( $\mu$ -OAc) <sub>2</sub> -Fe <sup>III</sup> (W <sub>1</sub> ) <sub>2</sub> ] <sup>3+</sup>	315 (8600)sh	3/2 (65%), (Fe <sup>IV</sup> S=1)	0.028	Fe <sup>III</sup> 0.36	Fe <sup>III</sup> -0.49	8.05 (S = 3/2)	6
	566 (1000)	1.990, 1.990, 1.975		Fe <sup>IV</sup> 0.05	Fe <sup>IV</sup> 1.114		
	912 (650)	1/2 (35%) (Fe <sup>IV</sup> S=2)		Fe <sup>III</sup> 0.38	Fe <sup>III</sup> -0.85		
		2.411, 1.921, 1.685		Fe <sup>IV</sup> -0.10	Fe <sup>IV</sup> 0.86		
[Fe <sup>IV</sup> -( $\mu$ -O)-( $\mu$ -OAc) <sub>2</sub> -Fe <sup>III</sup> (W <sub>2</sub> ) <sub>2</sub> ] <sup>3+</sup>	330 (10100)sh	3/2,	0.025	Fe <sup>III</sup> 0.44	Fe <sup>III</sup> -0.57	6.4	6
	571 (1100)	1.971, 1.971, 1.971		Fe <sup>IV</sup> 0.026	Fe <sup>IV</sup> 1.74		
	904 (600)						
[Fe <sup>IV</sup> -( $\mu$ -O)-( $\mu$ -OAc) <sub>2</sub> -Fe <sup>III</sup> (W <sub>3</sub> ) <sub>2</sub> ] <sup>1+</sup>	388 (6500)	3/2.	0.077	Fe <sup>III</sup> 0.45	Fe <sup>III</sup> -0.48	5.3	6
	445 (6000)sh	1.980, 1.980, 1.980		Fe <sup>IV</sup> 0.00	Fe <sup>IV</sup> 1.07		
	868 (250)						

<b>Table 1.1: Continued</b> Complex:	$\lambda$ (nm), ( $\epsilon$ M <sup>-1</sup> , cm <sup>-1</sup> )	$S_{\text{(total)}}$ , g (G)	E/D	$\delta$ (mm/s)	$\Delta E_Q$ (mm/s)	$D$ (cm <sup>-1</sup> )	ref
[Fe <sup>IV</sup> -( $\mu$ -O)-( $\mu$ -OAc) <sub>2</sub> ]	297 (11300)	3/2,	0.050	Fe <sup>III</sup> 0.45	Fe <sup>III</sup> -0.50	3.83 (Fe <sup>III</sup> )	6
Fe <sup>III</sup> (W <sub>2</sub> )(W <sub>3</sub> ) <sup>2+</sup>	364 (7600) 416 (7600) 552 (1200)sh 759 (210)	2.000, 2.000, 1.975		Fe <sup>IV</sup> 0.03	Fe <sup>IV</sup> 1.67	3.74 (Fe <sup>IV</sup> )	
[Fe <sup>IV</sup> -( $\mu$ -O)-Fe <sup>III</sup> -( $\mu$ -CXA) <sub>2</sub> ] <sup>3+</sup>	550 (1800) 878 (770)	-	-	0.07	1.57	-	9
[Fe <sup>IV</sup> -( $\mu$ -O)-Fe <sup>III</sup> -( $\mu$ -CXA) <sub>2</sub> ] <sup>4+</sup>	~575 (6000)sh	0	-	-0.05	2.14	-	9
[Fe <sup>IV</sup> <sub>2</sub> -( $\mu$ -O)(TAML) <sub>2</sub> ] <sup>2-</sup>	~430 (~14000) 542 (7500) 856 (5400)	0	-	-0.07	3.3	-	7
[Fe <sup>IV</sup> <sub>2</sub> -( $\mu$ -O)(TAML-OMe) <sub>2</sub> ] <sup>2-</sup>	~430 (~14000) 542 (8800) 856 (6600)	0	-	-0.03	3.00	-	7

<b>Table 1: Continued</b>	$\lambda$ (nm), ( $\epsilon$ M <sup>-1</sup> , cm <sup>-1</sup> )	$S_{\text{(total)}}$ , g (G)	E/D	$\delta$ (mm/s)	$\Delta E_Q$ (mm/s)	$D$ (cm <sup>-1</sup> )	ref
[Fe <sup>IV</sup> <sub>2</sub> -( $\mu$ -O) <sub>2</sub> (SR <sub>3</sub> TPA)] <sup>4+</sup> , <b>4A</b>	485 (9800) 875 (2200)	0	-	-0.04	+2.09	-	8,27
[O=Fe <sup>IV</sup> - $\mu$ -O-Fe <sup>IV</sup> - OH(SR <sub>3</sub> TPA) <sub>2</sub> ] <sup>3+</sup> <b>3A</b>	705 (2500) 620 (2200)sh	2 (2 S = 1 Fe <sup>IV</sup> )	Fe <sup>IV</sup> <sub>oxo</sub> 0 Fe <sup>IV</sup> <sub>OH</sub> 0.28	Fe <sup>IV</sup> <sub>oxo</sub> -0.03 Fe <sup>IV</sup> <sub>OH</sub> 0.0	Fe <sup>IV</sup> <sub>oxo</sub> +0.92 Fe <sup>IV</sup> <sub>OH</sub> +1.96	Fe <sup>IV</sup> <sub>oxo</sub> 27 Fe <sup>IV</sup> <sub>OH</sub> 17.7	13,27,47
[O=Fe <sup>IV</sup> - $\mu$ -O-Fe <sup>III</sup> - OH(SR <sub>3</sub> TPA) <sub>2</sub> ] <sup>2+</sup> <b>6(OH)A</b>	~410 (~3500)sh	½, 2.002 ( <sup>57</sup> Fe broadening)	-	Fe <sup>III</sup> 0.40 Fe <sup>IV</sup> 0.09	Fe <sup>III</sup> -0.60 Fe <sup>IV</sup> -0.40	-	13,15,48
[O=Fe <sup>IV</sup> - $\mu$ -O-Fe <sup>III</sup> -F(SR <sub>3</sub> TPA) <sub>2</sub> ] <sup>2+</sup> <b>6(F)A</b>	~390 (~5500)	½, 1.99, 2.02, 2.02 ( <sup>19</sup> F hyperfine interactions)	-	Fe <sup>III</sup> 0.45 Fe <sup>IV</sup> 0.10	Fe <sup>III</sup> 1.50 Fe <sup>IV</sup> 0.60	-	15,48
[Fe <sup>IV</sup> =O(NCMe)(SR <sub>3</sub> TPA)] <sup>2+</sup>	-	1	0	0.01	+0.95	27	13,27,47
[O=Fe <sup>IV</sup> - $\mu$ -O-Fe <sup>III</sup> - OMe(SR <sub>3</sub> TPA) <sub>2</sub> ] <sup>2+</sup> <b>6(OMe)A</b>	400 (5500)sh	½, 2.00 ( <sup>57</sup> Fe broadening)	-	-	-	-	14,15

<b>Table 1: Continued</b>	$\lambda$ (nm),	$S_{\text{(total)}}$ ,	E/D	$\delta$ (mm/s)	$\Delta E_Q$	$D$ (cm <sup>-1</sup> )	ref	
Enzyme Intermediate:	( $\epsilon$ M <sup>-1</sup> , cm <sup>-1</sup> )	g (G)			(mm/s)			
$[\text{O}=\text{Fe}^{\text{IV}}-\mu\text{-O}-\text{Fe}^{\text{IV}}=\text{O}(\text{SR}_3\text{TPA})_2]^{2+}$	450 (~6000)	0	-	2(S = 2),	2(S = 2),	-	49	
<b>7A<sub>trans</sub></b>				0.14	+0.52			
$[\text{O}=\text{Fe}^{\text{IV}}-\mu\text{-O}-\text{Fe}^{\text{IV}}=\text{O}(\text{SR}_3\text{TPA})_2]^{2+}$	450 (~6000)	3, (S = 2, S = 1)	0.288	S = 1, -0.02	S = 1, -1.17	2.28	49	
<b>7A<sub>syn</sub></b>		2.00		S = 2, 0.14	S = 2, -0.82			
$[\text{O}=\text{Fe}^{\text{IV}}-\mu\text{-O}-\text{Fe}^{\text{IV}}=\text{O}(\text{6-HPA})]^{2+}$	- i	0 (2 S = 2)	-	0.13	0.44	-	10,11	
$[\text{O}=\text{Fe}^{\text{IV}}-\mu\text{-O}-\text{Fe}^{\text{IV}}=\text{O}(\text{BPG}_2\text{E})]^{2+}$	- i	0 (2 S = 2)	-	0.13-0.26	0.40-0.55	-	12	
sMMO-Q	330 (7500)	0 (2 S = 2)	-	0.17	0.53	-	50-52	
(Methylosinus trichosporium)	430 (7500)						53,54	
Methylococcus capsulatus	420 (8400)	0 (2 S = 2)	-	0.21, 0.14	0.68, 0.55	-		
RNR-X		$\frac{1}{2}$	-	Fe <sup>III</sup> 0.56	Fe <sup>III</sup> -0.90	-	55,56	
		2.007, 1.999, 1.994		Fe <sup>IV</sup> 0.26	Fe <sup>IV</sup> -0.60			
		<sup>57</sup> Fe detected by ENDOR						

<b>Table 1 continued:</b>	Fe-Fe (Å)	E <sub>1/2</sub> (V) (Fc <sup>+/0</sup> )	v cm <sup>-1</sup> , ( <sup>18</sup> O) rRaman	Edge (eV)	Pre-edge (eV); Area (total)	ref
Complex:						
[Fe <sup>IV</sup> -(μ-O) <sub>2</sub> Fe <sup>III</sup> (TPA) <sub>2</sub> ] <sup>3+</sup>	-	1.05 <sup>e</sup>	666 (638) 416 (408)	-	-	39,40
[Fe <sup>IV</sup> -(μ-O) <sub>2</sub> Fe <sup>III</sup> (5-Me <sub>3</sub> TPA) <sub>2</sub> ] <sup>3+</sup>	2.89 <sup>c</sup> 1.77 <sup>c</sup>	0.96 <sup>e</sup>	656, 676 <sup>f</sup> (634)	7126 <sup>g</sup>	-	40
[Fe <sup>IV</sup> -(μ-O) <sub>2</sub> Fe <sup>III</sup> (5-Et <sub>3</sub> TPA) <sub>2</sub> ] <sup>3+</sup>	2.683(1) <sup>d</sup> 1.805(3) <sup>d</sup> 2.60 <sup>c</sup> 1.81 <sup>c</sup>	-	666 <sup>f</sup> (635) 411 (396)	-	-	4,41,42
[Fe <sup>IV</sup> -(μ-O) <sub>2</sub> Fe <sup>III</sup> (SR <sub>3</sub> TPA) <sub>2</sub> ] <sup>3+</sup> , <b>5A</b>	-	0.270-0.490 <sup>j</sup>	655, 667 <sup>f</sup> (628)	7129.0 <sup>b</sup>	- (19.7)	8
[O=Fe <sup>IV</sup> -μ-O-Fe <sup>III</sup> (6-MeTPA) <sub>2</sub> ] <sup>3+</sup>	-	-	-	-	-	43
[O=Fe <sup>IV</sup> -μ-O-Fe <sup>III</sup> -(OH) <sub>2</sub> (6-Me <sub>3</sub> TPA) <sub>2</sub> ] <sup>3+</sup>	-	-	840 (794)	-	-	44,45
{Fe <sup>IV</sup> Fe <sup>III</sup> (Ar <sup>Tol</sup> CO <sub>2</sub> ) <sub>4</sub> }	-	-	-	-	-	5,46
[Fe <sup>IV</sup> -(μ-O)-(μ-OAc) <sub>2</sub> -Fe <sup>III</sup> (W <sub>1</sub> ) <sub>2</sub> ] <sup>3+</sup>	-	1.23 <sup>a</sup>	-	-	-	6
[Fe <sup>IV</sup> -(μ-O)-(μ-OAc) <sub>2</sub> -Fe <sup>III</sup> (W <sub>2</sub> ) <sub>2</sub> ] <sup>3+</sup>	3.173(10) c 1.725(15) c	1.48 <sup>a</sup>	-	7123.2 <sup>b</sup>	7111.8, 7113.2; 3.5, 6.3 (9.8)	6
[Fe <sup>IV</sup> -(μ-O)-(μ-OAc) <sub>2</sub> -Fe <sup>III</sup> (W <sub>3</sub> ) <sub>2</sub> ] <sup>1+</sup>	-	1.64 <sup>a</sup>	-	-	-	6

<b>Table 1 continued:</b>	Fe-Fe (Å)	E <sub>1/2</sub> (V)	v cm <sup>-1</sup> , ( <sup>18</sup> O)	Edge	Pre-edge (eV);	ref
	Fe-O (Å)	(Fc <sup>+0</sup> )	rRaman	(eV)	Area (total)	
Complex:						
[Fe <sup>IV</sup> -(μ-O)-(μ-OAc) <sub>2</sub> -Fe <sup>III</sup> (W <sub>2</sub> )(W <sub>3</sub> )] <sup>2+</sup>	-	1.35 <sup>a</sup>	-	-	-	6
[Fe <sup>IV</sup> -(μ-O)-Fe <sup>III</sup> -(μ-CXA) <sub>2</sub> ] <sup>3+</sup>	3.07 <sup>c</sup> 1.71 <sup>c</sup>	-	-	7124.9	-	9
[Fe <sup>IV</sup> -(μ-O)-Fe <sup>III</sup> -(μ-CXA) <sub>2</sub> ] <sup>4+</sup>	3.08 <sup>c</sup> 1.70 <sup>c</sup>	+1.50	-	7125.6	-	9
[Fe <sup>IV</sup> <sub>2</sub> -(μ-O)(TAML) <sub>2</sub> ] <sup>2-</sup>	3.3497(9) d 1.7284(8) d	-0.23 <sup>e</sup>	-	-	-	7
[Fe <sup>IV</sup> <sub>2</sub> -(μ-O)(TAML-OMe) <sub>2</sub> ] <sup>2-</sup>	3.3834(8) d 1.730(2) <sup>d</sup> 1.744(3) <sup>d</sup>	-	-	-	-	7
[Fe <sup>IV</sup> <sub>2</sub> -(μ-O) <sub>2</sub> (SR <sub>3</sub> TPA)] <sup>4+</sup> , <b>4A</b>	2.73 <sup>c</sup> 1.77 <sup>c</sup>	0.76 <sup>e</sup>	674 (644 2- <sup>18</sup> O) (665 <sup>16</sup> O <sup>18</sup> O)	7130.1 <sup>b</sup>	7113.7, 7117.9; 13.8, 5.2 (19.0)	8,27
[O=Fe <sup>IV</sup> -μ-O-Fe <sup>IV</sup> -OH(SR <sub>3</sub> TPA) <sub>2</sub> ] <sup>3+</sup> <b>3A</b>	1.66 <sup>c</sup> 3.32 <sup>c</sup>	0.270-0.490 j	-	7128.8 <sup>b</sup>	7113.6, 7116.2 7119.2; 24.1, 5.8, 11.6 (41.5)	13,27,47
[O=Fe <sup>IV</sup> -μ-O-Fe <sup>III</sup> -OH(SR <sub>3</sub> TPA) <sub>2</sub> ] <sup>2+</sup> <b>6(OH)A</b>	-	0.270-0.490 j	-	-	-	13,15,48



<b>Table 1 continued:</b>	Fe-Fe (Å)	E <sub>1/2</sub> (V)	v cm <sup>-1</sup> , ( <sup>18</sup> O)	Edge	Pre-edge (eV);	ref
	Fe-O (Å)	(Fc <sup>+·0</sup> )	rRaman	(eV)	Area (total)	
Complex:						
[O=Fe <sup>IV</sup> -μ-O-Fe <sup>III</sup> -F(SR <sub>3</sub> TPA) <sub>2</sub> ] <sup>2+</sup> <b>6(F)A</b>	3.56 <sup>c</sup> 1.66 <sup>c</sup>	-	-	7124.8, <sup>h</sup> 7128.6 <sup>h</sup>	7113.8, 7115.5, 7117.1; 13.4, 7.5, 3.9 (24.8)	15,48
[Fe <sup>IV</sup> =O(NCMe)(SR <sub>3</sub> TPA)] <sup>2+</sup>	-	0.270-0.490 <sup>j</sup>	-	-	-	13,27,47
[O=Fe <sup>IV</sup> -μ-O-Fe <sup>III</sup> -OMe(SR <sub>3</sub> TPA) <sub>2</sub> ] <sup>2+</sup>	-	-	-	-	-	14,15
<b>6(OMe)A</b>						
[O=Fe <sup>IV</sup> -μ-O-Fe <sup>IV</sup> =O(SR <sub>3</sub> TPA) <sub>2</sub> ] <sup>2+</sup>	-	-	-	-	-	49
<b>7A<sub>trans</sub></b>						
[O=Fe <sup>IV</sup> -μ-O-Fe <sup>IV</sup> =O(SR <sub>3</sub> TPA) <sub>2</sub> ] <sup>2+</sup> <b>7A<sub>syn</sub></b>	-	-	-	-	-	
[O=Fe <sup>IV</sup> -μ-O-Fe <sup>IV</sup> =O(6-HPA)] <sup>2+</sup>	-	-	820 (777) 529 (506)	-	-	10,11
[O=Fe <sup>IV</sup> -μ-O-Fe <sup>IV</sup> =O(BPG <sub>2</sub> E)] <sup>2+</sup>	-	-	810 (774) <sup>k</sup>	-	-	12
sMMO-Q	2.46 <sup>c</sup>	-	690 (654 2- <sup>18</sup> O)	-	-	50-52
(Methylosinus trichosporium)	1.77 <sup>c</sup>		(673 <sup>16</sup> O <sup>18</sup> O)			53,54
Methylococcus capsulatus	-	-	-	-	-	
RNR-X	2.79 <sup>c</sup> 1.75 <sup>c</sup>	-	-	-	-	55,56

**Table 1 Key:**

a = anodic peak only; b = edge energy was taken as the maximum of the first derivative of the rising edge, c = Determined by EXAFS, d Determined by XRD; e = determined by CV; f = Fermi doublet; g = calibrated by 1s-3d peak in [E<sub>4</sub>N][FeCl<sub>4</sub>], h two maxima observed in first derivative; i = peroxy spectrum reported; j = determined by chemical oxidants; k = vibrational data from an IR experiment on a solid state sample;

The first high-valent nonheme iron model species synthesized has an intense green color ( $\lambda_{\text{max}} = 614 \text{ nm}$ ) and is supported by the TPA ligand (Figure 1.3, TPA = tris(2-pyridylmethyl)amine).<sup>39</sup> This species is derived from a diferric starting material and  $\text{H}_2\text{O}_2$  and exhibits a low isomer shift of  $\delta = 0.11 \text{ mm/s}$  in its Mössbauer spectrum and signals at  $g_x = 3.95$ ,  $g_y = 4.40$  and  $g_z = 2.00$  in the electron paramagnetic resonance (EPR) spectrum consistent, with an  $S = 3/2$  species.<sup>39</sup> This first high-valent nonheme model compound was obtained in a relatively low yield and no structural data could be obtained. The authors drew upon previous work by the porphyrin chemists and proposed the high-valent species to be a mononuclear  $\text{Fe}^{\text{IV}}=\text{O}$  ligand-radical.<sup>39,57</sup> A few years later, the ligand supporting the green high-valent model complex was modified by adding either methyl or ethyl groups to the pyridinyl rings of the unsubstituted ligand (Figure 1.3). The lifetime of the green species was increased and this facilitated its further characterization.<sup>4,40</sup> Importantly, the spectroscopic characteristics were nearly identical. The green species was later identified as the first high-valent  $\text{Fe}_2(\mu\text{-O})_2$  four-membered ring, which was entitled as a diamond core (Figure 1.3). A short Fe-Fe scatterer identified in the EXAFS data at  $2.6 \text{ \AA}$  and a crystal structure with an Fe-Fe distance of  $2.683(1)$  are signature characteristics of this core moiety.<sup>4,40</sup> Additionally, two vibrational modes at  $\sim 660$  and  $\sim 410 \text{ cm}^{-1}$  were assigned to the diamond core in the resonance Raman spectrum, and these vibrations became ubiquitous with complexes having the  $\text{Fe}_2(\mu\text{-O})_2$  core motif.<sup>39,40,42</sup> A mixed-valence  $S = 3/2$  assignment, resulting from  $S = 1/2$  and  $S = 1$  Fe centers coupling through a double exchange pathway, was assigned to the

green species using electronic absorption spectroscopy, magnetic circular dichroism, EPR and electronic structure calculations.<sup>41,42</sup> A  $\text{Cu}_2\text{O}_2$  diamond core was also identified, which shared similar resonance Raman and EXAFS characteristics with the  $\text{Fe}^{\text{IV}}\text{Fe}^{\text{III}}$  diamond core.<sup>58</sup> In addition to Cu cores, other late transition metal cores were identified including Co and Ni.<sup>59</sup> The diiron diamond core characteristics of the green species aided the identification of the same moiety in the reactive intermediates of soluble methane monooxygenase intermediate Q (sMMO-Q) and RNR intermediate X (RNR-X).<sup>51,60</sup>

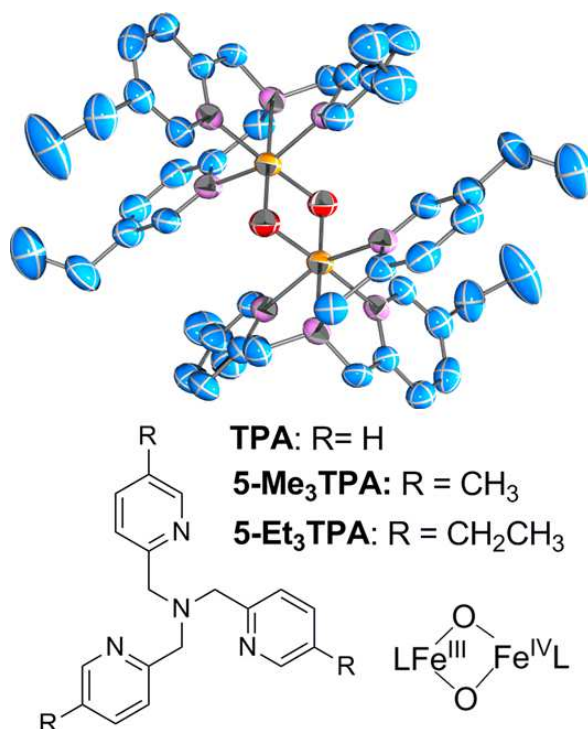


**Figure 1.3:** Top: the crystal structure of the first high-valent diiron complex with an  $\text{Fe}_2\text{O}_2$  core. Ellipsoids are drawn to the 50% probability level; hydrogen atoms are removed for clarity and atom colors are: carbon- blue, nitrogen- lilac, oxygen- red, iron- orange.<sup>4</sup> Bottom left- ligands used in the initial model complexes of nonheme enzymes; bottom right- high-valent diiron diamond core.

Two related mixed-valent Fe<sup>IV</sup>Fe<sup>III</sup> species were produced from the oxidation of the diferric starting materials by H<sub>2</sub>O<sub>2</sub>, electrochemical methods or one-electron chemical oxidants.<sup>43–45</sup> These brown mixed-valent species were supported by a variation of the ligand TPA with one or all of the pyridines having a methyl group substituted in the 6-position (Figure 1.4). The substitution of the sixth position of the pyridine group was shown to increase the Fe-N bond length, lowering the ligand field strength and resulting in a high-spin Fe atom.<sup>61</sup> The 6-MeTPA version had an intense electronic absorption feature around 350 nm. The lower ligand field of the Fe<sup>IV</sup>Fe<sup>III</sup> complexes supported by the 6-Me<sub>x</sub>TPA ligands resulted in two electronically distinct Fe environments. Two separate quadrupole doublets were observed in the Mössbauer spectrum with an isomer shift  $\delta \approx 0.1$  and 0.5 mm/s, consistent with localized Fe<sup>IV</sup> and Fe<sup>III</sup> centers, respectively.<sup>43–45</sup> Importantly, a signal in the EPR spectrum at  $g = 2.00$  was identified and was consistent with an  $S = 1/2$  spin state. Through an exchange coupling pathway, the  $S = 5/2$  Fe<sup>III</sup> center and the  $S = 2$  Fe<sup>IV</sup> center formed an overall  $S = 1/2$  spin state. The  $S = 1/2$  spin state also matched the EPR signal of RNR-X.<sup>43–45</sup> Resonance Raman spectroscopy was performed on the brown species supported by the 6-Me<sub>3</sub>TPA ligand and a vibration at 840 cm<sup>-1</sup> was observed that shifted to 794 cm<sup>-1</sup> when the isotope <sup>18</sup>O was used in the synthetic procedure. The vibration was assigned to a terminal LFe<sup>IV</sup>=O, with an -O-Fe<sup>III</sup>L moiety as the sixth ligand using extensive isotope labeling studies (Figure 1.4, L = 6-Me<sub>3</sub>TPA). The O=Fe<sup>IV</sup>-O-Fe<sup>III</sup>-X unit provided a second structural model for nonheme enzymes and complexes (Figure 1.4). Importantly, the brown species

was able to be formed from the decay of a well-characterized diferric-peroxo species upon addition of acid.<sup>44</sup> This conversion mimicked the important O-O bond breaking step in nonheme diiron enzymes.<sup>2</sup>

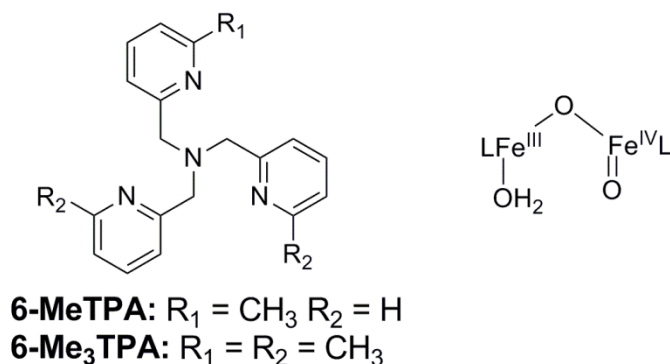


**Figure 1.4:** Left: TPA variations that support high-valent high-spin diiron compounds; Right: proposed core structure of the  $S = \frac{1}{2}$  Fe<sup>IV</sup>Fe<sup>III</sup> nonheme model complex.

Lippard's group advanced high-valent diiron model complex chemistry by synthesizing multiple Fe<sup>IV</sup>Fe<sup>III</sup> complexes supported by bulky carboxylate ligands (Ar<sup>Tol</sup>CO<sub>2</sub>, Figure 1.5).<sup>5,46</sup> The complex was synthesized from a diferrous precursor oxidized by dioxygen and was formed at -78° C. This well characterized complex had isomer shifts of  $\delta = 0.14$  and  $0.55$  mm/s in the Mössbauer spectrum and a signal at  $g = 1.986$ ,  $1.999$  and  $2.011$  in the EPR spectrum consistent with an  $S = \frac{1}{2}$  spin state. Overall this species was an excellent spectroscopic and functional model of RNR Intermediate-X.<sup>5,46</sup>

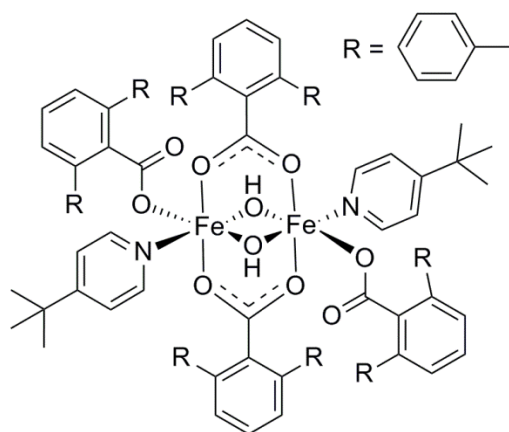


**Figure 1.5:** Proposed structure of an  $\text{Fe}^{\text{IV}}\text{Fe}^{\text{III}}$  complex supported by bulky carboxylates ( $\text{Ar}^{\text{Tol}}\text{CO}_2$ ) synthesized by the Lippard group.<sup>5</sup>

The Wieghardt group synthesized a series of  $\text{Fe}^{\text{IV}}\text{Fe}^{\text{III}}$  compounds that contained an interesting  $\{\text{Fe}^{\text{IV}}(\mu\text{-O})(\mu\text{-carboxylato})_2\text{Fe}^{\text{III}}\}^{3+}$  core (Figure 1.6), and were supported by both symmetric and asymmetric ligand environments.<sup>6</sup> In all cases, the electronic structure of the  $\text{Fe}^{\text{IV}}\text{Fe}^{\text{III}}$  cores were assigned as class II mixed-valence centers based on a low energy intervalence-charge-transfer-band in the electronic absorption spectra and distinct isomer shifts for the Fe centers at  $\delta = -0.1 - 0.05$  mm/s for the  $\text{Fe}^{\text{IV}}$  center and  $\delta = 0.36 - 0.45$  mm/s for the  $\text{Fe}^{\text{III}}$  center.<sup>6</sup> The highest populated spin state was 3/2 in all cases. However, one compound supported by the [9]aneN<sub>3</sub> ligand had a low-lying  $S = 1/2$  spin state. The cores represent another bonding motif in nonheme iron coordination chemistry.<sup>6</sup>

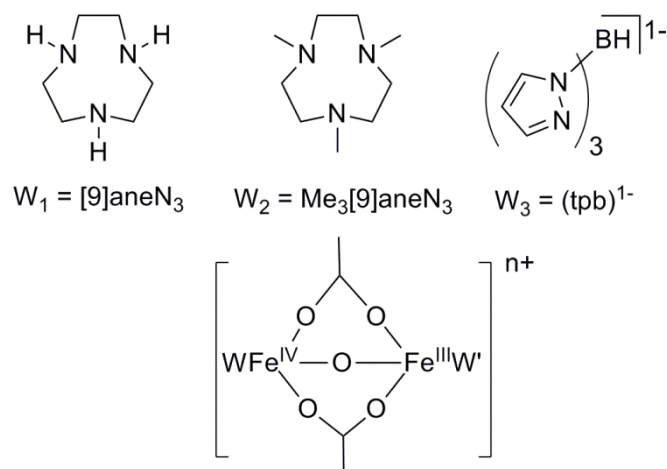


**Figure 1.6:** Mixed-valent  $Fe^{IV}Fe^{III}$  species supported by symmetric and asymmetric ligand environments synthesized by the Wieghardt group.<sup>6</sup>

The next major milestone was when Collins published the first ( $\mu$ -oxo)diiron(IV) model complexes (Figure 1.7).<sup>7</sup> Exposing five-coordinate ferric complexes supported by the tetraanionic TAML ligands to oxygen resulted in the formation of the  $[(TAML)Fe^{IV}(\mu-O)Fe^{IV}(TAML)]^{2-}$  species. Two variants were crystallographically characterized and contained linear  $Fe^{IV}-O-Fe^{IV}$  cores with 1.728-1.744 Å  $Fe-\mu-O$  bond lengths. The low isomer shift values of the complexes at  $\delta = -0.03$  to  $-0.07$  confirmed the  $Fe^{IV}$  oxidation state for both Fe atoms. Interestingly, the  $Fe^{IV}_2/Fe^{IV}Fe^{III}$  couple was found to be  $-0.23$  V vs  $Fc/Fc^+$  for the species  $X = H$  (Figure 1.7). The low redox potential was due to the tetraanionic ligand, which almost certainly facilitated the crystallization of the complex. Although not a strict structural model of enzyme active sites, the TAML-based high-valent species was shown to be catalytically active, using dioxygen as an oxidant, for the transformation of benzyl alcohols to ketones and  $Ph_3P$  to  $Ph_3P=O$ .<sup>7</sup>



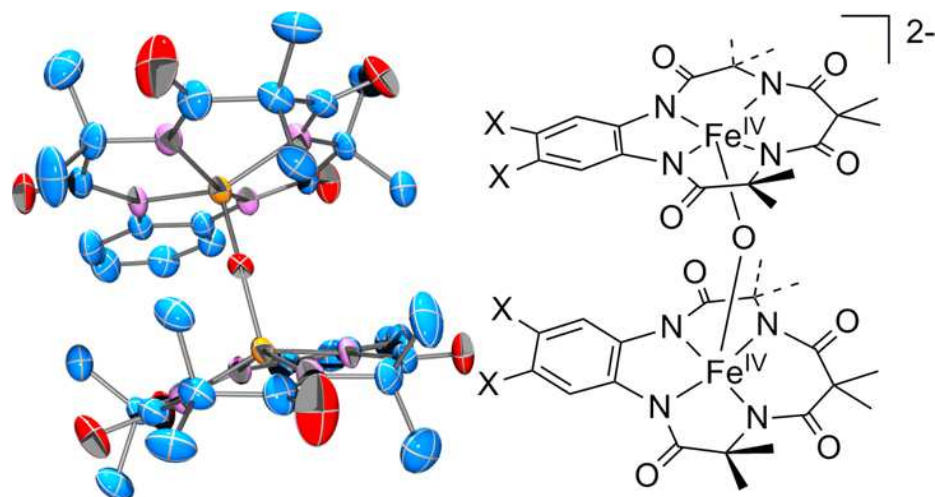


**Figure 1.7:** X-ray crystal structure and diagram of first diiron(IV) bis- $\mu$ -oxo complex.<sup>7</sup> The TAML ligand is tetraanionic and X = H or OMe, with X = H shown in the crystal structure. Ellipsoids are drawn to the 50% probability level, hydrogen atoms are removed for clarity and atom colors are: carbon-blue, nitrogen- lilac, oxygen- red and iron-orange.

Xue, Que and coworkers prepared the first bona fide high-valent diamond core model complex (**4A**, Figure 1.8, Scheme 1.1) by bulk electrolysis at  $-40^\circ\text{C}$  of an  $[\text{Fe}^{\text{IV}}(\mu\text{-O})_2\text{Fe}^{\text{III}}]^{3+}$  precursor at 760 mV vs. Fc. The  $[\text{Fe}^{\text{IV}}(\mu\text{-O})_2\text{Fe}^{\text{IV}}]^{4+}$  core was supported by a highly-substituted TPA variant (Figure 1.8,  $\text{SR}_3\text{TPA}$  = tris(4-methoxy-3,5-dimethylpyridylmethyl)amine, Ligand **A**).<sup>8</sup> This red species had electronic absorption bands around 485 and 875 nm. The EXAFS data was modeled with an Fe-Fe scatterer at 2.73 Å and two short Fe-O scatterers at 1.77 Å and is consistent with a diamond core moiety. Additionally, a vibration in the resonance Raman spectrum was observed at  $674\text{ cm}^{-1}$ , and was consistent with vibrations previously observed for other complexes with  $\text{Fe}^{\text{IV}}\text{Fe}^{\text{III}}$  diamond

cores.<sup>4,8,62</sup> A single quadrupole doublet with  $\delta = -0.04$  mm/s and  $\Delta E_Q = +2.09$  mm/s in the Mössbauer spectrum was assigned to two strongly coupled  $S = 1$  Fe atoms for an overall spin of  $S = 0$ .<sup>8</sup> Species **4A** directly oxidized the C-H bond of 9,10-dihydroanthracene (DHA) and the Fe complex was converted directly to the one-electron reduced  $\text{Fe}^{\text{IV}}\text{Fe}^{\text{III}}$  core with all oxidizing equivalents accounted for in the oxidation products of DHA. Additionally, the  $\text{Fe}^{\text{IV}}\text{Fe}^{\text{III}}$  species was also able to oxidize DHA at a rate 10 times slower than **4A** due to its lower redox potential.<sup>8</sup>

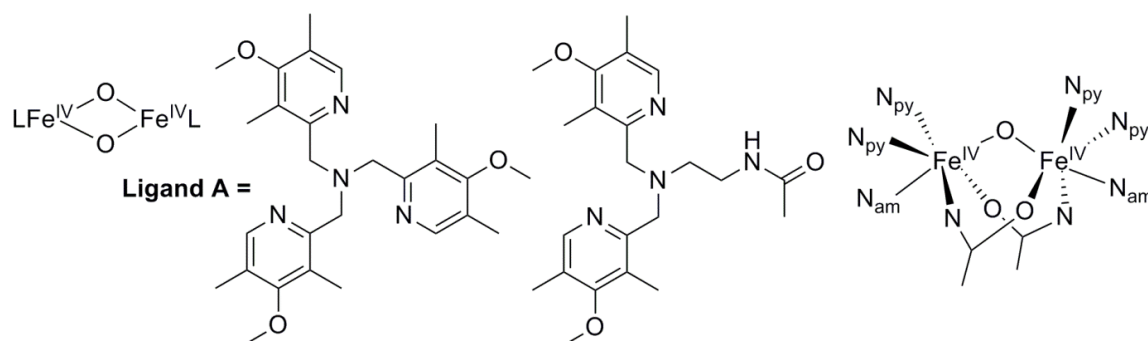
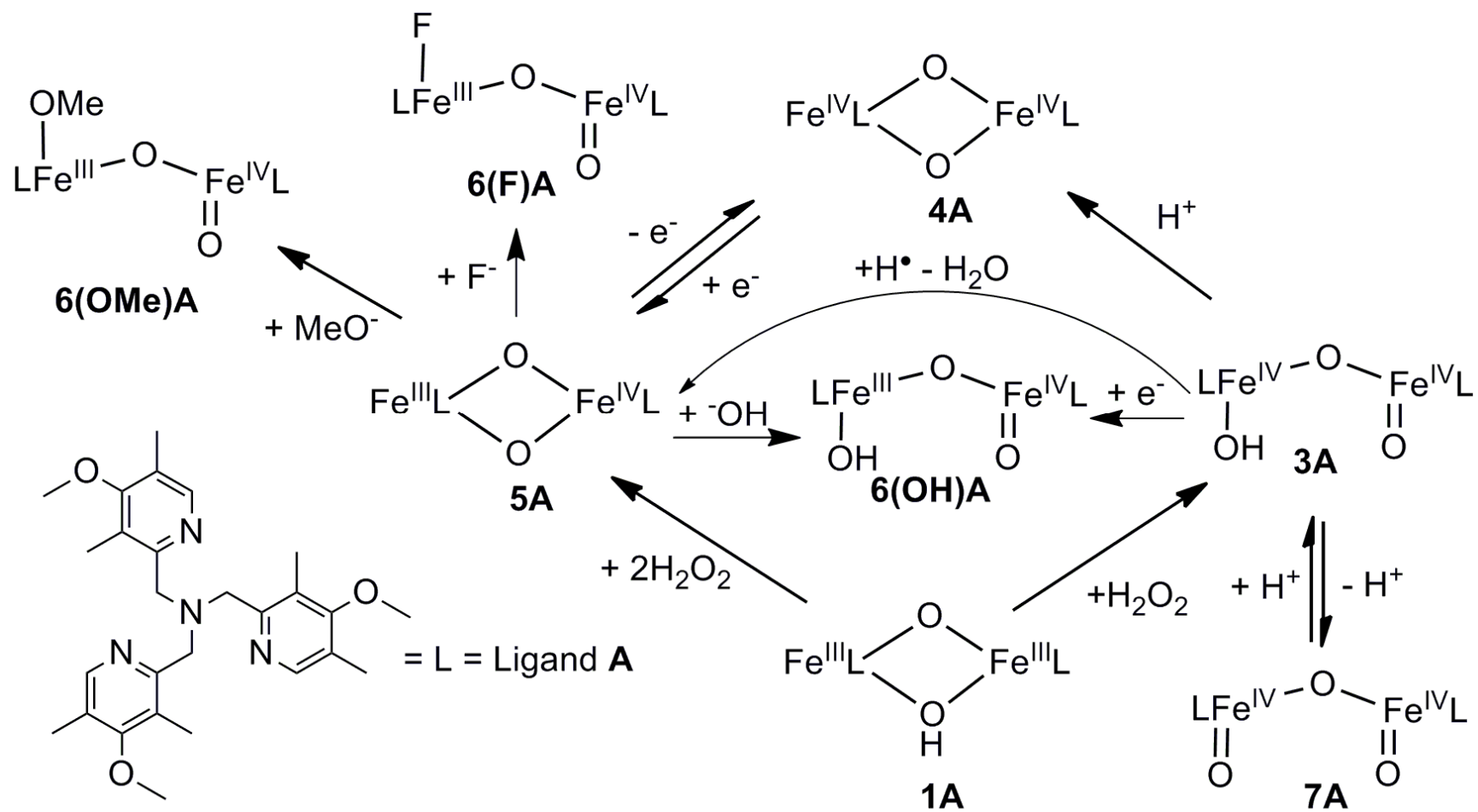


**Figure 1.8:** Diiron(IV) cores. Left: First diiron(IV) diamond core model complex supported by ligand **A** (tris(4-methoxy-3,5-dimethylpyridylmethyl)amine or  $\text{SR}_3\text{TPA}$ ).<sup>8</sup> Right: Second diiron(IV) core supported by carboxamido bridging ligands (CXA).<sup>9</sup>



**Scheme 1.1:** Synthetic scheme of high-valent diiron complexes supported by ligand **A** (tris(4-methoxy-3,5-dimethylpyridylmethyl)amine).

A more reactive  $\text{Fe}^{\text{IV}}_2\text{O}$  species was reported a few years later, which was supported by two pentadentate bridging ligands in a N-rich and carboxamido donor environment (CXA, Figure 1.8).<sup>9</sup> This species was also produced by bulk electrolysis, and had a relatively featureless electronic absorption spectrum resulting in its black color.<sup>9</sup> This species had an isomer shift of  $\delta = -0.05$  mm/s and an  $\text{Fe}^{\text{IV}}_2/\text{Fe}^{\text{V}}\text{Fe}^{\text{III}}$  redox couple at 1.50 V vs.  $\text{Fc}^+/\text{Fc}$ . The black species could oxidize substrates with C-H bonds as strong as cyclohexane (99 kcal/mol) and quantitatively formed a one-electron reduced  $\text{Fe}^{\text{IV}}\text{Fe}^{\text{III}}$  species. This  $\text{Fe}^{\text{IV}}\text{Fe}^{\text{III}}$  species was also formed by bulk electrolysis at a potential of 0.70 V vs.  $\text{Fc}^+/\text{Fc}$  and had an electronic absorption spectrum with features at 550 and 878 nm. Interestingly, one Mössbauer quadrupole doublet was observed for the  $\{\text{Fe}^{\text{IV}}\text{-O-Fe}^{\text{III}}(\text{CXA})_2\}$  at  $\delta = 0.07$  mm/s, which indicated the electron was delocalized over both Fe atoms.<sup>9</sup>

A steady stream of additional high-valent nonheme iron model complexes was reported and their abbreviations are summarized in Scheme 1.1. A diiron species with a core  $\{\text{O}=\text{Fe}^{\text{IV}}\text{-O-Fe}^{\text{IV}}\text{-OH}\}$  (**3A**) was synthesized by adding  $\text{H}_2\text{O}_2$  to the diferric precursor (**1A**, Scheme 1.1) at  $-40^\circ\text{C}$ .<sup>27</sup> The electronic absorption spectrum of **3A** had broad features at around 600 and 700 nm,<sup>27</sup> and resembled a peroxo species.<sup>5,44,63–68</sup> However, further investigation of **3A** by Mössbauer spectroscopy yielded two quadrupole doublets that had isomer shifts of  $\delta = -0.03$  and 0.00 and quadrupole splittings of  $\Delta E_Q = 0.92$  and 1.96 mm/s, respectively, and was consistent with two separate  $\text{Fe}^{\text{IV}}$  environments. Interestingly, an overall  $S = 2$  spin state was observed for **3A** and was due to ferromagnetic

coupling of the two  $S = 1$   $\text{Fe}^{\text{IV}}$  centers according to a thorough Mössbauer and DFT study.<sup>47</sup> An open-core  $\{\text{O}=\text{Fe}^{\text{IV}}-\text{O}-\text{Fe}^{\text{IV}}-\text{OH}\}$  formulation was determined based on an Fe-Fe scattering distance of 3.32 Å and two Fe-O scatterers at 1.65 and 1.80 Å assigned as a terminal oxo and a  $-\mu$ -oxo, respectively. The open core formulation was also supported by  $^{18}\text{O}$  isotope labeling studies.<sup>27</sup> A combined magnetic circular dichroism and DFT study found that the  $\text{Fe}^{\text{IV}}=\text{O}$  center in **3A** was very similar to the mononuclear  $\text{Fe}^{\text{IV}}=\text{O}$  species supported by ligand **A**.<sup>69</sup> A quadrupole doublet in the Mössbauer spectrum of the mononuclear  $\text{Fe}^{\text{IV}}=\text{O}$  species supported by ligand **A** had an isomer shift of  $\delta = 0.01$  mm/s and a quadrupole splitting of  $\Delta E_{\text{Q}} = +0.95$ ; these values were very close to one of the quadrupole doublets in the spectrum of **3A**, consistent with the MCD study.<sup>27,69</sup> The species **3A** was able to oxidize  $\text{H}_2\text{O}_2$  to form **5A**, which complicated the synthetic procedure of **3A**,<sup>27</sup> *vide infra*. Additionally, **3A** could be protonated to form **4A**, the complex with a  $[\text{Fe}^{\text{IV}}_2\text{O}_2]^{4+}$  diamond core.<sup>27</sup> This was the first report of a diiron complex activating the O-O bond of  $\text{H}_2\text{O}_2$  to form an observable high-valent species like that in sMMO-Q.<sup>2,27,70</sup>

Three related mixed-valence open core species supported by ligand **A** were reported and were formulated as  $\{\text{O}=\text{Fe}^{\text{IV}}-\text{O}-\text{Fe}^{\text{III}}-\text{X}\}$  (Scheme 1.1).<sup>13,14,48</sup> The mixed-valence open core species **6(OH)A** was prepared *in situ* by either adding 1 eq. ferrocene to **3A** or adding  $^-\text{OH}$  to a solution of **5A**.<sup>13</sup> Both methods used low temperatures in the range of  $-60^\circ\text{C}$  to  $-80^\circ\text{C}$  to improve the yields of the **6(OH)A**, which has a limited lifetime due its high C-H bond reactivity, *vide infra*. The two additional mixed-valence open-core species were synthesized by adding

1.5-5 eq of the desired Lewis base (**X**) to a solution of **5A** at  $-80^{\circ}$  C. The three **6(X)A** species had distinct spectroscopic characteristics (Table 1.1).<sup>14,48</sup> The Mössbauer spectrum of **6(OH)A** and **6(F)A** showed two quadrupole doublets with isomer shifts  $\delta \approx 0.10$  and  $0.45$  for the  $\text{Fe}^{\text{IV}}$  and  $\text{Fe}^{\text{III}}$  centers, respectively.<sup>13,48</sup> The  $g$  values for the three **6(X)A** species were found to be very close to 2.00. Broadening of the EPR spectra in samples prepared with  $^{57}\text{Fe}$  were observed for the **6(OH)A** and **6(OMe)A** species and distinct  $^{19}\text{F}$  superhyperfine splitting was observed in the **6(F)A** EPR spectrum showing that the unpaired spin density was on the Fe atom in all three cases.<sup>13,14,48</sup> The EPR and Mössbauer spectra of the **6(X)A** complexes were consistent with the mixed-valence brown species  $\{\text{LFe}^{\text{III}}\text{-O-Fe}^{\text{IV}}\text{=O}\}$  isolated over a decade before with distinct oxidation states of the iron atoms.<sup>45</sup> The overall  $S = \frac{1}{2}$  spin state is consistent with antiferromagnetically coupled  $S = 2$   $\text{Fe}^{\text{IV}}$  and  $S = 5/2$   $\text{Fe}^{\text{III}}$  centers.<sup>13,14,48</sup> Additionally, structural insights into the **6(X)A** complexes were obtained using ENDOR, EXAFS and DFT. Experimental evidence for the 6-membered ring of the Fe, O and H-Bonded proton of **6(OH)A** was observed using  $^1\text{H}$  ENDOR spectroscopy. An Fe-O-Fe angle of around  $130^{\circ}$  and a  $\text{Fe}^{\text{IV}}\text{=O}\cdots\text{H-O-Fe}^{\text{IV}}$  interaction was observed, consistent with earlier DFT calculations (Scheme 1.1).<sup>48,71</sup> The compound **6(F)A** was studied with XAS and an intense outer-shell scatterer was observed in the Fourier transform of the EXAFS data. The EXAFS data was modeled with an Fe-Fe scatterer at a distance of  $3.56 \text{ \AA}$  and two Fe-O scatterers at distances of  $1.66$  and  $1.83 \text{ \AA}$  assigned to the Fe=O and Fe- $\mu$ -O bonds, respectively; this assignment was consistent with a nearly linear Fe-O-Fe

moiety (Scheme 1.1).<sup>15</sup> An *anti*- geometry was assigned to the F-Fe<sup>III</sup>-O-Fe<sup>IV</sup>=O moiety to account for the EXAFS data and was corroborated by DFT calculations.<sup>15</sup> A linear Fe-O-Fe moiety with an *anti*- configuration was also assigned to **6(OMe)A** based on DFT and reactivity studies (*vide infra* Scheme 1.1).<sup>14</sup>

The most recent advances in nonheme enzyme model complexes were consecutive reports of diferryl species supported by similar ligand systems (Scheme 1.1, Figure 1.9).<sup>11,12,49</sup> Previously, Kodera *et al.* showed that a diferric-peroxo species supported by a di-nucleating ligand was involved in catalytic substrates oxidation. The peroxo system incorporated <sup>18</sup>O from labeled H<sub>2</sub><sup>18</sup>O<sub>2</sub> or labeled starting material {Fe-<sup>18</sup>O-Fe} into the oxidation product. A diferryl species was proposed to account for the labeling result (Figure 1.9).<sup>10</sup> Remarkably, the Kodera group was able to demonstrate reversible O-O bond cleavage of a diferric-peroxo species supported by two different ligand systems (Figure 1.9).<sup>11,12</sup> The transformation was monitored by Mössbauer spectroscopy and was observed only on solid samples (not in frozen solutions). Starting at ~25 K, two quadrupole doublets were observed with isomer shifts  $\delta \sim 0.4$  and  $\sim 0.2$  mm/s, consistent with a diiron-peroxo species and an S = 2 ferryl species, respectively.<sup>11,12</sup> As the temperature increased, the intensity of the 0.4 mm/s doublet decreased with concomitant increase in the intensity of the 0.2 mm/s signal, consistent with a diferryl species being formed from a peroxo species. When the temperature was lowered, the intensity of the peroxo species increased and that from the ferryl species decreased. These observations are

consistent with the O-O bond of the peroxo species breaking and reforming (Figure 1.9).<sup>11,12</sup> In both ligand systems, the solution electronic absorption spectra were reported to be consistent with a diferric-peroxo species with broad bands around 600 nm.<sup>11,12</sup> The diiron systems were studied with resonance Raman spectroscopy. An 820 cm<sup>-1</sup> vibration was observed in the resonance Raman spectrum of the 6-HPA system that red-shifted 43 cm<sup>-1</sup> when H<sub>2</sub><sup>18</sup>O<sub>2</sub> was used in the synthetic procedure. The vibration was assigned as an Fe=O vibration because the energy was closer to previously reported Fe-O stretches compared to O-O stretches. The shift due to <sup>18</sup>O incorporation was larger than expected and was rationalized as coupling between the Fe-O stretch and the Fe-O-Fe vibrational mode. To definitively assign the vibration as an Fe-O stretch, the mixed-isotope complex vibrations should be studied and appropriate shifts should be observed.<sup>11,45</sup> A second ligand system (BPG<sub>2</sub>E) was also studied with vibrational spectroscopy. A vibration at 835 cm<sup>-1</sup> was observed in the resonance Raman spectrum of the BPG<sub>2</sub>E species. The 835 cm<sup>-1</sup> vibration red-shifted 49 cm<sup>-1</sup> when prepared with the <sup>18</sup>O isotope, and was consistent with an O-O stretch of a diiron peroxo species.<sup>11,72</sup> Infrared spectroscopy (IR) was performed on the BPG<sub>2</sub>E species. A vibration at 810 cm<sup>-1</sup> was observed in the IR spectrum that shifted to 774 cm<sup>-1</sup> and was assigned to the Fe<sup>IV</sup>=O stretch.<sup>12</sup> In both Kodera systems, the cleavage of the O-O bond is believed to be the rate determining step of the catalytic oxidation, consistent with the diferryl species reacting with substrate before any measureable amount of the ferryl species accumulated.<sup>10-12</sup>



The ability of the Kodera system to reversibly break the O-O bond is an important milestone in modeling protein and enzyme systems.

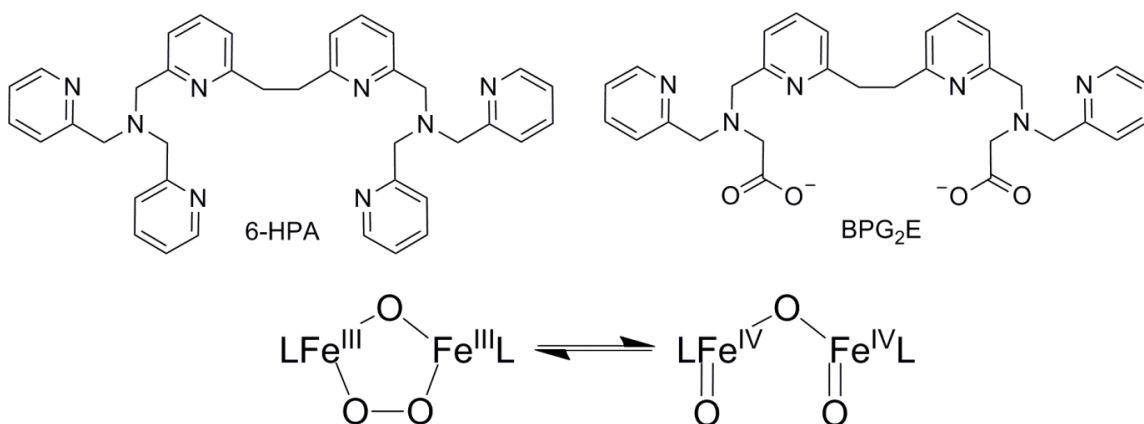


**Figure 1.9:** Top: di-nucleating ligands used by the Kodera group to support a diferryl model complex; Bottom: reversible O-O bond formation and formation of a diferryl species.<sup>10-12</sup>

The Münck and Que groups reported a different diferryl species when **3A** was deprotonated with base (OH<sup>-</sup>, F<sup>-</sup> or tetramethylimidazole) to form species **7A**.<sup>49</sup> **3A** was reversibly formed almost quantitatively when **7A** was protonated with HClO<sub>4</sub> (Scheme 1.1). Interestingly, two distinct isomers of **7A** were identified, as indicated by the three quadrupole doublets found in the Mössbauer spectrum; one isomer was in fact EPR active.<sup>49</sup> One quadrupole doublet had an isomer shift of  $\delta = 0.14$  mm/s and a quadrupole splitting of  $\Delta E_Q = +0.52$  mm/s and was consistent with two antiferromagnetically coupled  $S = 2$  centers, with an overall spin state of  $S = 0$ . The second isomer of **7A** had two Fe environments with isomer shifts of  $\delta = -0.02$  and  $0.14$  mm/s and quadrupole splitting values of  $\Delta E_Q = -1.17$  and  $-0.82$  mm/s, consistent with  $S = 1$  and  $S = 2$  ferryl centers,

respectively. A signal at  $g = 2.00$  was observed in the parallel mode EPR spectrum for the second isomer of **7A**, consistent with an overall spin state of  $S = 3$ .<sup>49</sup> Small differences in the concentration of water were hypothesized to change the H-bonding interactions with the ferryl oxygen atoms resulting in two diferryl species.<sup>49</sup> Even though the two diferryl model systems have similar spectroscopic properties compared to sMMO-Q, Stoian, *et al.* cautioned that the electronic environment of sMMO-Q may still be significantly different because of the lack of O-atom donors in the model systems compared to the O-rich environment of sMMO-Q.<sup>49</sup>

The family of high-valent diiron complexes exhibit large differences in C-H bond oxidation rates (Figure 1.10, Scheme 1.1) and the results are listed in Table 1.2. The DHA oxidation rate of the  $S = 1$  open-core species **3A** was about 250 times faster than **4A**.<sup>8,13</sup> The substrate oxidation rate of the open core **3A** was hypothesized to be more reactive than the diamond core **4A** based on two principles: 1) the higher basicity or spin density on the  $\text{Fe}^{\text{IV}}=\text{O}$  of **3A** would result in a stronger O-H bond relative to **4A**,<sup>8,73,74</sup> and 2) breaking two Fe-O(H)-Fe bonds in the diamond core species **4A** would be less favorable compared to breaking only one Fe-OH bond in the open-core species **3A**.<sup>74</sup> Strikingly, the reduction of **3A** by one electron to form **6(OH)A** increased the reaction rate by 1000 times.<sup>13</sup> The spin state for the  $\text{Fe}^{\text{IV}}=\text{O}$  moiety in the dinuclear complex changes from  $S = 1$  in **3A** to  $S = 2$  in **6(OH)A**.<sup>13,27,47</sup> This remarkable observation provided strong evidence computational insights that  $S = 2$   $\text{Fe}^{\text{IV}}=\text{O}$  units are much more reactive than  $S = 1$  units.<sup>75-77</sup> The increased rate of substrate

oxidation by **6(OH)A** is consistent with a 200-fold enhancement of the ability of **5A** to oxidize strong C-H bonds when water is present.<sup>74</sup> The substitution of the hydroxo ligand in **6(OH)A** with fluoride and methoxide Lewis bases lead to increased reactivities of an additional factor of 10.<sup>14,15</sup> This rate increase was attributed to the lack of a hydrogen bond for the **6(F)A** and **6(OMe)A** species.<sup>14,15,71</sup> Although the HAT reactivity of **7A** was not reported, the short lifetime and high-spin nature suggests the possibility of at least a statistical doubling of the reactivity compared to **6(OMe)A** because of the presence of two Fe<sup>IV</sup>=O moieties in **7A**.<sup>49</sup>

The reactivities of high-valent diiron compounds supported by ligand **A** span seven orders of magnitude (Figure 1.10). This series of high-valent diiron complexes provides a framework to help understand structure-function relationships of high-valent diiron species. Importantly, this is the only system to date able to activate H<sub>2</sub>O<sub>2</sub> to form a high-valent species that can directly oxidize C-H bonds.

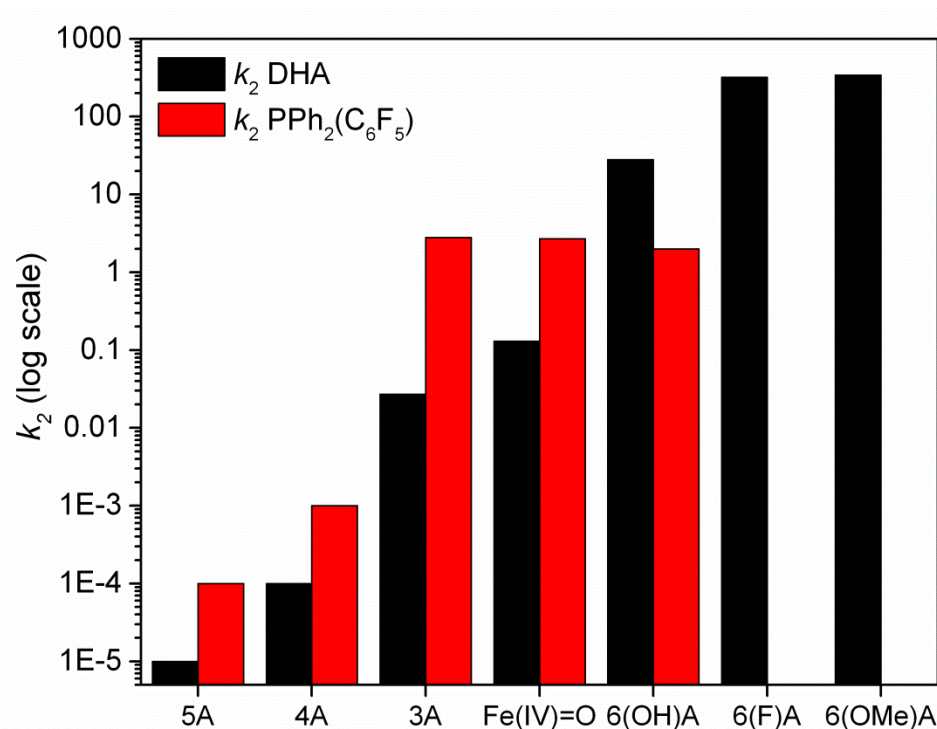


**Figure 1.10:** Rate constants ( $M^{-1}s^{-1}$ ) displayed on the  $\log_{10}$  scale of the oxidation of 9,10-dihydroanthracene (DHA, black columns) and diphenyl(pentafluorophenyl)phosphine ( $PPh_2(C_6F_5)$ , red columns) by high-valent iron complexes supported by ligand A at  $-80^\circ C$ . From references 13–15.

Oxygen atom transfer (OAT) reaction rates for this set of high-valent diiron complexes tracked mostly across the oxidation state and were not dependent on spin-state.<sup>13</sup> However, it was observed that the terminal ferryl species was over a 1000 times more reactive than the diiron(IV) diamond core for OAT reactions, perhaps due to the greater accessibility of the ferryl unit.<sup>13</sup>

**Table 1.2:** Rate constants of high-valent diiron model complexes supported by ligand L = SR<sub>3</sub>TPA (**A**).

Complex:	Substrate	Product (Yield)	Rate (KIE) M <sup>-1</sup> s <sup>-1</sup>	°C	ref
[Fe <sup>IV</sup> <sub>2</sub> -(μ-O) <sub>2</sub> (L)] <sup>4+</sup> , <b>5A</b>	DHA <sup>a</sup>	Anthracene (50%)	4.0 X 10 <sup>-5</sup> (9)	-30	8,13
	DHA	-	10 <sup>-5</sup>	-80	
	DPFP	-	10 <sup>-4</sup>	-80	
[Fe <sup>IV</sup> <sub>2</sub> -(μ-O) <sub>2</sub> (L)] <sup>4+</sup> , <b>4A</b>	DHA <sup>a</sup>	Anthracene (14%), Anthraquinone (13%)	5.1 X 10 <sup>-4</sup> (10)	-30	8,13
	DHA	-	10 <sup>-4</sup>	-80	
	DPFP	-	10 <sup>-3</sup>	-80	
[Fe <sup>IV</sup> =O(NCMe)(L)] <sup>2+</sup>	DHA <sup>a</sup>	Anthracene (50%)	4.2 X 10 <sup>-2</sup> (27)	-30	8,13
	DHA	Anthracene (55%)	0.13	-80	
	DPFP	DPFP=O (70%)	2.7	-80	
[O=Fe <sup>IV</sup> -μ-O-Fe <sup>IV</sup> -OH(L) <sub>2</sub> ] <sup>3+</sup> , <b>3A</b>	H <sub>2</sub> O <sub>2</sub>	-	5.9	-40	27
	DHA	Anthracene (80%)	0.027 (30, -30° C)	-80	
	DPFP	DPFP=O (99%)	2.8	-80	
[O=Fe <sup>IV</sup> -μ-O-Fe <sup>III</sup> -OH(L) <sub>2</sub> ] <sup>2+</sup> <b>6(OH)A</b>	DHA	Anthracene (44%)	28 (50)	-80	13,15
	DHA	-	13	-85	
	Fluorene	-	6.5	-80	
	DPFP	DPFP=O (65%)	2.0	-80	
	DHA act. par.	ΔH <sup>‡</sup> = 5.1(4) kcal mol <sup>-1</sup> , ΔS <sup>‡</sup> = -26(2) cal mol <sup>-1</sup> K <sup>-1</sup>			
[O=Fe <sup>IV</sup> -μ-O-Fe <sup>III</sup> -F(L) <sub>2</sub> ] <sup>2+</sup> <b>6(F)A</b>	DHA	Anthracene (75%)	320 (40)	-80	15
	DHA	-	180	-85	
	Fluorene	-	65	-80	

**Table 1.2 continued:** Rate constants of high-valent diiron model complexes supported by ligand L = SR<sub>3</sub>TPA (**A**).

Complex:	Substrate	Product (Yield)	Rate (KIE) M <sup>-1</sup> s <sup>-1</sup>	°C	ref
[O=Fe <sup>IV</sup> -μ-O-Fe <sup>III</sup> -OMe(L) <sub>2</sub> ] <sup>2+</sup> <b>6(OMe)A</b>	DHA	-	360	-80	14
Self-decay act. par. ΔH <sup>‡</sup> = 9.7(2) kcal mol <sup>-1</sup> , ΔS <sup>‡</sup> = -15(2) cal mol <sup>-1</sup> K <sup>-1</sup>					

All reactions conducted under an Ar atmosphere in a 3:1 CH<sub>2</sub>Cl<sub>2</sub> solvent system unless otherwise noted. L = SR<sub>3</sub>TPA, DHA = 9,10-dihydroanthracene, DPFP = diphenyl(pentafluorophenyl)phosphine, DPFP=O = diphenyl(pentafluorophenyl)phosphine oxide, <sup>a</sup> solvent CH<sub>3</sub>CN

Since the discovery of a diiron(IV) center in sMMO by Lipscomb in 1993, many high-valent diiron complexes have been synthesized. These models provide important structure-function relationships for both spectroscopic and reactivity studies. Additionally, they aid in the identification of important enzyme intermediates. Key spectroscopic features used to identify high-valent diiron species include: an  $^{18}\text{O}$ -isotope-sensitive vibration  $\sim 650\text{ cm}^{-1}$  in the resonance Raman spectrum, a low isomer shift in the Mössbauer spectrum and a short Fe-Fe distance observed in the X-ray crystallographic determined structures or from EXAFS studies. However, questions remain about how the O-O bond is activated by these model systems. Moreover, a more detailed structural picture of the diamond core species related to the reactive enzyme intermediates is desired.





*Chapter 2: Activating the O-O Bond to Form High-Valent Diiron Model  
Complexes*

## 2.1 Introduction:

Nature stores chemical energy in the strong bond of  $O_2$ . The reaction between  $O_2$ , with a triplet ground state, and a typical molecule in nature, with a singlet ground state, is spin forbidden. Although  $O_2$  is not reactive, its reduced forms,  $O_2^{\cdot-}$ ,  $H_2O_2$ , and  $HO^{\cdot}$ , are reactive. To release the energy in a controlled manner, nature uses metal cofactors, Fe in many cases, to release the energy.<sup>78</sup> The metal cofactor lowers the barrier of electron transfer to  $O_2$ . Moreover, protons are transferred in a controlled manner to further regulate the release of the stored energy in the O-O bond.<sup>78</sup> In the case of the diiron enzyme soluble methane monooxygenase (sMMO), two Fe atoms are used to activate oxygen (Figure 2.1).<sup>2</sup> The reduced state of sMMO, **F** (Scheme 2.1), binds  $O_2$  (**O**, Scheme 2.1) and upon electron transfer forms a peroxo species, **P** (Scheme 2.1). The decay of **P** was found to be pH dependent and formed the substrate oxidizing species **Q** (Scheme 2.1).<sup>2,25</sup>

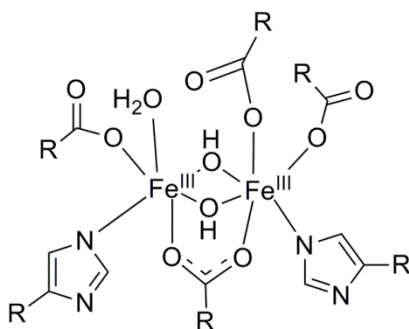
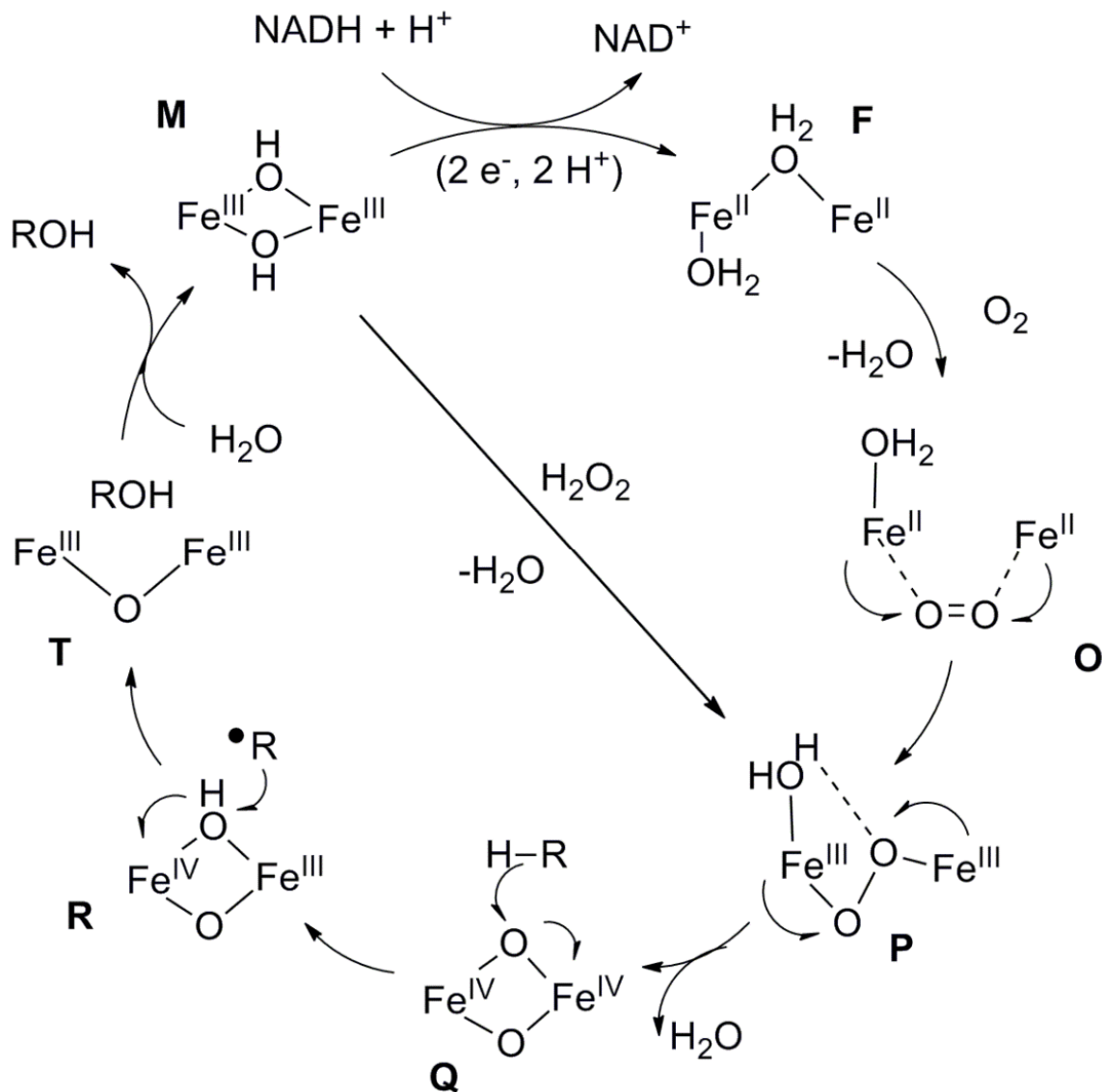


**Figure 2.1:** Active site of soluble methane monooxygenase (sMMO) responsible for activating  $O_2$ , with R representing the protein backbone.<sup>2</sup>



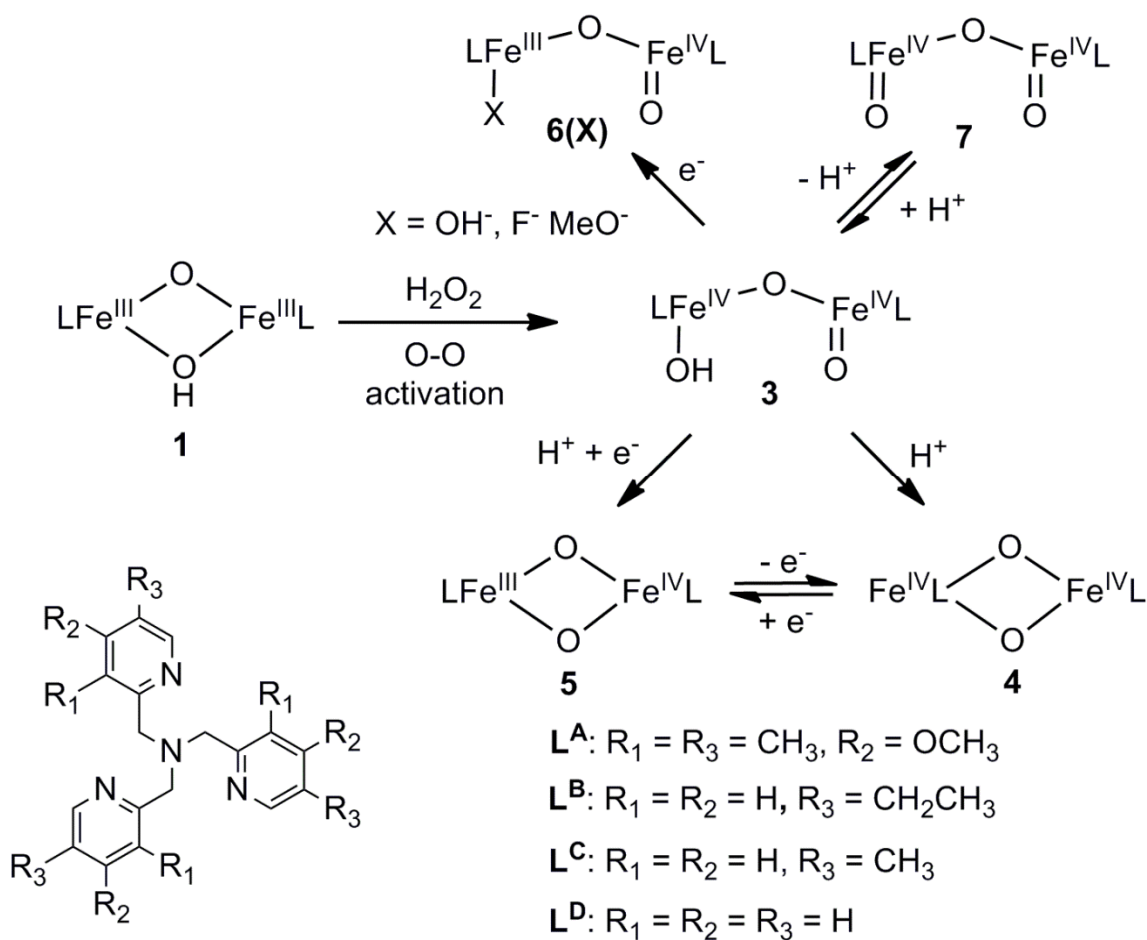
**Scheme 2.1:** Activation of O<sub>2</sub> by sMMO and peroxide shunt pathway displayed in the center.<sup>24,25</sup> The protein backbone is removed for clarity.

A peroxide shunt is used to easily model the O-O bond activation in various systems.<sup>78</sup> Diferrous species are much less stable than their diferric counterparts, because they react with oxygen. To overcome this experimental limitation, a ferric species is often combined with H<sub>2</sub>O<sub>2</sub> to form the reactive species. Although fewer electrons are available in the ferric iron, more are

present in the oxygen species. Using the example of sMMO, two fewer electrons are present starting from the ferric state, **M** (Scheme 2.1), but two additional electrons are now present in H<sub>2</sub>O<sub>2</sub> and can activate the O-O bond (center pathway, Scheme 2.1). Additionally, two protons are present which may or may not affect the reactivity depending on the system.

The peroxo species is a key intermediate in the activation of O<sub>2</sub> by sMMO,<sup>2,25</sup> and has been modeled by numerous synthetic examples over the last two decades.<sup>5,10-12,44,63-68,72,79-83</sup> Two routes were used to obtain the diferric peroxo species; a diferrous complex and O<sub>2</sub> or a diferric complex and H<sub>2</sub>O<sub>2</sub>. Both methods have the same number of electrons in the iron and oxygen atoms. Remarkably, five crystal structures of a diferric peroxo species were also solved,<sup>65,66,79,84</sup> and several peroxo species can reversibly bind O<sub>2</sub> like the nonheme oxygen carrier protein hemerythrin.<sup>65,67,80</sup> These model complexes provided a wealth of spectroscopic and structural data, however only three were able to convert to an Fe<sup>IV</sup>Fe<sup>III</sup> species stable enough to be studied.<sup>5,44,82</sup> An additional electron was proposed to be added to the system, resulting in the diiron(IV)oxo species (isoelectronic with the diferric peroxo) being proposed as transient intermediate. Additionally, high-valent diiron(IV) species have been invoked to explain the increased reactivity of the peroxo species in the presence of substrates or intramolecular oxidation, but direct evidence has been fleeting.<sup>10-12,79,85-87</sup> The diiron complexes supported by ligand **A** make up the only system able to activate H<sub>2</sub>O<sub>2</sub> to form a relatively stable high-valent system capable of oxidizing C-H bonds and oxygen atom transfer reactions (Scheme 2.2).<sup>8,13-15,27,49</sup>

However, the direct formation of the diiron(IV) species from the diferric precursors and H<sub>2</sub>O<sub>2</sub> has not been well-studied. Understanding how this model system activates the O-O bond will provide insights into the mechanism of oxygen activation as well as improving the ability of model systems to oxidize substrates.

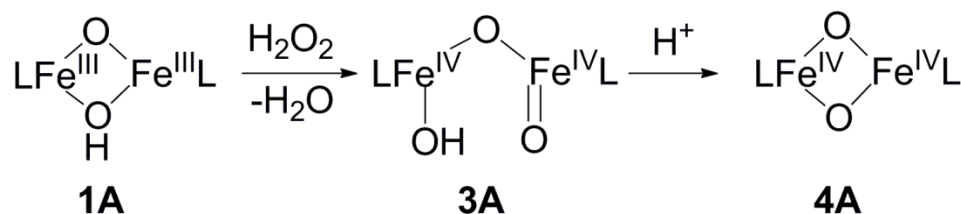


**Scheme 2.2:** Activation of H<sub>2</sub>O<sub>2</sub> by diiron complexes supported by the tris(4-methoxy-3,5-dimethylpyridylmethyl)amine ligand to form high-valent species.

## 2.2 Results:

### One-step formation of diiron(IV) core:

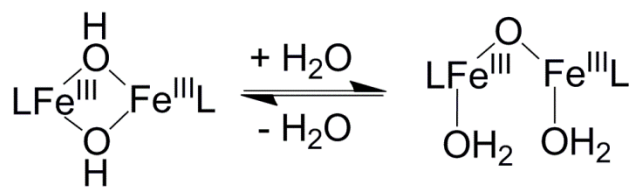
Previously, *in situ* synthetic methods were followed to obtain diiron(IV)-oxo compounds. The first route utilized bulk electrolysis with an applied potential of 900 mV vs. Fc to a solution of **5A** to carry out the 1-e<sup>-</sup> oxidation to produce the red [Fe<sub>2</sub>(μ-O)<sub>2</sub>]<sup>4+</sup> diamond core (**4A**) in a near-quantitative yield.<sup>8</sup> The second reported synthesis of the diiron(IV) complex was made *in situ* utilizing a diferric starting material [Fe<sub>2</sub>(μ-O)(μ-OH)]<sup>3+</sup> (**1A**) to activate H<sub>2</sub>O<sub>2</sub> to form a high-valent diiron complex formulated as [(O)Fe<sup>IV</sup>(μ-O)Fe<sup>IV</sup>(OH)]<sup>3+</sup> (**3A**), followed by protonation with HClO<sub>4</sub> and loss of one H<sub>2</sub>O molecule to form the [Fe<sub>2</sub>(μ-O)<sub>2</sub>]<sup>4+</sup> diamond core **4A** in moderate yields (Scheme 2.3).<sup>27</sup> Both methods utilized low temperatures to stabilize the reactive species; however the diiron(IV) compounds could not be crystalized.<sup>8,27</sup>



**Scheme 2.3:** Activation of H<sub>2</sub>O<sub>2</sub> by the diiron(III) complex supported by ligand **A** to form the high valent diamond core **4A**.

A third synthetic strategy was tested to determine if a higher-yielding one-step synthesis of **4A** was possible by switching the order in which H<sub>2</sub>O<sub>2</sub> and acid were added to **1A**. Complex **2A** (Scheme 2.4), the protonated version of **1A**, was synthesized (and characterized, *vide infra*) and tested for the direct

synthesis of the diiron(IV) species **4A** with H<sub>2</sub>O<sub>2</sub>, with **2A** providing the protons needed to break the O-O bond of H<sub>2</sub>O<sub>2</sub> as soon as the **2A** • H<sub>2</sub>O<sub>2</sub> adduct formed. Indeed, the addition of one equivalent H<sub>2</sub>O<sub>2</sub> to a 0.3 mM acetonitrile solution of **2A** at -40° C produced **4A** in 85% yield, based on the intensities of its characteristic electronic absorption bands at 485 and 875 nm (Figure 2.2).<sup>i</sup> The reaction was complete in less than 30 seconds. Compounds **1A** and **2A** are the only reported compounds able to activate H<sub>2</sub>O<sub>2</sub> to form a high-valent diiron species. This system can now be studied kinetically to help understand the peroxo bond breaking like in the conversion from sMMO-P to sMMO-Q or the formation of RNR-X and how the protonation of the starting material affects the reaction.



**Scheme 2.4:** Possible core formulations of **2A** based on previous diferric species.<sup>26</sup>

<sup>i</sup> Experiment originally performed by Dr. Genqiang Xue and checked by Gregory Rohde.

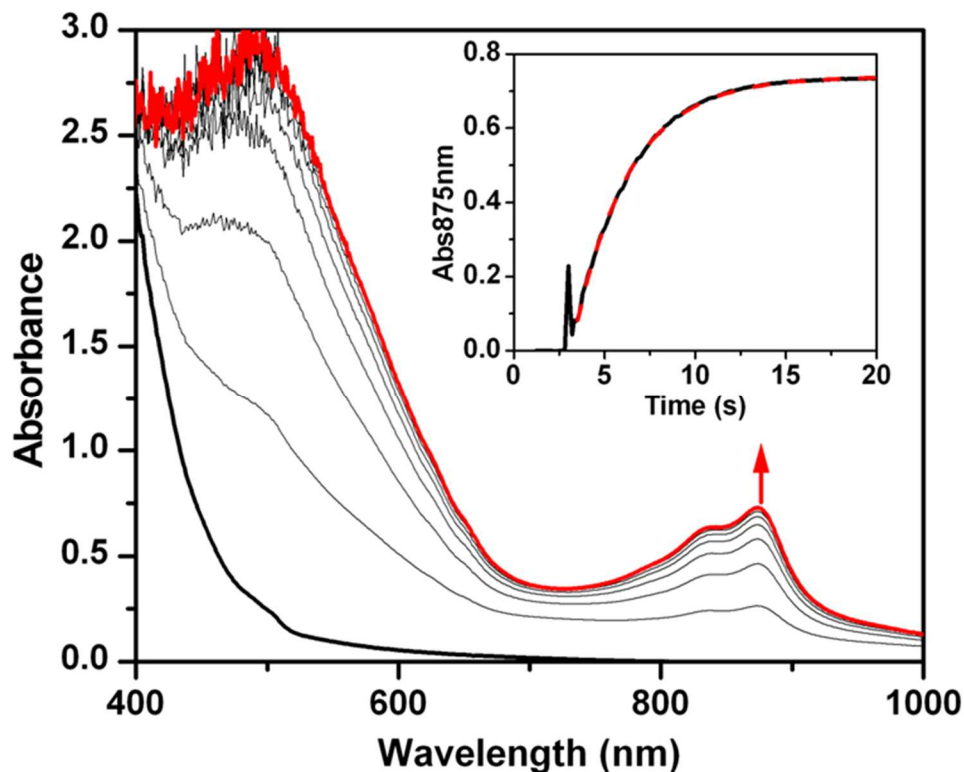


**Figure 2.2:** Formation of **4A** from the reaction of 0.3 mM **2A** and 1 eq H<sub>2</sub>O<sub>2</sub> in CH<sub>3</sub>CN at -40° C in 85% yield determined by UV-Vis spectroscopy.

#### *Structure of 2A:*

To understand how H<sub>2</sub>O<sub>2</sub> is activated, the structure of **2A** was investigated, as nonheme diferric iron model complexes have been shown to exist in both a diamond core and an open core form (Scheme 2.4).<sup>16,26</sup> Similar to **1A**, the crystal structure of **2A**, *vide infra*, was found in the closed core form and the bond distances of the core structure are comparable to those of similar nonheme diiron complexes.<sup>16,26</sup> Because the diiron core **1A** was found to open in the presence of H<sub>2</sub>O,<sup>16</sup> the solution geometry of **2A** was investigated with several techniques in order to elucidate the structure of the diferric starting



material. EXAFS was used to investigate both solid state and solution samples of **2A** to determine its core geometry. The Fourier transform ( $R'$  space) of the Fe K-edge EXAFS data of microcrystalline **2A** diluted with boron nitride (1:20 by mass) exhibits several prominent peaks (Figure 2.3 and Table 2.1). The prominent feature around 2.6 Å in  $R'$  space is nearly equal in intensity to the first shell and is characteristic of a heavy atom in a stiff environment like a diamond core.<sup>4,8</sup> Indeed the best fit consisted of four shells at 1.91 Å (two O scatterers), 2.10 Å (four N scatterers), 2.95 Å (six C scatterers) and 3.04 Å (one Fe scatterer) and the fitting combinations are noted in Table 2.1. In line with the crystal structure *vide infra*, the two O scatterers may be assigned to the bridging hydroxo ligands and the four N scatterers to the tetradentate ligand. The intense Fe scatterer modeled at 3.04 Å is in excellent agreement with a rigid diamond core motif observed in the crystal structure.

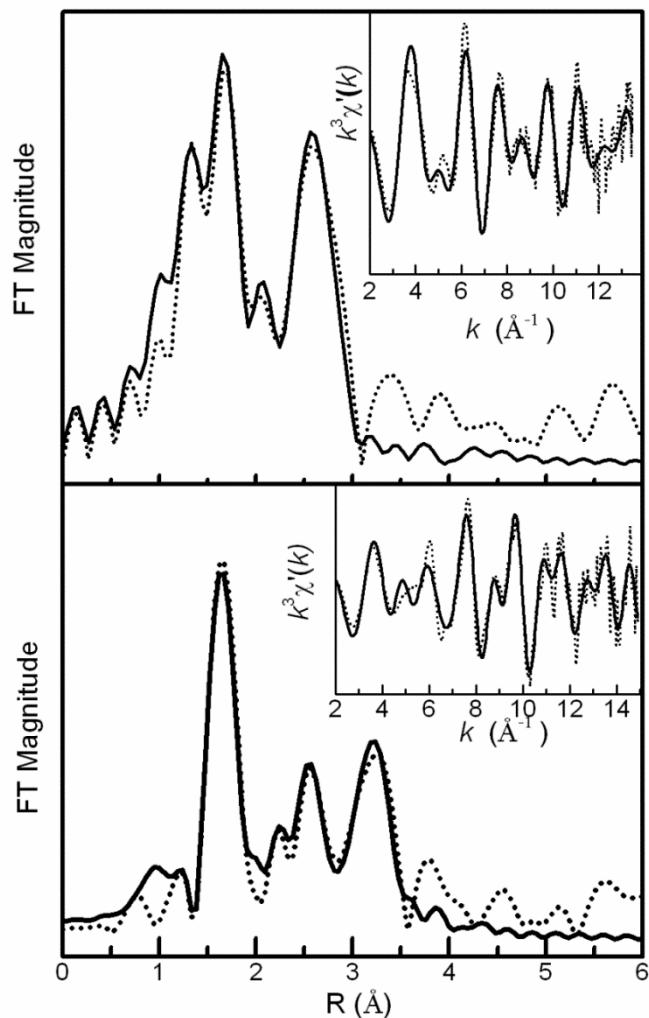


**Figure 2.3:** Fourier transform of the unfiltered EXAFS data (inset) of experimental data (dotted line) and best fit (solid line) of: **Top-** microcrystalline **2A** diluted 20:1 in boron nitride by mass. The best fit was accounted for by four shells at 1.91 Å (two O scatterers), 2.10 Å (four N scatterers), 2.95 Å (six C scatterers) and 3.04 Å (one Fe scatterer) and **Bottom-** 5 mM acetonitrile solution of **2A**. The best fit model contains five shells at 1.79 Å (one O scatterer), 2.12 Å (five N/O scatterers), 3.03 Å (six C scatterers), 3.42 Å (one Fe scatterer) and a 3.569 Å multiple scattering pathway modeled with a Fe-O-Fe moiety.

**Table 2.1** EXAFS fitting to unfiltered EXAFS data for crystalline **2A**  $[\text{Fe}^{\text{III}}_2(\mu\text{-OH})_2(\text{SR}_3\text{TPA})_2]^{4+}$  using  $F_{\text{eff}}$  phase and amplitude parameters listed in (Å).

Fit	Fe-N			Fe-O			Fe-C			Fe-Fe					
#	N	R	$\sigma^2$	N	R	$\sigma^2$	N	R	$\sigma^2$	N	R	$\sigma^2$	$E_0$	F	F'
Default phase and amplitude parameters															
1	4	2.113	2.2	2	1.939	5.1	4	2.957	1.4	1	3.017	1.4	-1.64	286	415
							6	3.108	1.1						
$F_{\text{eff}}$		2.11			1.94		2.96, 3.11				3.04				
2	4	2.094	2.9	2	1.908	5.5							-11.4	863	721
3	5	2.077	4.5	1	1.874	1.3							-11.6	881	729
4	4	2.105	12.1	1	1.931	1.9							-7.13	832	708
				1	2.080	-1.8									
5	4	2.109	2.9	2	1.925	6.7	8	3.019	2.1				-7.22	355	462
6*	4	2.098	2.3	2	1.911	5.4	4	2.945	-2.9	1	3.039	-1.2	-9.00	239	392
7	4	2.100	2.2	2	1.913	5.2	4	2.964	0.5	1	3.022 <sup>x</sup>	1.7	-8.93	246	398
8	4	2.101	2.5	2	1.913	5.8	6	3.001 <sup>f</sup>	3.7 <sup>f</sup>	1	3.001 <sup>f</sup>	3.7 <sup>f</sup>	-8.22	243	395

A second Fe-C scatterer gave non-sensible distances with only a minor improvement in quality factors

$k$  range = 2-13.5 Å<sup>-1</sup>, resolution = 0.137 Å, back transform range ~,  $\sigma^2$  = mean-squared deviation in units of 10<sup>-3</sup> Å<sup>2</sup>. Scale Factor  $S_0^2$  = 0.9. Goodness-of-fit = F calculated as  $F = \sqrt{\sum k^6 (\chi_{\text{exp}} - \chi_{\text{calc}})^2}$ .

$F' = \sqrt{\sum k^6 (\chi_{\text{exp}} - \chi_{\text{calc}})^2 / \sum k^6 \chi_{\text{exp}}^2}$ . x = distance fixed from average bond distance in crystal structure. f = Fe-C and Fe-Fe shells have their distance and Debye-Waller factors set equal to each other. \* = Best Fit

The crystalline sample of **2A** presented some fitting challenges due to the fact that the distances of the Fe-C scatterers and the Fe-Fe scatterer were within the resolution of the measurement and likely caused the negative Debye-Waller factors in Fit 6, Table 2.1. When the distance and Debye-Waller factors were set equal to each other (Fit 7, Table 2.1), a satisfactory Debye-Waller factor is observed with an approximately average distance of the Fe-C and Fe-Fe scatterers. Therefore, in combination with the crystal structure, *vide infra*, the best fit is assigned to Fit 6.

In contrast, **2A** adopts a different core structure in acetonitrile solution. EXAFS studies of a 5 mM frozen solution sample of **2A** in anhydrous acetonitrile showed that the prominent feature in the microcrystalline sample assigned to the rigid Fe-Fe scatterer in a diamond core was absent. Instead, a less intense feature around 3.3 Å was observed, suggesting the heavy atom scatterer was at a longer distance and in a more flexible environment compared to the solid state sample (Figure 2.3, Table 2.2).<sup>26</sup> The best fit model validated the qualitative assessment and consisted of five shells at 1.79 Å (one O scatterer), 2.12 Å (five N/O scatterers), 3.03 Å (six C scatterers), 3.42 Å (one Fe scatterer) and an Fe-O-Fe multiple scattering pathway. This model was most consistent with the open core diferric complexes with similar TPA based ligands in previously solved crystal structures.<sup>26</sup> The short O scatterer matches well with a bridging oxo ligand, the five N/O scatterers corresponded to four N scatterers from the ligand and one solvent, N (CH<sub>3</sub>CN) or O (H<sub>2</sub>O) scatterer; the H<sub>2</sub>O that may be present would originate from the H<sub>2</sub>O in the crystal lattice. A 146° Fe-O-Fe angle is

calculated using the Fe-Fe and Fe-O scattering distances and is most consistent with an open core. Conversely, the solid state structure of **1A** conserves the diamond core motif in solution with low H<sub>2</sub>O concentrations, and changes to an open core structure under higher H<sub>2</sub>O concentrations.<sup>16</sup>

**Table 2.2.** EXAFS fitting to unfiltered EXAFS data for **2A**, solution  $[\text{Fe}^{\text{III}}_2(-\mu\text{-O})(\text{OH}_2)_2(\text{SR}_3\text{TPA})_2]^{4+}$  using  $F_{\text{eff}}$  phase and amplitude parameters listed in (Å).

Fit #	Fe-N			Fe-O			Fe-C			Fe-Fe			$E_0$	F	F'
	N	R	$\sigma^2$	N	R	$\sigma^2$	N	R	$\sigma^2$	N	R	$\sigma^2$			
Feff	2.11			1.79			3.03			3.419(m)					
1	5	2.096	3.9	1	1.784	0.8							-14.0	X	711
2	4	2.070	2.4	2	1.778	5.7							-20.8	X	750
3	5	2.111	4.1	1	1.790	0.3	8	3.021	3.8				-9.01	812	615
4	5	2.118	4.2	1	1.788	0.2	8	3.021	3.6	1	3.375	0.5	-7.42	614	534
5*	5	2.118	4.3	1	1.789	0.0	8	3.030	2.6	1	3.418	0.1	-7.54	368	414
										4 <sup>m</sup>	3.569	0.8			
6	5	2.116	4.3	1	1.789	0.0	8	3.029	3.0	1	3.491	10.4	-8.06	365	412
										2 <sup>m</sup>	3.604	-2.7			
7	5	2.118	4.3	1	1.789	0.0	4	3.006	1.0	1	3.470	11.5	-7.75	363	411
							4	3.075	3.0	2 <sup>m</sup>	3.603	-2.5			
8	5	2.108	4.1	1	1.788	0.2	8	3.017	4.1	1	3.361	2.7	-9.80	392	427
							8	3.656	0.4						
9	5	2.058	3.8	1	1.761	1.0	8	3.246	-2.8	1	3.350	-3.6	-25.1	836	624
							1 <sup>m</sup>	3.509	16.9						

F drops to 313 when  $k$  range = 2-14 Å<sup>-1</sup> for fit 5 above

$k$  range = 2-15 Å<sup>-1</sup>, resolution = 0.122 Å, back transform range ~, Fitting parameters and variables are listed in Table 2.1, \* = Best Fit

As evident by the much improved quality factors going from Fit 4 to Fit 5 in Table 2.2, the additional multiple scattering pathway is necessary to provide a satisfactory fit. Fits that include alternative multiple scattering pathways at different distances, fits that include a C atom, or additional Fe-C shells did not provide a superior fit (Table 2.2). Therefore the best fit is assigned to Fit 5 of Table 2.2.

Resonance Raman infrared spectroscopy was performed on a frozen solution of **2A** to provide additional insight into the core structure.<sup>ii</sup> The  $\nu_{sym}(\text{Fe-O-Fe})$  and  $\nu_{asym}(\text{Fe-O-Fe})$  Raman active stretching frequencies of ( $\mu$ -oxo)diiron(III) complexes have been found to correlate well with the Fe-O-Fe angle.<sup>62</sup> Indeed, a vibration at  $835\text{ cm}^{-1}$  was observed that shifted under a  $\text{CH}_3\text{CN}$  solvent vibration at  $800\text{ cm}^{-1}$  when  $^{18}\text{O}$  was used in the synthetic procedure (Figure 2.4). To determine the magnitude of the shift due to  $^{18}\text{O}$ ,  $\text{CD}_3\text{CN}$  was used and the vibration was clearly seen at  $795\text{ cm}^{-1}$  with an observed shift of  $\sim 40\text{ cm}^{-1}$ , which is in agreement with the expected shift of a Fe-O diatomic oscillator according to Hooke's Law. The  $835\text{ cm}^{-1}$  vibration is assigned to the Fe-O-Fe asymmetric vibration. A vibration was observed at  $463\text{ cm}^{-1}$  that downshifted  $8\text{ cm}^{-1}$  with  $^{18}\text{O}$  isotope substitution and is consistent with the  $\nu_{sym}(\text{Fe-O-Fe})$  (Figure 2.4).<sup>62</sup> Together the two indicate an open core with an Fe-O-Fe angle between  $140\text{-}150^\circ$ .<sup>26,62</sup> The EXAFS and resonance Raman experiments strongly support the open core formulation of **2A** in solution

---

<sup>ii</sup> Resonance Raman spectroscopy performed by Dr. Genqiang Xue.

(Scheme 2.5). An H-bonded water molecule is found in the unit cell of the crystal structure of **2A** and is the likely source of the second aqua ligand. EXAFS cannot conclusively rule out an CH<sub>3</sub>CN ligand in place of the aqua ligand, but water is found bound to both Fe centers in other published structures recrystallized from CH<sub>3</sub>CN.<sup>26</sup>

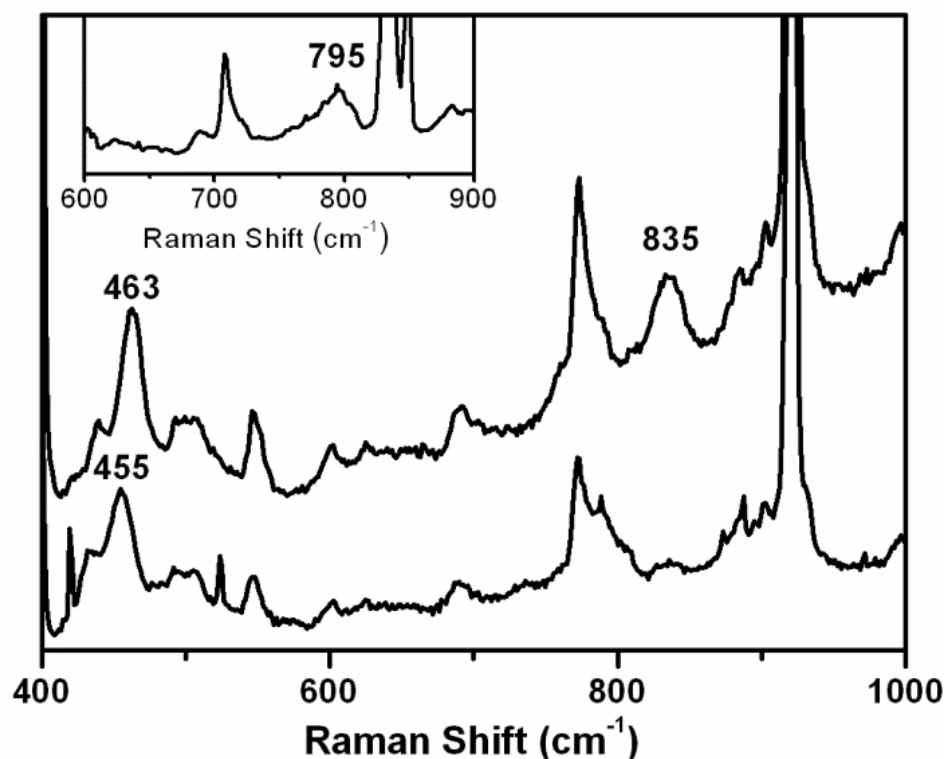
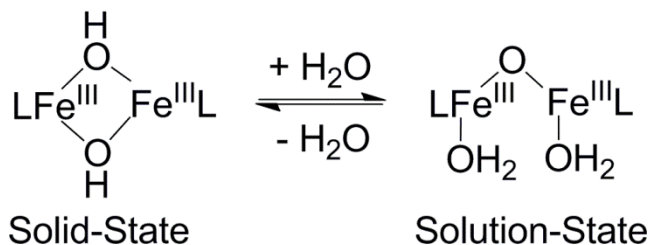


**Figure 2.4:** Main window: rRaman spectra of **2A** in a CH<sub>3</sub>CN solution using a 413.1 nm excitation energy at 100mW power collected at liquid N<sub>2</sub> temperature. Main window-Top spectra: natural abundance isotopes, bottom spectra: <sup>18</sup>O isotopically labeled **2** and Inset: CD<sub>3</sub>CN solvent was used with <sup>18</sup>O isotopically labeled **2** to move solvent peak obstructing the <sup>18</sup>O vibration.





**Scheme 2.5:** Structures of **2A** in the solid and solution state are shown in above. Acetonitrile may also play the role of the additional water molecule shown above.

#### *Acid/Base Chemistry of 1 and 2:*

To determine the *pKa* of the diferric compounds, solutions of **2A** and **2B** were titrated with small aliquots of a 3-bromopyridine solution in an  $\text{CH}_3\text{CN}$  solution and the changes were monitored spectrophotometrically.<sup>i</sup> Both spectra of **2A** and **2B** cleanly convert to **1A** and **1B**, respectively, as the concentration of 3-bromopyridine increases (Figure 2.5, the transformation from **2A** to **1A** is representative for both). A plot of the absorbance of the 550 nm band vs. concentration of 3-bromopyridine displayed in the inset of Figure 2.5 shows that the *pKa* of **1A** was determined to be at least 1 *pKa* unit higher than 3-bromopyridine (3-bromopyridine *pKa* = 2.84 in  $\text{H}_2\text{O}$ ). On the other hand, the same experiment carried out for **1B** and **2B** shows that the *pKa* of this acid-base pair is about 1 *pKa* unit lower than that of the **1A/2A** pair (the *pKa* of **1B** is comparable to 3-bromopyridine), consistent with the presence of fewer electron-donating substituents on the pyridine donors. The difference in *pKa* between the diferric complexes supported by ligands **A** and **B** appears to be an important difference. The complex supported by ligand **A** is the only diferric species able to

make the high-valent model complexes **3A** and **4A**. Other ligands have been shown to form the mixed valent complex **5**, but none has been able to stabilize the diiron(IV) species. The higher basicity of ligand **A** likely provides enough electron density to stabilize the highly oxidized centers.

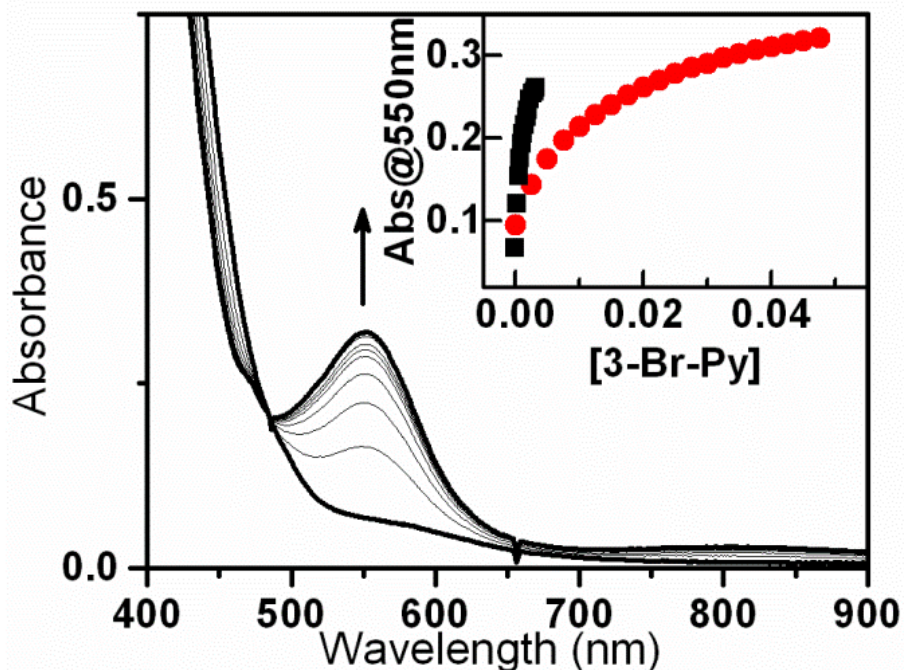


**Figure 2.5:** Titration of 0.3 mM solution of **2** in CH<sub>3</sub>CN with 3-bromopyridine to form the conjugate base **1A**. Monitoring the formation of **1A** (red circles) and **1B** (black squares) by the increase of the 550 nm band from the titration of **2A** and **2B** with 3-bromopyridine (Inset).

*Activation of H<sub>2</sub>O<sub>2</sub> by **1A** and **2A**:*

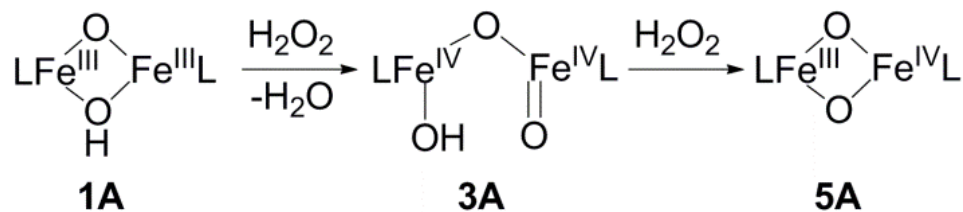
Complexes **1A** and **2A** are the only reported examples of diferric species able to activate H<sub>2</sub>O<sub>2</sub> to generate well-characterized high-valent diiron species. These complexes provide an opportunity to gain insight into how these centers cleave the O-O bond analogous to the conversion of sMMO-P to sMMO-Q.

Therefore, kinetic studies of H<sub>2</sub>O<sub>2</sub> activation by complexes **1A** and **2A** were conducted.

Prior to investigating **1A**, experimental challenges had to be overcome. The reaction product of **1A** and H<sub>2</sub>O<sub>2</sub> is **3A**; however, **3A** will oxidize H<sub>2</sub>O<sub>2</sub> at rates comparable to the reaction of **1A** and H<sub>2</sub>O<sub>2</sub> and form the one-electron reduced **5A** (Scheme 2.6). H<sub>2</sub>O<sub>2</sub> acts as an oxidizing agent first to convert **1A** to **3A**, and then as a reducing agent to convert **3A** to **5A**. This observation demonstrates how Fe is able to efficiently use the oxidizing equivalents stored in H<sub>2</sub>O<sub>2</sub>. The yield of **3A** increased by ~10% when D<sub>2</sub>O<sub>2</sub> was used and the higher yield was presumably due to the KIE for the oxidation of H<sub>2</sub>O<sub>2</sub>.<sup>27</sup> To experimentally illustrate the large KIE, **3A** was first formed with 0.8 equivalent H<sub>2</sub>O<sub>2</sub> added as the oxidant, and then additional aliquots H<sub>2</sub>O<sub>2</sub> or D<sub>2</sub>O<sub>2</sub> were added under pseudo-first order conditions to extract rate constants for each reaction.<sup>iii</sup> The oxidation of H<sub>2</sub>O<sub>2</sub> or D<sub>2</sub>O<sub>2</sub> by **3A** was monitored by the decay of the band at 705 nm and the growth of the 620 nm band associated with the 1-e<sup>-</sup> reduced **5A** (Figure 2.6). A large KIE of 25 was determined from the ratio of the rate constants (Figure 2.6). This value is close to the KIE of 30 for the oxidation of 9,10-dihydroanthracene by **3A**,<sup>13</sup> suggesting that O-H bond cleavage is a large component of the rate limiting step. Compared to the oxidation of H<sub>2</sub>O<sub>2</sub> by the mononuclear ferryl species Fe<sup>IV</sup>(O)N4Py and Fe<sup>IV</sup>(O)TMC,<sup>88</sup> the rates are 7.5 and 170 times faster even though oxidation of H<sub>2</sub>O<sub>2</sub> by **3A** was carried out at -40° C compared to -20° C and 25° C respectively.

---

<sup>iii</sup> Experiment performed by Dr. Genqiang Xue.



**Scheme 2.6:** Activation of H<sub>2</sub>O<sub>2</sub> by **1A** and subsequent oxidation of H<sub>2</sub>O<sub>2</sub>.

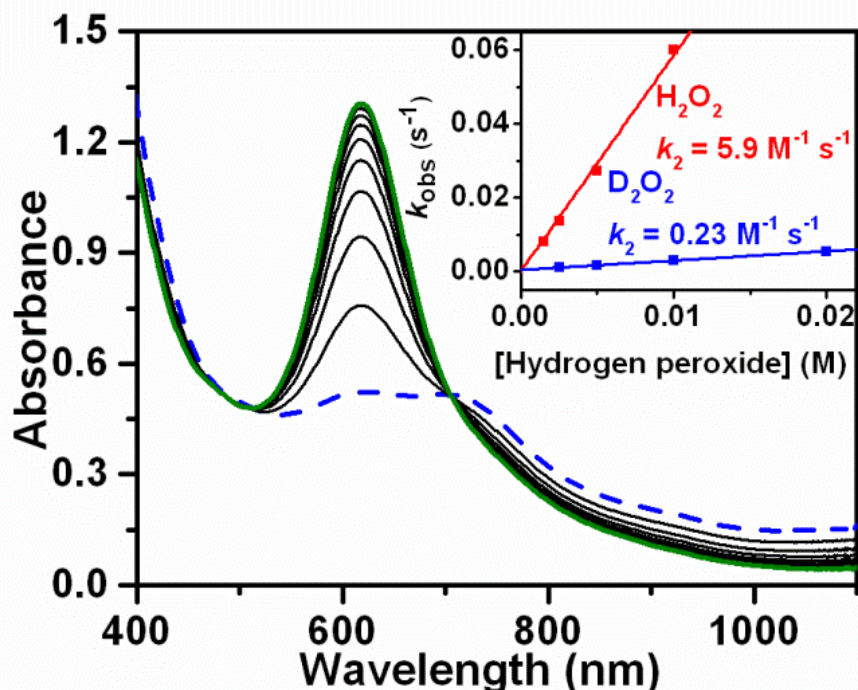
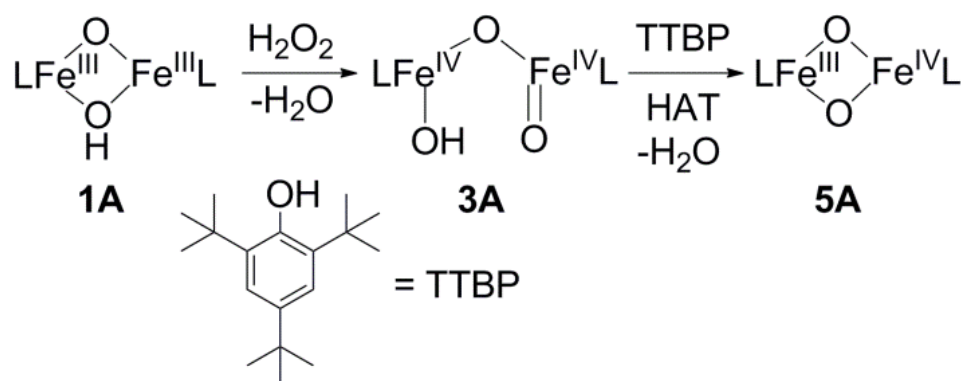


**Figure 2.6:** The oxidation of H<sub>2</sub>O<sub>2</sub> (under pseudo-first order conditions) by a 0.3 mM solution of **3A** in acetonitrile at -40° C (blue, dashed line) and the formation of the product **5A** (green, solid line). Inset: the rate of formation of **5A** from the reaction of **3A** and varying concentrations of H<sub>2</sub>O<sub>2</sub> (red) and D<sub>2</sub>O<sub>2</sub> (blue). The KIE was found to be 25.

The ability of **3A** to oxidize H<sub>2</sub>O<sub>2</sub> severely complicates any kinetic experiments performed under pseudo-first order conditions with excess H<sub>2</sub>O<sub>2</sub>. These complications may be circumvented by eliminating the reduction of **3A** to **5A** by H<sub>2</sub>O<sub>2</sub>. To accomplish this task, a more easily oxidized H-atom donor was employed to intercept **3A** as soon as it was formed. One or two equivalents of

2,4,6-tri-*tert*-butylphenol (TTBP) was found to react instantaneously with **3A** to form **5A** (Scheme 2.7).<sup>1</sup> When a 0.3 mM solution of the diiron(III) starting material, **1A**, and 1 eq TTBP was reacted with 1 eq H<sub>2</sub>O<sub>2</sub>, the characteristic band of **5A** at 620 nm grew in at the same rate as the 2,4,6-tri-*tert*-butylphenoxy radical band at 400 nm (Figure 2.7) and resulted in the formation of **5A** in 80% yield according to electronic absorption spectroscopy. Under these conditions, the activation of H<sub>2</sub>O<sub>2</sub> by **1A** becomes the rate limiting step followed by the fast oxidation of TTBP to form **5A**, with no accumulation of **3A**. Therefore, the rate of the appearance of **5A** is equal to the rate of formation of **3A** from the reaction of **1A** and H<sub>2</sub>O<sub>2</sub> when TTBP is present. Using the TTBP probe, the rate of H<sub>2</sub>O<sub>2</sub> activation by **1A** could be studied under pseudo-first-order conditions. The amount of H<sub>2</sub>O was kept constant and the H<sub>2</sub>O in the 70% stock solution of H<sub>2</sub>O<sub>2</sub> was accounted for. First order behavior was observed up to a concentration of 12.5 mM H<sub>2</sub>O<sub>2</sub> in an acetonitrile solution at -40° C, with a second order rate constant of 8 M<sup>-1</sup>s<sup>-1</sup> (Figure 2.8).



**Scheme 2.7:** Reaction of **1A** with H<sub>2</sub>O<sub>2</sub> in the presence of 2,4,6-tri-*tert*-butylphenol (TTBP).

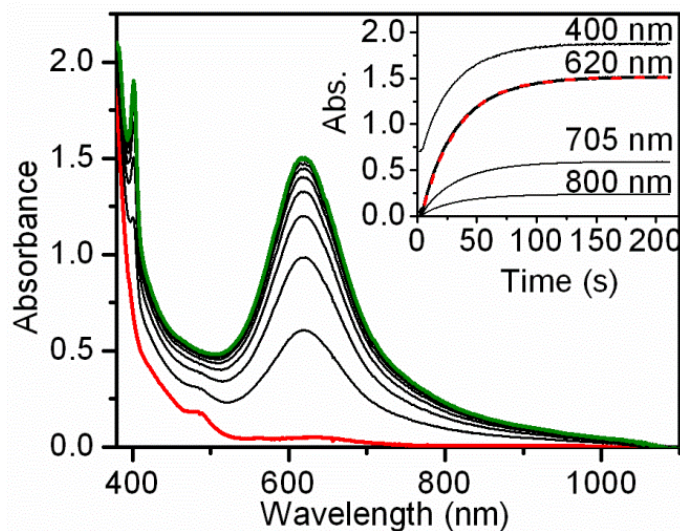


**Figure 2.7:** Formation of **5A** and 2,4,6-tri-*tert*-butylphenoxy radical from the reaction of 0.3 mM (**1<sup>WA</sup>**)<sup>16</sup> and 2,4,6-tri-*tert*-butylphenol (TTBP) and 0.1 M H<sub>2</sub>O in CH<sub>3</sub>CN at -40° C with 1 eq. mM H<sub>2</sub>O<sub>2</sub>. Kinetic traces of Formation of **5A** (620 nm) and 2,4,6-tri-*tert*-butylphenoxy radical (400 nm) from **1A**, H<sub>2</sub>O<sub>2</sub> and TTBP.

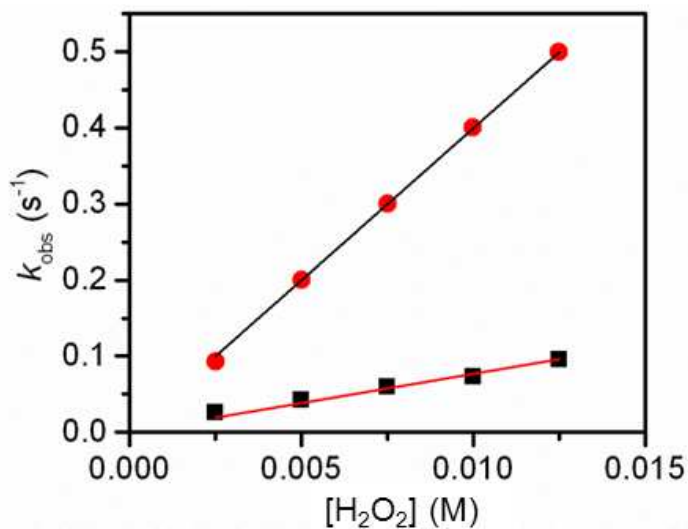


**Figure 2.8:** Activation of H<sub>2</sub>O<sub>2</sub> in an CH<sub>3</sub>CN solution at -40° C by 0.3 mM **1A** (black squares) 0.1 M H<sub>2</sub>O and 0.3 mM TTBP, and 0.5 mM **2A** (red circles) with H<sub>2</sub>O<sub>2</sub> in acetonitrile with 0.1 M H<sub>2</sub>O. The rate constants were determined to be 8 M<sup>-1</sup>s<sup>-1</sup> and 40 M<sup>-1</sup>s<sup>-1</sup> for **1A** and **2A** respectively. The concentration of water from the 70% H<sub>2</sub>O<sub>2</sub> was accounted in both reactions and was kept constant at 0.1 M H<sub>2</sub>O.

The formation of **4A** from the reaction of H<sub>2</sub>O<sub>2</sub> and **2A** was measured by the growth of the 875 nm band, and **4A** was not observed to react with excess H<sub>2</sub>O<sub>2</sub> under the reaction conditions. H<sub>2</sub>O<sub>2</sub> activation by **2A** was studied under similar pseudo-first order conditions as **1A**, except without the TTBP. A linear increase in rate was also observed for the activation of H<sub>2</sub>O<sub>2</sub> by **2A** with a second order rate constant of 40 M<sup>-1</sup>s<sup>-1</sup>, five times higher as compared to the same reaction with **1A** (Figure 2.8).<sup>†</sup> These results suggest that binding of the H<sub>2</sub>O<sub>2</sub> to the diiron center occurs before the rate controlling step or is actually the rate controlling step under these conditions.

*Competition of Water and H<sub>2</sub>O<sub>2</sub> binding to **1A** and **2A**:*

Water was found to inhibit the reaction between H<sub>2</sub>O<sub>2</sub> and **1A** to form **3A**,<sup>16</sup> but detailed studies of the water concentration dependence on rate were not previously carried out due to the side reactions detailed above, which can now be circumvented by addition of TTBP. The rate of H<sub>2</sub>O<sub>2</sub> activation by **1A** decreased with increasing [H<sub>2</sub>O] in an acetonitrile solution at -40° C (Figure 2.9). A plot of 1/ *k*<sub>obs</sub> vs. [H<sub>2</sub>O] showed a linear relationship (Figure 2.9 inset) consistent with a model in which water competes with H<sub>2</sub>O<sub>2</sub> for binding to **1A**.<sup>†</sup> This inverse relationship between *k*<sub>obs</sub> and [H<sub>2</sub>O] tells us that H<sub>2</sub>O<sub>2</sub> must displace an iron-bound water to be activated by **1A** to form **3A** (Scheme 2.8, top). The first step in the mechanism for the competitive binding of H<sub>2</sub>O and H<sub>2</sub>O<sub>2</sub> to **1A** is the formation of open-core derivatives of **1<sup>w</sup>A** and a **1A**-H<sub>2</sub>O<sub>2</sub> adduct that quickly decays to **3A** (Scheme 2.8). Parallel water concentration studies on the activation of H<sub>2</sub>O<sub>2</sub> by **2A** found similar observations that were consistent with



H<sub>2</sub>O competing with H<sub>2</sub>O<sub>2</sub> for binding to the Fe complex; however the H<sub>2</sub>O<sub>2</sub> activation rate was suppressed substantially less for **2A** (Figure 2.9, Scheme 2.8). Using a simple pre-equilibrium model in equation 2.1, the equilibrium constants,  $K_d$ , for **1A** and **2A** were determined by the slope of  $1/k_{obs}$  vs. [water] (Inset, Figure 2.9) and the  $K_d$  values were 340 and 47 for **1A** and **2A**, respectively. The larger inhibition of **1A** by water may be due to a stronger hydrogen bond network. Previously, a hydrogen bonding network was observed in **1<sup>w</sup>** species supported by similar TPA-based ligands and was formed by the aqua and hydroxo ligands.<sup>26</sup>

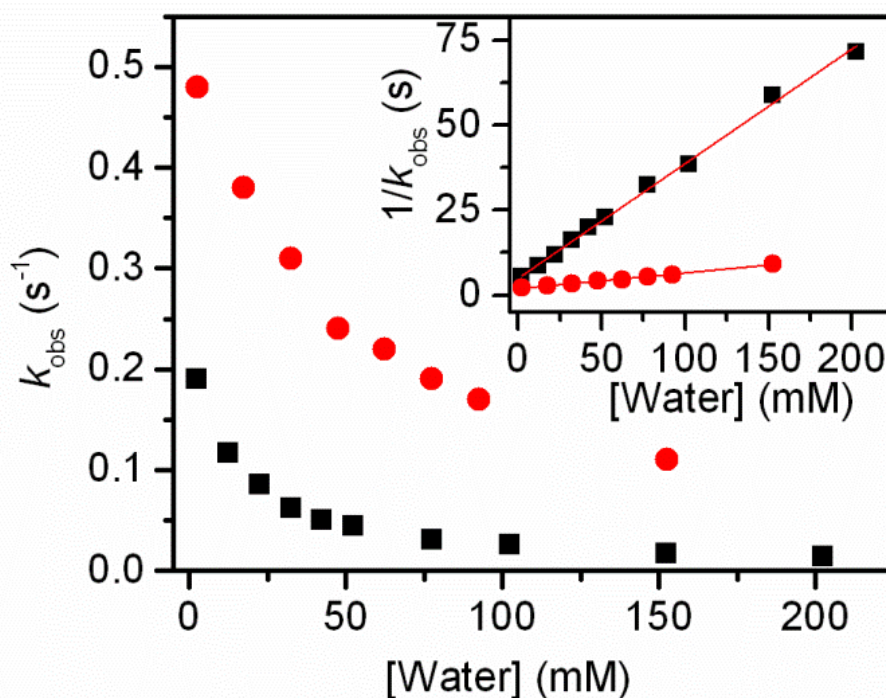
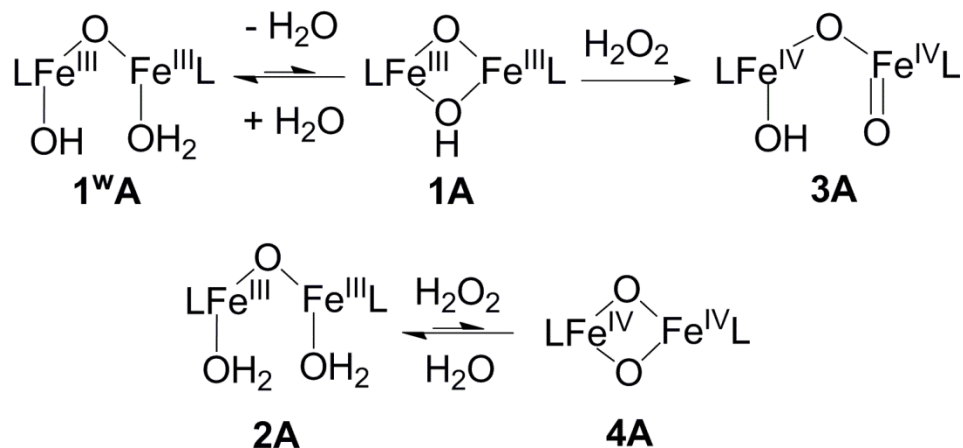


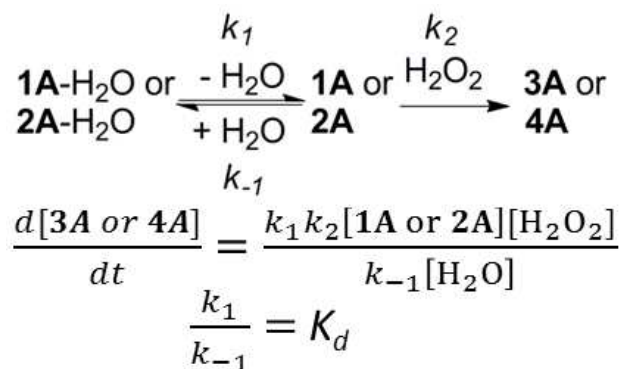
**Figure 2.9:** Dependence of the concentration of H<sub>2</sub>O on the activation of a 2.5 mM H<sub>2</sub>O<sub>2</sub> acetonitrile solution at -40 °C by 0.3 mM **1A** (black squares) and 0.5 mM **2A** (red circles). Inset: plot of  $1/k_{obs}$  vs. H<sub>2</sub>O.





**Scheme 2.8:** Water inhibition of the activation of H<sub>2</sub>O<sub>2</sub> by **1A**, top and **2A** bottom.

**Equation 2.1:** Proposed model of the activation of H<sub>2</sub>O<sub>2</sub> by diiron compounds.



**Acid Effect on the H<sub>2</sub>O<sub>2</sub> Activation by **1A** and **2A**:**

The effect of the H<sup>+</sup> concentration on the activation of H<sub>2</sub>O<sub>2</sub> was investigated. 3-bromopyridine was used to modulate the basicity of the reaction solution. No change in rate was observed for the reaction between **1A** and H<sub>2</sub>O<sub>2</sub> as a function of 3-bromopyridine concentration, suggesting that it is not a strong enough base to deprotonate **1A**. However, formation of **4A** from **2A** and H<sub>2</sub>O<sub>2</sub> was found to be sensitive to the amount of base present. When 2.7 mM 3-bromopyridine and 0.25 mM **2A** in an CH<sub>3</sub>CN solution were mixed with 1.3 mM

H<sub>2</sub>O<sub>2</sub>, a two-step reaction was observed (Figure 2.10). Within the first 10 seconds, a band grew in around 705 nm (corresponding to the formation of **3A**) and then decayed to **4A** during the second step in a manner that could be modeled with a single exponential (Figure 2.10). At higher concentrations of 3-bromopyridine, **3A** persisted long enough in solution and reacted with the excess H<sub>2</sub>O<sub>2</sub> present to prevent a more thorough study. However, fitting the rate of the first step by the method of initial rates yielded a linear dependence on 3-bromopyridine concentration up to about 2 mM, above which, saturation behavior was observed (Figure 2.11). The decay rate of the 705 nm band and the growth rate of the 875 nm band associated with **4A** determined from exponential fits (after the 705 nm band reached a maximum) were in reasonable agreement and decreased in a linear manner with increasing concentration of 3-bromopyridine, consistent with a smaller concentration of H<sup>+</sup> available for protonating **3A** to form **4A** (Figure 2.12).<sup>27</sup> A difference spectrum was obtained by subtracting a spectrum of pure **4A** from the blue trace in Figure 2.10 observed about 5 seconds after the start of the reaction (Figure 2.13). This difference spectrum compares well with an authentic spectrum of **3A**.<sup>27</sup> The rate increase of H<sub>2</sub>O<sub>2</sub> activation by **2A** due to the addition of a weak base suggests that a deprotonation event occurs at or before the rate limiting step. Because the rates of H<sub>2</sub>O<sub>2</sub> activation are 5 times higher for **2A**, even in the absence of added 3-bromopyridine, the deprotonation event does not occur prior to the binding of H<sub>2</sub>O<sub>2</sub> to **2A**, but takes place after the H<sub>2</sub>O<sub>2</sub> adduct is formed. This step would create a species with the same degree of protonation as a **1A** + H<sub>2</sub>O<sub>2</sub> derived

species, suggesting that  $\text{H}_2\text{O}_2$  activation by **1A** and **2A** goes through shared intermediates. The generation of **3A** en route to the formation of **4A** provides evidence that **1A** and **2A** activate  $\text{H}_2\text{O}_2$  on a shared path that converges prior to O-O bond breaking.

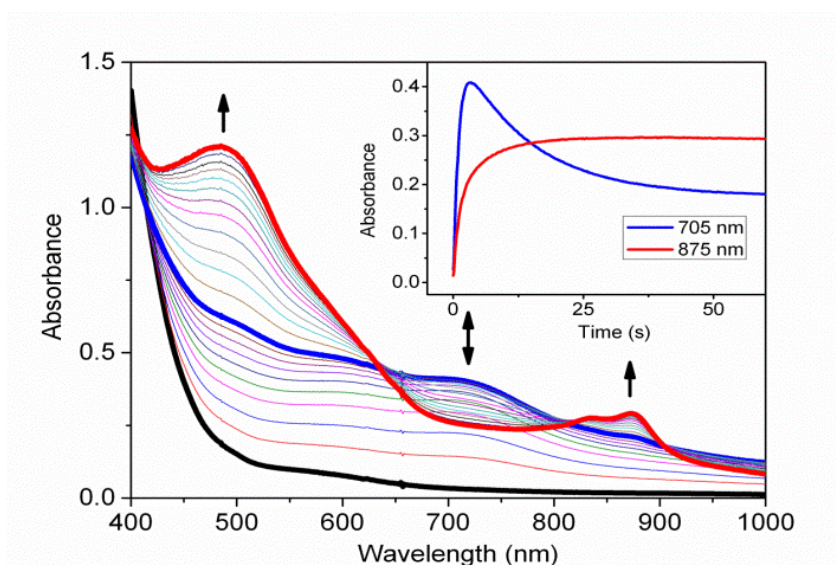


**Figure 2.10:** Reaction of 0.25 mM **2A** and 2.7 mM 3-bromopyridine (black) with 1.3 mM  $\text{H}_2\text{O}_2$  and 1.1 mM  $\text{H}_2\text{O}$  (from 70%  $\text{H}_2\text{O}_2$ ) to form an intermediate (blue) and **4A** (red). The time traces at 705 and 875 nm are shown in the inset.

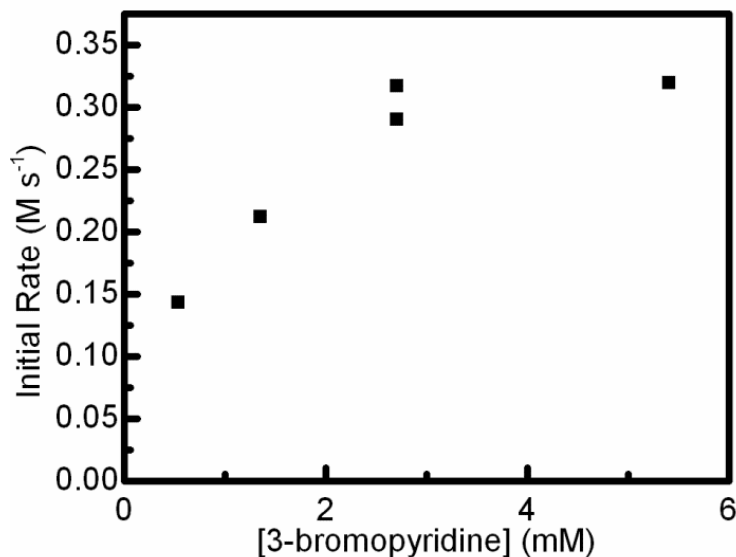


**Figure 2.11:** Monitoring the initial rate of the growth of the 705 nm band with increasing concentration of 3-bromopyridine in a 0.25 mM **2A**, 1.3 mM H<sub>2</sub>O<sub>2</sub> and 1.1 mM H<sub>2</sub>O (from 70% H<sub>2</sub>O<sub>2</sub>) in CH<sub>3</sub>CN.

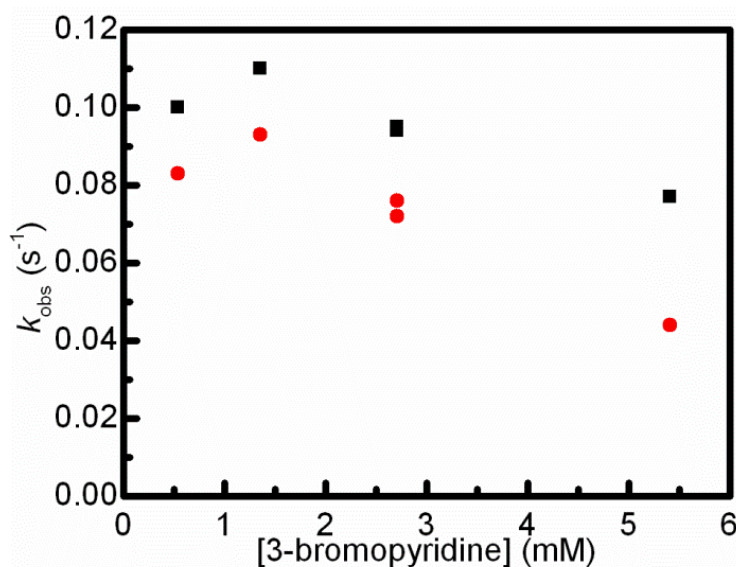


**Figure 2.12:** Monitoring the rate of the growth of the 475 nm band (black squares) and the decay of the 705 nm band (red circles) with increasing concentration of 3-bromopyridine in a 0.25mM **2A**, 1.3 mM H<sub>2</sub>O<sub>2</sub> and 1.1 mM H<sub>2</sub>O (from 70% H<sub>2</sub>O<sub>2</sub>) in CH<sub>3</sub>CN.

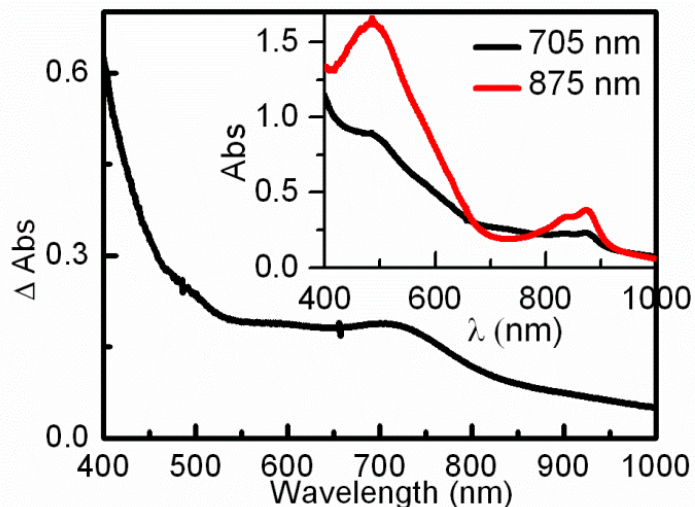
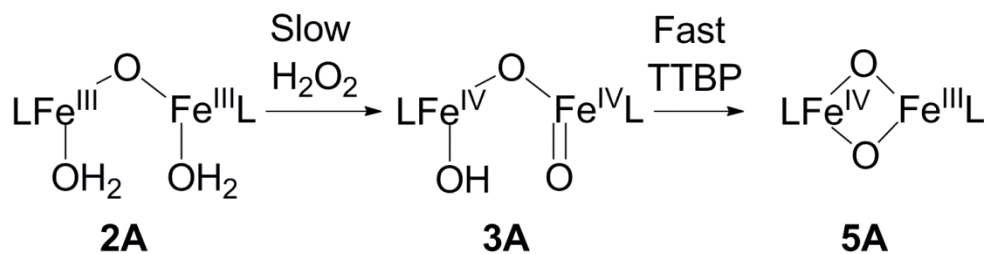


**Figure 2.13:** Difference spectrum of the spectrum of **4A** (inset red) from the spectrum at the maximum formation of the feature at  $\sim$ 705 nm (inset black) for the reaction of **2A** (0.25mM) and 3-bromopyridine (2.7 mM) with  $\text{H}_2\text{O}_2$  (1.3 mM).

Additional evidence that **1A** and **2A** activate  $\text{H}_2\text{O}_2$  on a shared path was obtained by the use of the 2,4,6-tri-*tert*-butylphenol (TTBP) probe. Similar to the way the  $[\text{H}_2\text{O}_2]$  dependence of **1A** was measured, an experiment was designed that takes advantage of the much faster rate of TTBP oxidation by **3A** compared to **4A** (instantaneous vs. 30 minutes when 1-2 eq of TTBP was added at  $-40^\circ\text{C}$ ). This difference suggests that TTBP should be able to intercept **3A** if it is a precursor of **4A** (Scheme 2.9). This is indeed the case. Addition of 1 eq  $\text{H}_2\text{O}_2$  to a 0.4 mM acetonitrile solution of **2A** and TTBP elicits a peak at 620 nm corresponding to **5A** with no evidence of **3A** or **4A** (Figure 2.14). The activation of  $\text{H}_2\text{O}_2$  by **1A** and **2A** is thus shown to go through convergent mechanisms.



**Scheme 2.9:** H<sub>2</sub>O<sub>2</sub> activation by **2A** in the presence of 2,4,6-tri-*tert*-butylphenol (TTPB).

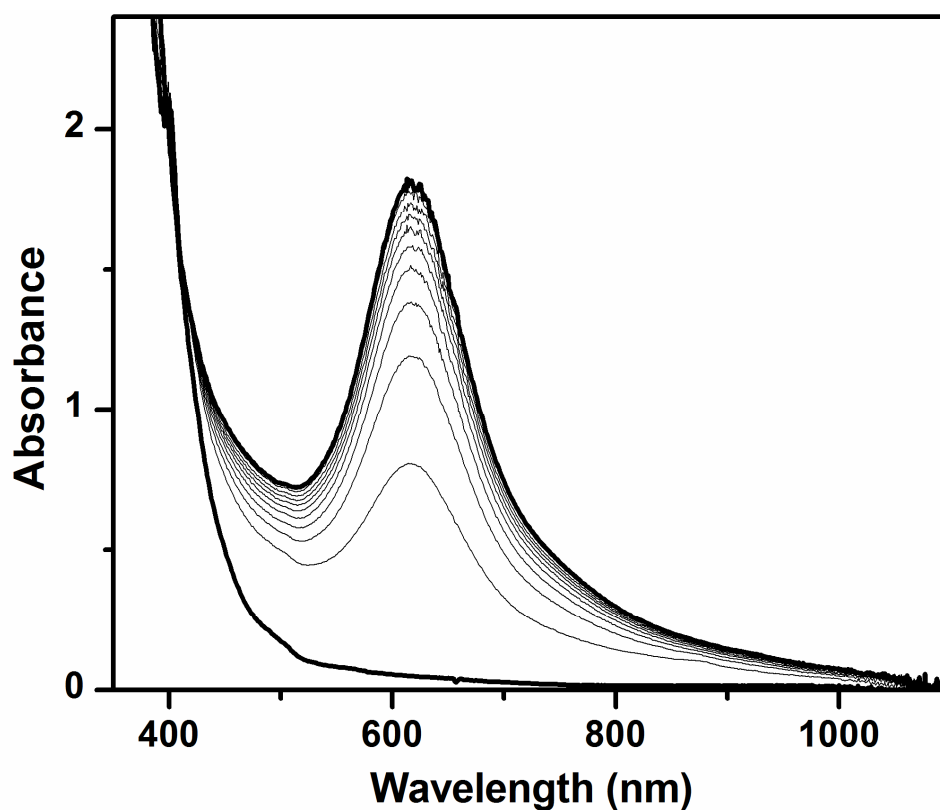


**Figure 2.14:** Reaction of 0.4 mM **2A** with 1 eq. H<sub>2</sub>O<sub>2</sub> in the presence of 1 eq. 2,4,6-tri-*tert*-butylphenol in CH<sub>3</sub>CN at -40° C to form **5A**.

As mentioned above, only a limited study of the effect of base on the activation of H<sub>2</sub>O<sub>2</sub> by **2A** could be conducted because **3A** was observed to form.

To observe the activation of H<sub>2</sub>O<sub>2</sub> by **2A**, the TTBP probe was employed as

described earlier to measure the activation of  $\text{H}_2\text{O}_2$  by **1A** to eliminate side reactions of **3A**. With TTBP in the reaction mixture prior to the addition of  $\text{H}_2\text{O}_2$ , the activation rate by **2A** was measured by the increase of the 620 nm band of **5A**. Increasing concentrations of the base 3-bromopyridine ( $\text{pK}_a = 2.84$  in water) increased the observed rate constant under excess  $\text{H}_2\text{O}_2$  (10 eq  $\text{H}_2\text{O}_2$  vs. 0.2 mM **2A** in acetonitrile at  $-40^\circ\text{C}$ ) (Figure 2.15).<sup>iv</sup> Consistent with previous experiments, as the concentration of 3-bromopyridine was increased to 1.25 mM and beyond, saturation behavior was observed, with a maximum increase in the rate by about 3 fold (Figure 2.15). Saturation behavior suggests that an equilibrium step is involved with the reaction of **2A** and  $\text{H}_2\text{O}_2$  with added base. Because the rate of  $\text{H}_2\text{O}_2$  activation by **2A** is faster than **1A** (Figure 2.8), the iron complex is not deprotonated from **2A** to **1A** prior to the reaction with  $\text{H}_2\text{O}_2$ . Instead, it is proposed that the base deprotonates the bound hydrogen peroxide in adduct **II** to form hydroperoxo species **I**, as illustrated in Scheme 2.10 below. Interestingly, if 1 eq of  $\text{HClO}_4$  was added to solution of **2A**, no reaction between **2A** and  $\text{H}_2\text{O}_2$  was observed until an equal amount of 3-bromopyridine was added. This highlights the acid/base balance necessary for the activation of  $\text{H}_2\text{O}_2$  by **2A**. Base enhancement was also observed for a mononuclear Fe system where adding the base 2,6-lutidine increased the rate of  $\text{H}_2\text{O}_2$  activation by about 5 times;<sup>89</sup> a similar enhancement ( $\sim 3$  times) was observed for **2A**. A

---

<sup>iv</sup> At 4mM [3-bromopyridine]  $\sim 80\%$  of **2A** converted to **1A** and higher concentrations of base were not used because the fraction of **1A** became significant enough to observe in the electronic absorption spectrum.

KIE of almost 4 was observed in the mono-Fe system in a D<sub>2</sub>O/D<sub>2</sub>O<sub>2</sub> system,<sup>89</sup> while a negligible KIE was observed for **2A** in a D<sub>2</sub>O/D<sub>2</sub>O<sub>2</sub> system (Figure 2.16).<sup>iii</sup>

The order of the p*K*<sub>a</sub> values of a few of the diiron acid/base pairs may be deduced from the experiments. The three sets of equilibria have the same charge, so the p*K*<sub>a</sub> values are relatively close and are independent of the oxidation state of the iron atoms. The largest p*K*<sub>a</sub> belongs to **1A** because only **3A** is formed from the reaction with H<sub>2</sub>O<sub>2</sub>. Starting from **2A**, both **3A** and **4A** can be formed by the addition of H<sub>2</sub>O<sub>2</sub> by adjusting the amount of base in solution. Because **3A** is protonated by the conjugate acid of the base that deprotonates **II**, the apparent p*K*<sub>a</sub> of **3a** is greater than **II**, which may be higher than the true p*K*<sub>a</sub> because of the increased entropy due to the loss of one H<sub>2</sub>O molecule after protonation. Therefore, the order of increasing apparent p*K*<sub>a</sub> values of the diiron acid base pairs is **IA/IIA** < **3A/4A** < **1A/2A**.



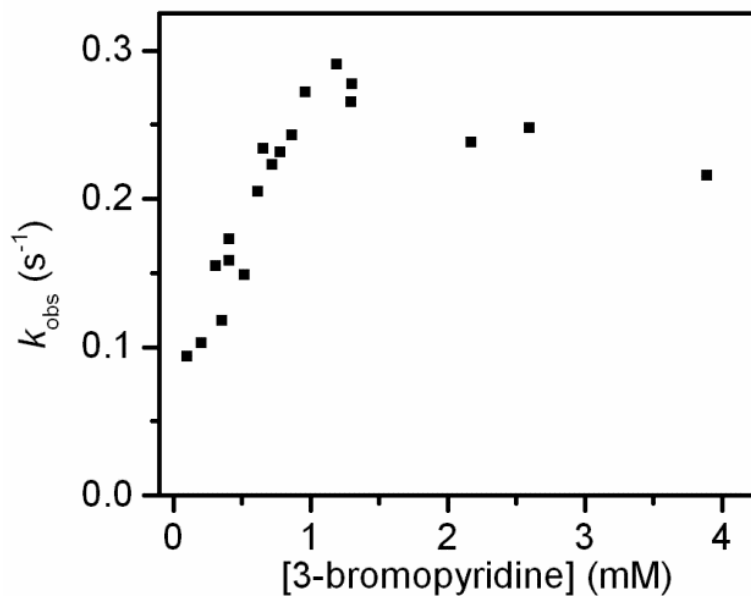


**Figure 2.15:** Reaction of 0.2 mM **2A**, 0.4 mM tri-*tert*-butylphenol and 3-bromopyridine with 2 mM H<sub>2</sub>O<sub>2</sub> in acetonitrile at -40° C.

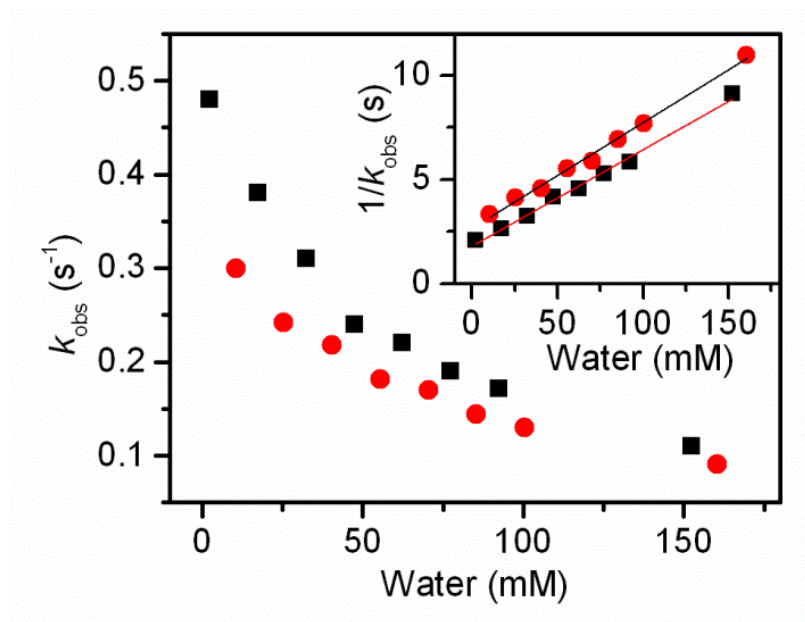
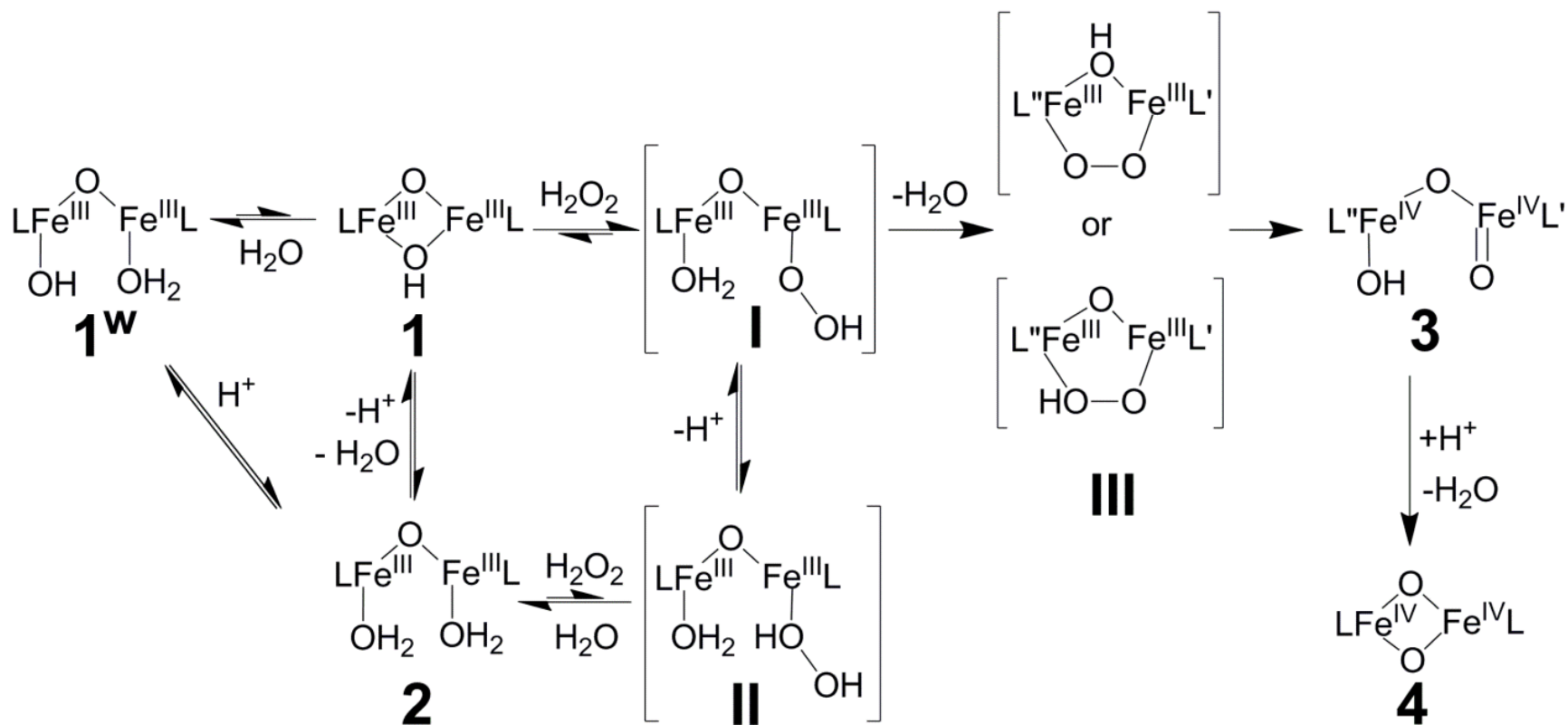


**Figure 2.16:** D<sub>2</sub>O (red circles) H<sub>2</sub>O (black squares) for the activation of H<sub>2</sub>O<sub>2</sub> or D<sub>2</sub>O<sub>2</sub> by a 0.5 mM solution of **2A** in acetonitrile at -40° C.



**Scheme 2.10:** Proposed mechanism for the activation of H<sub>2</sub>O<sub>2</sub> by diiron compounds **1A** and **2A**. The amine N atom is *trans* to the oxo or (hydro)peroxo ligand when noted L' and the substituted pyridine is *trans* to the hydroxo or(hydro)peroxo ligand when noted L". Brackets indicate a proposed transient intermediate.

## 2.3 Discussion:

### *H<sub>2</sub>O<sub>2</sub> Activation by 1A and 2A: Mechanism and Rates*

A series of steps is proposed for the mechanism of H<sub>2</sub>O<sub>2</sub> activation by **1A**. The H<sub>2</sub>O<sub>2</sub> activation rates by diferric complexes are summarized in Table 2.3. The initial step of H<sub>2</sub>O<sub>2</sub> binding with **1A** competes with water present for the open coordination site in the diamond core of **1A** to form either **IA** or **1<sup>w</sup>A** (Scheme 2.10). Once the H<sub>2</sub>O<sub>2</sub> is bound to **1A**, the next step involves a fast intramolecular neutralization of the hydrogen peroxide ligand by the hydroxo ligand in **IA**, resulting in the loss of a H<sub>2</sub>O molecule and formation of **IIIA**. The proton is assigned to the bridging oxo ligand in intermediate **IIIA** (Scheme 2.10, **IIIA** top), because previous studies have shown the oxo ligand to be more basic than the peroxo ligand, including a crystal structure of a diiron- $\mu$ -hydroxo- $\mu$ -peroxo complex.<sup>82,84,90</sup> However, the diiron- $\mu$ -oxo- $\mu$ -hydroperoxo complex (Scheme 2.10, **IIIA** bottom) cannot be ruled out, especially considering that only a Fe<sup>IV</sup>Fe<sup>III</sup> species has been formed thus far from a stable peroxo species.<sup>82</sup> The high-valent diiron(IV) complex is formed when **IIIA** undergoes fast O-O bond cleavage to form **3A**. Because high concentrations of H<sub>2</sub>O<sub>2</sub> cannot be attained due to experimental limitations, the peroxo intermediate was not observed, despite using multiple published methods.<sup>44,72,82,91</sup>

**Table 2.3:** Summary of rate constants for the activation of H<sub>2</sub>O<sub>2</sub> by diferric model complexes at -40° C in acetonitrile.

Complex	Variable	Kin. Value	Conditions	Notes
1A	H <sub>2</sub> O <sub>2</sub>	8 M <sup>-1</sup> s <sup>-1</sup> †	0.1 M H <sub>2</sub> O, 0.3 mM Fe <sub>2</sub>	k <sub>2</sub> , Measured formation of <b>5A</b> in presence of TTBP
2A	H <sub>2</sub> O <sub>2</sub>	40 M <sup>-1</sup> s <sup>-1</sup> †	0.1 M H <sub>2</sub> O, 0.5 mM Fe <sub>2</sub> ,	k <sub>2</sub> , Measured formation of <b>4A</b>
2A	3-bromopyridine	3 M s <sup>-1</sup> †	2 mM H <sub>2</sub> O <sub>2</sub> , 0.2 mM Fe <sub>2</sub> , 1.8 mM H <sub>2</sub> O	V <sub>max</sub> , Measured formation of <b>5A</b> in presence of TTBP.
2A	3-bromopyridine	3 M s <sup>-1</sup> †	1.3 mM H <sub>2</sub> O <sub>2</sub> , 0.25 mM Fe <sub>2</sub> , 1.2 mM H <sub>2</sub> O	V <sub>max</sub> , Measured formation of <b>3A</b> (705 nm band) in presence of TTBP.
2A	3-bromopyridine	-9 M <sup>-1</sup> s <sup>-1</sup>	1.3 mM H <sub>2</sub> O <sub>2</sub> , 0.25 mM Fe <sub>2</sub> , 1.2 mM H <sub>2</sub> O	k <sub>2</sub> , Measured decay of <b>3A</b> to form <b>4A</b> by protonation from 3-bromopyridinium ( <b>4A</b> formed in approximately the same rate). The rate observed suggests the protonation of <b>3A</b> is slower at higher base concentrations.
1A	H <sub>2</sub> O	340 †	2.5 mM H <sub>2</sub> O <sub>2</sub> , 0.3 mM Fe <sub>2</sub>	K <sub>d</sub> , 1/k <sub>obs</sub> vs. [H <sub>2</sub> O], Measured formation of <b>5A</b> in presence of TTBP
2A	H <sub>2</sub> O	47 †	2.5 mM H <sub>2</sub> O <sub>2</sub> , 0.5 mM Fe <sub>2</sub>	K <sub>d</sub> , 1/k <sub>obs</sub> vs. [H <sub>2</sub> O], Measured formation of <b>4A</b>

† Measured under pseudo-first order conditions. †† measured with the method of initial rates.

The pathway of H<sub>2</sub>O<sub>2</sub> activation by **2A** converges with the mechanism of **1A** (Scheme 2.10). Similar to the first steps of H<sub>2</sub>O<sub>2</sub> activation by **1A**, the reaction with **2A** followed first-order kinetics with increasing concentration of H<sub>2</sub>O<sub>2</sub> (5 times greater rate) and was consistent with competitive binding with water (Table 2.3). Conversely, saturation behavior in base concentration dependence studies on H<sub>2</sub>O<sub>2</sub> activation by **2A** was observed and is consistent with an acid/base equilibrium between **II** and **I**, where it joins the activation mechanism of H<sub>2</sub>O<sub>2</sub> by **1A** and forms the high-valent **3A** via intermediate **III**. Additionally, the 3-bromopyridium cation, produced from the first deprotonation step (**II** to **I**), protonates **3A** to form **4A**. Interestingly, the reverse reaction from **4A** to **3A** has not been observed, even with the addition of F<sup>-</sup> anion, which is a strong base in acetonitrile and was previously used as a base to make **7A**, the conjugate base of **3A** (Scheme 2.10).<sup>49,92</sup>

The rate constants for the activation of H<sub>2</sub>O<sub>2</sub> by **1A** and **2A** are much smaller than that reported rate constant of 230 M<sup>-1</sup>•s<sup>-1</sup> by the mono iron complex Fe<sup>II</sup>TMC at the same temperature.<sup>89</sup> However, no water inhibition was reported in this mono iron study. Using a pre-equilibrium approximation (Equation 2.1), the rate constant for H<sub>2</sub>O<sub>2</sub> activation in the absence of H<sub>2</sub>O by the diferric complexes may be estimated by dividing the *k*<sub>obs</sub> of the reaction by the *K*<sub>d</sub> determined from the [H<sub>2</sub>O] studies and then multiplying by the [H<sub>2</sub>O], resulting in values of ~250 M<sup>-1</sup>•s<sup>-1</sup> and ~200 M<sup>-1</sup>•s<sup>-1</sup> for **1A** and **2A**, respectively. These rate constants are similar to the mono iron complex. The addition of base increased the rate of H<sub>2</sub>O<sub>2</sub> activation for both **2A** and the Fe<sup>II</sup>TMC system by about 3-5

times.<sup>89</sup> For both the mono- and diiron complexes that are able to activate H<sub>2</sub>O<sub>2</sub> to a high-valent species, no peroxo intermediates were observed. Even though the breaking of the O-O bond is the last step in both cases; the binding of the H<sub>2</sub>O<sub>2</sub> to the iron center appears to be rate controlling at the H<sub>2</sub>O<sub>2</sub> concentrations used.

#### *Polarization the O-O Bond:*

Previously, diferric and diferrous compounds were observed to form peroxo complexes with H<sub>2</sub>O<sub>2</sub> or O<sub>2</sub>, which modeled the sMMO-P species.<sup>44,72,91</sup> However, no Fe<sup>IV</sup>Fe<sup>IV</sup> species were observed and only a few one-electron reduced species were isolated. The missing electron in the oxygen activation pathway prompted the authors to propose a transient Fe<sup>IV</sup>Fe<sup>IV</sup> species that reacted immediately with a solvent molecule or a redox partner which supplied the reducing equivalent.<sup>5,44,82</sup> The asymmetric ligand environment supported by ligand **A** may contribute to the inability to isolate a peroxo intermediate in the system studied here (Figure 2.17). The Fe atom on the left has a pyridine N atom *trans* to the peroxo, while the Fe atom on the right has a tertiary amine *trans* to the peroxo.<sup>69</sup> This difference in *trans* ligands may polarize the O-O bond enough to break, resulting in the formation of **3A**. This polarization may be the reason why the proposed peroxo intermediate formulated as **III** in Scheme 2.10 is not seen. Furthermore, the more basic nature of the ligand **A** likely stabilizes the highly charged diiron(IV) centers sufficiently to trap the only well-characterized high-valent diiron(IV) compounds reported to date.

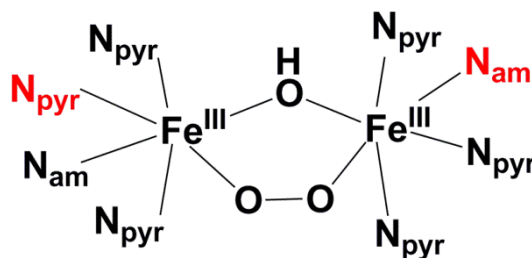


**Figure 2.17:** Proposed structure of diferric-hydroxo-peroxo species (III, scheme 5) with ligands trans to the peroxo highlighted in red.

Reversible O-O bond breaking and forming by a diiron complex was demonstrated by the Kodera group. They showed that a diferric peroxo complex could be isolated in the solid state at low temperatures and be reversibly converted to a diferryl species at higher temperatures (Figure 2.18).<sup>11,12</sup> The diferric crystal structures of the Kodera complexes suggest that there are different *trans* donors to the peroxo ligand like in Figure 2.17; however, the fact that the O-O bond does not break in solution suggests that either the unsubstituted pyridine or carboxylate donors are not basic enough to polarize the O-O bond or that the dinucleating ligand holds the ferryl units in close proximity favoring the peroxo species in solution.<sup>11,12</sup> Importantly, substrate oxidation was observed, strongly suggesting that any of the diferryl complex in equilibrium would react before it was able to accumulate.<sup>11,12</sup>

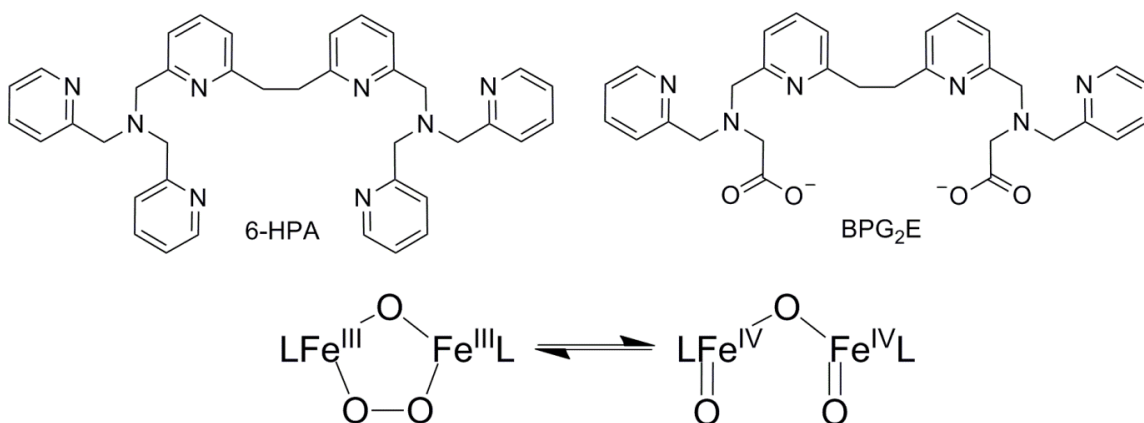


**Figure 2.18:** Top: di-nucleating ligands used by the Kodera group to support a diferryl model complex; Bottom: reversible O-O bond formation and formation of a diferryl species.<sup>10–12</sup>

## 2.4 Conclusion:

In conclusion, the rate of H<sub>2</sub>O<sub>2</sub> activation by **1A** and **2A** was found to be controlled by the binding of H<sub>2</sub>O<sub>2</sub>, and H<sub>2</sub>O<sub>2</sub> competes with H<sub>2</sub>O for binding to the ferric centers. The presence of base increased the H<sub>2</sub>O<sub>2</sub> activation rate for **2A** but not **1A**. After accounting for water inhibition, the H<sub>2</sub>O<sub>2</sub> activation rates by the diferric compounds are similar to that of [Fe<sup>II</sup>TMC]<sup>2+</sup>.<sup>89</sup> No peroxo intermediate supported by ligand **A** was observed likely because of the facile O-O bond cleavage due to the asymmetric Fe environment created by the substituted pyridine-based ligand **A**.



## 2.5 Experimental:

### *Materials and Synthesis:*

Anhydrous MeCN (>99.8%), 3-bromopyridine and 2,4,6-tri-tert-butylphenol were purchased from Aldrich and used as received. D<sub>2</sub>O<sub>2</sub> (30% in D<sub>2</sub>O, 98% D) was purchased from ICON Isotopes. 30% H<sub>2</sub>O<sub>2</sub> in H<sub>2</sub>O and 70% H<sub>2</sub>O<sub>2</sub> in H<sub>2</sub>O were obtained from Macron and Degussa respectively.

**[Fe<sub>2</sub>(R<sub>3</sub>TPA)<sub>2</sub>(μ-O)(μ-OH)](ClO<sub>4</sub>)<sub>3</sub> (1A)** was prepared according to the reported methods.<sup>16</sup>

**[Fe<sub>2</sub>(R<sub>3</sub>TPA)<sub>2</sub>(μ-OH)<sub>2</sub>](ClO<sub>4</sub>)<sub>4</sub>·H<sub>2</sub>O (2A)<sup>y</sup>** was prepared by individually dissolving 0.335 g Fe(ClO<sub>4</sub>)<sub>3</sub>·7.5H<sub>2</sub>O (0.688 mmol; the number of water molecules was calculated based on the iron content stated on the Aldrich Certification of Analysis) and 0.319 g (0.688 mmol) R<sub>3</sub>-TPA in 3 mL MeOH. Upon stirring, the ligand solution was added to iron solution dropwise. The mixture was stirred for 2 hour, and 1.23 mL of 0.500 M NaOH solution in MeOH (0.619 mmol) was added via a syringe utilizing a syringe pump over a period of 1 hour. The mixture was stirred at RT for another 5 hours and 5 mL water was then added drop-wise. Yellow powder formed upon stirring for 24 hours. The product was isolated by filtration and washed with 1:1 MeOH-H<sub>2</sub>O containing 1 mM HClO<sub>4</sub>. If allowed to sit longer than ~1 day, a previously characterized carboxylate bridged compound is formed, which was identified by its electronic absorption spectrum and previously reported unit cell.<sup>16</sup> Yield: 0.51 g, 90% yield. Cal for [Fe<sub>2</sub>(SR<sub>3</sub>-

---

<sup>y</sup> Developed by Genqiang Xue and checked by Gregory Rohde

$(\text{TPA})_2(\mu\text{-O})(\text{H}_2\text{O})_2](\text{ClO}_4)_4 \cdot \text{H}_2\text{O}$  ( $\text{C}_{54}\text{H}_{78}\text{Cl}_4\text{Fe}_2\text{N}_8\text{O}_{26}$ ): C, 42.99; H, 5.21; N, 7.43; Cl, 9.40. Found: C, 43.13; H, 5.05; N, 7.44; Cl, 9.20. For recrystallization, 10 mg complex was dissolved in 0.5 mL MeCN to obtain a clear orange solution, which was placed in an Et<sub>2</sub>O bath. Slight orange block-shaped crystals suitable for X-ray diffraction study, *vide infra*, were formed when about 0.5 mL Et<sub>2</sub>O was diffused into the solution.

*Electronic Absorption Spectroscopy:*

Electronic absorption spectra were recorded on a Hewlett-Packard (Agilent) 8453A diode array spectrometer cooled using a liquid nitrogen cooled cryostat from Unisoku Scientific Instruments (Osaka, Japan). This combination allows kinetic studies to be performed at temperatures below -85 °C and to record a spectrum every 0.1 second. For rapid reactions with a reaction time of 10 seconds, time traces at one wavelength can be obtained with about 100 data points for reliable kinetic fits.

*Resonance Raman Spectroscopy:*

IR Resonance Raman spectra were recorded on an Acton AM-506 spectrophotometer, using a Kaiser Optical holographic supernotch filter with a Princeton Instruments LN/CCD-1100-PB/UVAR detector cooled with liquid nitrogen. Laser excitation was provided by a Spectra Physics BeamLok 2060-RM argon ion laser. The spectra were obtained at 77 K by using a 135°-backscattering geometry, and the Raman frequencies were referenced to indene.

### *Reaction of diiron complexes with H<sub>2</sub>O<sub>2</sub>:*

Complex stock solutions were prepared by dissolving complexes into anhydrous MeCN purchased from Sigma-Aldrich and used without further purification. In some experiments, desired amount of water was added via an auto pipette to prepare solutions with certain concentration of water. The complex stock solutions were used within an hour, after which time signature bands in the UV-visible spectrum of the diferric  $\mu$ -acetato complex<sup>16</sup> were observed. H<sub>2</sub>O<sub>2</sub> solutions were prepared by dissolving 70% stock solution in anhydrous MeCN. This solution contains a 1:1 molar ratio of H<sub>2</sub>O<sub>2</sub>:H<sub>2</sub>O. For a typical kinetic experiment, 2.0 mL of 0.5 mM diiron complex stock solution in MeCN was transferred into a UV-vis cuvette, which was then placed into a Unisoku cryostat. The solution was allowed to cool to the temperature of choice. The desired amount of hydrogen peroxide and/or tri-*tert*-butylphenol stock solutions in MeCN or DCM were added through a gas-tight syringe. The formation of **4A** and **5A** were monitored by their characteristic absorption features at 620 nm or 875 nm respectively. The time traces were subjected to fittings with a pseudo-first-order kinetic model.

### *X-ray Absorption Spectroscopy:*

Iron K-edge X-ray absorption spectra were collected in fluorescence mode using a 30-element Ge detector on beamline X3B at the National Synchrotron Lightsource of Brookhaven National Laboratory (NSLS). The synchrotron ring was operated at 2.8 GeV and 100-300 mA beam current and a Si(111) double crystal monochromator was used. The monochromator was calibrated to 7112.0

eV at the Fe K-edge using Fe foil on  $I_3$ . Samples were collected at 15-20 K over an energy range of 6.9-8.0 keV. Data were collected on frozen 5 mM acetonitrile solution samples of **2A** or 20:1 boronitrile to crystalline **2A** by mass. The edge energies were routinely monitored during data collection for red-shifts indicative of sample photoreduction, but none were observed in the present study. Data reduction, averaging, and normalization were performed using the program EXAFSPAK.<sup>93</sup> A three-segment spline with fourth order components was then fit to the EXAFS region of the spectrum in order to extract  $\chi(k)$ . Theoretical phase and amplitude parameters for a given absorber-scatterer pair were calculated using FEFF 6.011 and were utilized by the “opt” program of the EXAFSPAK package during curve-fitting. FEFF parameters for the solid and solution samples of **2A** were calculated using similar coordinates of the crystal reported above. In all analyses, the coordination number of a given shell was a fixed parameter, and was varied iteratively while bond lengths ( $r$ ) and mean square deviation ( $\sigma^2$ ) were allowed to freely float. The amplitude reduction factor  $S_0$  was fixed at 0.9, while the edge shift parameter  $E_0$  was allowed to float as a single value for all shells (thus in any given fit, the number of floating parameters was typically equal to  $(2 \times \text{num shells}) + 1$ ).

*Chapter 3: Structural Investigation of the Diamond Core Motif in Nonheme Iron Chemistry.*

### 3.1 Introduction:

The structure of the high-valent diiron(IV) reactive intermediate of soluble methane monooxygenase (sMMO-Q) was first proposed as a diamond core when a short Fe-Fe scatterer at 2.46 Å was identified in the EXAFS data.<sup>2,25,51</sup> Additionally, one long and one short Fe-O bond were observed, which resulted in the diamond core being formulated as head-to-tail dimer of Fe<sup>IV</sup>-O units.<sup>51</sup> Two structural models for sMMO-Q emerged from computational studies in contrast to the original structure: the first was a structure proposed by Siegbahn with two bridging carboxylates to accommodate the short Fe-Fe distance observed experimentally,<sup>94,95</sup> and a second model from Friesner and Lippard was derived from the diferrous crystal structure of sMMO which has one bridging carboxylate and a terminal aqua ligand on one of the Fe atoms.<sup>96,97</sup> In both models, a longer Fe-Fe distance of about 2.7 Å is predicted; however it should be noted that a diamond core is still the accepted motif of sMMO-Q.<sup>95-97</sup> Indeed, vibrations consistent with the diamond core motif were observed in the resonance Raman spectrum for sMMO-Q, which provided compelling data to corroborate the original diamond core assignment.<sup>52</sup>

The structure of a related high-valent diiron core intermediate from ribonucleotide reductase, RNR-X, has also been investigated. The spectroscopy of RNR-X is richer than sMMO-Q because of its Kramer's system derived from its Fe<sup>IV</sup>Fe<sup>III</sup> core allowing for additional methods like EPR and MCD to help calibrate the calculated structures. A short 2.5 Å Fe-Fe scatterer distance in the EXAFS data of RNR-X lead the authors to assign a diamond core motif to the feature.<sup>60</sup>

As with sMMO-Q, a longer Fe-Fe distance was calculated causing this result to be called into question.<sup>56,95-97</sup> Indeed, a recent study of RNR-X found a much longer Fe-Fe distance of 2.8 Å in agreement with the computed models.<sup>56</sup> This study also raised concerns about the short Fe-Fe distance originally found for sMMO-Q.

About ten years after the synthesis of the Fe<sup>IV</sup>Fe<sup>III</sup> diamond core, a Fe<sup>IV</sup><sub>2</sub>(μ-O)<sub>2</sub> model complex (**4A**) was obtained (Figure 3.1).<sup>8</sup> Importantly, the Mössbauer spectrum displayed an isomer shift of -0.04 mm/s and was consistent with two antiferromagnetically coupled Fe<sup>IV</sup> centers; however, the Fe-Fe distance was observed to have a 2.73 Å Fe-Fe distance with EXAFS.<sup>8</sup> The Fe-Fe distance in **4A** is longer than found for sMMO-Q and the one-electron-reduced Fe<sup>IV</sup>Fe<sup>III</sup> model compounds supported by the 5-Et<sub>3</sub>TPA (**5B**) and 5-Me<sub>3</sub>TPA (**5C**) ligands (Figure 3.1).<sup>4,8,51</sup> This is a curious result because the Fe-O distances of the diamond core should not lengthen with an increased oxidation state and some other core perturbation must happen if the structure of **4A** determined by EXAFS is accurate.

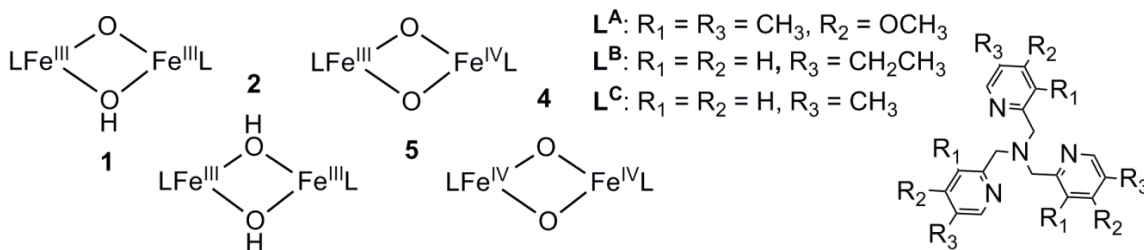


**Figure 3.1:** Summary of diiron cores in Chapter 3.

More accurate structural information would improve current models and provide evidence to help differentiate between the original head-to-tail dimer

model of sMMO-Q<sup>51</sup> and the computational core.<sup>51,95</sup> Additionally, the first Fe<sup>IV</sup>Fe<sup>III</sup> high-valent diamond core Fe-Fe distances determined by EXAFS were underestimated by 0.07 Å compared to the crystal structure; this was even after the EXAFS fit was calibrated by the crystal structure.<sup>4,40</sup> The goal of this study is to isolate and structurally characterized iron(III) and iron(IV) model compounds supported by ligand **A** and compare them to other known high-valent model complexes and enzyme intermediates (Figure 3.1). Both X-ray diffraction and EXAFS techniques were used to study the diamond core motifs when appropriate. The one-pot synthesis of **4A** described earlier provides a facile way to obtain X-ray diffraction quality crystals, and the crystal structure of **4A** may provide specific bond information to update the structure assigned by EXAFS as well as provide a larger reference set of bond lengths for high-valent diiron compounds.

### **3.2 Results and Discussion:**

#### *Isolation of a crystal of 4A:*

The one-step synthesis of **4A** discussed in Chapter 2 facilitated the crystallization of the Fe<sub>2</sub>O<sub>2</sub> diamond core. The lifetime of **4A** (*t*<sub>1/2</sub> ~10 hours at -40° C) did not prove long enough to isolate crystals at -40° C. Instead, crystals **1A** were identified by its previously published unit cell, presumably formed by solvent oxidation over the course of a week.<sup>16</sup> Crystallization of **4A** was achieved by first reacting 21 mg of **2A** with one equivalent each of H<sub>2</sub>O<sub>2</sub> and 3-bromopyridine in a 2 mL butyronitrile solution at -40° C for 20 minutes producing a dark red solution. The solution was then cooled to -80° C, and 1 mL of diethyl



ether was layered on the red solution. The dark red solution of **4A** was stable for weeks at  $-80^{\circ}\text{C}$  and yielded dark red crystals in the shape of blocks, which were stable for months in the mother liquor at  $-80^{\circ}\text{C}$ . At temperatures above  $-80^{\circ}\text{C}$  and in the presence of the mother liquor, the dark red blocks lost crystallinity and quickly decayed to a green species, the color of which closely resembled that of the  $1\text{-e}^{-}$  reduced species, **5A**. In the absence of the mother liquor, the dark red crystals quickly lost their luster and decayed to the green species at a slower rate. To obtain a structure of **4A**, a slide containing the dark red crystals was precooled with  $\text{N}_{2(l)}$  and a suitable crystal was quickly mounted on an X-ray diffractometer cooled to  $-150^{\circ}\text{C}$ . The amount of time the crystal was not in the mother liquor or above  $-150^{\circ}\text{C}$  was kept to a minimum. The crystal diffracted to a resolution of  $1.1\text{ \AA}$  and was solved using direct methods.

Along with one-half of two molecules of interest (both located on inversion centers), 4 perchlorate counter ions and 5.5 butyronitrile molecules were found in the asymmetric unit. The loss of long-range order above  $-80^{\circ}\text{C}$  was likely due to solvent loss rather than decay of **4A**. The solvent molecules, along with the counter ions, create pockets that shield the tetra-cationic iron complexes from neighboring cations and give rise to a crystalline solid. After the data collection, the single crystal was transferred from the diffractometer to a microscope where it was observed to decay to the green solid, most likely the one-electron reduced **5A**. A separate batch of crystals was washed with diethyl ether at  $-80^{\circ}\text{C}$  and then dissolved in acetonitrile at  $-40^{\circ}\text{C}$ , resulting in a solution that exhibited the characteristic electronic absorption and ESI-MS spectra of **4A**. The bond

distances are in good agreement with previously published EXAFS data;<sup>8</sup> however the higher resolution of the crystal structure allows for the differentiation between bonds that are ambiguous in the EXAFS experiment. The observation of the diamond core unequivocally established the structure of the previously characterized **4A** (Figure 3.2). Relevant bond distances comparing diiron complexes in different protonation and oxidation states are listed in Table 3.1, and are discussed below.

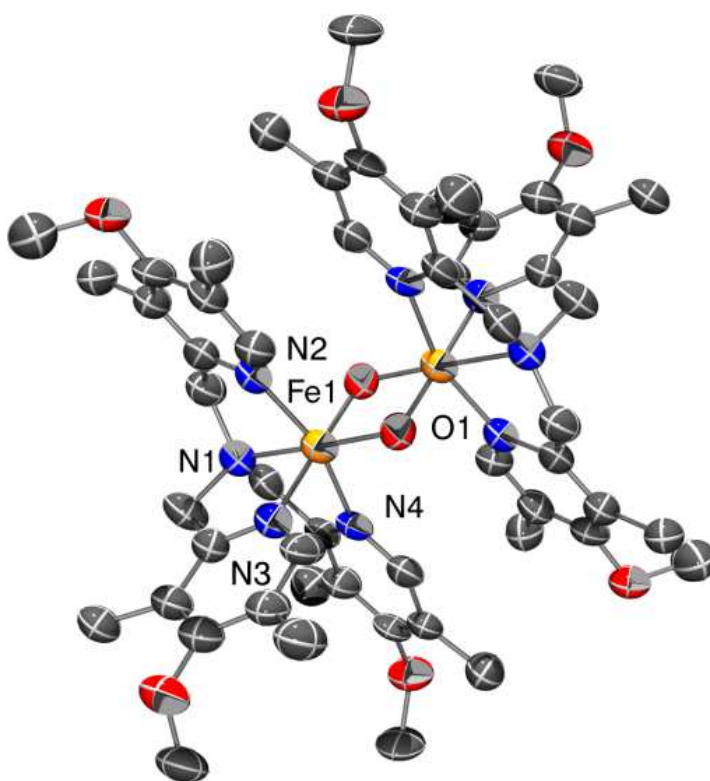


**Figure 3.2:** Structure of **4A** ( $[\text{Fe}^{\text{IV}}_2\text{-}\mu\text{-O}_2]^{4+}$ ), thermal ellipsoids drawn to the 50% probability level, with hydrogen atoms removed for clarity. An inversion center is present at the center of the  $\text{Fe}_2\text{O}_2$  core resulting in the one half of the molecule unique. Selected bond distances (Å) and angles ( $^\circ$ ): Fe1-O1, 1.787(6); Fe1-O1A, 1.810(9); Fe1-Fe1A, 2.711(4); Fe-N<sub>ave</sub>, 1.974; Fe1-O1-Fe1A, 97.8(4).

**Table 3.1:** Select bond distances and angles for diamond core structures obtained from XRD and XAS.

	<b>1A</b>	<b>1A</b>	<b>2A<sup>a</sup></b>	<b>5B<sup>c</sup></b>	<b>5B<sup>c</sup></b>	<b>5A</b>	<b>5A</b>	<b>4A<sup>a</sup></b>	<b>4A</b>
	<b>XRD<sup>b</sup></b>	<b>XAS</b>	<b>XRD</b>	<b>XRD</b>	<b>XAS</b>	<b>XRD</b>	<b>XAS</b>	<b>XRD</b>	<b>XAS<sup>g</sup></b>
Fe1-O1	1.883(3) <sup>d</sup>	1.80	1.926(2)	1.805(3)	1.83	1.780(4)	1.75	1.787(6)	1.78
Fe1-O1A	1.934(2) <sup>d</sup>	1.97	1.995(2)	1.860(3)	n/r	1.827(5)	n/r	1.810(9)	n/r
Fe1-N1	2.183(3)	n/r	2.150(3)	2.049(3)	n/r	2.012(6)	n/r	1.993(8)	n/r
Fe1-N2	2.147(3)	n/r	2.116(3)	2.025(3)	n/r	1.996(5)	n/r	1.970(9)	n/r
Fe1-N3	2.151(3)	n/r	2.088(3)	2.003(3)	n/r	1.988(6)	n/r	1.958(9)	n/r
Fe1-N4	2.134(3)	n/r	2.105(3)	2.025(3)	n/r	1.983(6)	n/r	1.973(8)	n/r
Fe1-Fe1A	2.7920(9)	2.80	3.0224(10)	2.683(1)	2.61	2.596(2)	2.57	2.711(4)	2.73
Fe-N <sub>py</sub> ave	2.144(9) <sup>e</sup>	n/a	2.103(14) <sup>e</sup>	2.018(13) <sup>e</sup>	n/a	1.991(5) <sup>e</sup>	n/r	1.967(8) <sup>e</sup>	n/r
Fe-N <sub>ave</sub>	2.154(21) <sup>e</sup>	2.14	2.115 (26) <sup>e</sup>	2.026 (19) <sup>e</sup>	2.00	1.995(13) <sup>e</sup>	1.95	1.974(15) <sup>e</sup>	1.97
Fe1-O1-Fe1A	94.01(11)	96 <sup>f</sup> <sub>ave</sub>	100.86(11)	94.1		92.1(2)		97.8(4)	
O1-Fe1-O1A	85.99(11)	84 <sup>f</sup>	79.14(11)	85.9		87.9(2)		82.2(4)	
Fe1-O <sub>oxo</sub> -Fe1A		102 <sup>f</sup>							
Fe1-O <sub>hyd</sub> -Fe1A		90 <sup>f</sup>							

The numbering scheme for all compounds is depicted in Figure 3.2. <sup>a</sup> Average of two molecules in the asymmetric unit, <sup>b</sup> from ref <sup>16</sup>, <sup>c</sup> from ref 4 using 5-Et<sub>3</sub>TPA Ligand, <sup>d</sup> oxo and hydroxo ligands were not resolved in XRD due to disorder over an inversion center, n/r = not resolved due to the resolution of the XAS measurement, <sup>e</sup> standard deviation reported from average of Fe-N distances specified from the crystal structures, <sup>f</sup> calculated from bond distance derived from EXAFS using a model with a 2-fold axis bisecting the  $\mu$ -oxo and  $\mu$ -hydroxo oxygen atoms. <sup>g</sup> from reference 8.

*Revisiting the diamond core of 1A:*

The crystal structure of **1A** was recently reported.<sup>16</sup> However, due to an inversion center being present in the diamond core of **1A**, the Fe- $\mu$ -O and Fe- $\mu$ -OH bonds were disordered over two positions. Traditional X-ray diffraction methods are unable to separate the two bond distances due to the crystallographic symmetry averaging. To differentiate the Fe- $\mu$ -O and Fe- $\mu$ -OH bond distances, EXAFS was used. The EXAFS measurement is only dependent on the local chemical environment and not the crystallographic symmetry. Similar bond distances may be differentiated if their difference is greater than the resolution of the measurement. A crystalline sample of **1A**<sup>vi</sup> was used to prepare the EXAFS sample.<sup>16</sup> The EXAFS data was collected at 20 K and is displayed with the best fits in Figure 3.3 and Table 3.2. Excellent agreement between the XAS and XRD data was observed with average Fe-N distances of 2.15(2) Å and 2.14 Å for XRD and EXAFS, respectively, and the Fe-Fe distance was also in excellent agreement (2.7920(9) Å XRD and 2.80 Å EXAFS). Importantly, the resolution of the EXAFS measurement, 0.12 Å, allowed for the differentiation of the two Fe- $\mu$ -O(H) distances, with an Fe- $\mu$ -O distance at 1.80 Å and an Fe- $\mu$ -OH distance at 1.97 Å. The Fe- $\mu$ -O distance of 1.80 Å of **1A** approaches the Fe-O bond distance of 1.78 Å from the linear Fe-O-Fe diferric complexes supported by similar tetradentate N-donor ligands and the Fe- $\mu$ -O(H) bond distances also compares well with similar bond distances (see below).<sup>26,98</sup> Alternative fits of the

---

<sup>vi</sup> The unit cell of the crystalline **1A** used to prepare the EXAFS sample matched the published parameters.<sup>16</sup>

EXAFS data including both Fe-O scatterers in the same shell resulted in lower quality fits to the experimental data (Table 3.2). The asymmetric core of **1A** was able to be accurately modeled by the EXAFS experiment.

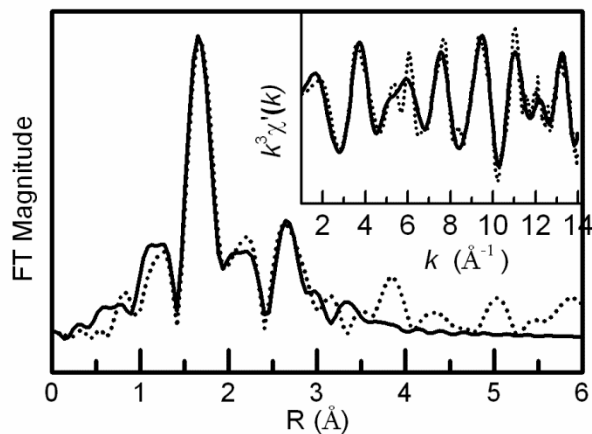


**Figure 3.3:** Fourier-transformed Fe K-edge EXAFS data obtained at 20 K of a 1:13 **1A**:BN solid state sample. (*Inset*)  $k^3\chi'(k)$  data. Fourier transform range 1-14  $\text{\AA}^{-1}$ ; experimental data (dotted line) and best fit solid line; scatterers consisting of 1 O at 1.80  $\text{\AA}$ , 1 O at 1.97  $\text{\AA}$ , 4 N at 2.14  $\text{\AA}$ , 1 Fe at 2.80  $\text{\AA}$  and an additional Fe-C shell at 3.01  $\text{\AA}$ .

**Table 3.2:** EXAFS fitting to unfiltered EXAFS data of a 1:13 **1A**: BN crystalline sample using Feff phase and amplitude parameters listed in (Å).

Fit	Fe-N			Fe-O			Fe-C			Fe-Fe					
#	N	R	$\sigma^2$	N	R	$\sigma^2$	N	R	$\sigma^2$	N	R	$\sigma^2$	$E_0$	F	F'
Default phase and amplitude parameters															
Feff	2.147			1.814 Oxo			2.086			2.772					
				1.994 OH											
1*	4	2.139	3.3	1	1.802	1.5	6	3.006	1.3	1	2.804	3.8	-5.63	124	386
				1 1.973 4.7											
2	4	2.123	3.2	2	1.829	9.3	6	2.996	1.6	1	2.793	3.5	-6.48	151	423

$k$  range = 1-14 Å<sup>-1</sup>, resolution = 0.12 Å,  $\sigma^2$  = mean-squared deviation in units of 10<sup>-3</sup> Å

<sup>2</sup>. Scale Factor  $S_0^2 = 0.9$ . Goodness-of-fit = F calculated as  $F = \sqrt{\sum k^6 (\chi_{\text{exp}} - \chi_{\text{calc}})^2}$ .

$$F' = \sqrt{\sum k^6 (\chi_{\text{exp}} - \chi_{\text{calc}})^2 / \sum k^6 \chi_{\text{exp}}^2} . * = \text{Best Fit}$$

### *Crystal Structure of 2A:*

Suitable crystals of **2A** for X-ray diffraction were grown from the slow diffusion of diethyl ether into an acetonitrile solution of microcrystalline **2A** and resulted in an orange crystal. The diamond core structure of **2A** (Figure 3.4, Table 3.1) is similar to those of ( $\mu$ -hydroxo)-( $\mu$ -oxo)diiron(III) (**1A**) complexes supported by similar ligands.<sup>16,26</sup> The Fe- $\mu$ -O(H) bond distances in each molecule are not symmetric, with Fe- $\mu$ -O(H) bond distances of 1.995(2) Å and 1.926(2) Å (Table 3.1), the first falling within the range of previously published bridging Fe- $\mu$ -O(H) bonds and very close to the Fe- $\mu$ -O(H) bond distance determined by EXAFS of **1A**. The second Fe- $\mu$ -O(H) bond distance is on the shorter end of the range, but significantly longer than the Fe- $\mu$ -O bond of **1A** determined by EXAFS.<sup>16,26</sup> The average Fe-N<sub>amine</sub> and Fe-N<sub>pyr</sub> bond lengths of **2A** are shorter by about 0.03 Å and 0.05 Å, respectively, compared to **1A**. The shorter Fe-N bonds of **2A** are due to the lower basicity of the hydroxo ligands of **2A** compared to the oxo and hydroxo ligands for **1A** (Table 3.1), making the iron centers more Lewis acidic than those of **1A**.<sup>16,26</sup> Interestingly, the longest Fe-Fe distance of the series was observed for compound **2A** at 3.0224(10) Å.

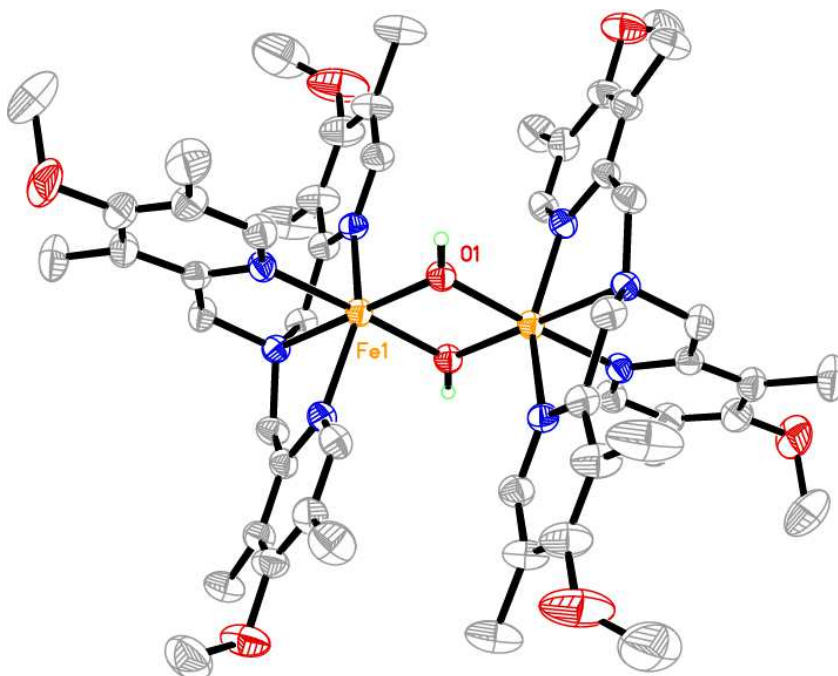


**Figure 3.4:** Thermal ellipsoid plot of **2A** showing 50% probability ellipsoids. Non-oxygen bound hydrogen atoms, counterions and solvent molecules were removed for clarity. Colors of atoms: carbon- gray, oxygen- red, nitrogen- blue, iron- orange, hydrogen- green sphere. Selected bond distances (Å) and angles (°): Fe1-O1, 1.926(2) ; Fe1-O1A, 1.995(2); Fe1-Fe1A, 23.0224(10); Fe-N<sub>ave</sub>, 2.115; Fe1-O1-Fe1A, 100.86(11).

#### *Crystal Structure of 5A:*

An X-ray diffraction quality crystal of **5A** was obtained by first generating **5A** in a butyronitrile solution by reacting **1A** with 2 equivalents H<sub>2</sub>O<sub>2</sub> and then layering the solution with diethyl ether at -80° C.<sup>8</sup> The green crystals of **5A** also were susceptible to solvent loss, although to a lesser degree than **4A**, with only 1 butyronitrile molecule in the asymmetric unit as compared to 5.5 for the red crystals of **4A**. A cold mount as described above was used to maintain the



crystallinity while the crystal of **5A** was being mounted on the diffractometer. Not surprisingly, Fe-O and Fe-N bond distances of the mixed-valent **5A** (Figure 3.5, Table 3.1) were found to be shorter by over 0.1 Å than the corresponding diferric species due to the 0.5 increase in the oxidation state and change of the spin state of the Fe atoms. Interestingly, the Fe-( $\mu$ -O)<sub>2</sub>-Fe diamond core of **5A** was also found on an inversion center, with two distinct Fe- $\mu$ -O bonds, supporting the valence delocalized Fe<sup>3.5+</sup> oxidation state, and consistent with the previously reported **5B**.<sup>4,8,40-42</sup> The Fe-O lengths are 0.025 and 0.033 Å shorter and the average Fe-N bonds are shorter by over 0.030 Å for **5A** than corresponding values for **5B**. The contraction of the Fe-N bonds is rationalized by the more Lewis basic ligand **A**. The shorter Fe-( $\mu$ -O) bonds of **5A** may be a result of the O-Fe-O angle being closer to the ideal 90°. Most notably, the Fe-Fe distances for **5A** and **5B** are 2.596(2) Å and 2.683(1) Å, respectively. The shorter Fe-Fe distance is mainly due to the contraction of the Fe-O bonds and the more acute Fe-O-Fe angle, which decreased from 94.1° to 92.1(2)° from **5B** to **5A**, respectively.<sup>4</sup>

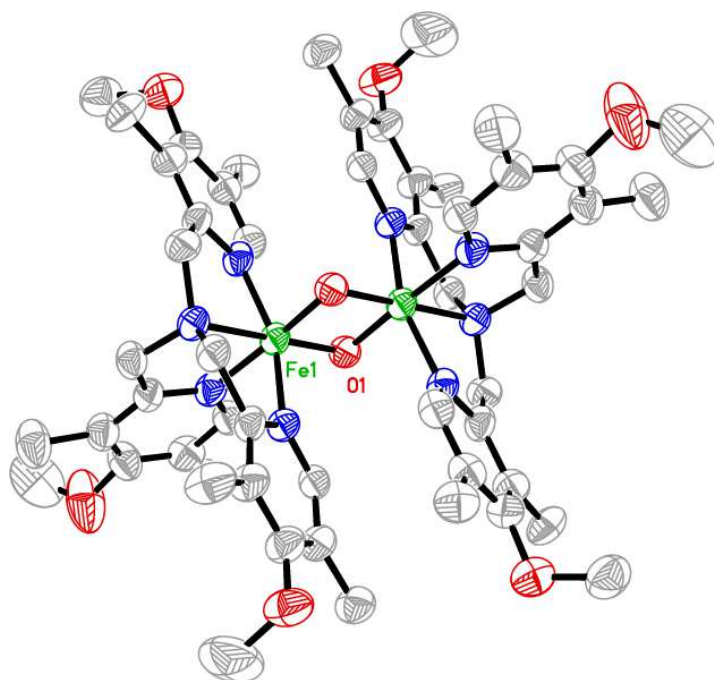


**Figure 3.5:** Structure of **5A** with hydrogen atoms, counterions and solvent molecules removed for clarity. Ellipsoids are displayed at 50% probability level. Atom colors: carbon- gray, oxygen- red, nitrogen- blue, iron-green. Selected bond distances (Å) and angles (°): Fe1-O1, 1.780(4) ; Fe1-O1A, 1.827(5); Fe1-Fe1A, 2.596(2); Fe-N<sub>ave</sub>, 1.995; Fe1-O1-Fe1A, 92.1(2).

*EXAFS analysis of 5A in Frozen Solution:*

The 8 mM frozen solution sample of **5A** was analyzed by EXAFS and had similar structural parameters as the crystal structure. The fitting table and EXAFS data are displayed in Figure 3.6 and Table 3.3. Five scattering shells were fit to a  $k$  range of 2-14 Å<sup>-1</sup> including two Fe-O scatterers at 1.75 Å , four Fe-N scatterers at 1.96 Å, an Fe-Fe scatterer at 2.57 Å and two sets of Fe-C scatterers at 2.77 and 2.92 Å (Figure 3.6, Table 3.3: Fit 13). The first coordination sphere Fe-O and Fe-N scatterers and the outer shell Fe-Fe

scatterer at 2.57 Å are in reasonable agreement with the crystallographically determined distances (Table 3.1 and Table 3.3: Fit 13). The intense scatterer at around 2.3 Å in the Fourier transform has a major contribution from the Fe-Fe scatterer (2.57 Å), and is consistent with the presence of a diamond core motif.

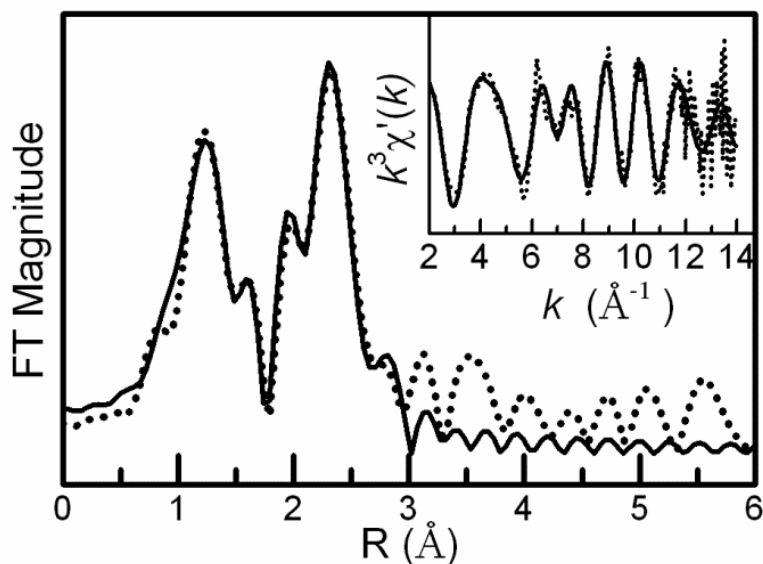


**Figure 3.6:** Fourier-transformed Fe K-edge EXAFS data obtained at 20 K of an 8 mM solution sample of **5A** in acetonitrile. (*Inset*)  $k^3\chi'(k)$  data. Fourier transform range 2-14 Å<sup>-1</sup>; experimental data (dotted line) and best fit (solid line), consisting of 1 O at 1.75 Å, 3 N at 1.95 Å, 1 Fe at 2.57 Å and two additional Fe-C shells at 2.77 and 2.93 Å modeled with 4 and 6 scatterers, respectively.

**Table 3.3:** EXAFS fitting to unfiltered EXAFS data of **5A** using Feff phase and amplitude parameters listed in (Å).

Fit	Fe-N			Fe-O			Fe-C			Fe-Fe					
#	N	R	$\sigma^2$	N	R	$\sigma^2$	N	R	$\sigma^2$	N	R	$\sigma^2$	$E_0$	F	F'
Default phase and amplitude parameters from EXAFSPAK															
	3	1.971	5.9	2	1.771	6.3	3	2.801	1.4	1	2.590	2.8	-5.90	148	450
							4	2.961	0.5						
Feff	1.98			1.77			2.96,			2.59					
1	3	1.968	6.0	2	1.765	6.1							-13.0	468	802
2	4	1.962	8.6	2	1.754	6.4							-13.0	474	807
3	4	1.946	9.7	1	1.747	3.0							-11.3	467	801
4	3	1.968	6.1	2	1.766	6.1							-13.0	468	802
5	3	1.975	6.1	2	1.773	6.6	6	2.875	8.1	1	2.569	4.1	-10.4	193	515
6	3	1.967	6.3	2	1.766	6.8	6	2.932	2.7	1	2.562	3.6	-10.9	159	468
							6	2.768	4.7						
7	4	1.956	8.8	2	1.749	7.2	6	2.928	2.3	1	2.560	2.4	-11.6	172	487
							6	2.765	4.0						
8	4	1.937	9.5	1	1.738	3.2	6	2.936	2.4	1	2.565	2.4	-10.5	160	469
							6	2.771	4.2						
9	3	1.946	6.8	1	1.751	2.8	6	2.938	2.6	1	2.566	2.5	-9.9	153	458
							6	2.772	4.5						
10	3	1.948	6.7	1	1.752	2.8	6	2.929	2.2	1	2.573	2.4	-9.6	148	451
							4	2.770	1.2						
11	3	1.969	6.4	2	1.767	7.0	6	2.922	2.0	1	2.568	2.4	-10.7	156	463
							4	2.764	1.2						
12	4	1.940	9.5	1	1.740	3.2	6	2.935	2.0	1	2.570	2.4	-10.2	154	461
							4	2.767	1.1						
13*	4	1.961	8.9	2	1.753	7.3	6	2.922	1.7	1	2.569	2.4	-11.1	167	479
							4	2.767	0.8						

$k$  range = 2-14 Å<sup>-1</sup>, resolution = 0.132 Å,  $\sigma^2$  = mean-squared deviation in units of 10<sup>-3</sup> Å<sup>2</sup>. Scale

Factor  $S_0^2$  = 0.9. Goodness-of-fit = F calculated as  $F = \sqrt{\sum k^6 (\chi_{\text{exp}} - \chi_{\text{calc}})^2}$ .

$F' = \sqrt{\sum k^6 (\chi_{\text{exp}} - \chi_{\text{calc}})^2 / \sum k^6 \chi_{\text{exp}}^2}$ . \* = Best Fit

### *Crystal Structure of 4A:*

The structure of **4A** (Figure 3.2, Table 3.1) also displays a contraction of the first coordination sphere of the Fe atoms in general compared to the lower oxidation state complexes supported by tetradentate N-rich ligands. Modest contractions are seen between **5A** and **4A**. The Fe-N<sub>amine</sub> distances contracted from 2.012(6) in **5A** to 1.995(8) in **4A** and the average Fe-N<sub>ave</sub> contracted from 1.995(6) in **5A** to 1.969(8) in **4A**. The short Fe-O distance barely increased from 1.780(4) in **5A** to 1.787(6) in **4A** (this difference is close to the s.u. of the measurement) and a decrease of the longer Fe-O bond from 1.827(5) in **5A** to 1.815(9) in **4A** was observed. The Fe-Fe distance increased substantially from 2.596(2) in **5A** to 2.715(4) in **4A**. This contraction of the first coordination sphere and expansion of the Fe-Fe distance resulted in a more distorted diamond core of **4A**, with the Fe-O-Fe angle deviating farther from the ideal 90° to 97.8° in **4A** as compared to 92.1° for **5A**. The initial structural characterization of **4A** with EXAFS is in excellent agreement with an Fe-O distance 1.77 Å and an Fe-Fe distance of 2.73 Å. The longer Fe-Fe distance compared to the one-electron reduced **5A** and **5B** was difficult to rationalize, but may now be properly interpreted by the unequal Fe-O bond distances in the diamond core and the larger Fe-O-Fe angle. The longer Fe-Fe distance for **4A** compared to **5A** may be explained by a greater repulsive force between two tetracationic point charges, compared to the smaller force from the 3.5+ charges on the Fe atoms in **5A**.

### *Comparison of High-Valent Model Complexes:*

The diamond core structure has flexibility, adjusting bond lengths and angles to accommodate the different charge and protonation states. The Fe-O distance of 1.80 Å for **1A** is indistinguishable within the error of EXAFS (0.02 Å) from the shortest Fe-O distances of both **4A** and **5A**. Thus the shortest Fe-O bond distance remains relatively constant for the three diamond core structures in different iron oxidation states, illustrating the consistency of the Fe- $\mu$ -oxo bond in a diamond core arrangement. The Fe-O(H) and Fe-N bond distances range from 1.81 – 2.00 Å for the Fe-O(H) bond lengths and 1.97 - 2.15 Å for the Fe-N<sub>ave</sub> bond lengths to adjust to the changes in core charges. In addition, the angles of the [Fe<sub>2</sub>( $\mu$ -O)<sub>2</sub>] diamond core also adjust to the varying charge on the Fe atoms and protonation states of the bridging oxygen atoms. Interestingly, the Fe-Fe distances vary widely from 2.60 – 3.02 Å, with **2A** having the longest distance and **5A** the shortest. The contraction of the Fe-Fe distances parallels the decrease in the bond distances of first coordination sphere except in complex **4A**. The tetracationic complexes **4A** and **2A** have the largest Fe-O-Fe angles at 99° and 101°, respectively, while the tricationic cores of **1A** and **3A** have angles much closer to 90°. The Lewis basicity of the supporting ligand has a dramatic effect on the Fe-Fe distance as illustrated by a difference of almost 0.09 Å found between the Fe-Fe distances of **5A** and **5B**. As there is about a 1 *pKa* unit difference in the precursor diferric compounds, the shorter Fe-Fe distance of **5A** may result from the more electron density donated by the Lewis basic ligand **A** than ligand **B** to the +3.5 charge on each iron center, which decreases the

repulsion of the two +3.5 point charges and allows for the angles of the  $\text{Fe}_2(\mu\text{-O})_2$  core to be closer to the ideal  $90^\circ$ . Finally, replacing the  $\mu$ -oxo ligand in **1A** with a  $\mu$ -hydroxo ligand in **2A** increases the Fe-Fe distance by over 0.2 Å.

*Comparison to High-Valent Enzyme Intermediates:*

The recent structural study on Class Ia Ribonucleotide Reductase Intermediate X (RNR-X) using EXAFS found a longer Fe-Fe distance of 2.8 Å for the enzyme intermediate,<sup>56</sup> which was 0.3 Å longer than the first Fe-Fe distance found by a study completed over 15 years previously (Table 3.4).<sup>60</sup> The large discrepancy was hard to rationalize especially considering the signal-to-noise ratios of the studies were reported to be comparable.<sup>56</sup> However, the new structural assignment is in better agreement with theoretical predictions<sup>99</sup> and was collected on a sample with a higher yield.<sup>56</sup> Interestingly, the two model complexes that have the same oxidation state as RNR-X, **5A** and **5B**, have Fe-Fe distances that fall between the two distances of RNR-X determined by EXAFS, the Fe-Fe distance of the most recent structural study on RNR-X is the same as the diferric structure **1A** at a distance of 2.79 Å.<sup>4,16,56,60</sup> However beyond demonstrating the flexibility of the diamond core, a strict structural comparison has limited utility because there are two distinct Fe centers in the RNR-X  $\text{Fe}^{\text{IV}}\text{Fe}^{\text{III}}$  core as compared to only one Fe environment in the model complexes.<sup>41,42,55</sup> However, combining one half of the **4A** core, representing the  $\text{Fe}^{\text{IV}}$  site in RNR-X, with one half of the **1A** core, representing the  $\text{Fe}^{\text{III}}$  site in RNR-X, an Fe-Fe distance of  $\sim 2.8$  Å is very reasonable, especially considering that the distance of the short Fe- $\mu$ -oxo bond is relatively constant.

**Table 3.4:** Number of scatterers and scatterer distances (Å) of reactive nonheme diiron enzyme intermediates from XAS.

<b>Fe-Scatterer</b>	<b>RNR-X<sup>a</sup></b>	<b>RNR-X<sup>b</sup></b>	<b>MMO-Q<sup>c</sup></b>
<b>Fe</b>	0.5 @ 2.5	0.65 @ 2.8	0.6 @ 2.5
<b>O</b>	0.5 @ 1.77	0.65 @ 1.75	0.6 @ 1.77
<b>O/N</b>	4 @ 2.04	5 @ 2.02	4 @ 2.05

Scatterer numbers less than one reflect the fact that the sample is not pure. Ref: <sup>a</sup> 60, <sup>b</sup> 56, <sup>c</sup> 51

The crystal structure of **4A** is most consistent with the calculated structures for sMMO-Q; both have an Fe-Fe distance of 2.7 Å. Additionally, the computational models propose two Fe-O bonds (~1.76 – 1.84 Å), which are consistent with the crystal structure of **4A** and are in contrast to the Fe-O bonds of the original head-to-tail dimer (1.77 and 2.05 Å).<sup>51,94–96</sup> Although the spin states are different with individual  $S = 1$  Fe sites in **4A** and  $S = 2$  Fe sites in sMMO-Q, the Fe-O bond lengths in the diamond core are not likely to change substantially. Well characterized  $S = 1$  and  $S = 2$  ferryl model complexes were found to have Fe=O distances between 1.65 – 1.70 Å, that are independent of spin state.<sup>37</sup> The bond lengths of the supporting ligand (protein) likely control the spin state. Moreover, the Fe<sub>2</sub>O<sub>2</sub> core vibrations observed in the resonance Raman spectrum of sMMO-Q closely match those of **4A**.<sup>8,52</sup> Although the properties of the sMMO-Q Fe<sub>2</sub>O<sub>2</sub> core are now better understood, more spectroscopic data, like X-ray spectroscopy, is necessary to further calibrate the computational models to understand how the diamond core is supported in the protein environment.



### 3.3 Experimental:

#### *Synthesis:*

**[Fe<sub>2</sub>(R<sub>3</sub>TPA)<sub>2</sub>(μ-O)(μ-OH)](ClO<sub>4</sub>)<sub>3</sub> (1A)** was prepared according to the reported methods.<sup>16</sup>

**[Fe<sub>2</sub>(R<sub>3</sub>TPA)<sub>2</sub>(μ-OH)<sub>2</sub>](ClO<sub>4</sub>)<sub>4</sub> •H<sub>2</sub>O (2A)** was prepared as previously discussed in Chapter 2.

**[Fe<sub>2</sub>(R<sub>3</sub>TPA)<sub>2</sub>(μ-O)<sub>2</sub>](ClO<sub>4</sub>)<sub>4</sub> •5.5 (PrCN) (4A)** was prepared by reacting 21 mg of **2A** with one equivalent each of H<sub>2</sub>O<sub>2</sub> and 3-bromopyridine in a 2 mL butyronitrile solution at -40° C for 20 minutes producing a dark red solution. The solution was then cooled to -80° C, and 1 mL of diethyl ether was layered on the red solution. The dark red solution of **4A** was stable for weeks at -80° C and yielded dark red crystals in the shape of blocks, which were stable for months in the mother liquor at -80° C. Crystals of **4A** dissolved in an acetonitrile solution exhibited the characteristic electronic absorption spectrum and m/z splitting pattern in the ESI-MS spectrum.<sup>8</sup>

**[Fe<sub>2</sub>(R<sub>3</sub>TPA)<sub>2</sub>(μ-O)<sub>2</sub>](ClO<sub>4</sub>)<sub>3</sub> •1 (PrCN) (5A)** was prepared as previously reported except in a butyronitrile solution and then layering the solution with diethyl ether at -80° C.<sup>4,8</sup>

### *X-Ray Diffraction:*

The crystals were mounted onto glass fibers or MiTeGen mounts and positioned on the diffractometer for a data collection with specific collection details displayed in Tables 3.5 below. A preliminary set of cell constants was calculated from reflections harvested from three sets of 12-20 frames. A randomly oriented region of reciprocal space was surveyed to the extent of one sphere consisting of four major sections of frames and was collected with  $0.50^\circ$  steps in  $\omega$  at four different  $\phi$  settings with a detector position of  $-28^\circ$  in  $2\theta$  for the MoK $\alpha$  radiation collections. A collection strategy was developed using the Queen program in the APEX II software suite to ensure full coverage for the CuK $\alpha$  radiation collections.<sup>100</sup> The intensity data were corrected for absorption and decay.<sup>101</sup> Final cell constants were calculated from the xyz centroids of strong reflections from the actual data collection after integration.<sup>102</sup> The space groups were determined based on systematic absences and intensity statistics with the program XPREP.<sup>103</sup> A direct-methods solution was calculated using SHELXS-97 (unless otherwise stated) which provided most non-hydrogen atoms from the E-map.<sup>20</sup> Full-matrix least squares / difference Fourier cycles were performed which located the remaining non-hydrogen atoms. The atoms were refined as with anisotropic displacement parameters with hydrogen atoms riding with relative isotropic displacement parameters. The structures were refined using SHELXL-97.<sup>20</sup> Specific refinement details are described below located in Table 3.5.

**Table 3.5:** Crystal structure collection and refinement information of diiron compounds

	<b>2A</b>	<b>5A</b>	<b>4A</b>
Empirical formula	C <sub>62</sub> H <sub>88</sub> Cl <sub>4</sub> Fe <sub>2</sub> N <sub>12</sub> O <sub>25</sub>	C <sub>62</sub> H <sub>90</sub> Cl <sub>3</sub> Fe <sub>2</sub> N <sub>10</sub> O <sub>22</sub>	C <sub>152</sub> H <sub>221</sub> Cl <sub>8</sub> Fe <sub>4</sub> N <sub>27</sub> O <sub>48</sub>
Temp. (K)	173(2)	123 (2)	123 (2)
λ (Å)	0.71073	1.54178	1.54178
Space group	P-1	C2/c	P-1
a (Å)	11.6839(13)	27.9262(12)	14.2183(9)
b (Å)	13.3450(15)	11.1080(4)	15.7200(10)
c (Å)	25.013(3)	22.8446(10)	21.5627(13)
α (°)	75.1520(10)	90	86.579(4)
β (°)	84.9130(10)	105.110(3)	71.452(4)
γ (°)	87.7530(10)	90	72.753(4)
Z	2	4	1
θ max (°)	26.37	25.37	47.23
Complete	98.7%	99.3%	99.0%
R(int) <sup>a</sup>	0.0391	0.0564	0.1290
Data	15161	6021	7795
Restraints	98	68	578
Parameters	1090	496	971
R1 <sup>b</sup> [I > 2σ(I)]	0.0557	0.0875	0.0991
wR2 <sup>c</sup>	0.1544	0.2723	0.2926
GooF <sup>d</sup>	1.030	1.023	1.030

$$^a R_{\text{int}} = \frac{\sum |F_o^2 - \langle F_o^2 \rangle|}{\sum |F_o^2|}, \quad ^b R_1 = \frac{\sum ||F_o| - |F_c||}{\sum |F_o|}, \quad ^c wR2 = \left[ \frac{\sum [w(F_o^2 - F_c^2)^2]}{\sum [w(F_o^2)^2]} \right]^{1/2} \text{ where } w = \frac{q}{[\sigma^2(F_o^2) + (a^*P)^2 + b^*P + d + e^*\sin(\theta)]}, \quad ^d \text{GooF} = S = \left[ \frac{\sum [w(F_o^2 - F_c^2)^2]}{(n-p)} \right]^{1/2}$$

*Refinement details for 4A:*

Refinement of complex **4A** was carried out in a routine manner as previously described. The asymmetric unit is displayed in Figure 3.7. Additionally, two distinct halves of the molecule of interest located on an inversion center. Oxygen atoms of the perchlorate counterions and all atoms in the butyronitrile solvent molecules were refined with isotropic displacement parameters. All hydrogen atoms were placed in ideal positions and refined as riding atoms with relative isotropic displacement parameters. All  $\alpha$  and  $\beta$  distances for all atoms in the molecule of interest were restrained to be the same using the SAME.<sup>20</sup> Two of the four perchlorate counterions were disordered and modeled over two positions in a 54:46 and 91:9. All perchlorate counterions were modeled as perfect tetrahedrons using the distance restraint DFIX.<sup>20</sup> All Cl-O distances were restrained to be equal and freely refined to 1.431 Å and all O-O distances were restrained to be equal and freely refined to 1.431 Å times 1.633, the factor to model the ion as a perfect tetrahedron. Additionally, all  $\alpha$  and  $\beta$  distances in the perchlorate counterions were restrained to be the same using the SAME.<sup>20</sup> The 5.5 butyronitrile solvent molecules were clearly visible on the E-map after full-matrix least squares / difference Fourier cycles were performed. All like bonds of the butyronitrile, C-N, C $_{\alpha}$ -C $_{\beta}$ , ect., were set to be equal and allowed to freely refine to a chemically reasonable 1.127, 1.439, 1.494 and 1.516 Å for the bonds in butyronitrile starting from the nitrile bond. Remarkably, the only butyronitrile molecule that was disordered was located on an inversion center and was modeled as over the inversion center in a 50:50 ratio using the

Part -1 statement in SHELXL. The butyronitrile molecules formed a solvent channel throughout the crystal lattice (Figure 3.8), which likely lead to the instability of the crystals even at low temperature. All overlapping atom pairs were constrained to have the same displacement parameters using the EADP command.<sup>20</sup> The data to parameter ratio was closely monitored and was 8.0, which is lower than the 10 recommended by the IUCr community for a centrosymmetric structure (8 for a noncentrosymmetric structure).<sup>104</sup> However, in addition to an acceptable GooF of 1.03 and reasonable R factor of 9.9, the presence of two molecules in the asymmetric unit allows for internal averaging which supports the argument that the reported distances and standard uncertainties are reasonable. Although the resolution is low at 1.01 Å, the structure and standard deviations are representative of the structure.

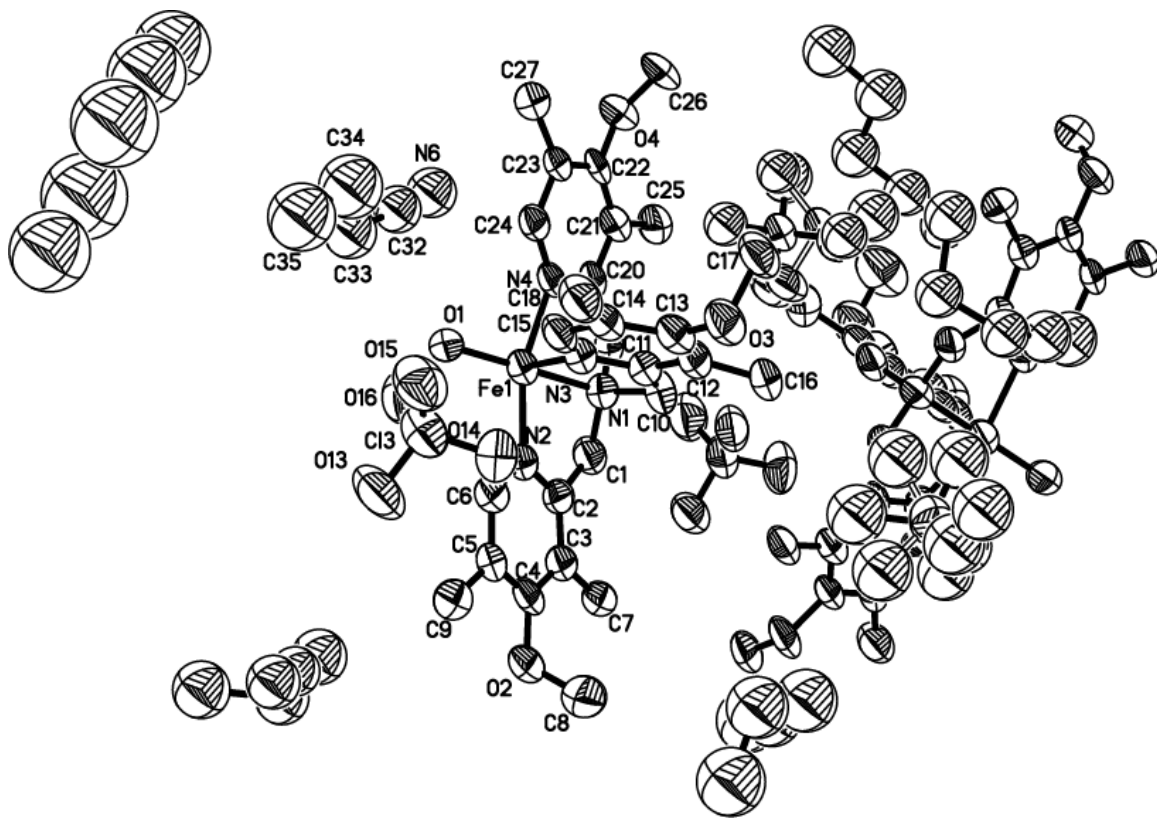


**Figure 3.7:** Asymmetric unit of **4A** with thermal ellipsoids drawn to the 50% probability level with hydrogen atoms removed for clarity.

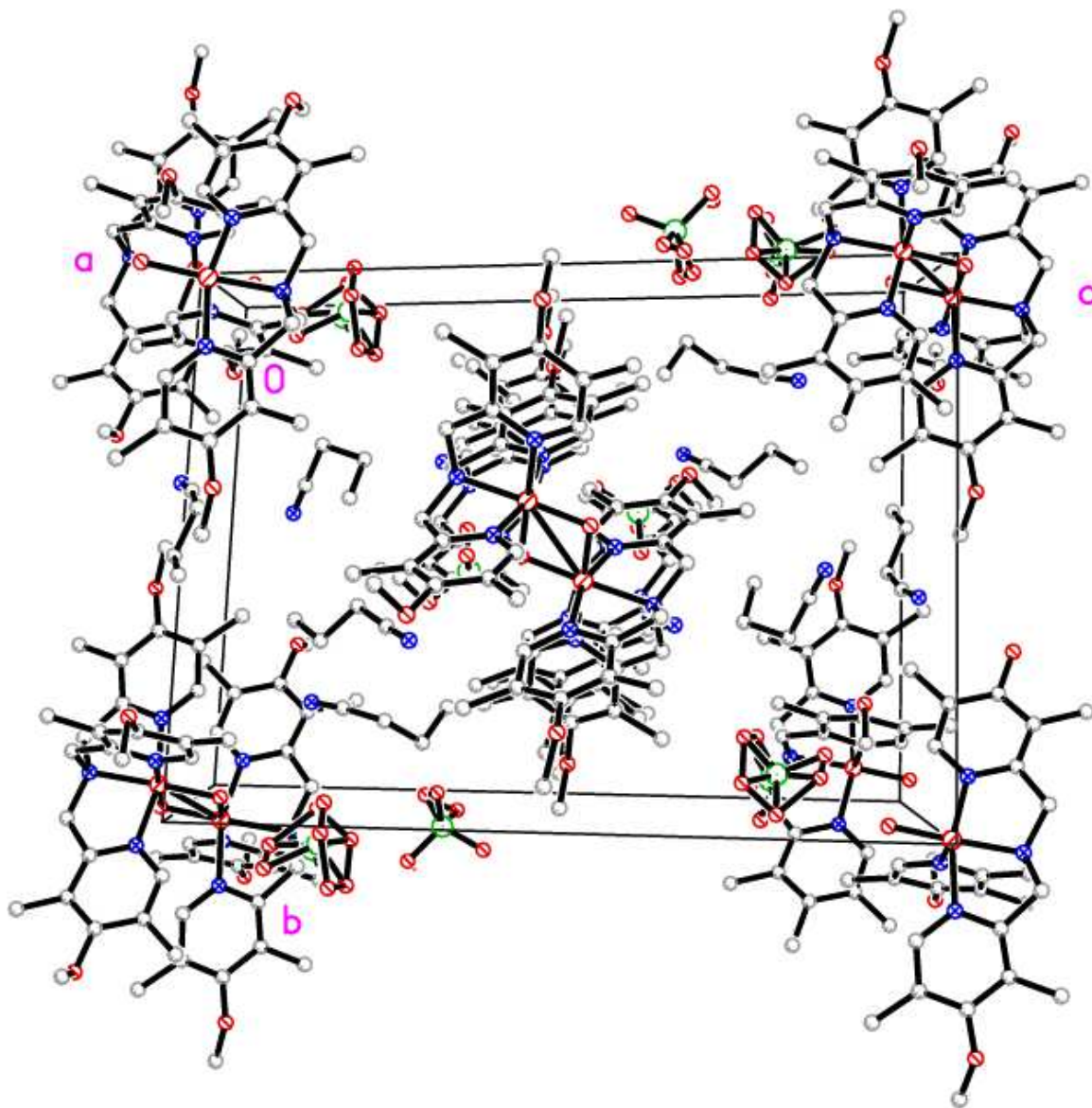


**Figure 3.8:** Packing diagram of **4A** looking down the a-axis. Hydrogen atoms are removed for clarity. The butyronitrile solvent molecules and the perchlorate counterions form a channel surrounding the tetra-cationic compound of interest, likely buffering the large positive charged cations from their neighbors. Atom colors: carbon- gray, oxygen- small red, nitrogen- blue, iron- large red, chlorine- green.

*Refinement details for 5A:*

Refinement of complex **5A** was carried out in a routine manner as previously described, except it was solved using SIR2011.<sup>105</sup> The asymmetric unit is displayed in Figure 3.9. Additionally, one water molecule was located in the unit cell and H-bonded to perchlorate counter anions. The two water hydrogens were first located on a difference map and then refined as riding atoms with relative isotropic displacement parameters. All non-water hydrogen atoms were placed in ideal positions and refined as riding atoms with relative isotropic displacement parameters. The two perchlorate counterions and the butyronitrile molecule were modeled over two positions with occupancy ratios of 91:9, 91:9 and 69:31 respectively. All atoms pairs in the disordered anions and solvent molecules were constrained to have the same anisotropic displacement parameters (EADP),<sup>20</sup> and restrained to have all bond distances the same (SAME).<sup>20</sup> All perchlorate ions and butyronitrile molecules were refined in a similar manner as discussed in the refinement of **4A**.



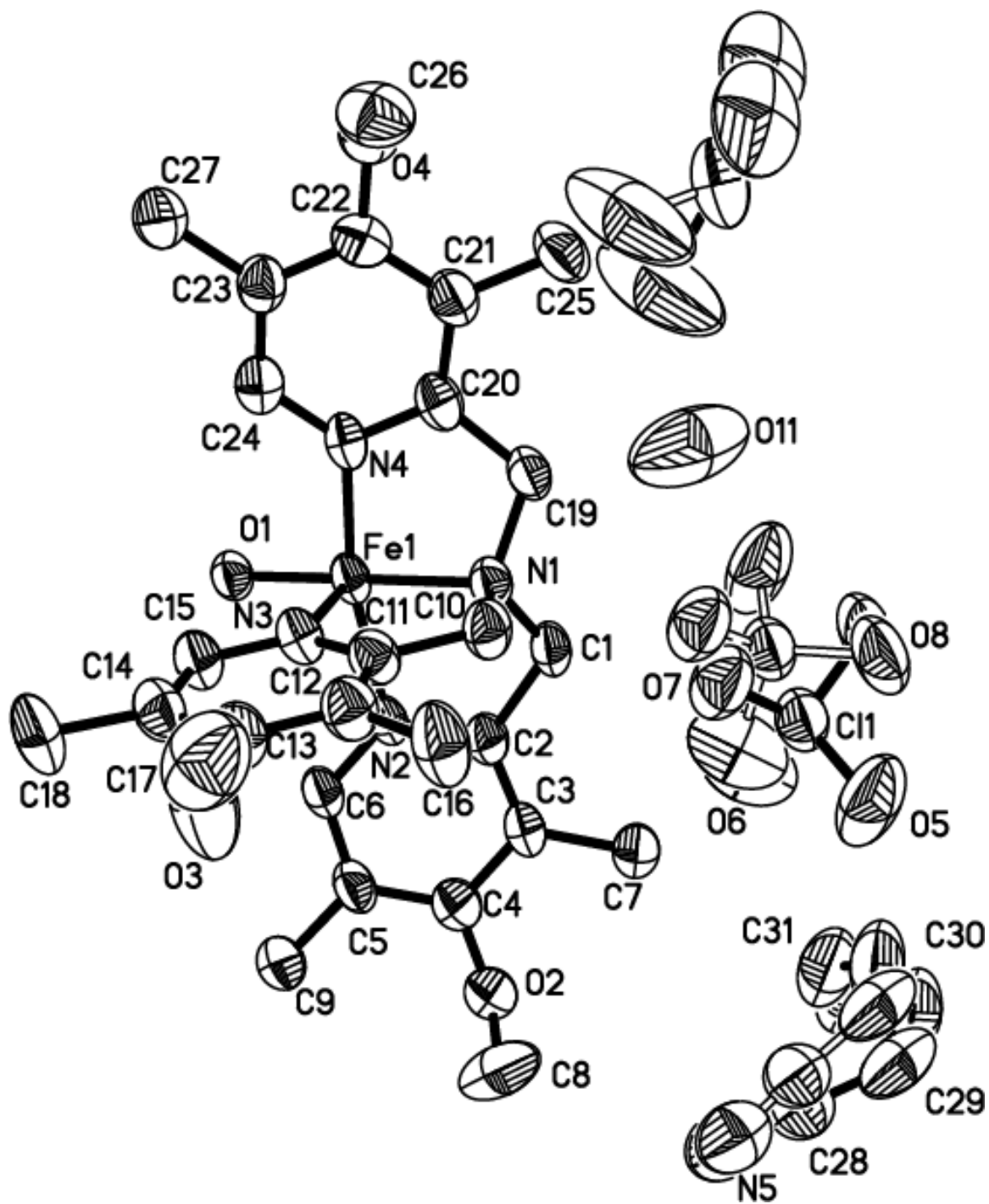


**Figure 3.9:** Asymmetric unit of **5A** with thermal ellipsoids drawn to the 50% probability level with hydrogen atoms removed for clarity.

*Refinement details for 2A:*

Refinement of complex **2A** was carried out in a routine manner as previously described. The asymmetric unit is displayed in Figure 3.10. All non-hydrogen atoms were refined with anisotropic displacement parameters. All hydrogen atoms bonded to carbon atoms were placed in ideal positions and refined as riding atoms with relative isotropic displacement parameters. Hydrogen atoms H1 and H1' were located on a difference Fourier map and refined with isotropic displacement parameters. Hydrogen atoms H2O and H3O were located on a difference Fourier map and refined as riding atoms at 0.85 Å with relative isotropic displacement parameters. The methyl group bonded to O2 was modeled over two positions (55:45). Four acetonitrile molecules were located in the asymmetric unit and one of acetonitrile molecules was modeled over two positions (77:33). Four disordered perchlorate ions were modeled as perfect tetrahedrons over at least two positions in the asymmetric unit and their occupancies were allowed to refine freely. The  $\mu$ -hydroxo ligand had disordered H-bonded acceptors and H-bonded to the O21 water molecule and a perchlorate counter ion in a 90:10 ratio, respectively.

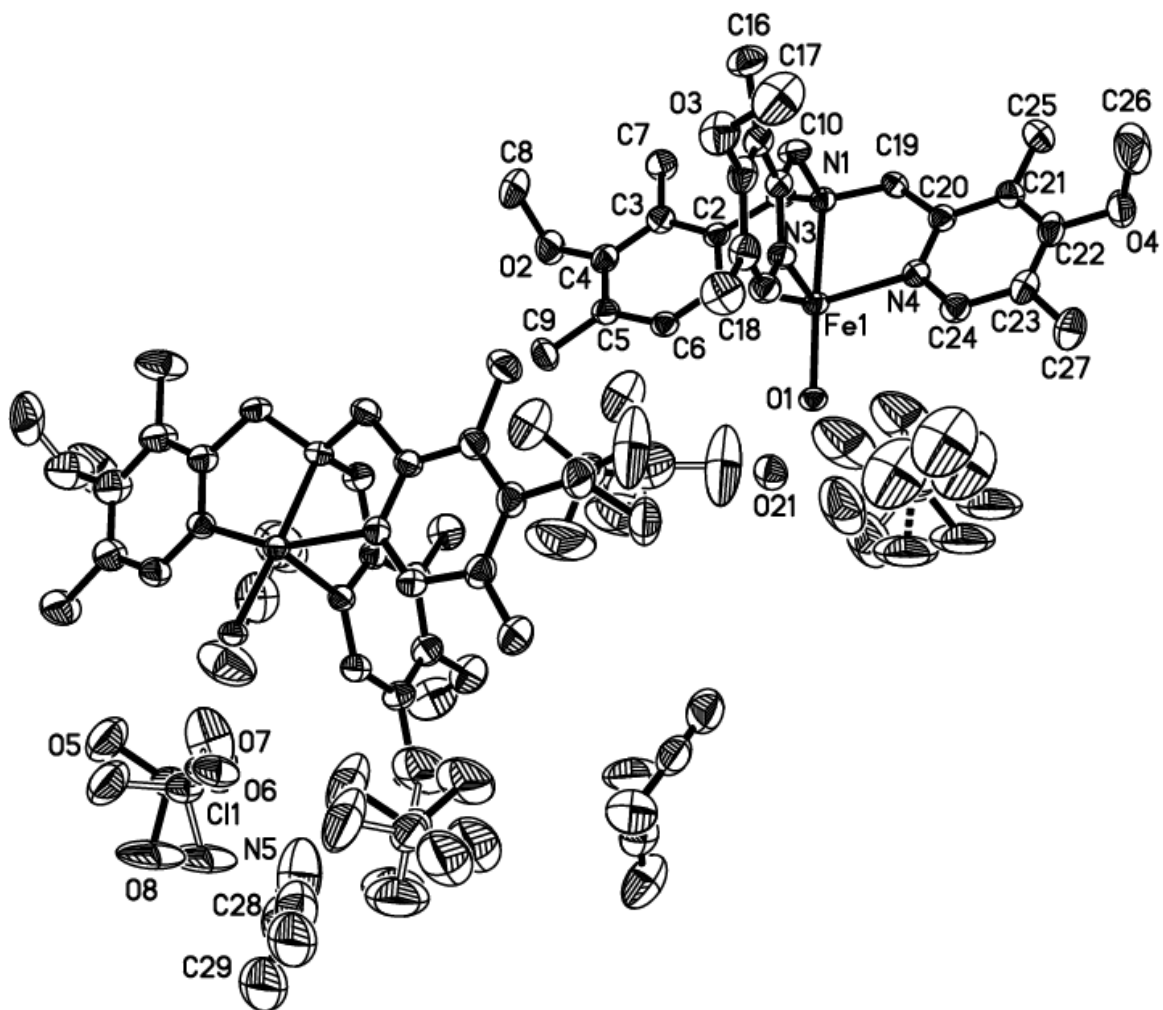


**Figure 3.10:** Asymmetric unit of **2A** with thermal ellipsoids drawn to the 50% probability level with hydrogen atoms removed for clarity.

*X-ray Absorption Spectroscopy:*

Iron K-edge X-ray absorption spectra were collected and analyzed as previously described in Chapter 2.



*Chapter 4: X-ray Crystallographic Investigation of Ferryl, Ferric and Ferrous  
Complexes Supported by the TMC Ligand*

This chapter in part was adapted with permission from Prakash *et al*, *J. Am. Chem. Soc.* **2015**, 3478-3481. Copyright 2015 American Chemical Society.

#### 4.1 Introduction:

In 2003, spectroscopic evidence was reported for an  $\text{Fe}^{\text{IV}}=\text{O}$  moiety of an  $\alpha$ -ketoglutarate-dependent nonheme iron enzyme taurine dioxygenase (TauD).<sup>106,107</sup> TauD is a member of a superfamily of enzymes that reductively activate  $\text{O}_2$  by an Fe atom supported by a 2-His-1-carboxylate facial triad. The enzymatic  $\text{Fe}^{\text{IV}}=\text{O}$  moiety is believed to be the active oxidant for important biochemical transformations in many nonheme enzymes including hydroxylation, epoxidation, halogenation and desaturation.<sup>1</sup>

During the same year, the first well characterized nonheme ferryl model complex supported by the ligand 1,4,8,11-tetramethyl-1,4,8,11-tetraazacyclotetradecane (TMC) was reported (**4.1**, Figure 4.1).<sup>17</sup> The crystal structure of the  $\text{Fe}^{\text{IV}}=\text{O}$  unit provided important structural characteristics to match with the spectroscopic features and was a benchmark for all future synthetic ferryl model complexes.<sup>17,37</sup> Since 2003, over 50 ferryl species and six additional ferryl complex crystal structures have been reported.<sup>37,108–113</sup>

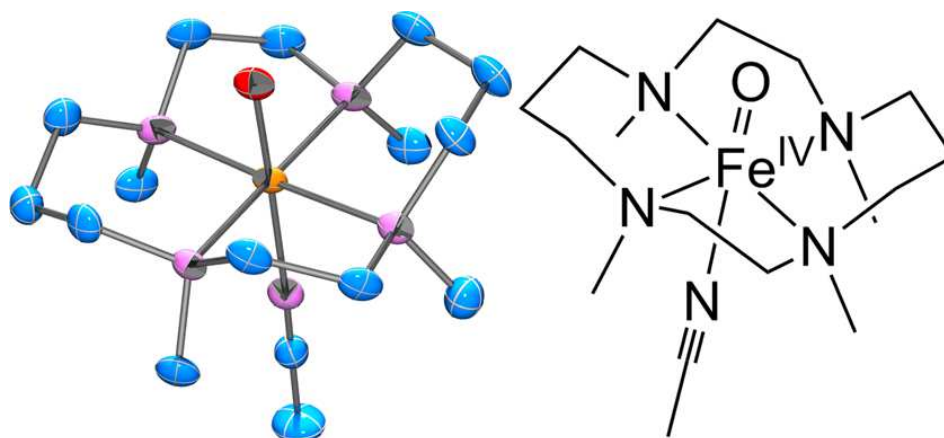


**Figure 4.1:** Crystal structure and cartoon of  $[\text{Fe}^{\text{IV}}(\text{O})\text{TMC}(\text{CH}_3\text{CN})]^{2+}$  (**4.1**), the first well characterized  $\text{Fe}^{\text{IV}}=\text{O}$  complex.<sup>17</sup>

Addition of a Lewis acid to **4.1** increased the reactivity of the ferryl complex many orders of magnitude.<sup>114</sup> This interesting observation was followed by the report of the crystal structure of **4.2** (Figure 4.2).<sup>18</sup> In it, the Fe is in a five-coordinate environment, bound by the tetradentate TMC ligand and an oxo ligand bridging to a scandium atom. Additionally, the scandium atom is supported by four triflate (OTf) ligands and an apical oxygen-based ligand assigned as a hydroxo moiety. The oxidation state of the iron atom was assigned to Fe<sup>IV</sup>, was based solely on the assignment of one proton found on the apical oxygen-based ligand during the refinement process. The protonation state assignment is dubious, because X-rays are diffracted by electrons and a proton does not have core electrons to locate its nuclear position. Indeed, an independent computational study and an X-ray diffraction bond-distance survey assigned the iron oxidation state to be in the +3 state and an aqua atom as the apical ligand of the scandium atom.<sup>19</sup>

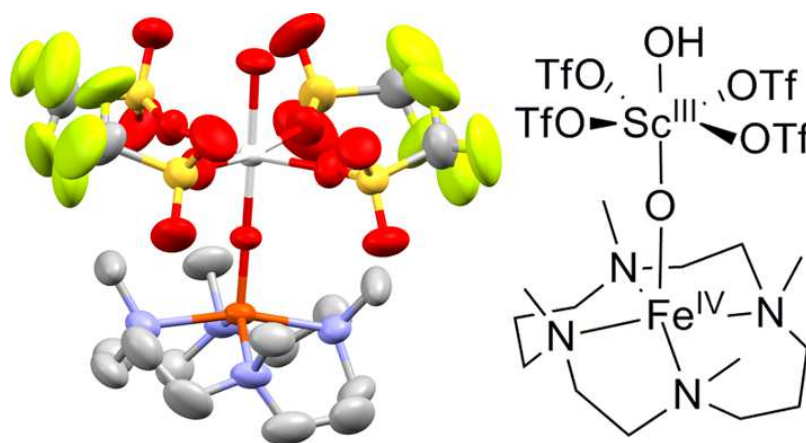


**Figure 4.2:** Crystal structure and of [(OTf)<sub>4</sub>(OH)Sc<sup>III</sup>-O-Fe<sup>IV</sup>TMC], **4.2**.<sup>18</sup> An independent computational study by Swart assigned the oxidation state of the iron atom to be Fe<sup>3+</sup> with a terminal aqua bound to the scandium atom.<sup>19</sup>

## 4.2 Results:

### *Crystal Structure of 4.2a:*

The synthesis of **4.2** could not be reproduced under the reported conditions.<sup>18</sup> Instead, a modified synthesis was developed and a new solvate of the original complex, **4.2a**, was isolated in its place (Figure 4.3).<sup>115</sup> The higher-yielding synthesis of **4.2a** (~50%) allowed for sufficient quantities to be isolated so that additional spectroscopic analysis could be performed in addition to X-ray diffraction studies (Figure 4.3). The first coordination sphere of **4.2a** is nearly identical to that originally reported for **4.2** (Table 4.1), verifying that the Fe atom in **4.2** and **4.2a** has the same oxidation state. Specifically, the Fe-O distances are 1.748(5) Å for **4.2a** and 1.753(3) Å for **4.2**, and the average Fe-N distances are 2.167(6) and 2.175(3) Å for **4.2a** and **4.2**, respectively.<sup>18,115</sup> The Fe-N bond distances are typical for Fe<sup>III</sup>TMC complexes,<sup>116–119</sup> and additionally, the Fe-O distance matches well with those in five-coordinate Fe<sup>III</sup>-O-Fe<sup>III</sup> complexes.<sup>120</sup> More importantly, the overlay of the Fe,  $\mu$ -O, Sc and all non-hydrogen atoms of the TMC ligand of **4.2** and **4.2a** results in a root-mean-square deviation of 0.0742 Å, as calculated by the OFIT command of SHELXP (Figure 4.4).<sup>20,115</sup> An oxidation state of Fe<sup>III</sup> can be confidently assigned to the iron atom in the crystal structure of **4.2a**, based on charge balance arguments, as there is no ambiguity with respect to the charge of the neutral acetonitrile ligand bound to the Sc<sup>3+</sup> atom. This is in contrast to the difficulty in assigning an oxidation state of a molecule based on the ambiguous protonation state of an aqua or hydroxo ligand using X-ray diffraction methods. Additionally, two hydrogen bond acceptors are



found to be within appropriate distances to the Sc-bound oxygen ligand in the crystal structure of **4.2** (Figure 4.5), further supporting the assignment of the apical oxygen as an aqua ligand.<sup>18,21</sup>

**Table 4.1:** Select bond lengths of Fe-O-Sc complexes, Å.

	<b>4.2</b>	<b>4.2a</b>
Fe-O <sub>oxo</sub>	1.753(3)	1.748(5)
Fe-N <sub>ave</sub>	2.175(3)	2.167(6)
Sc-O <sub>oxo</sub>	1.933(3)	1.888(5)
Sc-O <sub>OTf Ave</sub>	2.095	2.083
Sc-O/N <sub>apical</sub>	2.188(3)	2.310(10)
RMS	0.0742	

RMS = root-mean-squared deviation of atomic positions of the overlay of the Fe,  $\mu$ -O, Sc and all non-hydrogen atoms of the TMC macrocycle using the SHELXP command OFIT.<sup>20</sup>

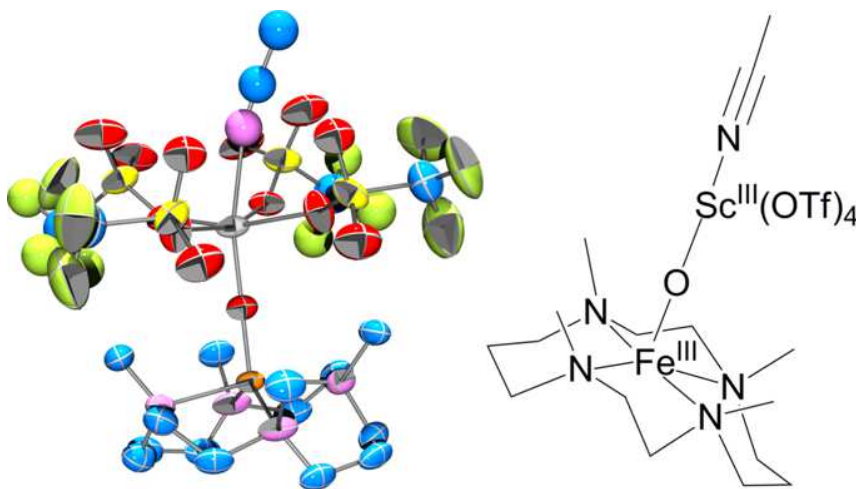


**Figure 4.3:** Crystal structure of **4.2a**. Thermal ellipsoids are drawn to the 50% probability level with hydrogen atoms and solvent molecules removed for clarity. Select bond distances (Å): Fe1-O1, 1.748(5); Fe-N<sub>Ave</sub>, 2.083; Sc1-O1, 1.888(5); Sc1-O<sub>OTf Ave</sub>, 2.083; Sc1-N<sub>CH<sub>3</sub>CN</sub>, 2.310(10); Fe1-Sc1, 3.6358(16).

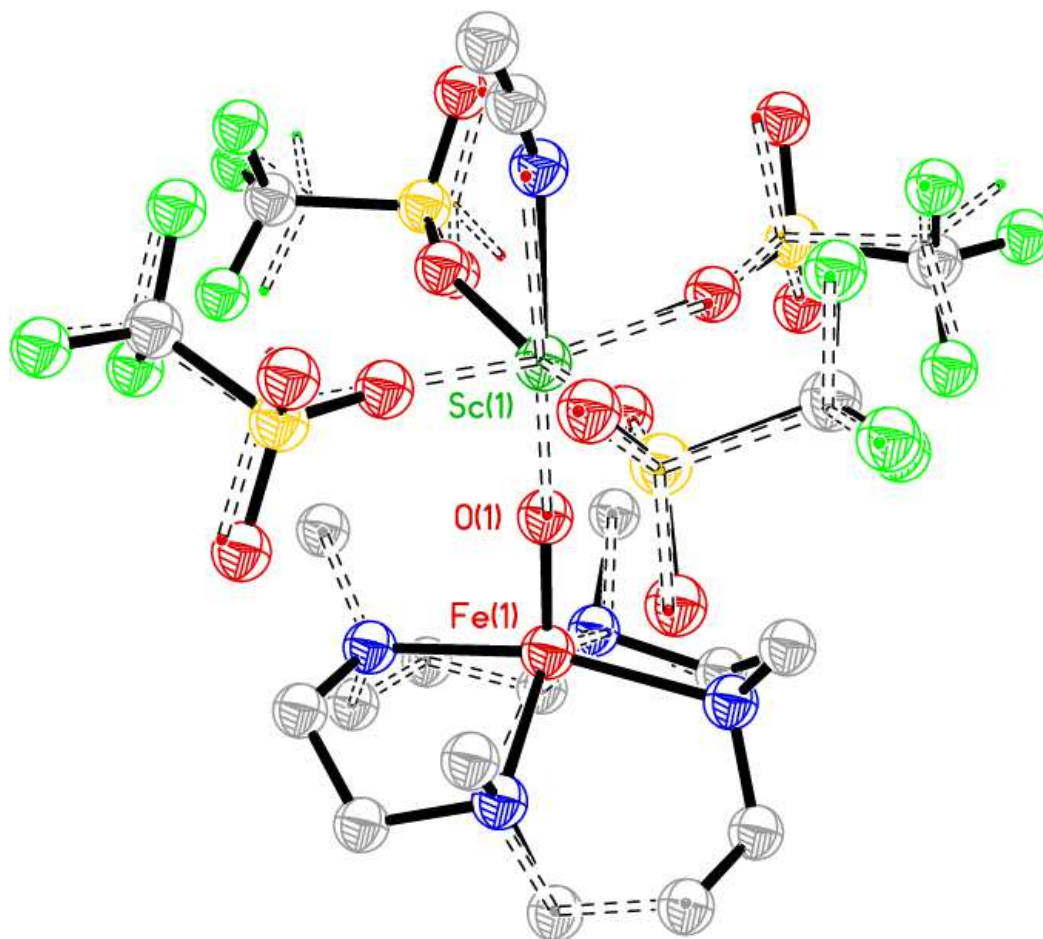


**Figure 4.4:** Overlay of the Fe,  $\mu$ -O, Sc and all non-hydrogen atoms of the TMC ligand of **4.2** and **4.2a** resulting in a root-mean-square deviation of 0.0742 Å, as calculated by the OFIT command of SHELXP.<sup>20</sup> Atoms of **4.2a** are modeled as isotropic to the 25% probability level and atoms of **4.2** are displayed as small dots. Hydrogen atoms are removed for clarity.

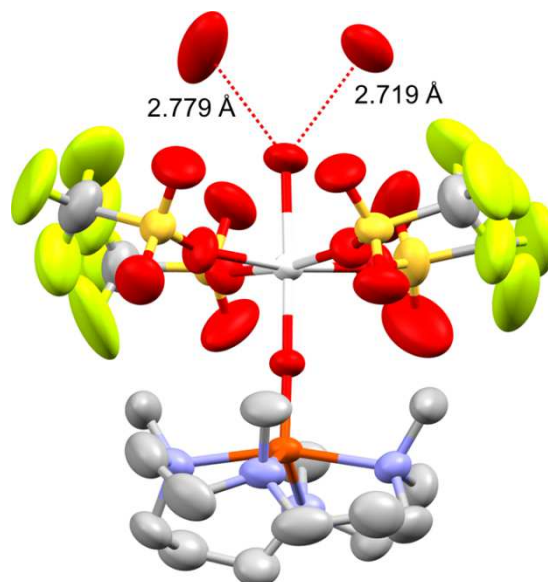


**Figure 4.5:** H-bond acceptors of **4.2** located at standard donor-acceptor distances.<sup>21</sup> Figure 4.5 was created from the published crystal structure of **4.2** by the program Mercury CSD 3.31.<sup>18</sup>

#### *Spectroscopic Analysis of 4.2a:*

Crystals of **4.2a** (unit cell matched that of **4.2a**) were ground to a fine powder and diluted with boron nitride in preparation for EXAFS and Mössbauer analysis. The Fe-scatterer distances in the EXAFS sample matched the crystallographically determined bond distances, notably reproducing the Fe-O distance at 1.74 Å and an Fe-Sc distance at 3.69 Å.<sup>115</sup> These results provided evidence that the crystalline sample was still intact. The parallel solid-state Mössbauer sample of **4.2a** displayed an  $\delta = 0.36$  mm/s, which clearly showed that it was a high-spin ferric iron complex. A crystalline sample of **4.2a** dissolved in acetonitrile produced an EPR spectrum with signals from two of the Kramers doublets of a high-spin ferric signal and was consistent with the Mössbauer

spectrum.<sup>115</sup> The spectroscopic and crystallographic studies conclude that samples **4.2** and **4.2a** contain ferric iron. This is a cautionary tale advising against the assignment of an oxidation state based solely on a proton, which is invisible in an X-ray experiment.

*The Anti- to Syn- Conversion of the Ferryl Species:*

Close examination of **4.2** and **4.2a** shows the methyl groups of the TMC macrocycle have a different orientation and changed from *anti* to the *oxo* in the starting material **4.1** to *syn* relative to **4.2** and **4.2a**.<sup>17,18</sup> This observation suggests some rearrangement must have occurred. The electronic absorption spectrum observed in the reaction of  $[\text{Fe}^{\text{II}}\text{TMC}(\text{CH}_3\text{CN})]^{2+}$  and 1 equivalent of 1-(*tert*-butylsulfonyl)-2-iodosylbenzene (<sup>s</sup>ArIO) in acetonitrile revealed a unique ferryl species, **4.3**, which was distinguished from **4.1** by a slight blue-shift in the near-infrared absorption band from 824 in **4.1** to 815 nm in **4.3** and by a subtle change in the vibronic coupling pattern.<sup>vii</sup> The <sup>1</sup>H NMR (CD<sub>3</sub>CN) and Mössbauer spectra of the ferryl species generated using <sup>s</sup>ArIO also showed a new ferryl species, **4.3**. Species **4.3** was found to make up ~72% of the sample, with **4.1** as the minor component, according to Mössbauer and <sup>1</sup>H NMR (CD<sub>3</sub>CN) analysis.<sup>vii</sup> The Mössbauer spectrum of **4.3** was notably different from **4.1** with the parameters  $\delta = 0.16$  mm/s and  $\Delta E_{\text{Q}} = 1.51$  mm/s for **4.3** and  $\delta = 0.17$  mm/s and  $\Delta E_{\text{Q}} = 1.24$  mm/s for **4.1**.<sup>viii,17</sup> The <sup>1</sup>H NMR (CD<sub>3</sub>CN) spectrum of **4.3** revealed

---

<sup>vii</sup> Electronic absorption and NMR data contributed by Dr. Jai Prakash (Manuscript in Preparation).

<sup>viii</sup> Mössbauer analysis performed by the Eckard Münck group in Carnegie Mellon University, Pittsburgh, PA, USA (Manuscript in Preparation).

that it retained the effective  $C_{2v}$  symmetry of **4.1**, both with seven clearly resolvable peaks, albeit at different chemical shifts. Additionally, **4.3** slowly converted to **4.1** as monitored by  $^1\text{H}$  NMR ( $\text{CD}_3\text{CN}$ ) and UV-Vis-NIR spectroscopies with a half-life of about 4 hours at room temperature. The growth of **4.1** and the decay of **4.3** could each be modeled by a single exponential consistent with the first-order conversion of **4.3**  $\rightarrow$  **4.1**.<sup>vii</sup>

To gain additional structural information, X-ray absorption spectroscopy was performed on 6 mM frozen solution samples of **4.1** and **4.3**. The X-ray absorption-near-edge spectroscopy (XANES) region is displayed in Figure 4.6 and the two spectra show modest differences between **4.1** and **4.3**. The K-edge energies, which represented the energy required to excite an electron from the 1s shell to the continuum, were found to be the same at 7123.8 eV, consistent with an  $\text{Fe}^{\text{IV}}$  oxidation state and in agreement with Mössbauer spectroscopy. However a notable difference was found in the pre-edge region with **4.3** having a pre-edge area 10 units higher as compared to **4.1** (42 a.u. vs. 32 a.u.<sup>121</sup> when accounting for sample purity determined by Mössbauer spectroscopy<sup>ix</sup>). The pre-edge absorption is a symmetry forbidden  $1s \rightarrow 3d$  transition and the larger area of **4.3** signifies a less symmetric environment that leads to greater mixing of 3d and 4p orbitals. The increased pre-edge area is consistent with the shortening of the Fe=O bond and lengthening of the bond *trans* to the oxo for **4.3**.

---

<sup>ix</sup> The XAS sample used to determine the pre-edge of **4.3** contained 72% **4.3**, 14% **4.1** and 14% **4.6** as determined by Mössbauer spectroscopy performed by the Eckard Münck lab in Carnegie Mellon University in Pittsburgh, PA.

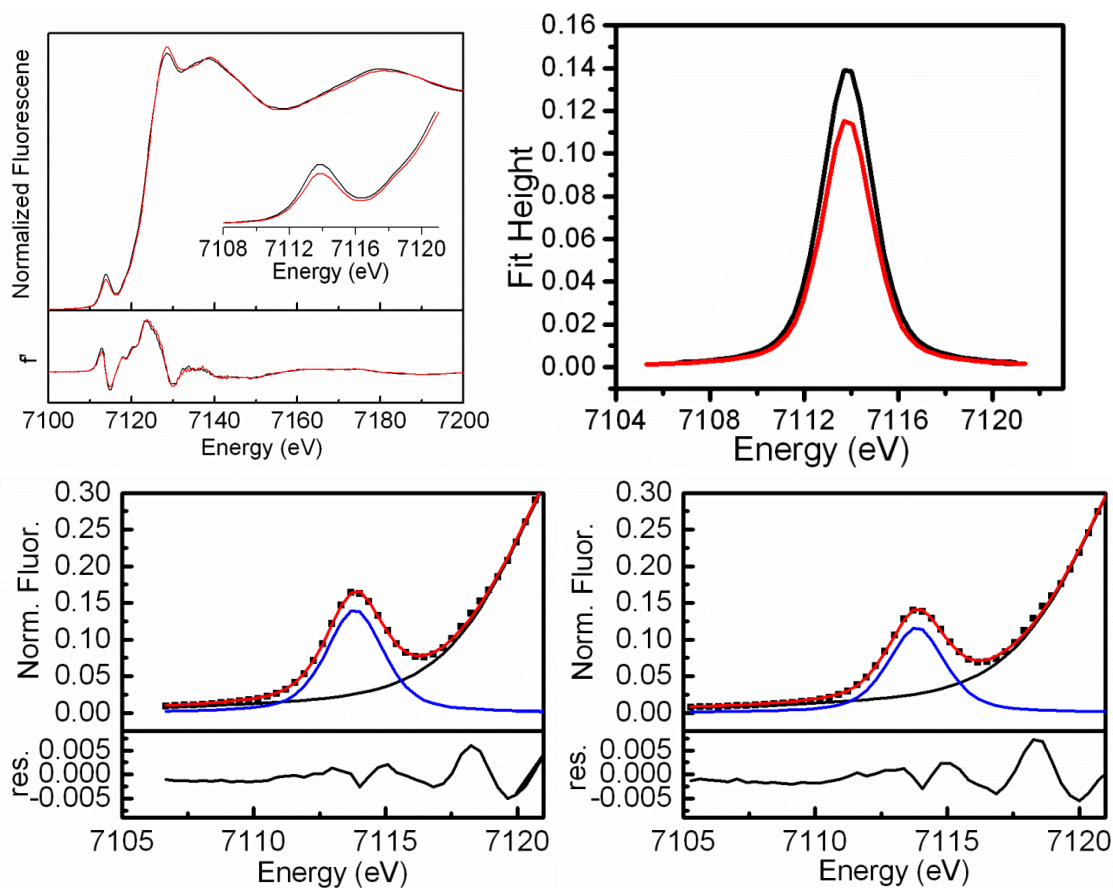


**Figure 4.6:** Top Left: XANES spectra of the **4.3** (black) and **4.1** (red) with the first derivative of the XANES spectra and pre-edge region displayed for comparison. The edge energies were found to be equal at 7123.8 eV and were determined by the maximum intensity of the first derivative in the rising edge. The pre-edge areas were found to be 42 a.u. for **4.3** and 32 a.u. for **4.1** when accounting for sample purity determined by Mössbauer spectroscopy. Top Right: functions used to model pre-edge transition for **4.3** (black) and **4.1** (red). Bottom: Fit of **4.3** (Left) and **4.1** (Right) with experimental data displayed with dots, rising edge modeled with the black line, pre-edge transition modeled with the blue line and over all fit displayed in red. The residuals of the data from the fit are displayed below.

### *Crystal Structures of Reaction Products Derived from 4.1 and 4.3:*

A kinetic trap based on the reaction with a Lewis acid was employed to determine how the ferryl species **4.1** and **4.3** differed structurally. Inspired by the Fukuzumi work,<sup>18,115</sup> one equivalent [Et<sub>4</sub>N][FeCl<sub>4</sub>] was added to acetonitrile solutions of **4.1** and **4.3** at room temperature to see if the two isomers could be trapped by the Lewis acid. Both reaction mixtures upon layering with diethyl ether at -40 ° C produced diffraction quality crystals.<sup>x</sup> A solution of **4.1** and [FeCl<sub>4</sub>](Bu<sub>4</sub>N) afforded crystals of (TMC)Fe-O-FeCl<sub>3</sub> complex. Its structure revealed a  $\mu$ -oxo ligand *anti* to the methyl groups of the TMC ligand. This structure is designated **4.4** (Figure 4.7, left) and is consistent with a direct reaction between **4.1** and the Lewis acid Fe<sup>3+</sup> with no rearrangement. Conversely, starting with a solution of **4.3** and [FeCl<sub>4</sub>](Bu<sub>4</sub>N) <sup>x</sup> afforded crystals of a complex designated as **4.5** whose structure revealed the  $\mu$ -oxo ligand to be *syn* to the methyl groups (Figure 4.7, right). These results suggest that the oxo ligand of the starting material, **4.3**, is *syn* to the methyl groups of the TMC ligand. Because **4.5** is five coordinate like **4.2**, the *syn* isomer does not rule out the possibility of rearrangement after the reaction similar to what was observed for **4.2**.<sup>18,115</sup> However, the crystal structure of **4.5** is the first indirect evidence that the structure of **4.3** has the position of the methyl groups inverted relative to the oxo group compared to **4.1**.

---

<sup>x</sup> Crystals supplied by Dr. Jai Prakash (Manuscript in Preparation).



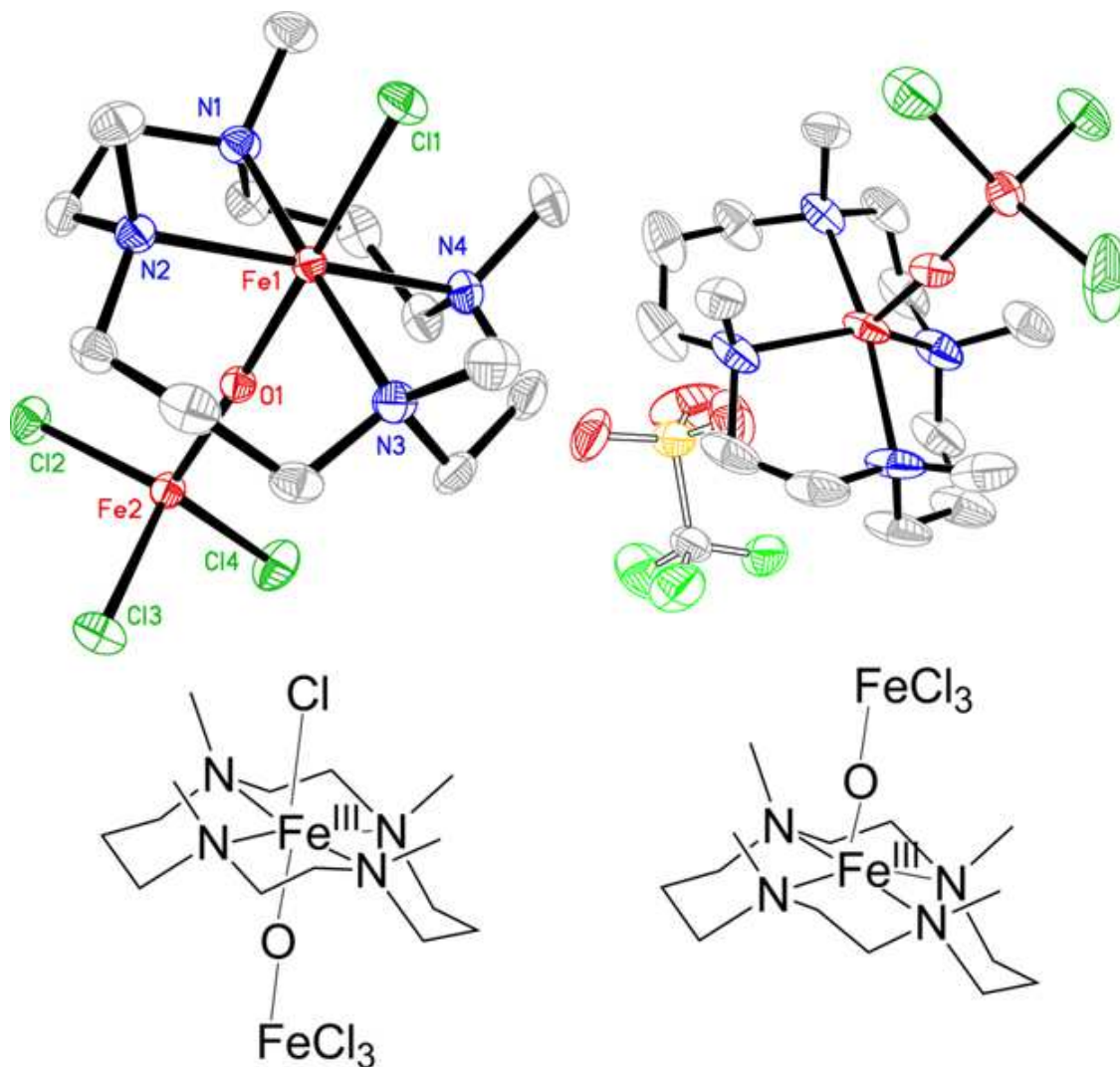


**Figure 4.7:** Thermal ellipsoids of the crystal structures of **4.4** and **4.5** are drawn at the 50% probability level with hydrogen atoms removed for clarity. **Left:** top-structure of **4.4** produced from the reaction of **4.1** and one equivalent  $[\text{Et}_4\text{N}][\text{FeCl}_4]$ . One acetonitrile molecule removed for clarity. Bottom Left-cartoon of **4.4**; **Right:** top- structure of **4.5** produced from the reaction between **4.3** and one equivalent  $[\text{Et}_4\text{N}][\text{FeCl}_4]$ . The OTf counter anion is included in the picture and two acetonitrile molecules were removed for clarity. Bottom right-cartoon of **4.5**. Select bond distances ( $\text{\AA}$ ) and angles ( $^\circ$ ): **4.4**: Fe1-O1, 1.8511(12); Fe1-N<sub>ave</sub>, 2.206; Fe1-Cl1, 2.3586(5); Fe2-O1, 1.7712(12); Fe1-O1-Fe2, 1.77.31(9); Fe1-Fe2 3.6213(5) **4.5**: Fe1-O1, 1.771(2); Fe1-N<sub>ave</sub>, 2.166; Fe2-O1, 1.771(2); Fe1-O1-Fe2, 171.21(14); Fe1-Fe2, 3.5056(7).



### *Crystal Structure of 4.3<sub>DCM</sub>:*

To obtain more conclusive evidence, diffraction quality crystals of **4.3** were grown. A solution of Fe<sup>IV</sup>TMC(OTf)<sub>2</sub> in dichloromethane at -50° C was treated with 1 equivalent <sup>s</sup>ArIO and quickly cooled to -78° C with dry ice. The iron solution was layered with pentane and allowed to crystallize at -80° C in a freezer. Diffraction quality crystals were obtained.<sup>x</sup> Interestingly, the crystals of **4.3** exhibited dichroic behavior changing from a deep blue to a pale yellow depending on which face was visible. The crystals of **4.1** behaved in the same manner. The blue crystals were very susceptible to solvent loss, which resulted in a loss of crystallinity if handled at temperatures above ~-40° C. The twinned data set was solved and the result is displayed in Figure 4.8. A OTf ligand was found coordinated *trans* to the oxo and the complex is formulated as [Fe<sup>IV</sup>(O)TMC(OTf)](OTf) or (**4.3<sub>DCM</sub>**). A second OTf counterion and two molecules of dichloromethane were also found in the unit cell. The oxo ligand was found to be *syn*- to the methyl groups of the TMC ligand and the structure is direct structural proof of the *syn*-isomer (Figure 4.8). Interestingly, the Fe=O bond distance of 1.625(4) Å is the shortest crystallographically determined to date for ferryl complexes. The short Fe=O bond is consistent with the higher pre-edge area observed in the XANES spectrum of **4.3** above. Moreover, the crystallographically determined distance is in excellent agreement with the calculated Fe=O distance of the CH<sub>3</sub>CN analog reported in 2008 (1.628 Å).<sup>22</sup>

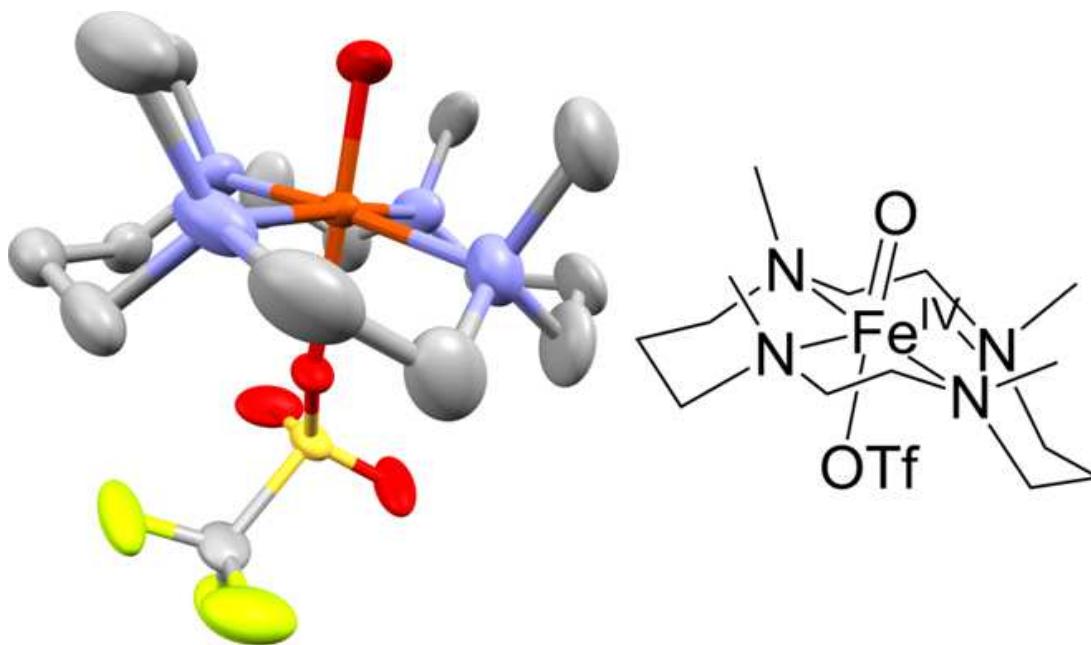


**Figure 4.8:** Left : X-ray crystal structure of **4.3<sub>DCM</sub>** with thermal ellipsoids drawn to the 50% probability level. Hydrogen atoms, one OTf counterion and two dichloromethane solvent molecules were removed for clarity. Right: cartoon of **4.3<sub>DCM</sub>**. Select bond distances (Å): Fe1-O1, 1.626(4); Fe-N<sub>ave</sub>, 2.065; Fe-O<sub>OTf</sub>, 2.146(4).

*Crystal Structure of [Fe<sup>II</sup>TMC(OTf)](OTf):*

The crystal structure of the ferrous starting material has not been previously reported even though the Fe<sup>II</sup>TMC(OTf)<sub>2</sub> complex, **4.6**, was used in many nonheme iron model chemistry studies by several groups.<sup>37,38</sup> Cell constants for the related complex, [Fe<sup>II</sup>TMC(NCCH<sub>3</sub>)](BF<sub>4</sub>)<sub>2</sub>, were reported in 1979; however the authors abandoned the structure when they discovered that the two-fold symmetric molecule was located on a crystallographic four-fold special position.<sup>122</sup> Complex **4.6** was prepared according to previous reports<sup>17</sup> and diffraction quality crystals were grown from a dry dichloromethane solution

layered with ether.<sup>x</sup> The structure of **4.6** was solved and complete data collection and refinement details are described in the Experimental Section below. The Fe atom in **4.6** is in a distorted square pyramidal geometry ( $\tau = 0.58$ )<sup>123</sup> supported by the tetradentate TMC ligand and an apical OTf ligand is bound to the ferrous Fe atom (Figure 4.9). The bound OTf ligand is located *syn* to the methyl groups, consistent with binding on the less sterically hindered side of the TMC ligand. A second OTf counter anion is located in the unit cell for charge balance.

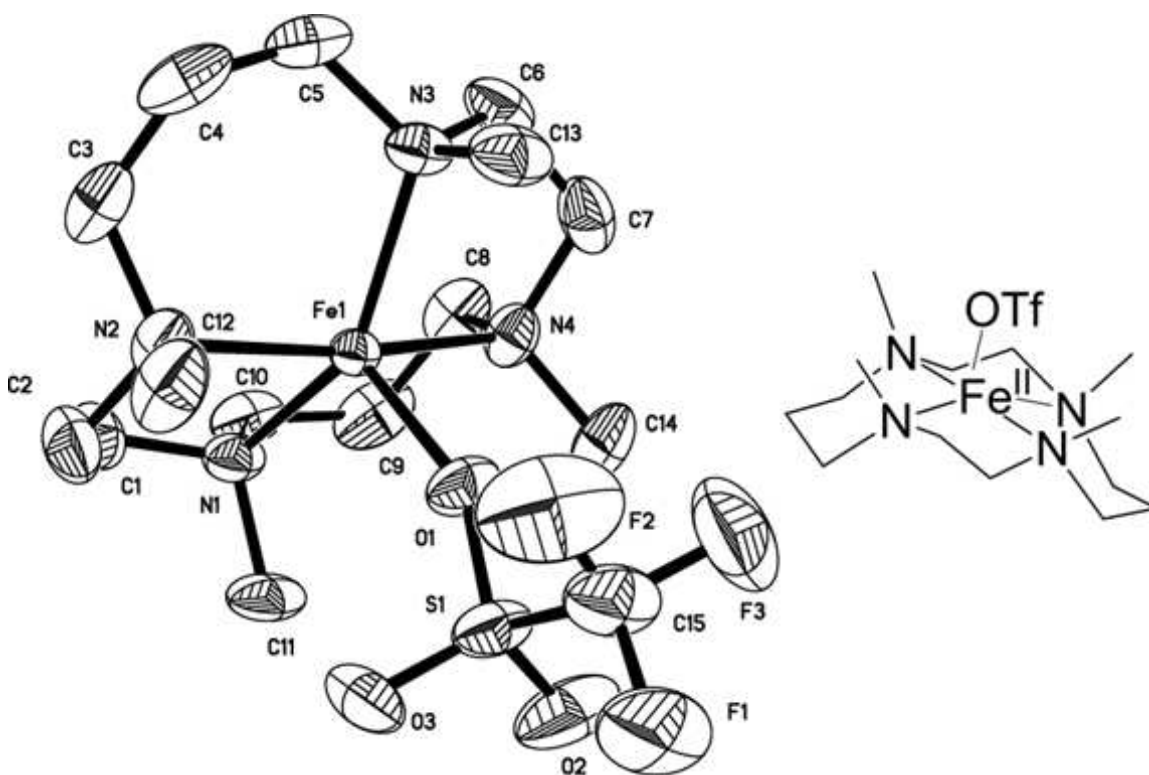


**Figure 4.9:** Crystal structure and cartoon of **4.6** with ellipsoids drawn to the 50% probability level and hydrogen atoms, solvent molecules and OTf counter anions removed for clarity. Three molecules of **4.6** were located in the unit cell and only one is displayed for clarity. Select bond distances (Å), average of the two non-disordered molecules in the unit cell: Fe1-O1, 2.032(3); Fe-N<sub>ave</sub>, 2.181.

### *Crystal Structure of a Trimeric Fe<sup>III</sup>TMC Complex:*

During the course of the Lewis acid studies with **4.1** and **4.3**, (Bu<sub>4</sub>N)<sub>2</sub>[Fe<sup>II</sup>Cl<sub>4</sub>] was added to **4.1** to serve as a reducing agent and form a stable diferric adduct. When **4.1** and one equivalent (Bu<sub>4</sub>N)<sub>2</sub>[Fe<sup>II</sup>Cl<sub>4</sub>] were mixed in an acetonitrile solution, an immediate color change of the solution from the bluish-green to orange was observed. The reaction mixture was allowed to crystallize at -20° C for a week, which did not produce any diffraction quality crystals. Upon standing for ~two additional weeks at room temperature, diffraction quality crystals were observed and yielded a trimeric structure, **4.8** (Figure 4.10).<sup>x</sup> Three Fe atoms in two different coordination environments are bridged by two oxo ligands. The middle Fe atom (Fe<sub>TMC</sub>) of **4.8** is in a pseudo-tetragonal geometry and is supported by the tetradentate TMC ligand in the equatorial plane with two tetrahedral [Fe<sup>III</sup>(μ-O)(Cl)<sub>3</sub>] units binding to the Fe<sub>TMC</sub> in the axial positions. The Fe-ligand bond distances of both tetrahedral Fe atoms are very similar and consistent with [Fe<sup>III</sup>(μ-O)(Cl)<sub>3</sub>] moieties in the literature CSD with Fe-(μ-O) bond distances of 1.76 Å and Fe-Cl bond distances of ~2.23 Å.<sup>124–128</sup> Interestingly, the two Fe<sub>TMC</sub>-oxo bond distances differ by 0.1 Å, even though the ligands are the same. The Fe-O bond distance *syn*- to the methyl groups of the TMC macrocycle is 1.835(7) Å, while the Fe-O bond distance *anti* to the methyl groups is 1.931(8) Å. The difference in Fe-O bond lengths depending on the steric environment highlights how much influence the larger steric bulk of the ethylene and propylene groups of the TMC macrocycle can impose on a bond.

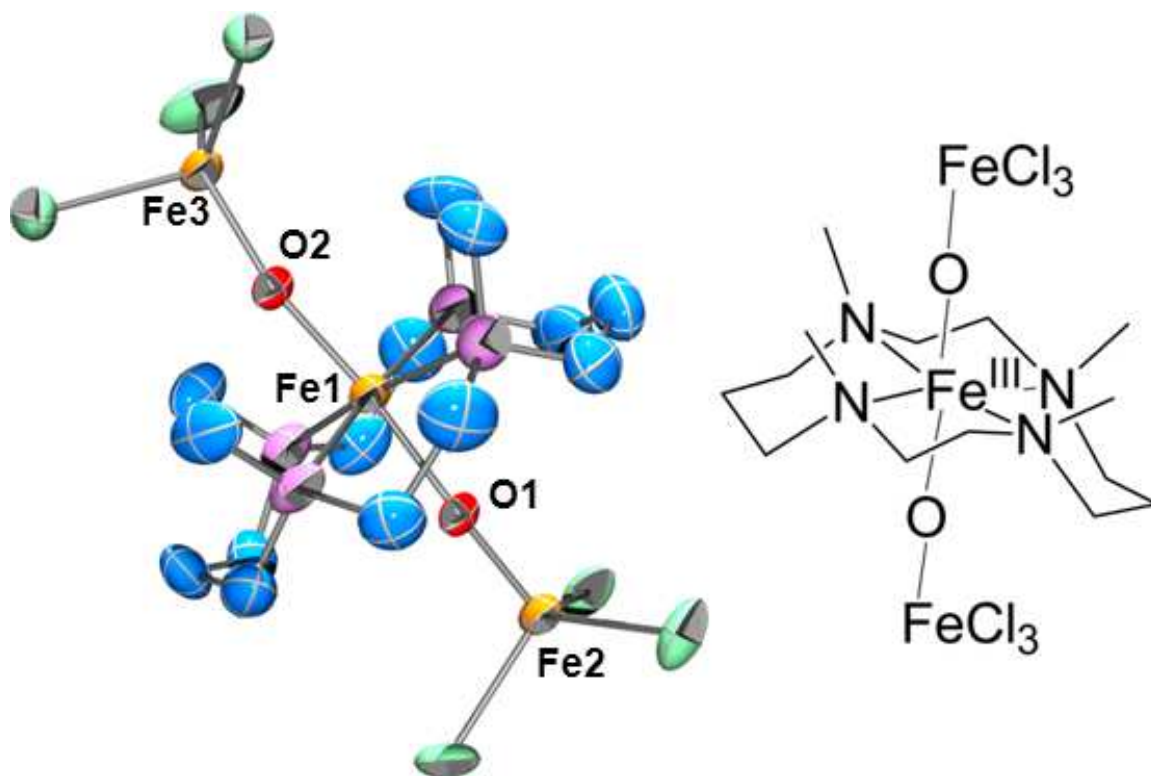


**Figure 4.10:** X-ray crystal structure of **4.8**. Thermal ellipsoids are drawn at the 50% probability level and hydrogen atoms and the counter cation  $[(\text{Bu})_4\text{N}]^+$  are removed for clarity. The complex of interest is disordered over two positions and only one is displayed for clarity. Select bond distances ( $\text{\AA}$ ) and angles ( $^\circ$ ) from an average of two positions in disorder modeling: Fe1-O1, 1.931; Fe1-O2, 1.835; Fe2-O1, 1.763; Fe3-O2, 1.758; Fe-N<sub>ave</sub>, 2.211; Fe1-Fe2, 3.6705(32); Fe1-Fe3, 3.5738(32); Fe1-O1-Fe2, 166.5; Fe1-O2-Fe3, 169.1, O1-Fe1-O2, 172.8.

### 4.3 Discussion:

A compilation of FeTMC metrics is displayed in Table 4.2. The ferryl complexes have similar pseudo-tetragonal coordination environments, but with notable differences. Interestingly, the 1.626  $\text{\AA}$  Fe-oxo bond of **4.3<sub>DCM</sub>** is 0.02  $\text{\AA}$  shorter than the 1.646  $\text{\AA}$  Fe-oxo distance of **4.1**. The shorter Fe-oxo distance of

**4.3<sub>DCM</sub>** is a result of the weaker donating ability of the OTf ligand located *trans* to the oxo, with a Fe-O<sub>OTf</sub> distance of 2.146 Å compared to the 2.058 Å Fe-N<sub>CH<sub>3</sub>CN</sub> bond distance of **4.1**. The weaker donating ability of the OTf ligand is also reflected in the shorter average Fe-N<sub>TMC</sub> distance of **4.3<sub>DCM</sub>** compared to **4.1**.

The Fe ligand bond lengths increase with decreasing Fe oxidation state. The average Fe-N<sub>ave</sub> bond distances lengthen from about 2.1 Å in the ferryl structures to about 2.2 Å in the six-coordinate ferric complexes. The five coordinate ferric complexes, **4.2**, **4.2a** and **4.3<sub>syn</sub>**, have similar bond lengths with an Fe-O bond distances around 1.75 Å and an average Fe-N distances of about 2.17 Å. As expected, the bond distances of the ferrous complex **4.6** increase, with an Fe-O distance of 2.032 Å and a more modest increase was observed for the Fe-N<sub>ave</sub> distance compared to **4.5**. The iron atom is pulled out of the N plane of the TMC ligand by about 0.5 Å for all five-coordinate structures and is virtually in the N plane of the TMC ligand for the 6-coordinate species.

The Fe-metal distances reflect the coordination environment of the metals. A longer Fe-Fe distance was observed for the six-coordinate FeTMC moiety at about 3.6 Å in **4.4** and **4.8**, while a shorter distance of 3.51 Å was seen for the five-coordinate FeTMC moiety in **4.5**. The shorter Fe-O bond is consistent with the more Lewis-acidic five-coordinate **4.5**. Two different Fe-Fe distances were observed in **4.8**. The shorter Fe-Fe distance of 3.57 Å in **4.8** is *syn* to the methyl groups of TMC; the methyl groups are less sterically bulky compared to the ethylene and propylene groups and thus allow for the almost 0.1 Å shorter Fe-Fe distance. The Fe-Fe distance *anti* to the methyl groups in **4.8** is 3.67 Å and is

longer than the comparable Fe-Fe distance in **4.4** at 3.62 Å. This reflects the larger steric bulk of the *trans* ligand of the second –OFeCl<sub>3</sub> group in **4.8** relative to Cl in **4.4**. The –OFeCl<sub>3</sub> group *anti* to the methyl groups forces the TMC ligand toward the –OFeCl<sub>3</sub> group *syn* to the methyl groups, causing the Fe-Fe distance to increase. The Fe-Sc distances of **4.2** and **4.2a** are similar at 3.69 and 3.63 Å, respectively, with the Sc-O bond distances accounting for the difference in Fe-M lengths. The Fe-O-M angles are about 170° in all cases.

**Table 4.2:** Structural metrics of TMC supported Fe complexes

	Fe Oxidation State	Fe-O, Å	Fe-N <sub>TMC</sub> average, Å	Fe- <i>trans</i> , Å, Ligand	Distance Fe is above N4 TMC plane, <sup>d</sup> Å	Fe-Metal, Å
<b>4.1<sup>a</sup></b>	4+	1.646(3)	2.091	2.058(3), CH <sub>3</sub> CN	0.03	-
<b>4.3<sub>DCM</sub></b>	4+	1.626(4)	2.065	2.146(4), OTf	0.06	-
<b>4.2<sup>b</sup></b>	3+	1.753(3)	2.175	-	0.57	3.687
<b>4.2a<sup>c</sup></b>	3+	1.748(5)	2.167	-	0.54	3.6358(16)
<b>4.5</b>	3+	1.771(2)	2.166	-	0.49	3.5056(7)
<b>4.4</b>	3+	1.8511(12)	2.206	2.3586(5), Cl	-0.04	3.6213(5)
<b>4.8 -<i>syn</i> oxo</b>	3+	1.835(7) <sup>f</sup>	2.211 <sup>f</sup>	<sup>e</sup>	0.02 <sup>f</sup>	3.5738(32) <sup>f</sup>
<b>-<i>anti</i> oxo</b>	3+	1.931(8) <sup>f</sup>				3.6705(32) <sup>f</sup>
<b>4.6</b>	2+	2.032(3) <sup>g</sup>	2.181	-	0.43	-

<sup>a</sup> ref <sup>17</sup>, <sup>b</sup> ref <sup>18</sup>, <sup>c</sup> ref (Prakash 2015), <sup>d</sup> positive number is in the direction of the oxo ligand, <sup>e</sup> *trans* ligand is the oxo ligand *anti* to the methyl groups of the TMC ligand. <sup>f</sup> Average of two positions from disorder modeling, <sup>g</sup> average of two non-disordered molecules in the asymmetric unit.



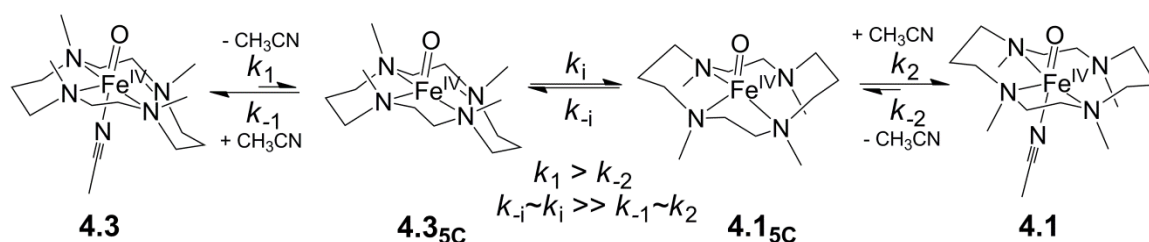
### **4.3** → **4.1** Conversion Mechanism Discussion:

A series of equilibria is proposed in Scheme 4.1 to describe the conversion of **4.3** → **4.1**. Complex **4.3** first loses acetonitrile to form a five-coordinate species **4.3<sub>5c</sub>**. The species **4.3<sub>5c</sub>** is in equilibrium with its *anti* isomer, **4.1<sub>5c</sub>**, and then acetonitrile binds to either five-coordinate species to form **4.1** or **4.3**. The equilibrium constant between **4.1<sub>5c</sub>** and **4.3<sub>5c</sub>** is proposed to be close to 1 because of the small size of the oxo ligand. The decoordination rate of the *trans* ligand is faster in **4.3** as compared to **4.1** because of the larger unfavorable interactions of the *trans* ligand in **4.3** with the propylene and ethylene groups as compared to the interactions of the *trans* ligand with methyl groups in **4.1**. The larger unfavorable interactions are illustrated by the longer Fe-O bond distance for the oxo group *syn* to the propylene and ethylene groups in the crystal structure of complex **4.8**, compared to the shorter Fe-O bond distance on the methyl side. Likewise, the rate of acetonitrile binding to **4.1<sub>5c</sub>** is faster due to its binding in a less sterically hindered pocket. The steric interactions between the *trans* ligand and TMC macrocycle drive the equilibrium all the way to the right of Scheme 4.1.

Ligand exchange experiments with **4.3<sub>DCM</sub>** provided additional evidence for the inversion mechanism present in Scheme 4.1. When crystals of **4.3<sub>DCM</sub>** are dissolved in acetonitrile-*d*<sub>3</sub>, a ~60:40 ratio of **4.3** to **4.1** is observed in the <sup>1</sup>H NMR spectrum, and **4.3** converts to **4.1** at the same rate as previously described. Acetonitrile binding to the five-coordinate species must be slower than the inversion of **4.3<sub>5c</sub>** and **4.1<sub>5c</sub>**, because both **4.3** and **4.1** are produced from

crystals of **4.3<sub>DCM</sub>** dissolved in acetonitrile. The inversion ( $k_i/k_{-i}$ , Scheme 4.1) equilibrium constant is close to 1 and the acetonitrile binding rate constant to **4.3<sub>5c</sub>** or **4.1<sub>5c</sub>** ( $k_{-1}$  and  $k_2$  respectively, Scheme 4.1) are similar because of the 60:40 ratio of **4.3:4.1** prepared from the crystals of **4.3<sub>DCM</sub>** dissolved in acetonitrile. Interestingly, the conversion of **4.3** to **4.1** in dichloromethane- $d_2$  was complete in about 1 minute at RT, as monitored by  $^1\text{H}$  and  $^{19}\text{F}$  NMR spectroscopies.<sup>129</sup> The faster inversion rate in dichloromethane is due to the faster rate of decooordination of the weaker OTf ligand. Thus, the rate limiting step of the **4.3** to **4.1** inversion is assigned to the decooordination of the *trans* ligand from the six-coordinate Fe center.

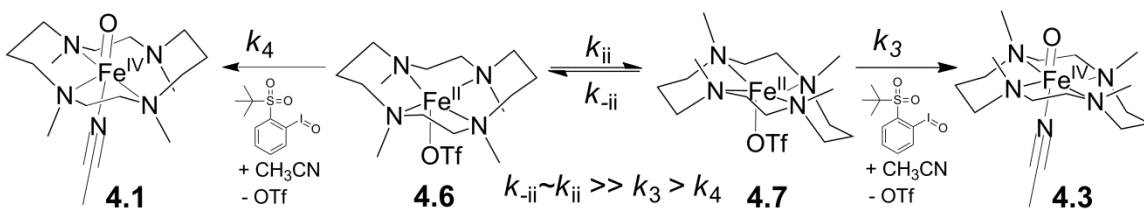
**Scheme 4.1:** Proposed  $[\text{Fe}^{\text{IV}}(\text{O})\text{TMC}(\text{CH}_3\text{CN})]^{2+}$  Inversion Mechanism



How does species **4.3** form from the ferrous starting material? The  $[\text{Fe}^{\text{II}}\text{TMC}(\text{OTf})](\text{OTf})$  complex is five-coordinate in the crystalline solid with the OTf ligand bound on the *syn*- side (**4.6**, Scheme 4.2). The five-coordinate geometry in solution is maintained in solution as evidenced by NMR. The  $^1\text{H}$  NMR ( $\text{CD}_3\text{CN}$ ) spectrum of **4.6** shows only four signals with an intensity ratio of 3:2:1.<sup>17</sup> This observation suggests signal averaging between pairs of diastereotopic protons that result from fast interconversion between **4.6** and **4.7** (Scheme 4.2). The inversion of **4.6** can occur by the OTf anion exchanging

between *syn*- and *anti*- positions. Because of its size, 1-(*tert*-butylsulfonyl)-2-iodosylbenzene favors binding to **4.7** due to the sterically more accessible open site *syn* to the methyl groups (Scheme 4.2), so complex **4.7** forms preferentially over **4.6** in a ratio of about 85:15.<sup>129</sup> The yields of **4.3** and **4.1** suggest that the rate constant of the formation of **4.3** from **4.7** ( $k_3$ ) is at least 6 times faster than the rate constant of **4.1** forming from **4.6** ( $k_4$ ), assuming that  $k_{ii}$  and  $k_{-ii}$  are much faster than  $k_3$  and  $k_4$  and the inversion equilibrium is close to, but less than one, because the OTf ligand in **4.6** is *syn* to the methyl groups (Scheme 4.2). The ~6 times faster rate for  $k_3$  compared to  $k_4$  is a low estimate considering that **4.6** is thermodynamically favored.

**Scheme 4.2:** Proposed  $[\text{Fe}^{\text{IV}}(\text{O})\text{TMC}(\text{CH}_3\text{CN})]^{2+}$  Synthesis Mechanism

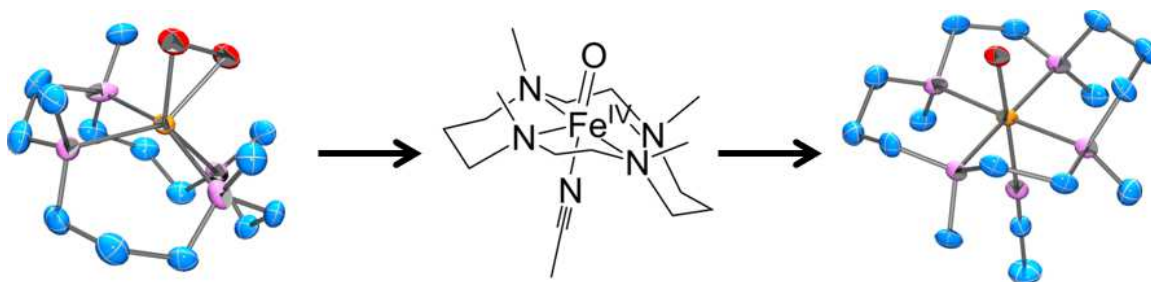


The *syn*-isomer was likely produced in earlier studies and was not recognized. Cho et al. crystallized the  $[\text{Fe}^{\text{III}}(\text{O}_2^{2-})\text{TMC}]^+$  with the peroxo ligand *syn* to the methyl groups of TMC.<sup>116</sup> The resulting ferryl complex formed after O-O bond breaking should have the oxo ligand *syn* to the methyl as in species **4.3**, and the conversion from the ferric-peroxo precursor to the ferryl complex is depicted in Scheme 4.3. The direct conversion of an  $\text{Fe}^{\text{III}}\text{TMC-syn-hydroperoxo}$  species to a ferryl species was also reported in 2011.<sup>117</sup> Although the ferryl species was assumed to be **4.1**, the Mössbauer spectra revealed that this ferryl

species was different. The isomer shifts of **4.1** and the ferryl species produced from the Fe<sup>III</sup>TMC-*syn*-hydroperoxo complex were within the error of the measurement, but their quadrupole splitting values were different, with **4.1** having 1.24 mm/s vs 1.40 mm/s for the Fe<sup>III</sup>TMC-*syn*-hydroperoxo-derived ferryl complex. This new species has a quadrupole splitting closer to **4.3** ( $\Delta E_Q = 1.51$  mm/s). The difference may arise from the presence of water and base in the reaction mixture.<sup>17,115,117</sup>

**Scheme 4.3:** Proposed Ferric-peroxo Precursor to Ferryl Complex Conversion.

The crystal structure of the ferric-peroxo starting material is displayed on the left,<sup>116</sup> and the crystal structure of the ferryl product, **4.1**, is displayed on the right.<sup>17</sup>



An earlier study claimed the synthesis of the *syn*- isomer of **4.1** in 2008;<sup>22</sup> however the composition of this unique ferryl species is now in question. Unlike **4.3**, this complex exhibited near infrared bands at about 800 and 1050 nm. This spectrum can be reproduced by adding [Bu<sub>4</sub>N][F] to a solution of [Fe<sup>IV</sup>(O)(TMC)]<sup>2+</sup> in dichloromethane and is termed **4.1-F** (Figure 4.11).<sup>22</sup> The slow decomposition of the BF<sub>4</sub> counter anion used in the 2008 study is the likely source of F<sup>-</sup>. The large change in the near-infrared band in the electronic

absorption spectrum is reasonable for the substitution of CH<sub>3</sub>CN with F<sup>-</sup>, but the subtle difference in the near-infrared band between **4.1** and **4.3** is more consistent with the slight change in the ligand field between **4.1** and **4.3**.

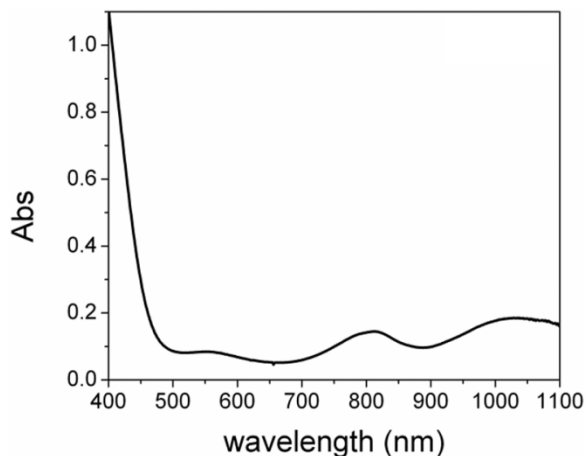


**Figure 4.11:** Resulting electronic absorption spectrum of adding one equivalent F<sup>-</sup> to 1 mM [Fe<sup>IV</sup>(O)TMC(OTf)](OTf) in dichloromethane at -40° C. The double-hump feature in the near-infrared region closely resembles the electronic absorption spectrum of the oxo-iron(IV) species reported in reference 22.

The structure of **4.3<sub>DCM</sub>** provides a steric model to help understand the increased reactivity of **4.3** compared to **4.1**. Steric factors have been shown to affect the reactivity of S = 1 ferryl species, because the frontier molecular orbitals (FMOs) of these species are composed of Fe d<sub>xz,yz</sub> and O p<sub>x,y</sub> orbitals that make up the π\* bond.<sup>130,131</sup> Because the FMOs are off the Fe-O axis, the steric bulk normal to the Fe=O bond plays a significant role in the reactivity of S = 1 ferryl complexes.<sup>131</sup> Space filling models of **4.1** and **4.3<sub>DCM</sub>** are displayed in Figure 4.12 to illustrate the different steric environments of *syn*- and *anti*- isomers. Clearly, the ferryl unit is more open in **4.3<sub>DCM</sub>** as compared to **4.1**. However,

**4.3<sub>DCM</sub>** has a shorter Fe=O bond and additionally, the TMC ligand is forced up by the ligand *trans* to the oxo causing the methyl groups *syn* to the oxo to close slightly. These factors partially counteract the smaller steric bulk of the methyl groups, resulting in a modest increase of the access to the oxo unit of **4.3**.

The solvent exposed areas of **4.1** and **4.3<sub>DCM</sub>** were calculated to be 6.7 and 7.5 Å<sup>2</sup>, respectively by the program PyMOL v1.3r1 and are illustrated in Figure 4.13. This ~12% increase in solvent exposed area of **4.3<sub>DCM</sub>** agrees with the 1.5 times faster C-H bond oxidation rate of **4.3**.(Prakash, MIP) The 800-times-faster thioanisole oxidation rate by **4.3** compared to **4.1** suggests that the solvent exposed area and reaction trajectory are not major factors in oxygen atom transfer reactions and other factors, like decoordination of the *trans* ligand may be more influential.

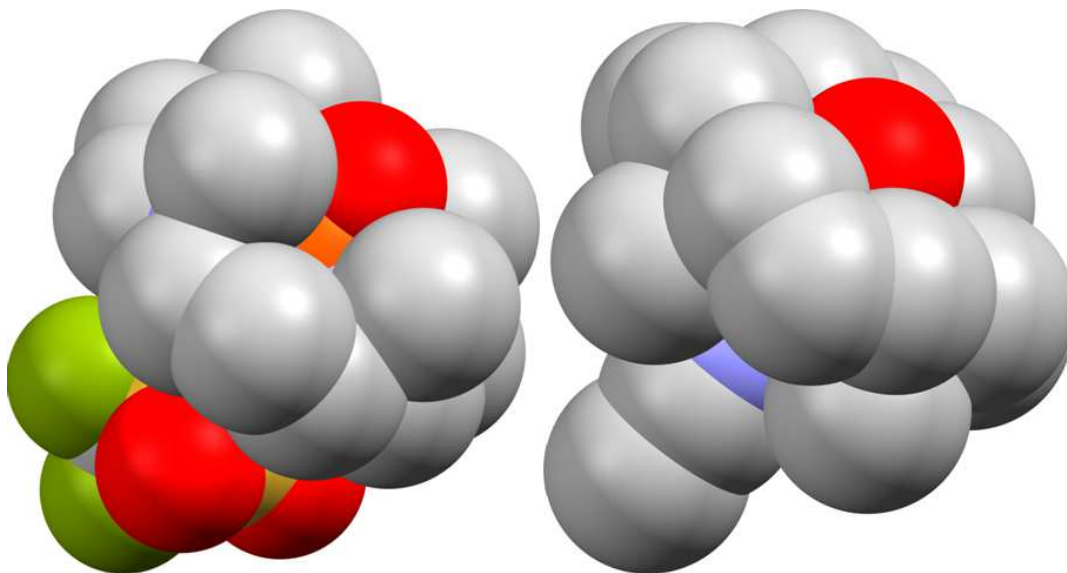


**Figure 4.12:** Space filling models of the complexes **4.3<sub>DCM</sub>** (left) and **4.1** (right).

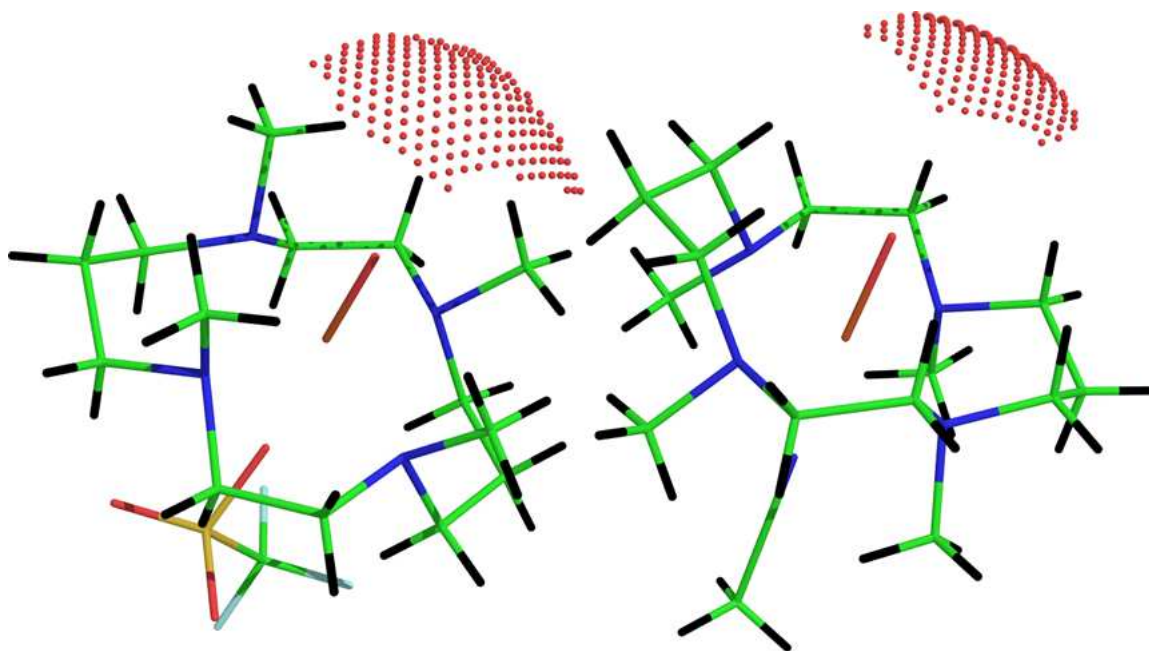


**Figure 4.13:** The solvent exposed areas of **4.3<sub>DCM</sub>** (left) **4.1** (right) illustrated by dots. Values of 7.5 and 6.7 Å<sup>2</sup> were calculated for **4.3<sub>DCM</sub>** and **4.1**, respectively by the program PyMOL v1.3r1.

#### 4.4 Experimental:

##### *X-Ray Diffraction:*

The single crystal X-ray diffraction data of the crystals of **4.2a**, **4.4**, **4.5**, **4.3<sub>DCM</sub>**, **4.6** and **4.8** were collected as previous describe in Chapter 3. Specific data collection, and refinement information are located in Table 4.3. Any non-standard data treatment or refinement information is described below for individual samples.

**Table 4.3:** Crystal structure collection and refinement information of TMC supported compounds

	<b>4.2a</b>	<b>4.4</b>	<b>4.5</b>
Empirical formula	C <sub>24</sub> H <sub>41</sub> F <sub>12</sub> FeN <sub>7</sub> O <sub>13</sub> S <sub>4</sub> Sc	C <sub>16</sub> H <sub>35</sub> Cl <sub>4</sub> Fe <sub>2</sub> N <sub>5</sub> O	C <sub>19</sub> H <sub>33</sub> Cl <sub>3</sub> F <sub>3</sub> Fe <sub>2</sub> N <sub>6</sub> O <sub>4</sub> S
Temp. (K)	102(2)	173(2)	173(2)
$\lambda$ (Å)	0.71073	0.71073	0.71073
Space group	Pbam	P2(1)2(1)2(1)	P2(1)/c
<i>a</i> (Å)	18.0006(13)	12.8738(11)	10.1776(8)
<i>b</i> (Å)	22.0279(15)	12.8805(11)	9.2395(7)
<i>c</i> (Å)	11.4933(8)	14.9102(12)	33.194(3)
$\alpha$ (°)	90	90	90
$\beta$ (°)	90	90	91.9480(10)
$\gamma$ (°)	90	90	90
Z	4	4	4
$\theta$ max (°)	25.37	27.48	26.41
Complete	99.9%	99.9%	100.0%
<i>R</i> (int) <sup>a</sup>	0.0703	0.0342	0.0376
Data	4399	5674	6404
Restraints	547	0	85
Parameters	426	258	425
R1 <sup>b</sup> [I > 2 $\sigma$ (I)]	0.0791	0.0227	0.0473
wR2 <sup>c</sup>	0.2196	0.0517	0.1213
Goof <sup>d</sup>	1.043	1.020	1.028



**Table 4.3 continued**

	<b>4.3<sub>DCM</sub></b>	<b>4.6</b>	<b>4.8</b>
Empirical formula	C <sub>18</sub> H <sub>36</sub> Cl <sub>4</sub> F <sub>6</sub> FeN <sub>4</sub> O <sub>7</sub> S <sub>2</sub>	C <sub>49</sub> H <sub>98</sub> Cl <sub>2</sub> F <sub>18</sub> Fe <sub>3</sub> N <sub>12</sub> O <sub>18</sub> S <sub>6</sub>	C <sub>30</sub> H <sub>68</sub> Cl <sub>6</sub> Fe <sub>3</sub> N <sub>5</sub> O <sub>2</sub>
Temp. (K)	173(2)	173(2)	173(2)
λ (Å)	0.71073	0.71073	0.71073
Space group	P2(1)/n	P-1	P-1
a (Å)	15.896(5)	8.7708(8)	13.5508(13)
b (Å)	12.544(4)	20.3255(19)	14.1408(14)
c (Å)	16.658(8)	23.608(2)	14.4658(14)
α (°)	90	71.5030	111.3430(10)
β (°)	108.575(4)	89.3450(10)	103.7190(10)
γ (°)	90	88.7260(10)	111.2580(10)
Z	4	2	2
θ max (°)	25.05	27.49	25.03
Complete	98.5%	98.9%	99.8%
<i>R</i> (int) <sup>a</sup>	0.0593 <sup>e</sup>	0.0342	0.0361
Data	5489	18152	7690
Restraints	384	466	241
Parameter	497	1114	559
s			
R1 <sup>b</sup> [I > 2σ(I)]	0.0646	0.0690	0.0536
wR2 <sup>c</sup>	0.1482	0.2077	0.1381
Goof <sup>d</sup>	1.041	1.061	1.059

<sup>a</sup>  $R_{\text{int}} = \sum |F_o^2 - \langle F_o^2 \rangle| / \sum |F_o^2|$ , <sup>b</sup>  $R_1 = \sum ||F_o| - |F_c|| / \sum |F_o|$ , <sup>c</sup>  $wR2 = [\sum [w(F_o^2 - F_c^2)^2] / \sum [w(F_o^2)^2]]^{1/2}$  where  $w = q / [\sigma^2(F_o^2) + (a^*P)^2 + b^*P + d + e^*\sin(\theta)]$ , <sup>d</sup>  $\text{Goof} = S = [\sum [w(F_o^2 - F_c^2)^2] / (n-p)]^{1/2}$ , <sup>e</sup> twinned data set,  $R_{\text{int}}$  estimated by TWINABS.<sup>20</sup>

*Structure solution for 4.2a:*

To rule out a lower symmetry space group, the structure was solved using all possible lower symmetry space groups, which resulted in an inferior solution for each case. Additionally, integration on a twinned monoclinic cell was not successful and no satellite reflections (modulated structure) were observed in the reflection data; however due to the disordered solvent channel these reflection would be extremely weak if they were present. Due to these observations, the structure is best modeled with space group  $Pb\bar{a}m$ .

The Fe complex is disordered by a 90 degree rotation over a mirror plane bisecting the Fe-O-Sc axis causing alternating ethylene and propylene groups to be disordered over two positions (Figure 4.14). Only one-half of the molecule is unique, with the other half generated by the mirror operation performed on the second position of the TMC ring two give alternating ethylene and propylene groups (Figure 4.3). If the mirror operates on the same ring, a non-sensible chemical connectivity is produced. The volume occupied by the two carbon chains is very similar and the occupancy of each position refined to a 50.3(4):49.7(4) ratio. Disordered pairs of Fe-N distances were restrained to be equal and allowed to refine freely (DFIX command).<sup>20</sup> The internal symmetry of the Fe complex was utilized and chemically equivalent 1-2 and 1-3 bond distances were restrained to be the same (SAME command).<sup>20</sup> Consistent with the 90° rotation disorder, the two bound triflate anions in the asymmetric unit were disordered over two and four positions, respectively. The Sc-O<sub>OTf</sub> distances were restrained to be the equal and were allowed to refine freely (DFIX

command).<sup>20</sup> The CF<sub>3</sub> group on the triflate disordered over 4 positions was modeled with isotropic displacement parameters. The displacement parameters for all atoms in close proximity were constrained to be the same (EADP command).<sup>20</sup>

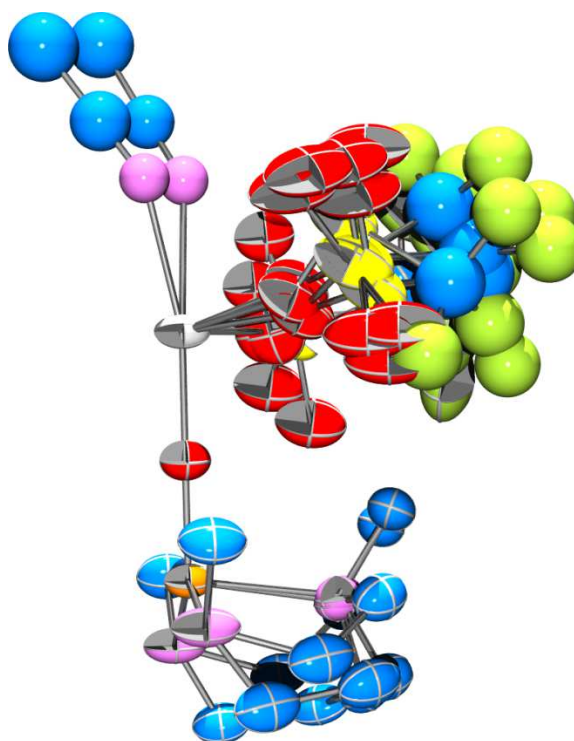


**Figure 4.14:** The mirror bisecting the Fe-O-Sc axis and displaying the main-molecule disorder of **4.2a**.

The 90 degree disorder was also propagated in the apical CH<sub>3</sub>CN molecule bound to the Sc resulting in four positions for the acetonitrile for the Fe complex. The occupancies of the bound CH<sub>3</sub>CN were constrained to 0.25 because it was disordered over a 2/m special position. The four positions of the CH<sub>3</sub>CN molecule were modeled with two CH<sub>3</sub>CN molecules disordered over the

mirror plane with the Part-X statement (Figure 4.15, top), and were modeled with isotropic displacement parameters. The Fe complex packs in a head-to-head arrangement (related by the 2/m special position), and two positions of the bound CH<sub>3</sub>CN are utilized to allow for proper packing with pairs of  $\alpha$ -carbons of CH<sub>3</sub>CN ~3.6 Å apart (Figure 4.15, middle and bottom). The Sc-N<sub>CH<sub>3</sub>CN</sub> distances were restrained to be equal and allowed to refine freely (DFIX command).<sup>20</sup> The pairs of N-C and C-C bond distances of the bound CH<sub>3</sub>CN were restrained to be equal and freely refined to 1.129 Å and 1.445 Å, respectively(DFIX command).<sup>20</sup> Additionally, the sum of the C-N and C-C bonds were restrained to be equal to the N-C( $\alpha$ ) distance to maintain linearity (SUMP command).<sup>20</sup> If the mirror plane was removed, the space group would drop in symmetry to Pba2 and the crystallographic symmetry would be able to accommodate the alternating ethylene and propylene groups of the TMC ligand. However, the two orientations of the Fe complex observed would have to be accommodated by a twinned cell related by a mirror plane perpendicular to the c-axis. However, a meaningful solution in this space group was not obtained taking this into consideration. Therefore the molecules are likely packing in head-to-head pairs in a random order with acetonitrile solvent molecules filling the space between the Fe complexes.

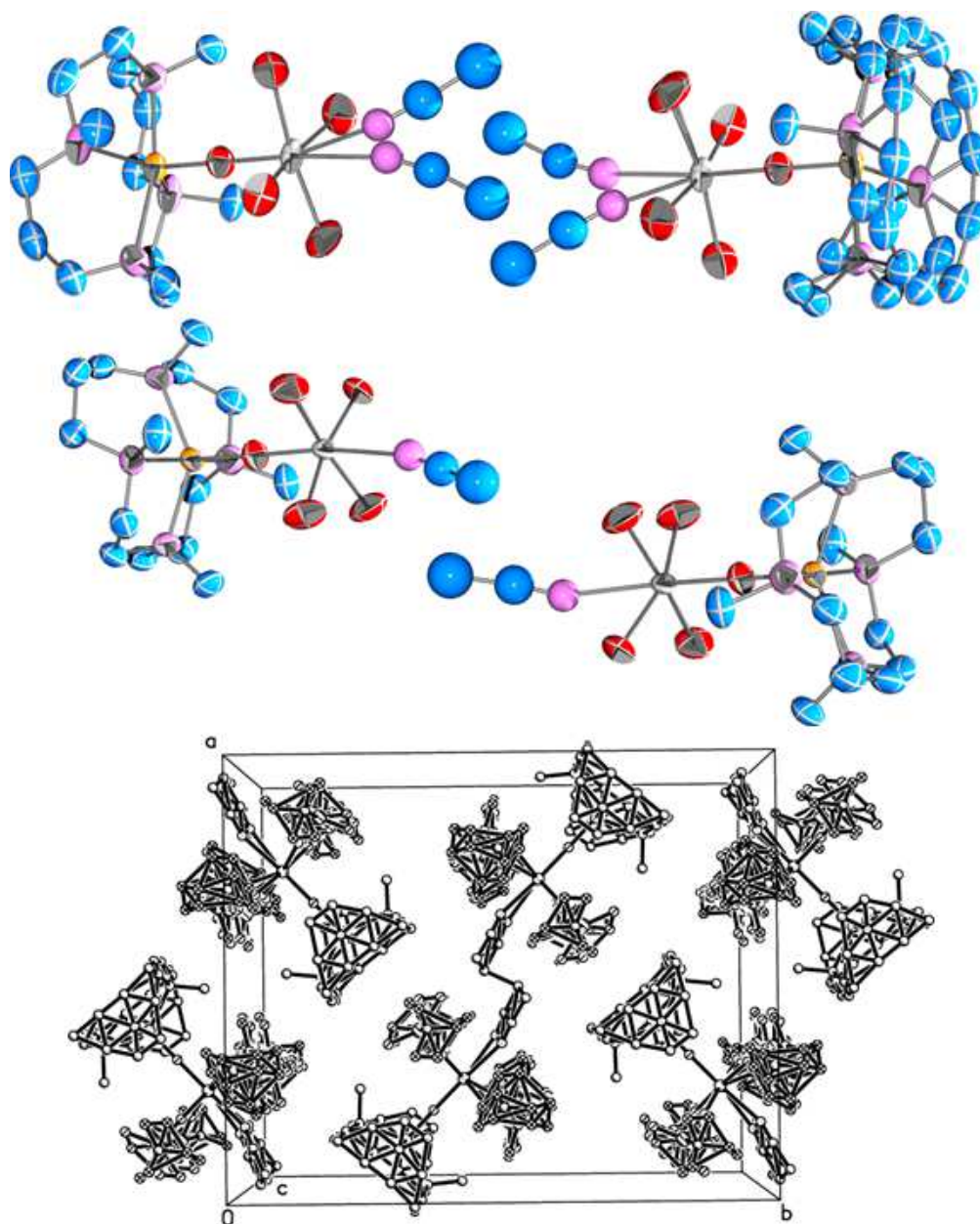


**Figure 4.15:** Disorder modeling of **4.2a**. Thermal ellipsoids are drawn to the 50% probability level and hydrogen atoms and solvent molecules are removed for clarity. Top: Four positions of the Sc-bound acetonitrile ligand. Middle: Pair of **4.2a** with crystallographically reasonable nonbonding distances between acetonitrile ligands; the pairs of  $\alpha$ -carbons are  $\sim 3.6$  Å apart. Bottom: Head-to-head packing diagram of **4.2a** looking down the c-axis.

Additionally, one CH<sub>3</sub>CN solvent molecule was found in the asymmetric unit disordered over four positions in a solvent channel located on the ab plane at c = 0 (Figure 4.16). The occupancies were constrained to 0.25 and refined with isotropic displacement parameters. Hard bond distance restraints were employed with the solvent CH<sub>3</sub>CN molecules using 1.211 Å for the N-C distance and 1.464 Å for the C-C distance and were also restrained to be linear (DFIX & SUMP command).<sup>20</sup> The solvent channels are displayed in Figure 4.16. Figure 4.16 top displays the unit cell looking down the a-axis, with the molecule of interest packed between layers of CH<sub>3</sub>CN. Figure 4.16 bottom is displayed looking down the c-axis with the disordered CH<sub>3</sub>CN molecules colored green. The solvent channel fills the voids between the top layers of the TMC, triflate and bound CH<sub>3</sub>CN ligands in a winding fashion. The different positions of the methyl group of the TMC ligand and the bound triflate create voids which appear to be filled with a solvent molecule. The different positions of the Fe complex and CH<sub>3</sub>CN appear to be correlated; but because of the mirror and 2/m special position, the refinement was not able to relate the partial occupancies with a high degree of certainty.

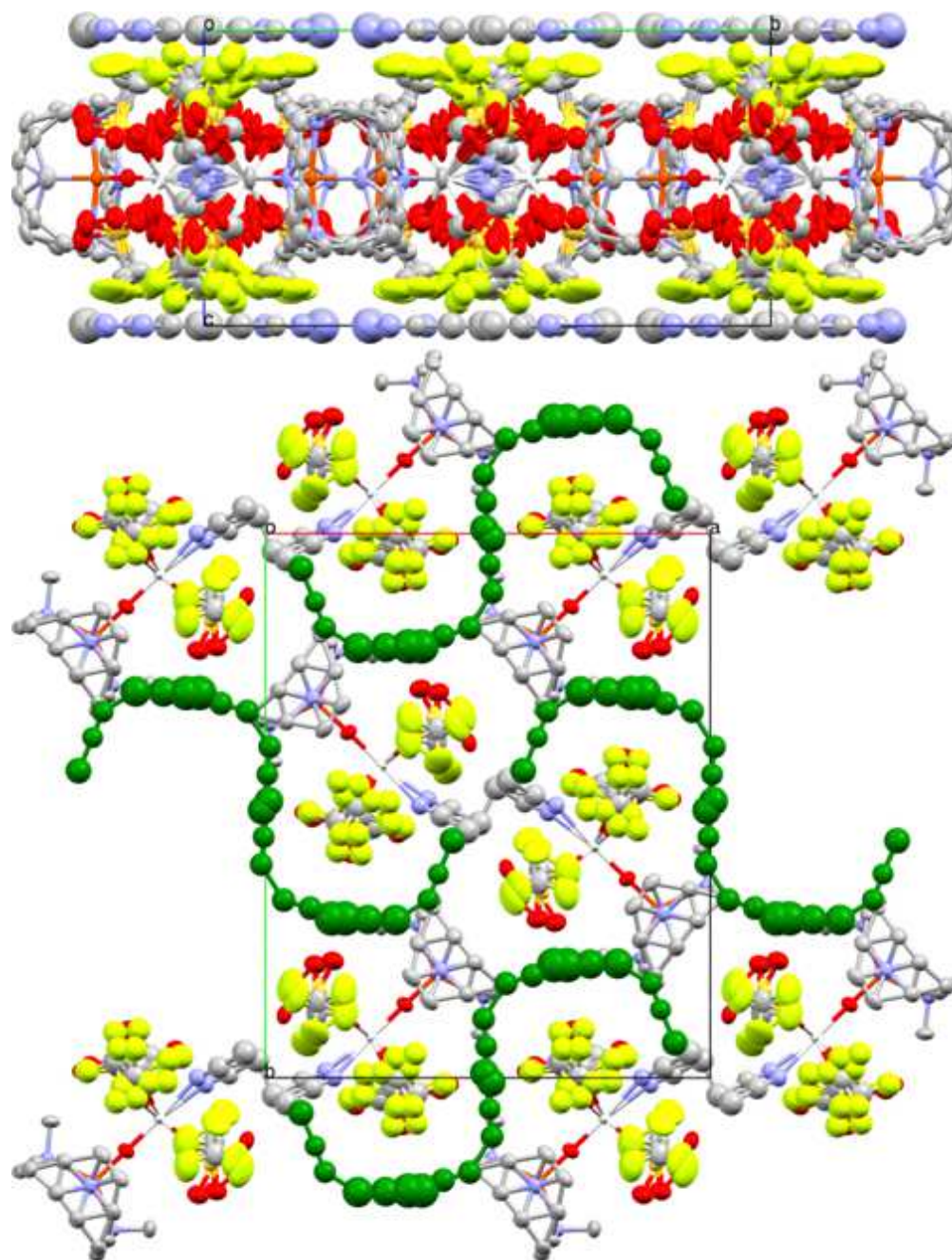


**Figure 4.16:** Packing diagrams of **4.2a**. Thermal ellipsoids drawn to the 50% probability level and hydrogen atoms are removed for clarity. Top: Looking down the a-axis, layers of acetonitrile are visible surrounding a layer of **4.2a**. Bottom: Looking down the c-axis. Acetonitrile solvent molecules are colored green to highlight the solvent channels.

*Refinement of the Crystal Structure of 4.4:*

Refinement of the complex **4.4** was carried out in a routine manner as previously described. The asymmetric unit is displayed in Figure 4.17.

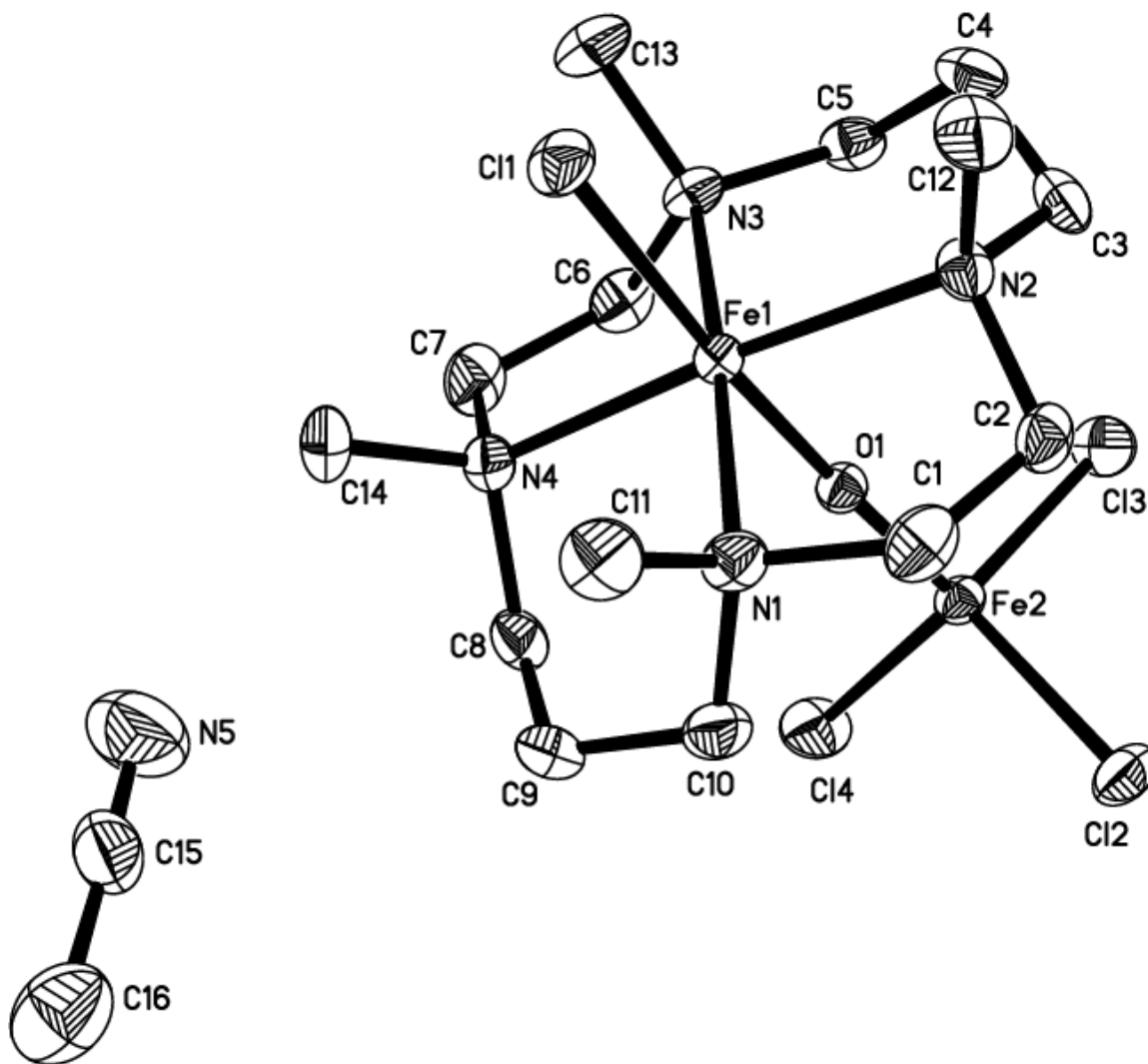


**Figure 4.17:** Asymmetric unit of **4.4** with thermal ellipsoids drawn to the 50% probability level and hydrogen atoms removed for clarity.



#### *Refinement of the Crystal Structure of 4.5:*

Refinement of the complex **4.5** was carried out in a routine manner as previously described. In addition, the OTf counter anion was found to be disordered and was modeled over two positions. All atoms in the two OTf counter anions were restrained to have the same 1-2 and 1-3 bond distances using the SAME command.<sup>20</sup> Symmetry equivalent Fe-N distances (Fe1-{N1, N3} and Fe1-{N2, N4}) were restrained to be equal and allowed to freely refine using the DFIX command.<sup>20</sup> The atoms in the Fe complex were subjected to a rigid bond restraint using the DELU command.<sup>20</sup> Pairs of overlapping atoms in the OTf counter anion were constrained to have equal anisotropic displacement parameters by the EADP command.<sup>20</sup> The asymmetric unit is displayed in Figure 4.18.

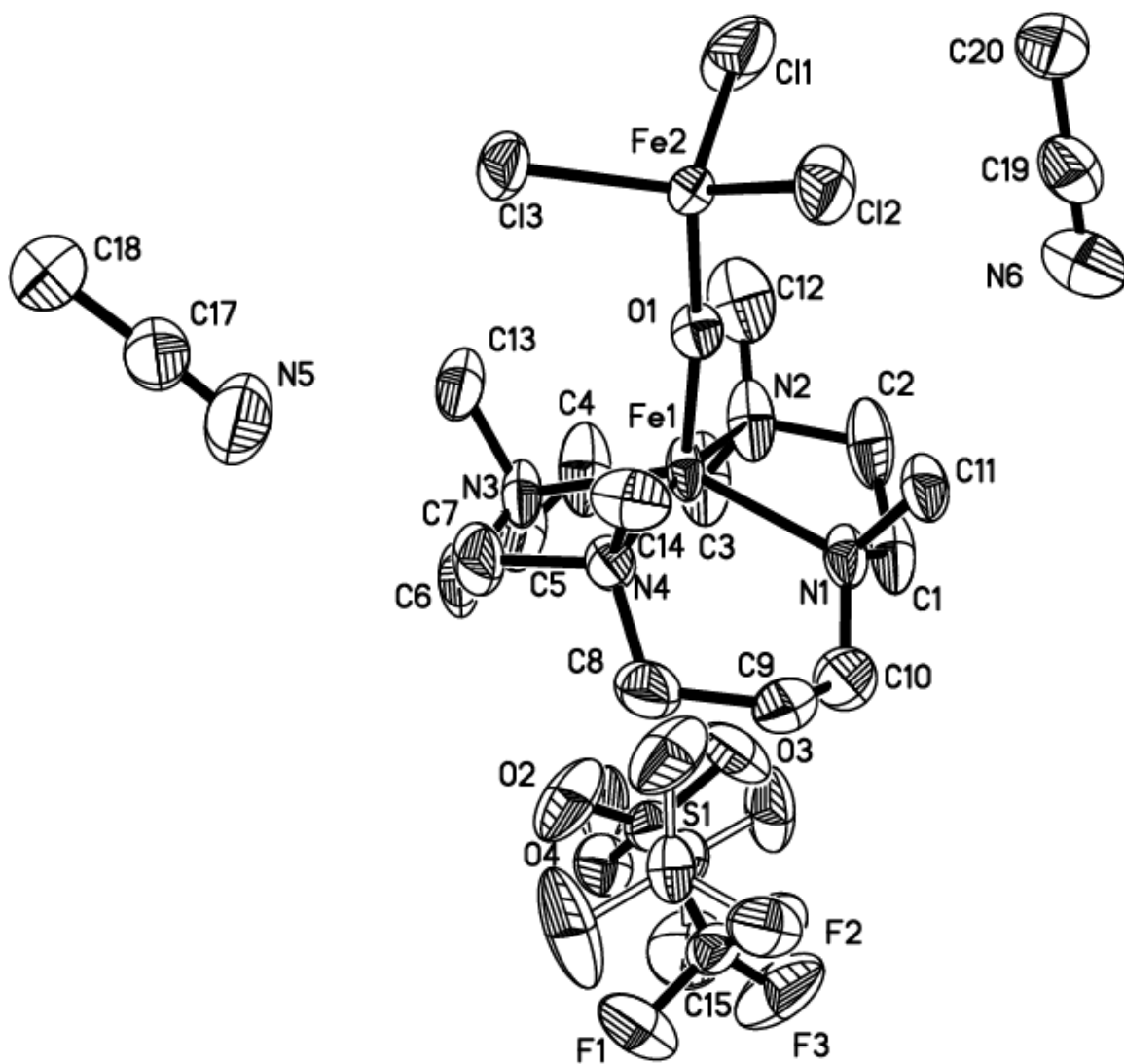


**Figure 4.18:** Asymmetric unit of **4.5** with thermal ellipsoids drawn to the 50% probability level with hydrogen atoms removed for clarity. The two positions of the OTf counter anion are displayed above.

#### *Refinement of the Crystal Structure 4.3<sub>DCM</sub>:*

The data set of 4.3<sub>DCM</sub> was modeled as a non-merohedral twin. The program Cell\_Now<sup>132</sup> was used to find two unit cells related by the twin matrix  $\begin{pmatrix} 0 & 0 & 0 \\ 1 & 0 & -1 \\ 0 & 1 & 0 \\ 0 & 0 & 1 \end{pmatrix}$ , or exchanging the a and c axes. The two major components were integrated separately. The intensity data were corrected for absorption and decay by TWINABS.<sup>101</sup> The data was refined on the major component of the twined data set. Whole molecule disorder was observed with a 90° turn down the Fe-O axis and the two components refined to a 57:43 ratio. The pairs of Fe-oxo and Fe-OTf bonds were restrained to be equal and allowed to freely refine for the two positions of the disordered Fe complex by the DFIX command.<sup>20</sup> Symmetric bonds in the macrocycle were restrained to have the same 1-2 and 1-3 bond distances by the SAME command and a ridged bond restraint was applied to the Fe complex macrocycle by the DELU command.<sup>20</sup> Unreasonable thermal ellipsoids were restrained to be more isotropic by the ISOR command.<sup>20</sup> Additionally, one dichloromethane molecule located on the ab and bc faces was found to be disordered, and the 1-2 and 1-3 bond distances of the disordered dichloromethane were restrained to be equal to the non-disordered dichloromethane molecule in the unit cell by the SAME command.<sup>20</sup> In all disorder modeling, pairs of overlapping atoms were constrained to have equal anisotropic displacement parameters by the EADP command.<sup>20</sup> The asymmetric unit with the disorder is displayed in Figure 4.19.

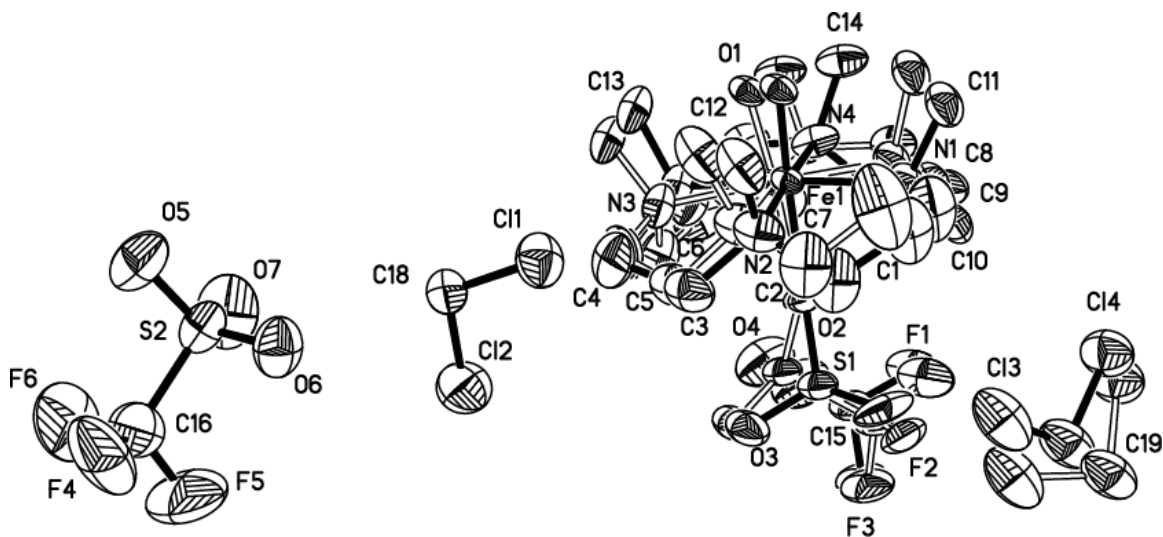


**Figure 4.19:** Asymmetric unit of **4.3<sub>DCM</sub>** with thermal ellipsoids drawn to the 50% probability level and hydrogen atoms removed for clarity. The two positions of the Fe complex and one dichloromethane molecule are displayed above.

#### *Refinement of the Crystal Structure of 4.6:*

Refinement of the complex **4.6** was carried out in a routine manner as previously described. Additionally, one dichloromethane molecule, two OTf counter anions and one of the three iron complexes were disordered and each was modeled over two positions. The OTf counter anion and dichloromethane solvent molecule were modeled in a similar manner as described for the OTf counter anion in structure **4.5**. The disordered iron complex was modeled in a similar manner as the iron complex in **4.3<sub>DCM</sub>**. Bond metrics were reported from the average of the two non-disordered iron complexes due to chemically unreasonable differences in the bond distances of the disordered molecule. The asymmetric unit with the disorder is displayed in Figure 4.20.

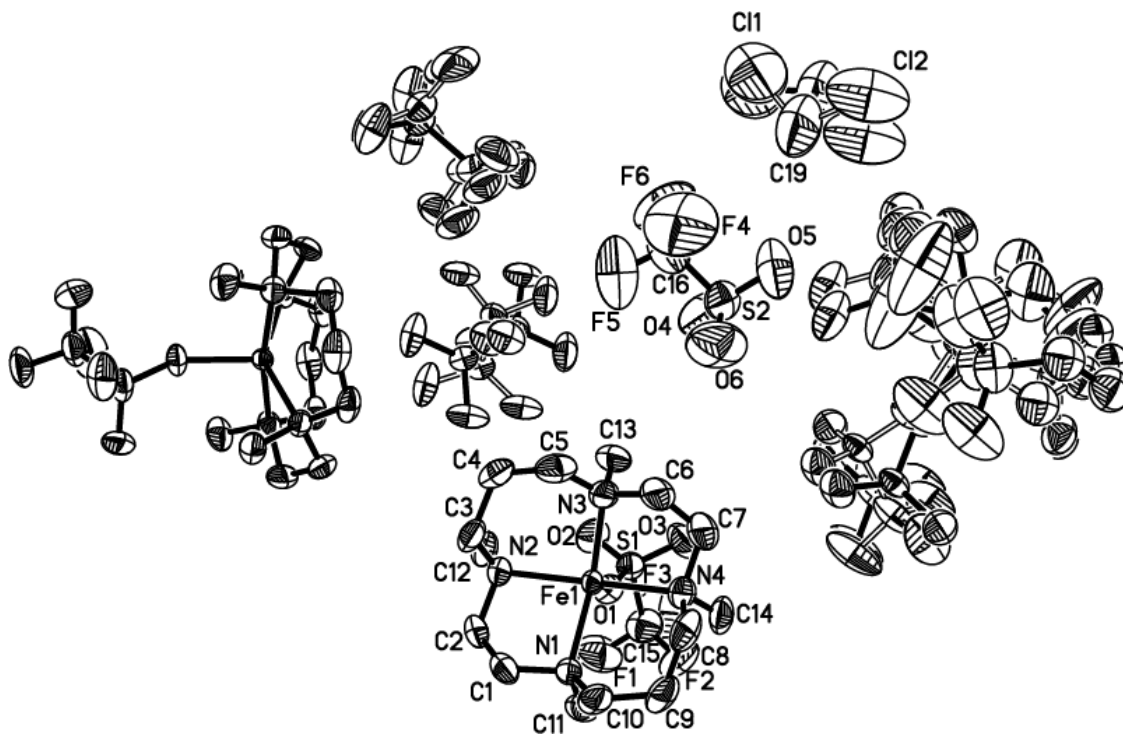


**Figure 4.20:** Asymmetric unit of **4.6** with thermal ellipsoids drawn to the 50% probability level and hydrogen atoms removed for clarity. The two positions one Fe complex, two OTf counter anions and one dichloromethane molecule are displayed above.

Interestingly, three molecules are located in the unit cell, or  $Z' = 3$ , of the structure of **4.6**. Usually if the  $Z'$  is greater than 1, the number will be even. Pseudo symmetry is likely present if the number is odd, and indeed this is the case in the structure of **4.6**. The cell also has angles  $\beta \approx \gamma \approx 90$  and  $b \approx c$  and the unit cell with two asymmetric units is shown in Figure 4.21. Pseudo tetragonal and trigonal cells, complete with -4 or -3 pseudosymmetry operation at  $(0, 0, 0)$ , can be found and is displayed in Figure 4.21. The main deviation from these two symmetries is the  $\alpha$  angle at  $\sim 70^\circ$ . If  $\alpha$  increases to  $90^\circ$ , the symmetry can approximate tetragonal and if the  $\alpha$  angle decreases to  $60^\circ$ , the symmetry approximates trigonal.

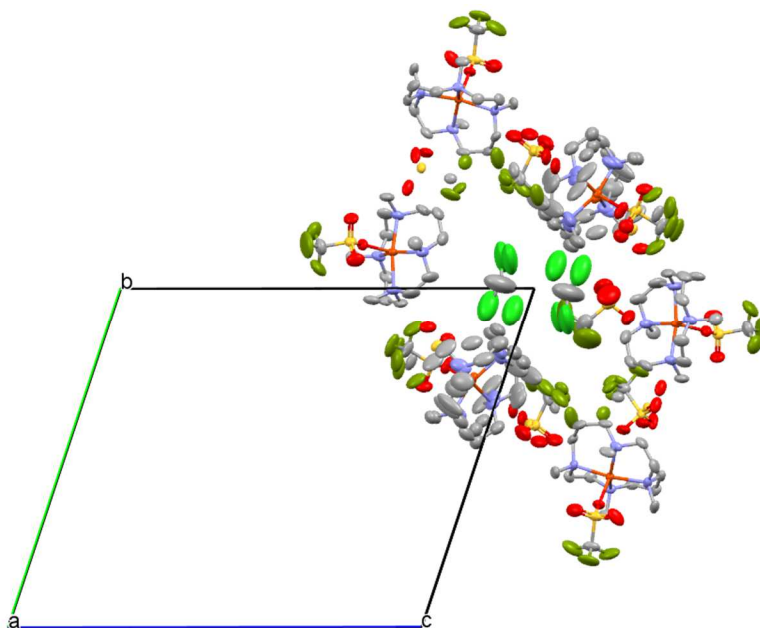


**Figure 4.21:** Unit cell of **4.6** displayed looking down the a-axis. A group of six Fe complexes are located around a pseudo-rotation element at (0, 0, 0).

*Refinement of the Crystal Structure of 4.8:*

Refinement of the complex **4.8** was carried out in a routine manner as previously described. Additionally, the  $[\text{Bu}_4\text{N}]^+$  counter cation was disordered and modeled over two positions similar to the OTf counter anion in the structure of **4.5** and **4.6**. The molecule of interest was also disordered and modeled by a non-crystallographic 2-fold rotation axis which bisected the N1-Fe1-N3 axis. This resulted in a analogous disorder as **4.3<sub>DCM</sub>** and was modeled in a similar fashion. Fe-Cl and chemically symmetric Fe-N bond distances were restrained to be equal and allowed to freely refine using the command DFIX.<sup>20</sup> The 1-2 and 1-3 bond distances of the Fe2-O2-Fe1-O1-Fe3 units were restrained to equal using the SAME command.<sup>20</sup> The asymmetric unit with the disorder is displayed in Figure 4.22.

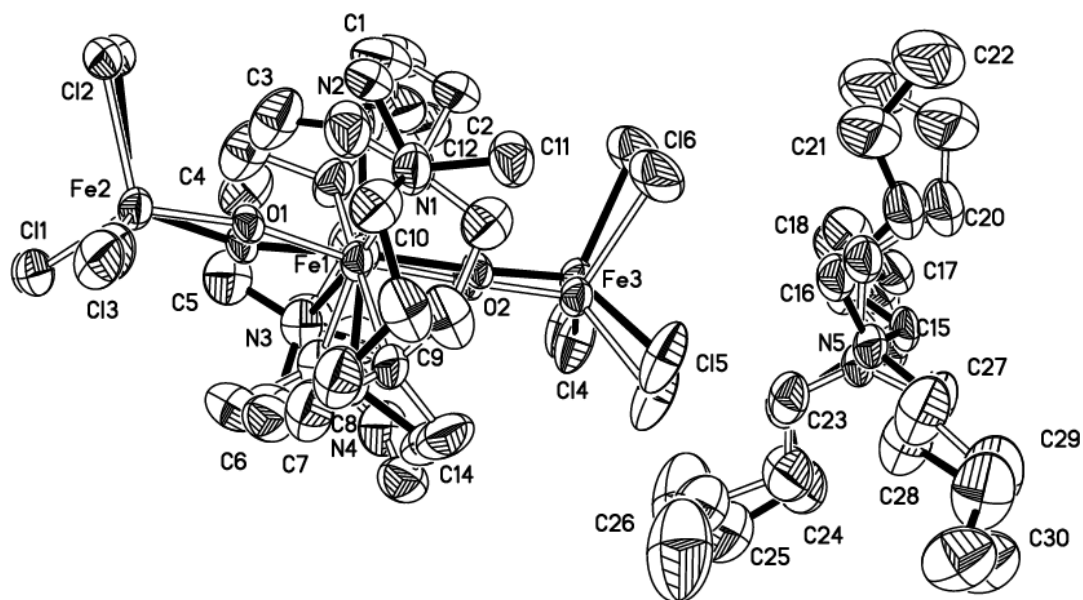


**Figure 4.22:** Asymmetric unit of **4.8** with thermal ellipsoids drawn to the 50% probability level and hydrogen atoms removed for clarity. The two positions of the Fe complex and  $[\text{Bu}_4\text{N}]^+$  are displayed above.

#### *X-ray Absorption Spectroscopy:*

XAS data collected at Stanford Synchrotron Radiation Lightsource in Menlo Park, CA. Data collection and process was performed as previously discussed in Chapter 2. The freeware program Fityk 0.9.8 was used for pre-edge area calculations.<sup>133</sup> The pre-edge peaks were modeled with 50:50 pseudo-Voigt functions and the rising edge was modeled with an additional 50:50 pseudo-Voigt function. The pre-edge area was calculated by multiplying the peak height and full-width-at-half-maximum and the resulting areas were multiplied by 100.





*Chapter 5: The cis- Substitution Effect on Reactivity of S = 2 and S = 1 Ferryl  
Complexes*

## 5.1 Introduction:

Mononuclear nonheme iron enzymes carry out a variety of difficult C-H bond oxidation reactions via an  $S = 2$  ferryl moiety, which has been trapped for some enzymes.<sup>1</sup> However, most model complexes synthesized so far have an  $S = 1$  spin state.<sup>37</sup> High-spin ferryl complexes are implicated as stronger oxidants than their  $S = 1$  ferryl complexes due to exchange stabilization of the high-spin ferric transition state.<sup>76</sup> There is little experimental data corroborating the higher reactivity of synthetic  $S = 2$  ferryl compounds. The most compelling data thus far in support of this notion was observed between a pair of diiron complexes, where a  $[\text{HO-Fe}^{\text{III}}\text{-O-Fe}^{\text{IV}}\text{=O}]^{2+}$  complex was found to be about 1000 times more reactive than the  $[\text{HO-Fe}^{\text{IV}}\text{-O-Fe}^{\text{IV}}\text{=O}]^{3+}$  complex even though the former complex was one-electron-reduced in oxidation state compared to the latter.<sup>13</sup> The important difference between these two compounds is that the ferryl unit in the  $[\text{HO-Fe}^{\text{III}}\text{-O-Fe}^{\text{IV}}\text{=O}]^{2+}$  species is in the  $S = 2$  state, while the ferryl unit in the  $[\text{HO-Fe}^{\text{IV}}\text{-O-Fe}^{\text{IV}}\text{=O}]^{2+}$  species is in the  $S = 1$  state. This observation supports the DFT-based hypothesis that  $S = 2$  ferryl units are more reactive than  $S = 1$  ferryl units.<sup>76</sup> Additional evidence supporting the superior reactivity of the  $S = 2$  ferryl species was recently published, which reported the fastest rates of cyclohexane oxidation published to date; however, a related  $S = 1$  complex was found to exhibit nearly equal rates.<sup>134,135</sup> The high reactivity of the  $S = 1$  ferryl complex was attributed to a low-lying  $S = 2$  excited state on the reaction path.<sup>135</sup> It would thus be useful to have additional reactivity studies on  $S = 2$  ferryl complexes to clarify the major energetic factors that control reactivity.

The first high spin ferryl species to be thoroughly studied, **5.1** (Figure 5.1), was synthesized using a bulky ligand that enforced a trigonal environment around the Fe center.<sup>112,136</sup> However, unlike what was anticipated, the high-spin ferryl species displayed sluggish reactivity with substrates. The lack of reactivity for **5.1** compared to its  $S = 1$  counterparts was attributed to the bulky nature of the ligand, which hindered substrate access to the oxo group. To improve the reactivity of the trigonal species, one bulky guanidinyl arm from the ligand supporting complex **5.1** was removed, resulting in complex **5.2** (Figure 5.1).<sup>28</sup> Complex **5.2** retained an  $S = 2$  spin state and oxidized the substrates 1,4-cyclohexadiene (CHD) and 9,10-dihydroanthracene (DHA) at rates 15 and 600 times faster, respectively, compared to **5.1**. The increased substrate oxidation rates, especially the substantial increase in the rate for the bulky DHA, were explained by the increased accessibility of the ferryl moiety.<sup>28</sup>

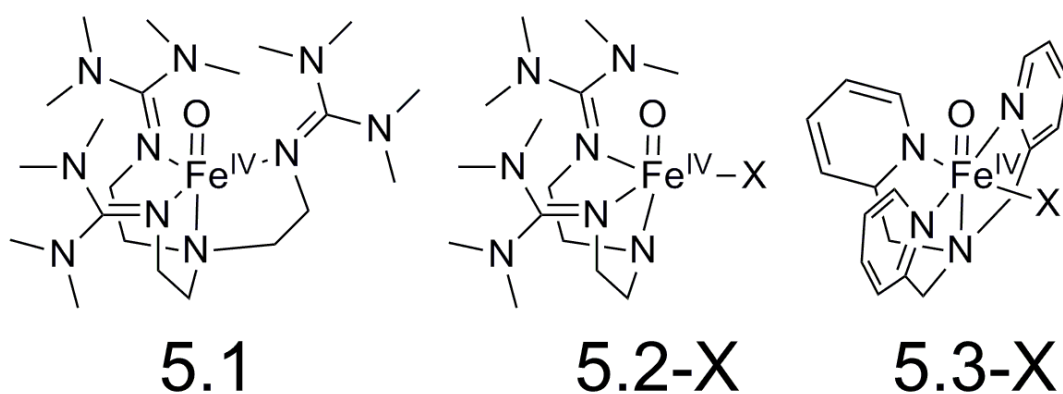


**Figure 5.1:** Nonheme ferryl complexes: left-  $[\text{Fe}^{\text{IV}}(\text{O})\text{TMG}_3\text{tren}]^{2+}$  (**5.1**); center-  $[\text{Fe}^{\text{IV}}(\text{O})\text{TMG}_2\text{dien}(\text{X})]^{2+,+}$  (**5.2-X**),  $\text{X} = \text{CH}_3\text{CN}, \text{Cl}^-, \text{Br}^-, \text{CH}_3\text{CO}_2^-, \text{CF}_3\text{CO}_2^-$  and  $\text{N}_3^-$ ; right-  $[\text{Fe}^{\text{IV}}(\text{O})\text{TPA}(\text{X})]^{2+,+}$  (**5.3-X**),  $\text{X} = \text{CH}_3\text{CN}, \text{Cl}^-, \text{CH}_3\text{CO}_2^-, \text{CF}_3\text{CO}_2^-$ .  $\text{TMG}_3\text{tren} = 1,1,1\text{-tris}\{2\text{-}[\text{N}_2\text{-}(1,1,3,3\text{- tetramethylguanidino})]\text{ethyl}\}$ amine,  $\text{TMG}_2\text{dien} = 1,1\text{-bis}\{2\text{-}[\text{N}_2\text{-}(1,1,3,3\text{- tetramethylguanidino})]\text{ethyl}\}$  methylamine,  $\text{TPA} = \text{tris}(2\text{-pyridylmethyl})\text{amine}$ .

The ferryl complex (**5.2**) has an exchangeable site *cis* to the oxo ligand, which can be systematically varied to perturb the electronic environment of the Fe center. Previous ligand substitution studies of ferryl complexes have reported increases in the rates of substrate oxidation.<sup>75,137–139</sup> Interestingly, *cis* and *trans* ligand substitutions in ferryl complexes have caused opposite trends in the substrate oxidation rates of  $S = 1$  nonheme ferryl complexes, with more electron-donating *trans* ligands accelerating substrate oxidation rates and more electron-donating *cis* ligands decreasing the rate of substrate oxidation.<sup>137,138</sup> Complex **5.2** presents the first opportunity to study how *cis* substitutions will affect substrate oxidation reactivity for a series of  $S = 2$  ferryl complexes.

## 5.2 Results and Discussion:

Because  $\text{TMG}_2\text{dien}$  is a facially-coordinating tridentate ligand, **5.2** has an exchangeable site *cis* to the oxo ligand, and its acetonitrile ligand can be substituted with Lewis bases after the formation of the ferryl complex (Figure 5.1).<sup>28</sup> The substitution was typically accomplished by treatment of **5.2** with two equivalents of the desired Lewis base ( $\text{X}$ ),<sup>28</sup> which resulted in an immediate shift

in the characteristic near-infrared band of **5.2**, representing the formation of the new species **5.2-X** (Figure 5.2). One equivalent of the oxidant 1-(*tert*-butylsulfonyl)-2-iodosylbenzene (<sup>s</sup>ArIO) was used to synthesize **5.2**, compared to the 2.5-3 eq of <sup>s</sup>ArIO used to synthesize **5.2** in the original report.<sup>28</sup> When excess oxidant was used in substrate oxidation reactions, the near-infrared band did not decay in a manner that could be modeled with a single exponential function. When only one equivalent of <sup>s</sup>ArIO was used in the synthesis of **5.2**, the near-infrared absorption features of **5.2** or the **5.2-X** species were red-shifted compared to the species formed from excess <sup>s</sup>ArIO.

Six TMG<sub>2</sub>dien-supported ferryl species were investigated. In addition to the previously published Cl<sup>-</sup> and N<sub>3</sub><sup>-</sup> species,<sup>28</sup> the Br<sup>-</sup>, acetate (OAc) and CF<sub>3</sub>CO<sub>2</sub><sup>-</sup> species were synthesized and the spectra are displayed in Figure 5.2. Complex **5.2-OAc** exhibits the most significant change in the near-infrared band, red-shifting almost 100 nm from the 824 nm band of **5.2** to 919 nm for **5.2-OAc**; other anions gave rise to intermediate shifts that are listed in Table 5.1. Interestingly, the electronic absorption spectrum of **5.2-N<sub>3</sub>** closely resembled that of **5.1**, with a visible feature around 410 nm and a double-humped near-infrared feature that was shown to arise from Fano interference in the case of **5.1**.<sup>131</sup> The red shift of the **5.2-X** spectra suggests a weakening of the ligand field splitting that may reflect the *pi*-donor characteristics of the halogen and carboxylate ligands. The Mössbauer spectra of the **5.2-X** family of complexes displayed quadrupole doublets with isomer shifts close to 0.1 mm/s and quadrupole

splitting values  $\sim |0.3|$  and  $|0.6|$  mm/s.<sup>xi</sup> When subjected to an applied magnetic field, these species gave rise to a more complex magnetic hyperfine splitting pattern consistent with an  $S = 2$  spin state (Table 5.1).<sup>28</sup>

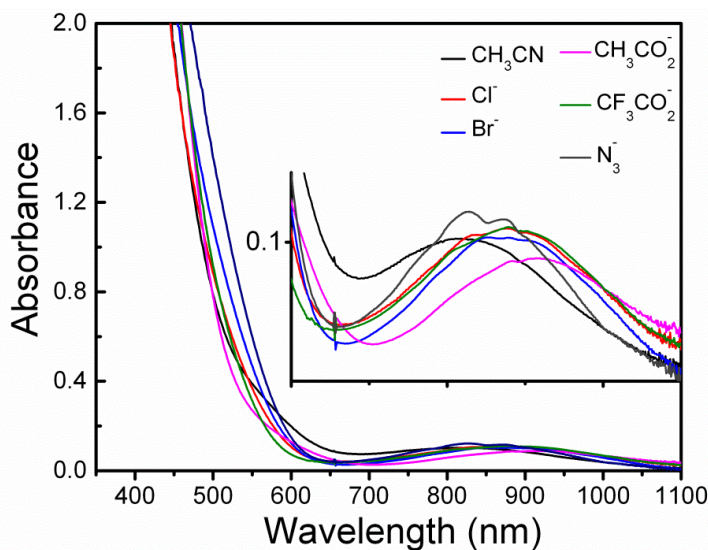


**Figure 5.2:** Electronic absorption spectra of **5.2** (black), **5.2-Cl** (red), **5.2-Br** (blue), **5.2-OAc** (magenta), **5.2-O<sub>2</sub>CCF<sub>3</sub>** (green) and **5.2-N<sub>3</sub>** (grey) in a 0.4 mM [Fe] CH<sub>3</sub>CN solution at -30° C.

<sup>xi</sup> Samples for Mössbauer analysis were prepared by Dr. Jason England and analyzed by the Eckard Münck group at Carnegie Mellon University in Pittsburgh PA and the spectra of CH<sub>3</sub>CN, Cl<sup>-</sup> and N<sub>3</sub><sup>-</sup> were originally reported in reference 28.

**Table 5.1:** Spectroscopic Parameters of Fe<sup>IV</sup>(O)L(X) Complexes and Second-Order Rate Constants for the Oxidation of Triphenylmethane.

L =TMG <sub>2</sub> dien	$\lambda$ [nm, ( $\epsilon$ [M <sup>-1</sup> cm <sup>-1</sup> ]) <sup>a</sup>	$\Delta E_Q$ [mm/s]	$\delta$ [mm/s]	$k_2$ <sup>d</sup> (M <sup>-1</sup> s <sup>-1</sup> )
CH <sub>3</sub> CN <sup>b</sup>	824 (270)	0.58	0.078	0.20
N <sub>3</sub> <sup>-b</sup>	828 (290), 875 (275)	0.30	0.115	0.21
Br <sup>-</sup>	877 (270)	0.41	0.084	0.78
Cl <sup>-b</sup>	879 (290)	0.41	0.084	0.90
CF <sub>3</sub> CO <sub>2</sub> <sup>-</sup>	881 (290)	-	-	2.1
OAc <sup>-</sup>	914 (230)	0.33 -0.59	0.13 0.14	3.0
L =TPA				
CH <sub>3</sub> CN <sup>c</sup>	700 (300)	0.92	0.01	0.11
CF <sub>3</sub> CO <sub>2</sub> <sup>-c</sup>	722 (300)	0.92	0.02	0.04
CH <sub>3</sub> CO <sub>2</sub> <sup>-</sup>	753 (200)	-	-	0.53
Cl <sup>-c</sup>	760 (200)	0.95	0.04	0.70

<sup>a</sup>  $\epsilon$  values determined by comparing to the published band intensity of the starting material **5.2** or **5.3**. <sup>b</sup> originally reported in reference 28. <sup>c</sup> originally reported in reference <sup>140</sup>. <sup>d</sup> Triphenylmethane oxidations performed under pseudo-first order conditions in 0.2-1.0 mM [Fe] in acetonitrile.

The substrate C-H bond oxidation rates of the *cis*-substituted trigonal bipyramidal complexes were investigated. The reactions were carried out in acetonitrile solutions at -30° C under pseudo-first-order conditions. Observed rate constants ( $k_{obs}$ ) were extracted from single exponential fits to the decay of the electronic absorption features of the **5.2-X** species under investigation

(Figure 5.3). The first ~10 seconds of the reaction were not modeled in the exponential fit to allow time for the reactants to mix. The plots of  $k_{obs}$  vs. the concentration of triphenylmethane are displayed in Figure 5.4 and the  $k_2$  values are tabulated in Table 5.1. Interestingly, the rate constants of the *cis*-substituted **5.2-X** complexes were up to 15 times faster than the parent complex **5.2**. The faster observed rates of substrate oxidation by the introduction of carboxylate or halogen donors in **5.2-X** suggest that these donors found in the biological system may also play an important role in modulating the reactivity of the ferryl center in the enzyme active site.

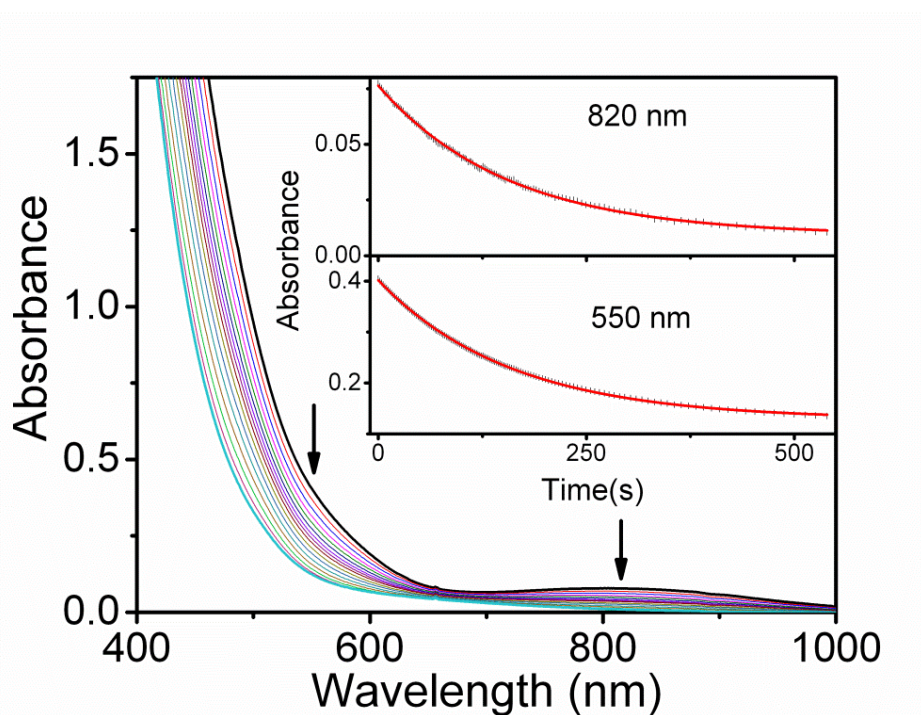


**Figure 5.3:** Decay of the spectrum of **5.2** in the presence of substrate. A single exponential function fit to the time traces at 550 and 820 nm resulted in the same observed rate constant ( $k_{obs}$ ). The spectra and time traces are representative of all kinetic experiments. The first ~10 seconds of the reaction were not modeled in the exponential fit to allow for the reactants to mix.



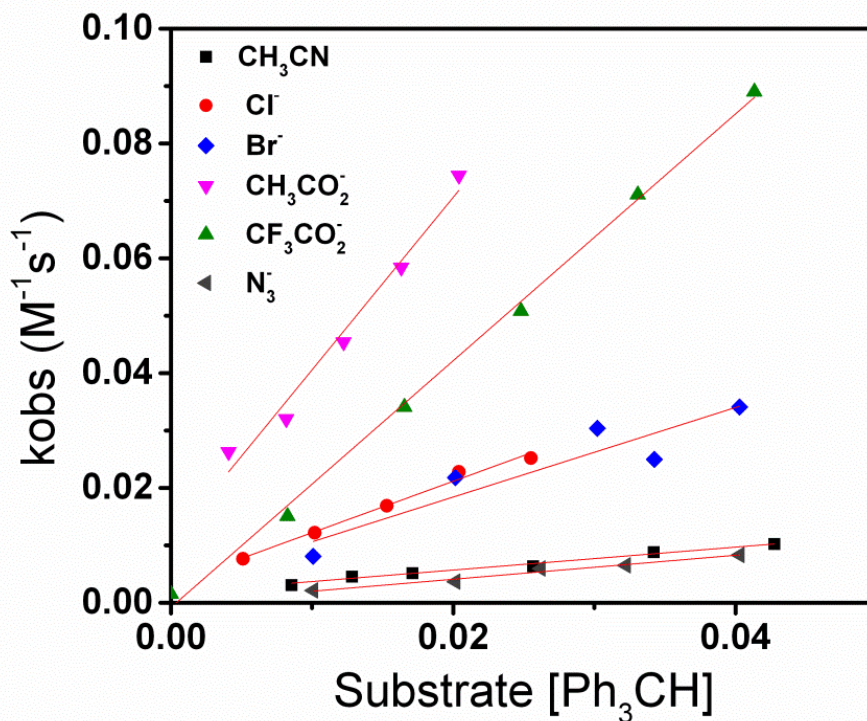


**Figure 5.4:** Observed rate constants of **5.2-X** complexes plotted vs. substrate concentration to obtain second-order rate constants ( $k_2$ ). Triphenylmethane oxidation rate constants were determined for **5.2** (black squares), **5.2-Cl** (red circles), **5.2-Br** (blue diamonds), **5.2-OAc** (magenta down triangles), **5.2-O<sub>2</sub>CCF<sub>3</sub>** (green up triangles) and **5.2-N<sub>3</sub>** (grey left triangles) in a 1 mM [Fe] CH<sub>3</sub>CN solutions at -30° C.

For comparison, the reactivities of the anion-substituted complexes of the  $S = 1$  complex **5.3** were investigated under the same conditions as **5.2-X** to probe a second series of ferryl complexes with a *cis* site available for substitution. The complexes of **5.3-X** with  $X = \text{CH}_3\text{CN}$ ,  $\text{Cl}^-$  and  $\text{CF}_3\text{CO}_2^-$  were previously reported.<sup>140</sup> In the earlier report, peracetic acid was used to form

complex **5.3** followed by addition of the Lewis base to carry out the substitution.<sup>140</sup> In this study, the oxidant <sup>s</sup>ArIO was used to synthesize the parent complex **5.3**, and the  $\lambda_{\text{max}}$  of the near-infrared absorption features of the **5.3-X** were also red-shifted compared to the original report.<sup>140</sup> Along with the previously reported **5.3-X** complexes, the **5.3-OAc** complex is reported here and has a near-infrared band at 753 nm in its electronic absorption spectrum, consistent with previously reported ferryl complexes supported by the TPA ligand.<sup>69,140</sup> Two equivalents of the Lewis base (**X**) were added to the solution of **5.3** and changes in the electronic absorption spectra were observed, consistent with the earlier report (Figure 5.5).<sup>140</sup> The Cl<sup>-</sup> anion caused the largest shift of the near-infrared band in the electronic absorption spectrum of **5.3** from 700 to 760 nm for **5.3-Cl**. Shifts to 722 and 753 nm were observed for **5.3-O<sub>2</sub>CCF<sub>3</sub>** and **5.3-OAc**, respectively (Figure 5.5, Table 5.1).

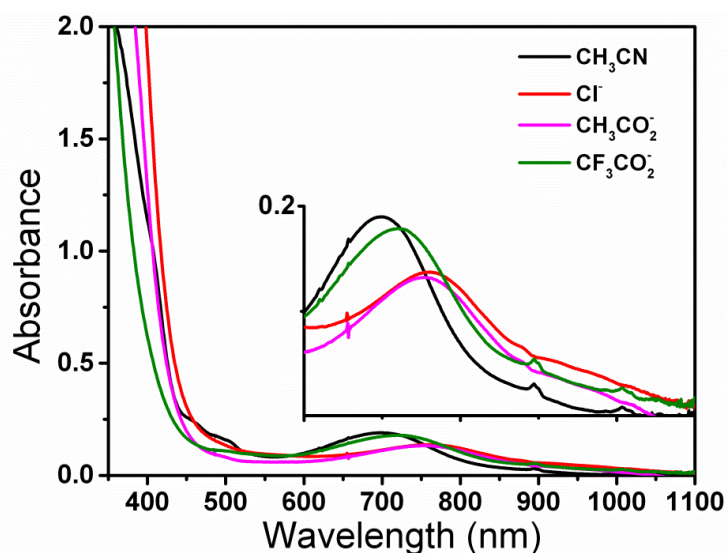


**Figure 5.5:** Electronic absorption spectra of **5.3** (black), **5.3-Cl** (red), **5.3-OAc** (magenta) and **5.3-CF<sub>3</sub>CO<sub>2</sub><sup>-</sup>** (green) in a 0.6 mM [Fe] acetonitrile solution.

The C-H bond cleavage reactivities of the **5.3-X** species were studied in the same manner as **5.2-X**. Plots of  $k_{obs}$  of **5.3-X** species vs. [triphenylmethane] are displayed in Figure 5.6 and rate constants are listed in Table 5.1. The C-H bond oxidation rate constants of **5.3-X** generally increased compared to the parent complex, with a maximum increase of about seven times for the **5.3-Cl** species. Interestingly, **5.2** and **5.3** had similar triphenylmethane oxidation rates as did **5.2-Cl** and **5.3-Cl**, even though each pair consisted of an  $S = 1$  and an  $S = 2$  complex. The *cis* substitution of the  $S = 1$  ferryl complexes induces a similar acceleration as compared to the  $S = 2$  ferryl complexes. This suggests the possibility that similar energetic factors control the reactivity of both  $S = 1$  and  $S = 2$  ferryl complexes.

Previously, the rate of C-H bond oxidation by **5.3** was observed to decrease by about 3 times when more electron donating pyridine-N-oxide ligands were substituted into the *cis* position.<sup>137</sup> The pyridine-N-oxide study is in contrast to the results here, and has subtle differences compared to the **5.3-X** study. Benzyl alcohol was used as the substrate in the 2008 study, which has been known to react differently from hydrocarbon substrates.<sup>9,14,141</sup> Additionally, the pyridine-N-oxide donors used are neutral ligands compared to the anionic ligands in this study.<sup>137</sup>

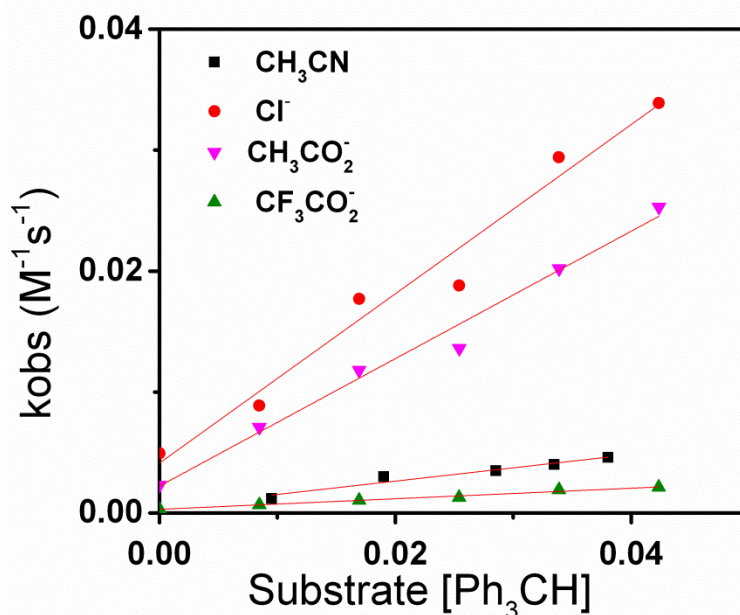


**Figure 5.6:** Observed rate constants of **5.3-X** complexes plotted vs. substrate concentration to obtain second-order rate constants ( $k_2$ ). Triphenylmethane oxidation rate constants were determined for **5.3** (black squares), **5.3-Cl** (red circles), **5.3-OAc** (magenta down triangles) and **5.3-O<sub>2</sub>CCF<sub>3</sub>** (green up triangles) in a 1 mM [Fe] CH<sub>3</sub>CN solutions at -30° C.

Several substrates of varying sizes and bond strengths were investigated to further probe the reactivity of **5.2**. The different substrates were investigated under pseudo-first-order conditions and the results are listed in Table 5.2. An Evans/Polanyi plot was made,<sup>142</sup> with the log of the normalized rate constants ( $k_2'$ , the rate constant is normalized relative to the number of available C-H bonds) plotted vs. the C-H bond dissociation energy (BDE) of the substrate (Figure 5.7). The linear trend over a variety of differently sized substrates suggests that the access to the reactive ferryl unit in **5.2** is not affected by the

steric interactions with the substrate. The slope illustrates that the C-H bond breaking contributes significantly to the reaction barrier. Most nonheme ferryl complexes exhibit a slope of the Evans/Polanyi plot to be between about -0.2 and -0.45: these slopes are smaller than what is seen for **5.2**, which has a slope of -0.56.<sup>14,134,138,143–145</sup> The more negative slope of **5.2** suggests that the substrate energy factors, like BDE, contribute more to the reaction barrier than the energy factors of the ferryl complex. This is why only relatively weak C-H bonds can be broken by **5.2** compared to the other ferryl complexes. A smaller slope of the BDE Evans/Polanyi plot for ferryl complexes is more desirable, because stronger bonds can be oxidized at a faster rate.

**Table 5.2:** Second-order rate constants of substrate oxidation by  $[\text{Fe}^{\text{IV}}(\text{O})\text{TMG}_2\text{dien}(\text{CH}_3\text{CN})]^{2+}$

Substrate	$k_2$ ( $\text{M}^{-1} \text{s}^{-1}$ )	$k_2'$ <sup>b</sup> ( $\text{M}^{-1} \text{s}^{-1}$ )
Cyclohexene	0.085	0.021
Triphenylmethane	0.20	0.20
Fluorene	0.58	0.29
1,4-cyclohexadiene	18 <sup>a</sup>	4.5
9,10-dyhydroanthracene	57 <sup>a</sup>	14

<sup>a</sup> Published in reference 28. Reactions conducted with 0.2-1.0 mM [Fe] in acetonitrile at -30° C. <sup>b</sup>  $k_2'$  values are determined by dividing the  $k_2$  of a reaction by the number of C-H bonds available for oxidation.

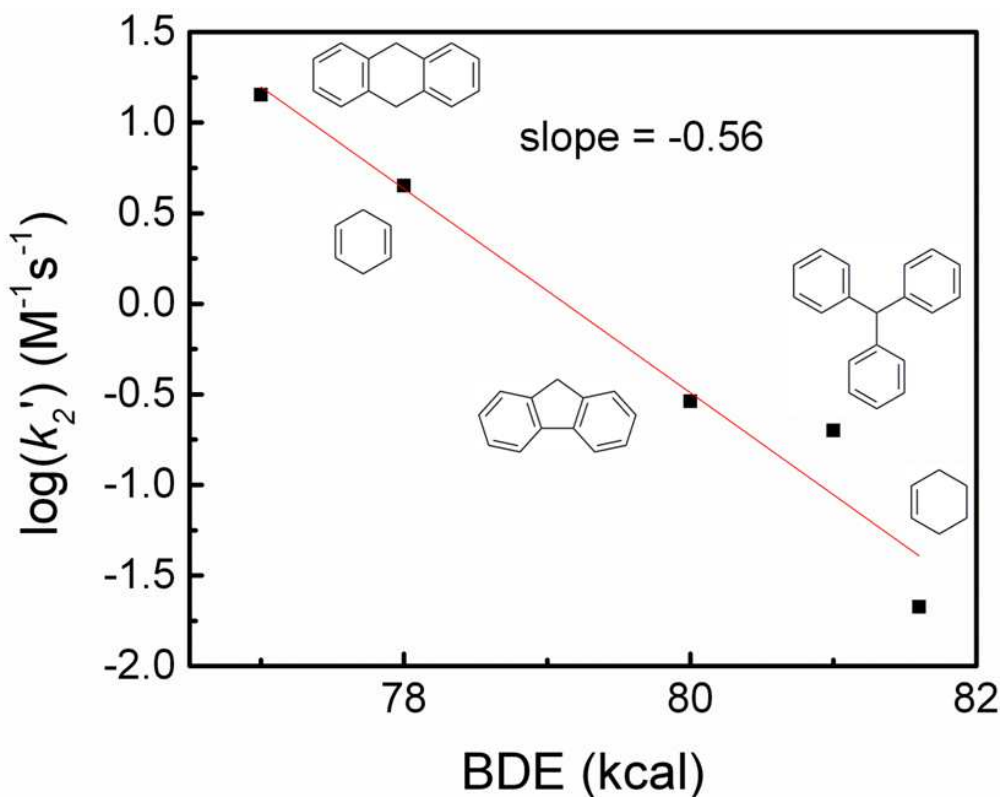


**Figure 5.7:** Normalized second-order rate constants ( $k_2'$ ) of the oxidation of substrates by **5.2** plotted vs. the bond dissociation energy of the substrates.  $k_2'$  values are determined by dividing the  $k_2$  of a reaction by the number of C-H bonds available for oxidation. Reactions were conducted in CH<sub>3</sub>CN at -30° C under pseudo-first-order conditions.

Curiously, a linear correlation was observed when the energy of the near-infrared features in the electronic absorption spectrum of **5.2** and **5.3** were plotted vs. the Gibbs Free energy ( $\Delta G^\ddagger$ ) of triphenylmethane oxidation (Figure 5.8). The  $\Delta G^\ddagger$  values were determined from the rate constant using Transition State Theory (Equation 5.1) and expresses the rate constant ( $k_2$ ) in energy units. Expressing the  $k_2$  in terms of energy, or  $\Delta G^\ddagger$ , allows for comparing the reaction

rate in the same units as the energy variable in question. The slopes for the plots for both **5.2** and **5.3** were 0.39 and 0.34, respectively; however only four points were available for **5.3**. The slopes reveal that the energy changes in the NIR band and the reaction barrier are on the same scale, with about one-third of the energy change in the NIR band reflected in the substrate oxidation reaction barrier. The correlation indicates that the two energy variables are likely connected. Interestingly, the pairs **5.2** and **5.3**, and **5.2-Cl** and **5.3-Cl** have comparable rates of triphenylmethane oxidation, and the energy of the NIR features of the **5.2-Cl** and **5.3-Cl** adducts have comparable changes at about 5 kcal lower than their parent complexes. A comparison to published data of the oxidation of four substrates by the *trans*-substituted  $[\text{Fe}^{\text{IV}}(\text{O})\text{TMC}(\text{X})]^{2+,+}$  ( $\text{X} = \text{CH}_3\text{CN}, \text{CF}_3\text{CO}_2^-$  and  $\text{N}_3^-$ ) nonheme iron complexes found a similar slope for C-H bond oxidation rate – NIR band energy plot.<sup>138</sup> These low-energy transitions observed in the NIR spectrum have been assigned to the transitions within the d-orbital manifold. The C-H bond oxidation rate – NIR band energy correlation suggests the possibility that the difference in the d-orbital energies contributes to the reaction barrier for substrate oxidation.

**Equation 5.1:** Transition State Theory Equations

$$k = \frac{k_{\text{B}}T}{h} \Delta K^{\ddagger} ; \Delta G^{\ddagger} = -RT \ln K^{\ddagger} ; \Delta G^{\ddagger} = -RT \ln \frac{kh}{k_{\text{B}}T}$$

$k$  = rate constant,  $T$  = temperature,  $\Delta G^{\ddagger}$  = Gibbs Free energy of activation,  $R$  = gas constant,  $h$  = Planck's constant,  $k_{\text{B}}$  = Boltzmann constant



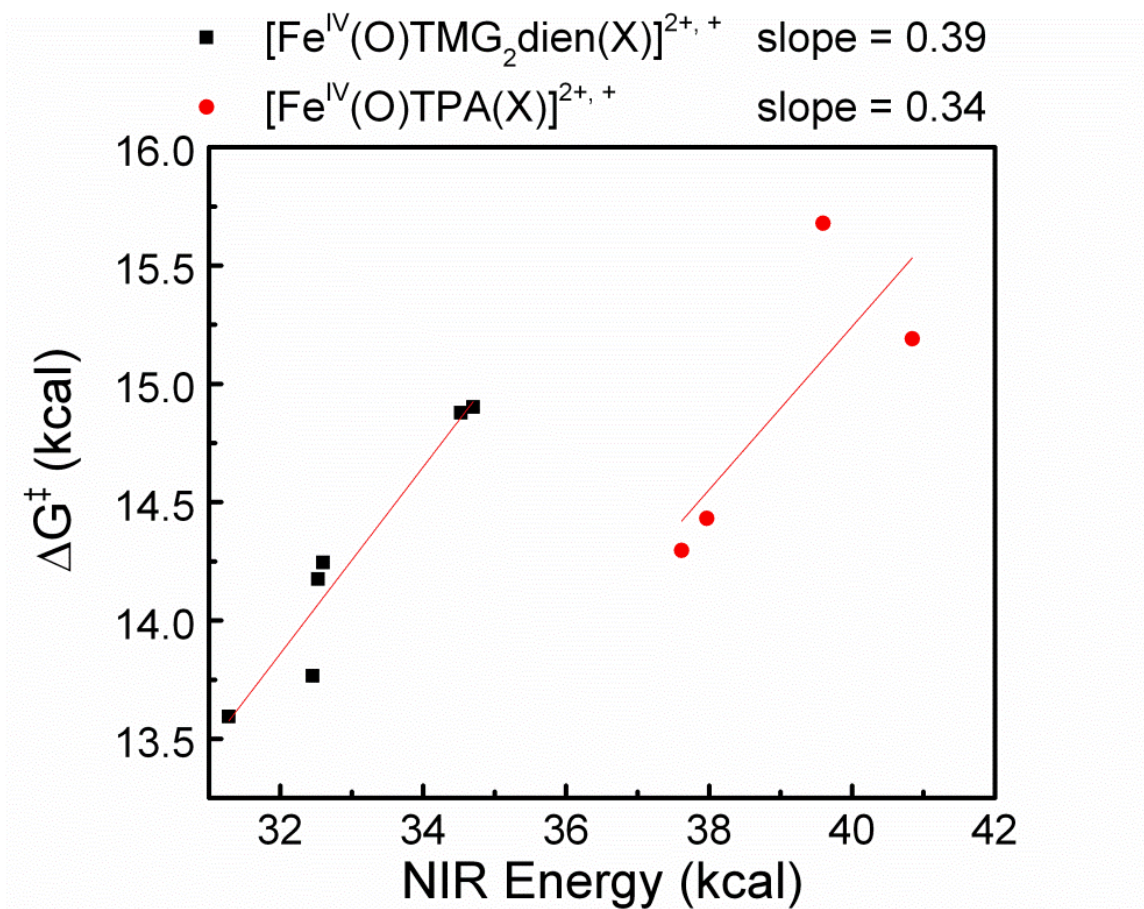


**Figure 5.8:** Gibbs free energy of activation ( $\Delta G^\ddagger$ ) of triphenylmethane oxidation plotted vs. the energy of the near-infra red band of in the electronic absorption spectra of the ferryl complexes **5.2-X** (black squares) and **5.3-X** (red circles).

The oxygen atom transfer (OAT) and hydrogen atom transfer (HAT) abilities of the ferryl complexes were compared. An Eyring analysis for HAT and OAT reactions was completed for complex **5.2**. The observed rate constants of thioanisole and triphenylmethane oxidation by **5.2** were determined as described above and the plots of  $k_{obs}$  vs. concentration of thioanisole at different temperatures are displayed in Figures 5.9 and 5.10 and tabulated in Table 5.3. The enthalpy of activation for the oxidation of thioanisole was 57.4 (4) kJ/mol and



the entropy of activation is -34 (17) J/mol (Figure 5.11), while the enthalpy of activation for the oxidation of triphenylmethane was 22 (2) kJ/mol and the entropy of activation is -165 (9) J/mol (Figure 5.11). The difference in the OAT and HAT activation parameters of **5.2** illustrates the fact that HAT and OAT reactions are governed by different energy contributions. The HAT reactions have a significant entropy contribution, while the OAT reactions are primarily driven by the enthalpy term. The thioanisole oxidation rate by **5.3** was investigated to compare to the rate by **5.2**. Because triphenylmethane HAT rates of **5.2** and **5.3** are similar, understanding the rates of other reactions may provide insight into what energetic factors control the reaction. The rate of thioanisole oxidation by **5.3** was  $0.53 \text{ M}^{-1}\text{s}^{-1}$ , which is over 60 times faster than **5.2** (Figure 5.12, Table 5.3). Even though the HAT rates are similar, the OAT rates differ substantially.

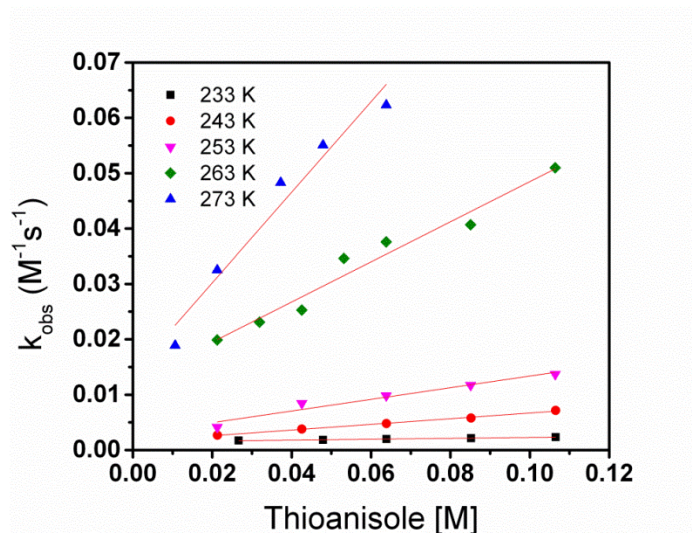


**Figure 5.9:** Observed rate constants ( $k_{obs}$ ) of thioanisole oxidation by **5.2** plotted vs. thioanisole concentration to obtain second-order rate constants ( $k_2$ ). The reactions were in a 0.2-1.0 mM [Fe] acetonitrile solutions.

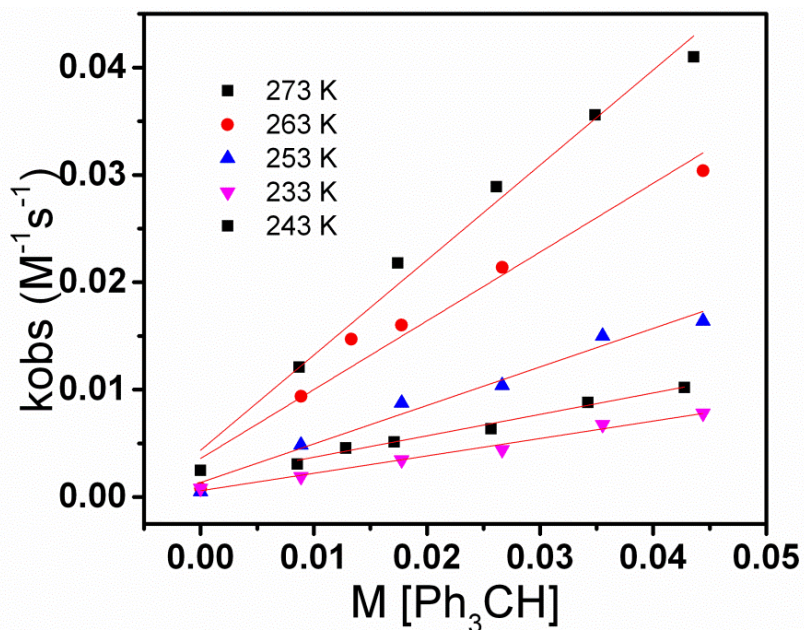


**Figure 5.10:** Observed rate constants ( $k_{obs}$ ) of triphenylmethane oxidation by **5.2** plotted vs. triphenylmethane concentration to obtain second-order rate constants ( $k_2$ ). The reactions were in a 0.2-1.0 mM [Fe] acetonitrile solutions.

**Table 5.3:** Second-order rate constants for substrate oxidation rates

Temperature (K)	PH <sub>3</sub> CH	PhSMe
		$k_2$ (M <sup>-1</sup> s <sup>-1</sup> )
273	0.89	0.82
263	0.64	0.36
253	0.36	0.11
243	0.20	0.051
233	0.16	0.0080
[Fe <sup>IV</sup> (O)TPA(CH <sub>3</sub> CN)] <sup>2+</sup>		
233	-	0.53
Reactions conducted with 0.2-1.0 mM [Fe] in acetonitrile under pseudo-first-order reaction conditions.		

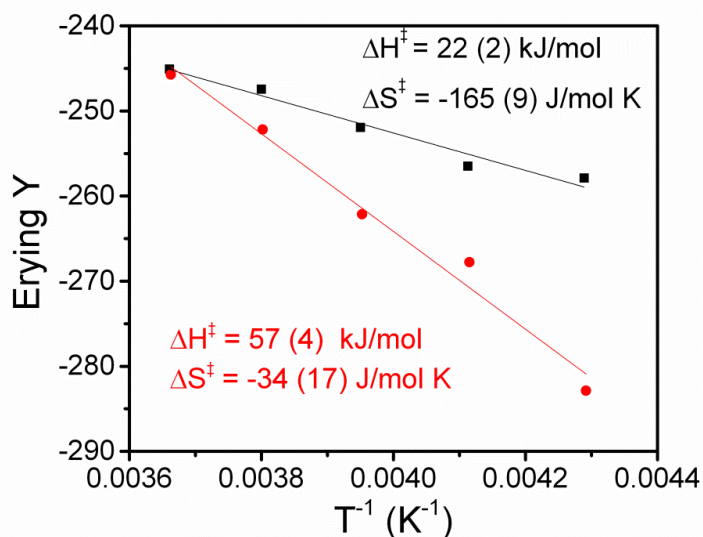


**Figure 5.11:** Eyring plot of the oxidation of thioanisole (red circles) and triphenylmethane (black squares) by **5.2** in a 0.2-1 mM [Fe] acetonitrile solution between 233-273 K. Eyring Y axis is equal to  $R(\ln(k \cdot h \cdot k_B^{-1} \cdot T^{-1}))$  with the variables defined in equation 5.1.

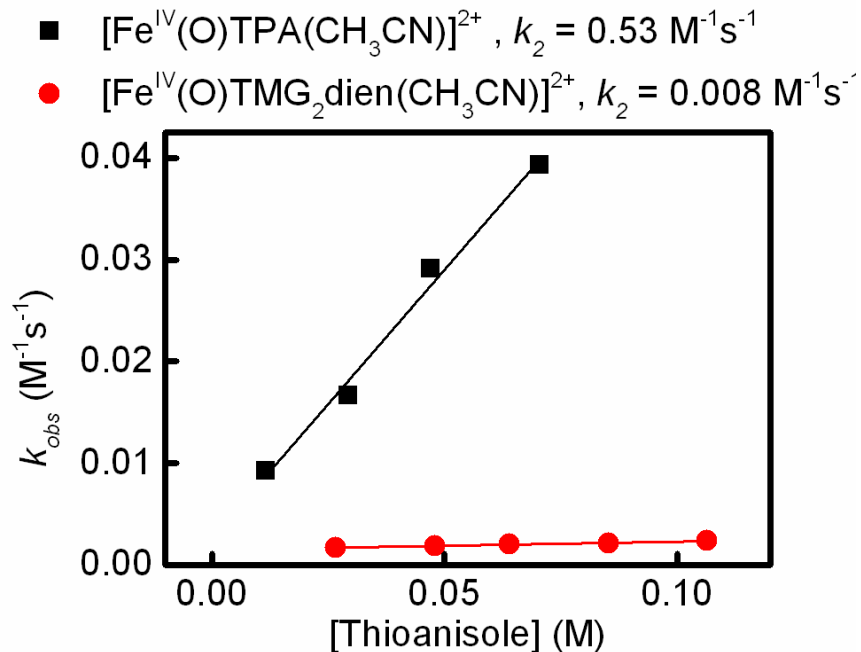


**Figure 5.12:** Oxidation of rates of thioanisole by **5.2** (red dots) and **5.3** (black squares) in a 1 mM [Fe] acetonitrile solution at  $-40^\circ \text{C}$ .

The electrochemical behavior of the ferrous precursor of **5.2** was measured by cyclic voltammetry (Figure 5.13) A quasi-reversible wave was observed at high scan rates where the reduction peak nearly matched the intensity of the oxidation peak. However this match deteriorated at lower scan rates, suggesting the possibility of an electron-transfer-chemical-reaction mechanism. An  $\text{Fe}^{\text{III}}/\text{Fe}^{\text{II}}$  couple of 450 mV vs  $\text{Fc}^{+/0}$  was estimated by taking the average of the cathodic and anodic peak currents, which was very close to the previously published value of 460 mV for **5.3**.<sup>61</sup> The  $\text{Fe}^{\text{III}}/\text{Fe}^{\text{II}}$  redox couples of the ferrous starting materials of a series of ferryl complexes supported pentadentate ligands correlated well with their  $k_2$  values for thioanisole oxidation.<sup>23</sup> These previously published values are plotted in Figure 5.14 (black squares),<sup>23</sup> and in addition, the ferrous precursors of **5.2** and **5.3** are plotted for comparison (Figure 5.14, red circles). Interestingly, the thioanisole  $k_2$  – redox potential correlation from a 2013 study<sup>23</sup> predicts a much higher redox potential for the ferrous precursors of **5.2** and **5.3** than what was experimentally observed. Even more interesting is the substantial difference between the thioanisole oxidation rates of **5.2** and **5.3**, despite having comparable  $\text{Fe}^{\text{III}}/\text{Fe}^{\text{II}}$  potentials. Even though strong correlations of the  $k_2$  values for thioanisole oxidation versus redox potential have been previously seen,<sup>23,113</sup> this correlation does not translate well to different ligand systems.

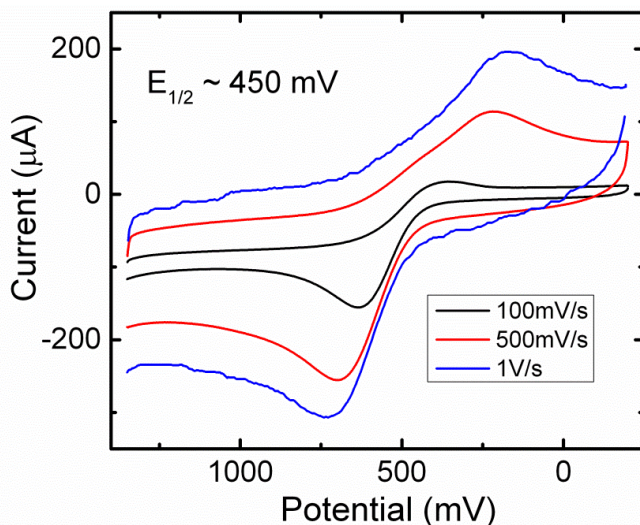


**Figure 5.13:** Cyclic voltammograms of a 1 mM  $[\text{Fe}^{\text{II}}\text{TMG}_2\text{dien}(\text{OTf})_2]$  in acetonitrile (1.0 mM  $[\text{Bu}_4\text{N}][\text{PF}_6]$  as supporting electrolyte) in a  $\text{N}_2(\text{g})$  environment using a glassy carbon working electrode with a Pt wire as the auxiliary and reference electrodes. Potential is referenced to ferrocenium/ferrocene couple.

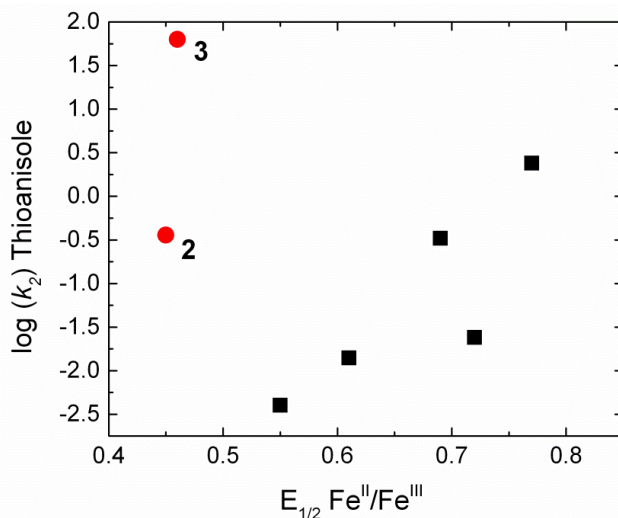


**Figure 5.14:** Plot of the  $\log k_2$  values for the oxidation of thioanisole by nonheme ferryl complexes at  $-10^\circ\text{C}$  vs. the  $E_{1/2}$  of the  $\text{Fe}^{\text{III}}/\text{Fe}^{\text{II}}$  of the Fe starting materials (vs. the ferrocenium/ferrocene couple). Red circles: compounds **5.2** and **5.3**; black squares: nonheme ferryl complexes supported by pentadentate ligands reported in reference 23. The  $k_2$  value for thioanisole oxidation at  $-10^\circ\text{C}$  by species **5.3** was estimated by scaling the rate of thioanisole oxidation of **5.2** at  $-10^\circ\text{C}$  with the ratio of the thioanisole oxidation rates of **5.2** and **5.3** at  $-40^\circ\text{C}$ .

### 5.3 Conclusion:

The substrate oxidation rates of the *cis*- substituted ferryl complexes **5.2-X** and **5.3-X** were investigated. The C-H bond oxidation rates of the pairs **5.2** and **5.3** and **5.2-Cl** and **5.3-Cl** were similar even though their spin states were different, but the thioanisole oxidation rate of **5.3** was found to be more than 60 times greater than that of **5.2**. An interesting correlation between the C-H bond oxidation rates and the near-infrared band in the electronic absorption spectra of **5.2-X** and **5.3-X** species was observed, suggesting the possibility that the difference in the d-orbital energies is reflected in substrate oxidation rate. Many different factors control the HAT rate of nonheme iron complexes, and spin state is not the sole predictor of the oxidation ability of the ferryl species.

### 5.4 Experimental:

#### *Synthesis of Fe compounds:*

$[\text{Fe}^{\text{IV}}(\text{O})\text{TMG}_2\text{dien}(\text{CH}_3\text{CN})]^{2+}$  and  $[\text{Fe}^{\text{IV}}(\text{O})\text{TPA}(\text{CH}_3\text{CN})]^{2+}$  were synthesized using previously reported methods,<sup>28,140</sup> except one equivalent of 1-(*tert*-butylsulfonyl)-2-iodosylbenzene was used as the oxidant in both cases. In a typical experiment, 1.5 – 2 mL of an acetonitrile solution containing 0.2-1.0 mM Fe<sup>II</sup> starting material was prepared in an Ar environment and added to an air-free quartz cuvette. The cuvette was cooled to the desired temperature in a temperature controlled cryostat prior to the addition of one equivalent 1-(*tert*-butylsulfonyl)-2-iodosylbenzene dissolved in about 40  $\mu\text{L}$  of dichloromethane. The formation of the ferryl species was monitored by the electronic absorption

spectrum. After full formation, two equivalents of the desired anion were added to the reaction solution as tetraalkylammonium salts solutions in dichloromethane. Substrates were added as dichloromethane solutions in at least 10 fold excess compared to the Fe concentration.

*Electronic Absorption Spectroscopy:*

The electronic absorption spectra were collected in the same manner as previously described in Chapter 2.

## Bibliography:

1. Costas, M., Mehn, M. P., Jensen, M. P. & Que, L., Jr. Dioxygen Activation at Mononuclear Nonheme Iron Active Sites: Enzymes, Models, and Intermediates. *Chem. Rev.* **104**, 939–986 (2004).
2. Wallar, B. J. & Lipscomb, J. D. Dioxygen Activation by Enzymes Containing Binuclear Non-Heme Iron Clusters. *Chem. Rev.* **96**, 2625–2658 (1996).
3. Solomon, E. I. *et al.* Geometric and Electronic Structure/Function Correlations in Non-Heme Iron Enzymes. *Chem. Rev.* **100**, 235–349 (2000).
4. Hsu, H., Dong, Y., Shu, L., Young, V. G., Jr. & Que, L., Jr. Crystal Structure of a Synthetic High-Valent Complex with an  $\text{Fe}_2(\mu\text{-O})_2$  Diamond Core. Implications for the Core Structures of Methane Monooxygenase Intermediate Q and Ribonucleotide Reductase Intermediate X. *J. Am. Chem. Soc.* **121**, 5230–5237 (1999).
5. Lee, D. *et al.* Formation of Fe(III)Fe(IV) Species from the Reaction between a Diiron(II) Complex and Dioxygen: Relevance to Ribonucleotide Reductase Intermediate X. *J. Am. Chem. Soc.* **121**, 9893–9894 (1999).
6. Slep, L. D. *et al.* Mixed-Valent  $\{\text{FeIV}(\mu\text{-O})(\mu\text{-carboxylato})_2\text{Fe}^{\text{III}}\}^{3+}$  Core. *J. Am. Chem. Soc.* **125**, 15554–15570 (2003).
7. Ghosh, A. *et al.* Catalytically Active  $\mu$ -Oxodiiron(IV) Oxidants from Iron(III) and Dioxygen. *J. Am. Chem. Soc.* **127**, 2505–2513 (2005).
8. Xue, G. *et al.* A synthetic precedent for the  $[\text{Fe}^{\text{IV}}_2(\mu\text{-O})_2]$  diamond core proposed for methane monooxygenase intermediate Q. *Proc. Natl. Acad. Sci. U. S. A.* **104**, 20713–8 (2007).
9. Wang, D., Farquhar, E. R., Stubna, A., Münck, E. & Que, L., Jr. A diiron(IV) complex that cleaves strong C-H and O-H bonds. *Nat. Chem.* **1**, 145–150 (2009).
10. Kodera, M., Itoh, M., Kano, K., Funabiki, T. & Reglier, M. A diiron center stabilized by a bis-TPA ligand as a model of soluble methane monooxygenase: predominant alkene epoxidation with  $\text{H}_2\text{O}_2$ . *Angew. Chemie (Int. ed.)* **44**, 7104–7106 (2005).
11. Kodera, M. *et al.* Reversible O-O bond scission of peroxodiiron(III) to high-spin oxodiiron(IV) in dioxygen activation of a diiron center with a bis-tpa dinucleating ligand as a soluble methane monooxygenase model. *J. Am. Chem. Soc.* **134**, 13236–13239 (2012).
12. Kodera, M. *et al.* Roles of carboxylate donors in O–O bond scission of peroxodi-iron(III) to high-spin oxodi-iron(IV) with a new carboxylate-containing dinucleating ligand. *Chem. Sci.* **5**, 2282–2292 (2014).
13. Xue, G., De Hont, R., Münck, E. & Que, L., Jr. Million-fold activation of the  $[\text{Fe}_2(\mu\text{-O})_2]$  diamond core for C-H bond cleavage. *Nat. Chem.* **2**, 400–5 (2010).



14. Xue, G., Pokutsa, A. & Que, L., Jr. Substrate-triggered activation of a synthetic  $[\text{Fe}_2(\mu\text{-O})_2]$  diamond core for C-H bond cleavage. *J. Am. Chem. Soc.* **133**, 16657–67 (2011).
15. Xue, G. *et al.* Hydrogen-Bonding Effects on the Reactivity of  $[\text{X-Fe}^{\text{III}}\text{-O-Fe}^{\text{IV}}\text{=O}]$  (X = OH, F) Complexes toward C-H Bond Cleavage. *Inorg. Chem.* **52**, 3976–3984 (2013).
16. Do, L. H., Xue, G., Que, L., Jr. & Lippard, S. J. Evaluating the identity and diiron core transformations of a ( $\mu$ -oxo)diiron(III) complex supported by electron-rich tris(pyridyl-2-methyl)amine ligands. *Inorg. Chem.* **51**, 2393–2402 (2012).
17. Rohde, J.-U. *et al.* Crystallographic and spectroscopic characterization of a nonheme Fe(IV)-O complex. *Science (80)*. **299**, 1037–1039 (2003).
18. Fukuzumi, S. *et al.* Crystal structure of a metal ion-bound oxoiron(IV) complex and implications for biological electron transfer. *Nat. Chem.* **2**, 756–759 (2010).
19. Swart, M. A change in the oxidation state of iron: scandium is not innocent. *Chem. Commun.* **49**, 6650–6652 (2013).
20. Sheldrick, G. M. A short history of SHELX. *Acta Crystallogr. Sect. A Found. Crystallogr.* **A64**, 112–122 (2008).
21. Rowland, R. S. & Taylor, R. Intermolecular Nonbonded Contact Distances in Organic Crystal Structures: Comparison with Distances Expected from van der Waals Radii. *J. Phys. Chem.* **100**, 7384–7391 (1996).
22. Ray, K. *et al.* An inverted and more oxidizing isomer of  $[\text{Fe}(\text{IV})(\text{O})(\text{tmc})(\text{NCCH}_3)]^{2+}$ . *Angew. Chemie (Int. ed.)* **47**, 8068–8071 (2008).
23. Wang, D. *et al.* Nonheme Oxoiron(IV) Complexes of Pentadentate N5 Ligands: Spectroscopy, Electrochemistry, and Oxidative Reactivity. *Chem. Sci.* **4**, 282–291 (2013).
24. Banerjee, R., Meier, K. K., Münck, E. & Lipscomb, J. D. Intermediate P\* from soluble methane monooxygenase contains a diferrous cluster. *Biochemistry* **52**, 4331–42 (2013).
25. Tinberg, C. E. & Lippard, S. J. Dioxygen activation in soluble methane monooxygenase. *Acc. Chem. Res.* **44**, 280–188 (2011).
26. Zheng, H., Zang, Y., Dong, Y., Young, V. G., Jr. & Que, L., Jr. Complexes with  $\text{Fe}^{\text{III}}_2(\mu\text{-O})(\mu\text{-OH})$ ,  $\text{Fe}^{\text{III}}_2(\mu\text{-O})_2$ , and  $[\text{Fe}^{\text{III}}(\mu_2\text{-O})_3]$  Cores: Structures, Spectroscopy, and Core Interconversions. *J. Am. Chem. Soc.* **121**, 2226–2235 (1999).
27. Xue, G., Fiedler, A. T., Martinho, M., Münck, E. & Que, L., Jr. Insights into the P-to-Q conversion in the catalytic cycle of methane monooxygenase from a synthetic model system. *Proc. Natl. Acad. Sci. U. S. A.* **105**, 20615–20620 (2008).
28. England, J. *et al.* A more reactive trigonal-bipyramidal high-spin oxoiron(IV) complex with a cis-labile site. *J. Am. Chem. Soc.* **133**, 11880–11883 (2011).

29. Matthews, M. L. *et al.* Substrate-triggered formation and remarkable stability of the C-H bond-cleaving chloroferryl intermediate in the aliphatic halogenase, SyrB2. *Biochemistry* **48**, 4331–4343 (2009).
30. Galonic Fujimori, D. *et al.* Spectroscopic Evidence for a High-Spin Br-Fe(IV)-Oxo Intermediate in the  $\alpha$ -Ketoglutarate-Dependent Halogenase CytC3 from *Streptomyces*. *J. Am. Chem. Soc.* **129**, 13408–13409 (2007).
31. Galonić, D. P., Barr, E. W., Walsh, C. T., Bollinger, J. M. & Krebs, C. Two interconverting Fe(IV) intermediates in aliphatic chlorination by the halogenase CytC3. *Nat. Chem. Biol.* **3**, 113–116 (2007).
32. Solomon, E. I., Decker, A. & Lehnert, N. Non-heme iron enzymes: contrasts to heme catalysis. *Proc. Natl. Acad. Sci. U. S. A.* **100**, 3589–3594 (2003).
33. Hegg, E. L. *et al.* Herbicide degrading alpha-keto acid dependent enzyme TfdA: Metal coordination environment and mechanistic insights. *Biochemistry* **38**, 16714–16726 (1999).
34. Vu, V. V. *et al.* Human deoxyhypusine hydroxylase, an enzyme involved in regulating cell growth, activates O<sub>2</sub> with a nonheme diiron center. *Proc. Natl. Acad. Sci. U. S. A.* **106**, 14814–14819 (2009).
35. Makris, T. M. *et al.* An Unusual Peroxo Intermediate of the Arylamine Oxygenase of the Chloramphenicol Biosynthetic Pathway. *J. Am. Chem. Soc.* **137**, 1608–1617 (2015).
36. Warui, D. M. *et al.* Detection of Formate, Rather than Carbon Monoxide, As the Stoichiometric Coproduct in Conversion of Fatty Aldehydes to Alkanes by a Cyanobacterial Aldehyde Decarbonylase. *J. Am. Chem. Soc.* **133**, 3316–3319 (2011).
37. McDonald, A. R. & Que, L., Jr. High-valent nonheme iron-oxo complexes: Synthesis, structure, and spectroscopy. *Coord. Chem. Rev.* **257**, 414–428 (2013).
38. Kleespies, S. T., Oloo, W. N., Mukherjee, A. & Que, L., Jr. C–H Bond Cleavage by Bioinspired Nonheme Oxoiron(IV) Complexes, Including Hydroxylation of n-Butane. *Inorg. Chem.* DOI: 10.1021/ic502786y (2015).
39. Leising, R. A., Brennan, B. A., Que, L., Jr., Fox, B. G. & Münck, E. Models for Non-Heme Iron Oxygenases: A High-Valent Iron-Oxo Intermediate. *J. Am. Chem. Soc.* **113**, 3988–3990 (1991).
40. Dong, Y. *et al.* A High-Valent Nonheme Iron Intermediate. Structure and Properties of [Fe<sub>2</sub>( $\mu$ -O)<sub>2</sub>(5-Me-TPA)<sub>2</sub>](ClO<sub>4</sub>)<sub>3</sub>. *J. Am. Chem. Soc.* **117**, 2778–2792 (1995).
41. Skulan, A. J. *et al.* EPR Spectroscopy of [Fe<sub>2</sub>O<sub>2</sub>(5-Et<sub>3</sub>-TPA)<sub>2</sub>]<sup>3+</sup>: Electronic Origin of the Unique Spin-Hamiltonian Parameters of the Fe<sub>2</sub><sup>III,IV</sup>O<sub>2</sub> Diamond Core. *Inorg. Chem.* **42**, 6489–6496 (2003).
42. Skulan, A. J., Hanson, M. A., Hsu, H., Que, L., Jr. & Solomon, E. I. Spectroscopic Study of [Fe<sub>2</sub>O<sub>2</sub>(5-Et<sub>3</sub>-TPA)<sub>2</sub>]<sup>3+</sup>: Nature of the Fe<sub>2</sub>O<sub>2</sub> Diamond Core and Its Possible Relevance to High-Valent Binuclear Non-Heme Enzyme Intermediates. *J. Am. Chem. Soc.* **125**, 7344–7356 (2003).

43. Dong, Y., Que, L., Jr., Kauffmann, K. & Münck, E. An Exchange-Coupled Complex with Localized High-Spin Fe<sup>IV</sup> and Fe<sup>III</sup> Sites of Relevance to Cluster X of Escherichia coli Ribonucleotide Reductase. *J. Am. Chem. Soc.* **117**, 11377–11378 (1995).
44. Dong, Y. *et al.* Models for Nonheme Diiron Enzymes . Assembly of a High-Valent Fe<sub>2</sub>(μ-O)<sub>2</sub> Diamond Core from Its Peroxo Precursor. *J. Am. Chem. Soc.* **119**, 12683–12684 (1997).
45. Zheng, H., Yoo, S. J., Münck, E. & Que, L., Jr. The Flexible Fe<sub>2</sub>(μ-O)<sub>2</sub> Diamond Core: A Terminal Iron(IV)-Oxo Species Generated from the Oxidation of a Bis(μ-oxo)diiron(III) Complex. *J. Am. Chem. Soc.* **122**, 3789–3790 (2000).
46. Lee, D. *et al.* Functional Mimic of Dioxygen-Activating Centers in Non-Heme Diiron Enzymes: Mechanistic Implications of Paramagnetic Intermediates in the Reactions between Diiron(II) Complexes and Dioxygen. *J. Am. Chem. Soc.* **124**, 3993–4007 (2002).
47. Martinho, M. *et al.* Mössbauer and DFT study of the ferromagnetically coupled diiron(IV) precursor to a complex with an Fe<sup>IV</sup><sub>2</sub>O<sub>2</sub> diamond core. *J. Am. Chem. Soc.* **131**, 5823–30 (2009).
48. De Hont, R. F. *et al.* Mössbauer, electron paramagnetic resonance, and density functional theory studies of synthetic S = 1/2 Fe(III)-O-Fe(IV)=O complexes. Superexchange-mediated spin transition at the Fe(IV)=O site. *Inorg. Chem.* **49**, 8310–22 (2010).
49. Stoian, S. A., Xue, G., Bominaar, E. L., Que, L., Jr. & Münck, E. Spectroscopic and Theoretical Investigation of a Complex with an [O=Fe<sup>IV</sup>-O-Fe<sup>IV</sup>=O] Core Related to Methane Monooxygenase Intermediate Q. *J. Am. Chem. Soc.* **136**, 1545–1558 (2014).
50. Lee, S.-K., Fox, B. G., Froland, W. A., Lipscomb, J. D. & Münck, E. A Transient Intermediate of the Methane Monooxygenase Catalytic Cycle Containing an Fe<sup>IV</sup>Fe<sup>IV</sup> Cluster. *J. Am. Chem. Soc.* **115**, 6450–6451 (1993).
51. Shu, L. *et al.* An Fe<sub>2</sub><sup>IV</sup>O<sub>2</sub> Diamond Core Structure for the Key Intermediate Q of Methane Monooxygenase. *Science (80)*. **275**, 515–518 (1997).
52. Banerjee, R., Proshlyakov, Y., Lipscomb, J. D. & Proshlyakov, D. A. Structure of the key species in the enzymatic oxidation of methane to methanol. *Nature* **518**, 431–434 (2015).
53. Liu, K. E. *et al.* Kinetic and Spectroscopic Characterization of Intermediates and Component Interactions in Reactions of Methane Monooxygenase from *Methylococcus capsulatus* (Bath). *J. Am. Chem. Soc.* **117**, 10174–10185 (1995).
54. Tinberg, C. E. & Lippard, S. J. Revisiting the mechanism of dioxygen activation in soluble methane monooxygenase from *M. capsulatus* (Bath): Evidence for a multi-step, proton-dependent reaction pathway. *Biochemistry* **48**, 12145–12158 (2009).
55. Sturgeon, B. E. *et al.* Reconsideration of X , the Diiron Intermediate Formed during Cofactor Assembly in *E. coli* Ribonucleotide Reductase. *J. Am. Chem. Soc.* **118**, 7551–7557 (1996).
56. Dassama, L. M. K. *et al.* A 2.8 Å Fe–Fe Separation in the Fe<sub>2</sub><sup>III/IV</sup> Intermediate, X, from Escherichia coli Ribonucleotide Reductase. *J. Am. Chem. Soc.* **135**, 16758–16761 (2013).

57. Groves, J. T., Haushalter, R. C., Nakamura, M., Nemo, T. E. & Evans, B. J. High-Valent Iron-Porphyrin Complexes Related to Peroxidase and Cytochrome P-450. *J. Am. Chem. Soc.* **103**, 2884–2886 (1981).
58. Mahapatra, S. *et al.* A New Intermediate in Copper Dioxygen Chemistry: Breaking the O-O Bond to Form a  $\{\text{Cu}_2(\mu\text{-O})_2\}^{2+}$  Core. *J. Am. Chem. Soc.* **117**, 8865–8866 (1995).
59. Que, L., Jr. & Tolman, W. B. Bis ( $\mu$ -oxo)dimetal ‘Diamond’ Cores in Copper and Iron Complexes Relevant to Biocatalysis. *Angew. Chemie (Int. ed.)* **41**, 1114–1137 (2002).
60. Riggs-Gelasco, P. J. *et al.* EXAFS Characterization of the Intermediate X Generated During the Assembly of the Escherichia coli Ribonucleotide Reductase R2 Diferric Tyrosyl Radical Cofactor. *J. Am. Chem. Soc.* **120**, 849–860 (1998).
61. Zang, Y. *et al.* Models for Nonheme Iron Intermediates: Structural Basis for Tuning the Spin States of Fe(TPA) Complexes. *J. Am. Chem. Soc.* **119**, 4197–4205 (1997).
62. Wilkinson, E. C. *et al.* Raman Signature of the  $\text{Fe}_2\text{O}_2$  ‘Diamond’ Core. *J. Am. Chem. Soc.* **120**, 955–962 (1998).
63. Dong, Y. *et al.* Dioxygen Binding to Diferrous Centers. Models for Diiron-Oxo Proteins. *J. Am. Chem. Soc.* **115**, 1851–1859 (1993).
64. Kitajima, N. *et al.* Monomeric Carboxylate Ferrous Complexes as Models for the Dioxygen Binding Sites in Non-Heme Iron Proteins. The Reversible Formation and Characterization of  $\mu$ -Peroxo Diferric Complexes. *J. Am. Chem. Soc.* **116**, 9071–9085 (1994).
65. Ookubo, T. *et al.* cis- $\mu$ -1,2-Peroxo Diiron Complex: Structure and Reversible Oxygenation. *J. Am. Chem. Soc.* **118**, 701–702 (1996).
66. Kim, K. & Lippard, S. J. Structure and Mossbauer Spectrum of a ( $\mu$ -1,2-Peroxo)bis( $\mu$ -carboxylato)diiron(III) Model for the Peroxo Intermediate in the Methane Monooxygenase Hydroxylase Reaction Cycle. *J. Am. Chem. Soc.* **118**, 4914–4915 (1996).
67. Hayashi, Y. *et al.* Synthesis, Characterization, and Reversible Oxygenation of  $\mu$ -Alkoxo Diiron(II) Complexes with the Dinucleating Ligand N,N,N',N'-Tetrakis{(6-methyl-2-pyridyl)methyl}-1,3-diamino-propan-2-olate. *J. Am. Chem. Soc.* **117**, 11220–11229 (1995).
68. Hagadorn, J. R., Que, L., Jr. & Tolman, W. B. A Bulky Benzoate Ligand for Modeling the Carboxylate-Rich Active Sites of Non-Heme Diiron Enzymes. *J. Am. Chem. Soc.* **120**, 13531–13532 (1998).
69. Ye, S. *et al.* Magnetic circular dichroism and computational study of mononuclear and dinuclear iron(IV) complexes. *Chem. Sci.* **6**, 2909–2921 (2015).
70. Tinberg, C. E. & Lippard, S. J. Oxidation reactions performed by soluble methane monooxygenase hydroxylase intermediates H(peroxo) and Q proceed by distinct mechanisms. *Biochemistry* **49**, 7902–12 (2010).
71. Shanmugam, M., Xue, G., Que, L., Jr. & Hoffman, B. M.  $^1\text{H}$ -ENDOR evidence for a hydrogen-bonding interaction that modulates the reactivity of a nonheme Fe(IV)=O unit. *Inorg. Chem.* **51**, 10080–2 (2012).

72. Fiedler, A. T. *et al.* Spectroscopic and computational studies of ( $\mu$ -oxo)( $\mu$ -1,2-peroxo)diiron(III) complexes of relevance to nonheme diiron oxygenase intermediates. *J. Phys. Chem. A* **112**, 13037–44 (2008).
73. Mayer, J. M. Hydrogen Atom Abstraction by Metal-Oxo Complexes: Understanding the Analogy with Organic Radical Reactions. *Acc. Chem. Res.* **31**, 441–450 (1998).
74. Johansson, A. J., Noack, H., Siegbahn, P. E. M., Xue, G. & Que, L., Jr. Observed enhancement of the reactivity of a biomimetic diiron complex by the addition of water - mechanistic insights from theoretical modeling. *Dalton Trans.* 6741–50 (2009).
75. Hirao, H., Que, L., Jr., Nam, W. & Shaik, S. A two-state reactivity rationale for counterintuitive axial ligand effects on the C-H activation reactivity of nonheme Fe<sup>IV</sup>=O oxidants. *Chem. A Eur. J.* **14**, 1740–1756 (2008).
76. Shaik, S., Chen, H. & Janardanan, D. Exchange-enhanced reactivity in bond activation by metal-oxo enzymes and synthetic reagents. *Nat. Chem.* **3**, 19–27 (2011).
77. Hirao, H., Kumar, D., Que, L., Jr. & Shaik, S. Two-State Reactivity in Alkane Hydroxylation by Non-Heme Iron-Oxo Complexes. *J. Am. Chem. Soc.* **128**, 8590–8606 (2006).
78. Bertini, I., Gray, H. B., Stiefel, E. I. & Valentine, J. S. *Biological Inorganic Chemistry Structure and Reactivity*. (University Science Books, 2007).
79. Dong, Y., Yan, S., Young, V. G., Jr. & Que, L., Jr. Crystal Structure Analysis of a Synthetic Non-Heme Diiron-O<sub>2</sub> Adduct: Insight into the Mechanism of Oxygen Activation. *Angew. Chemie (Int. ed.)* **35**, 618–620 (1996).
80. Kodera, M. & Kano, K. Reversible O<sub>2</sub>-Binding and Activation with Dicopper and Diiron Complexes Stabilized by Various Hexapyridine Ligands. Stability, Modulation, and Flexibility of the Dinuclear Structure as Key Aspects for the Dimetal/O<sub>2</sub> Chemistry. *Bull. Chem. Soc. Jpn.* **80**, 662–676 (2007).
81. Frisch, J. R., McDonnell, R., Rybak-akimova, E. V & Que, L., Jr. Factors Affecting the Carboxylate Shift Upon Formation of Nonheme Diiron-O<sub>2</sub> Adducts. *Inorg. Chem.* **52**, 2627–2636 (2013).
82. Cranswick, M. A. *et al.* Protonation of a Peroxodiiron(III) Complex and Conversion to a Diiron(III/IV) Intermediate: Implications for a Proton-Assisted O-O Bond Cleavage in Nonheme Diiron Enzymes. *Inorg. Chem.* **51**, 10417–10426 (2012).
83. Pap, J. S. *et al.* An Iron(II)(1,3-bis(2'-pyridylimino)isoindoline) Complex as a Catalyst for Substrate Oxidation with H<sub>2</sub>O<sub>2</sub>- Evidence for a Transient Peroxodiiron(III) Species. *Eur. J. Inorg. Chem.* 3858–3866 (2013).
84. Zhang, X. *et al.* Structural and spectroscopic characterization of ( $\mu$ -hydroxo or  $\mu$ -oxo)( $\mu$ -peroxo)diiron(III) complexes: models for peroxo intermediates of non-heme diiron proteins. *J. Am. Chem. Soc.* **127**, 826–7 (2005).
85. Avenier, F., Dubois, L. & Latour, J.-M. Intramolecular aromatic hydroxylation mediated by a dinuclear iron complex: an oxo-Fe<sup>IV</sup>Fe<sup>IV</sup> active intermediate is suggested. *New J. Chem.* **28**, 782–784 (2004).

86. Avenier, F., Dubois, L., Dubourdeaux, P. & Latour, J.-M. A diiron complex mediates an intramolecular aliphatic hydroxylation by various oxygen donors. *Chem. Commun.* 480–482 (2005).
87. Coggins, M. K., Toledo, S. & Kovacs, J. A. Isolation and Characterization of a Dihydroxo-Bridged Iron(III,III)( $\mu$ -OH)<sub>2</sub> Diamond Core Derived from Dioxygen. *Inorg. Chem.* **52**, 13325–13331 (2013).
88. Braymer, J. J., O'Neill, K. P., Rohde, J.-U. & Lim, M. H. The reaction of a high-valent nonheme oxoiron(IV) intermediate with hydrogen peroxide. *Angew. Chemie (Int. ed.)* **51**, 5376–80 (2012).
89. Li, F., England, J. & Que, L., Jr. Near-Stoichiometric Conversion of H<sub>2</sub>O<sub>2</sub> to Fe IV=O at a Nonheme Iron(II) Center. Insights into the O-O Bond Cleavage Step. *J. Am. Chem. Soc.* **132**, 2134–2135 (2010).
90. Do, L. H., Hayashi, T., Moenne-Loccoz, P. & Lippard, S. J. Carboxylate as the Protonation Site in (Peroxo)diiron(III) Model Complexes of Soluble Methane Monooxygenase and Related Diiron Proteins. *J. Am. Chem. Soc.* **132**, 1273–1275 (2010).
91. Kryatov, S. V., Rybak-Akimova, E. V., Macmurdo, V. L. & Que, L., Jr. A Mechanistic Study of the Reaction between a Diiron(II) Complex [Fe<sup>II</sup><sub>2</sub>( $\mu$ -OH)<sub>2</sub>(6-Me<sub>3</sub>-TPA)<sub>2</sub>]<sup>2+</sup> and O<sub>2</sub> to Form a Diiron(III) Peroxo Complex. *Inorg. Chem.* **40**, 2220–2228 (2001).
92. Sun, H. & DiMugno, S. G. Anhydrous tetrabutylammonium fluoride. *J. Am. Chem. Soc.* **127**, 2050–1 (2005).
93. George, G. N. & Pickering, I. J. EXAFSPAK: A Suite of Computer Programs for Analysis of X-ray Absorption Spectra. *EXAFSPAK (Stanford Synchrotron Radiat. Lab. Stanford, CA)* (2000).
94. Siegbahn, P. E. M. Theoretical Model Studies of the Iron Dimer Complex of MMO and RNR. *Inorg. Chem.* **38**, 2880–2889 (1999).
95. Han, W.-G. & Noodleman, L. Structural Model Studies for the High-Valent Intermediate Q of Methane Monooxygenase from Broken-Symmetry Density Functional Calculations. *Inorganica Chim. Acta* **361**, 973–986 (2008).
96. Baik, M.-H., Newcomb, M., Friesner, R. A. & Lippard, S. J. Mechanistic studies on the hydroxylation of methane by methane monooxygenase. *Chem. Rev.* **103**, 2385–419 (2003).
97. Gherman, B. F., Baik, M.-H., Lippard, S. J. & Friesner, R. A. Dioxygen activation in methane monooxygenase: a theoretical study. *J. Am. Chem. Soc.* **126**, 2978–90 (2004).
98. Zang, Y., Dong, Y., Que, L., Jr., Kauffmann, K. & Münck, E. The First Bis( $\mu$ -oxo)diiron(III) Complex. Structure and Magnetic Properties of [Fe<sub>2</sub>( $\mu$ -O)<sub>2</sub>(6TLA)<sub>2</sub>](ClO<sub>4</sub>)<sub>2</sub>. *J. Am. Chem. Soc.* **117**, 1169–1170 (1995).
99. Han, W. & Noodleman, L. DFT Calculations for Intermediate and Active States of the Diiron Center with a Tryptophan or Tyrosine Radical in Escherichia coli Ribonucleotide Reductase. *Inorg. Chem.* **50**, 2302–2320 (2011).

100. Bruker AXS Inc. APEX2 v2013.6-2. (2013).
101. Bruker AXS Inc. TWINABS. (2008).
102. Bruker AXS Inc. SAINT. (2007).
103. Bruker AXS Inc. XPREP. (2008).
104. Müller, P. Practical suggestions for better crystal structures. *Crystallogr. Rev.* **15**, 57–83 (2009).
105. Burla, M. C. *et al.* SIR2011: A new package for crystal structure determination and refinement. *J. Appl. Crystallogr.* **45**, 357–361 (2012).
106. Bollinger, J. M., Price, J. C., Hoffart, L. M., Barr, E. W. & Krebs, C. Mechanism of Taurine:  $\alpha$ -Ketoglutarate Dioxygenase (TauD) from *Escherichia coli*. *Eur. J. Inorg. Chem.* 4245–4254 (2005).
107. Price, J. C., Barr, E. W., Tirupati, B., Bollinger, J. M. J. & Krebs, C. The first direct characterization of a high-valent iron intermediate in the reaction of an  $\alpha$ -ketoglutarate-dependent dioxygenase: A high-spin Fe(IV) complex in taurine/ $\alpha$ -ketoglutarate dioxygenase (TauD) from *Escherichia coli*. *Biochemistry* **42**, 7497–7508 (2003).
108. Klinker, E. J. *et al.* Structures of nonheme oxoiron(IV) complexes from X-ray crystallography, NMR spectroscopy, and DFT calculations. *Angew. Chemie (Int. ed.)* **44**, 3690–3694 (2005).
109. Lacy, D. C. *et al.* Formation, Structure, and EPR Detection of a High Spin Fe<sup>IV</sup>-Oxo Species Derived from Either an Fe<sup>III</sup>-Oxo or Fe<sup>III</sup>-OH Complex. *J. Am. Chem. Soc.* **132**, 12188–12190 (2010).
110. Thibon, A. *et al.* Proton- and reductant-assisted dioxygen activation by a nonheme iron(II) complex to form an oxoiron(IV) intermediate. *Angew. Chemie (Int. ed.)* **47**, 7064–7067 (2008).
111. Meyer, S., Klawitter, I., Demeshko, S., Bill, E. & Meyer, F. A tetracarbene-oxoiron(IV) complex. *Angew. Chemie (Int. ed.)* **52**, 901–905 (2013).
112. England, J. *et al.* The crystal structure of a high-spin oxoiron(IV) complex and characterization of its self-decay pathway. *J. Am. Chem. Soc.* **132**, 8635–8644 (2010).
113. England, J. *et al.* An Ultra-Stable Oxoiron(IV) Complex and Its Blue Conjugate Base. *Chem. Sci.* **5**, 1204–1215 (2014).
114. Fukuzumi, S. Electron-transfer properties of high-valent metal-oxo complexes. *Coord. Chem. Rev.* **257**, 1564–1575 (2013).
115. Prakash, J. *et al.* Spectroscopic Identification of an Fe<sup>III</sup> Center, not Fe<sup>IV</sup>, in the Crystalline Sc–O–Fe Adduct Derived from [Fe<sup>IV</sup>(O)(TMC)]<sup>2+</sup>. *J. Am. Chem. Soc.* **137**, 3478–3481 (2015).

116. Cho, J. *et al.* Structure and reactivity of a mononuclear non-haem iron(III)-peroxo complex. *Nature* **478**, 502–5 (2011).
117. Li, F. *et al.* Characterization of a High-Spin Non-Heme Fe<sup>II</sup>-OOH Intermediate and Its Quantitative Conversion to an Fe<sup>IV</sup>=O Complex. *J. Am. Chem. Soc.* **133**, 7256–7259 (2011).
118. Li, F., Heuvelen, K. M. Van, Meier, K. K. & Que, L., Jr. Sc<sup>3+</sup>-Triggered Oxoiron(IV) Formation from O<sub>2</sub> and its Non-Heme Iron(II) Precursor via a Sc<sup>3+</sup>-Peroxo-Fe<sup>3+</sup> Intermediate. *J. Am. Chem. Soc.* **135**, 10198–10201 (2013).
119. Lee, Y.-M. *et al.* A Mononuclear Nonheme Iron(III)-Peroxo Complex Binding Redox-Inactive Metal Ions. *Chem. Sci.* **4**, 3917–3923 (2013).
120. Kurtz, D. M. J. Oxo- and Hydroxo-Bridged Diiron Complexes: A Chemical Perspective on a Biological Unit. *Chem. Rev.* **90**, 585–606 (1990).
121. Jackson, T. A. *et al.* Axial Ligand Effects on the Geometric and Electronic Structures of Nonheme Oxoiron(IV) Complexes. *J. Am. Chem. Soc.* **130**, 12394–12407 (2008).
122. Hodges, K. D. *et al.* Preparations and Properties of Nitrosyl Complexes of Iron Tetratmethylcyclam. X-ray Structures of [Fe(C<sub>14</sub>H<sub>32</sub>N<sub>4</sub>)-NO](BF<sub>4</sub>)<sub>2</sub>, a S = 3/2-1/2 Spin-Equilibrium Complex, and [Fe(C<sub>14</sub>H<sub>32</sub>N<sub>4</sub>)(NO)(OH)](ClO<sub>4</sub>)<sub>2</sub>·CH<sub>3</sub>CN. *J. Am. Chem. Soc.* **101**, 906–917 (1979).
123. Addison, A. W., Rao, T. N., Reedijk, J., van Rijn, J. & Verschoor, G. C. Synthesis, Structure, and Spectroscopic Properties of Copper(II) Compounds containing Nitrogen-Sulphur Donor Ligands; the Crystal and Molecular Structure of Aqua[1,7-bis(N-methylbenzimidazol-2'-yl)-2,6-dithiaheptane]copper(II) Perchlorate. *J. Chem. Soc. Dalton Trans.* 1349–1356 (1984).
124. Matsuura, Y., Tanaka, Y. & Akita, M. p-Diethynylbenzene-based molecular wires, Fe-C≡C-ρ-C<sub>6</sub>H<sub>2</sub>X<sub>2</sub>-C≡C-Fe [Fe = Fe(η<sup>5</sup>-C<sub>5</sub>Me<sub>5</sub>)(dppe)]: Synthesis, substituent effects and unexpected formation of benzodifuran complex. *J. Organomet. Chem.* **694**, 1840–1847 (2009).
125. Benhamou, L., Jaafar, H., Thibon, A., Lachkar, M. & Mandon, D. Asymmetry and steric hindrance in tripodal ligands: Reaching the limit for octahedral geometry with the newly synthesized [(6-bromo 2-pyridylmethyl)(6-fluoro 2-pyridylmethyl)(2-pyridylmethyl)]amine tripod in FeCl<sub>2</sub> complexes. *Inorganica Chim. Acta* **373**, 195–200 (2011).
126. Silva, T. F. S., Guedes Da Silva, M. F., Mishra, G. S., Martins, L. M. D. R. S. & Pombeiro, A. J. L. Synthesis and structural characterization of iron complexes with 2,2,2-tris(1-pyrazolyl)ethanol ligands: Application in the peroxidative oxidation of cyclohexane under mild conditions. *J. Organomet. Chem.* **696**, 1310–1318 (2011).
127. Milione, S. & Bertolasi, V. Tautomerism in bis(oxazolines): An experimental and theoretical study of proton transfer in 1,1-bis(4,4-dimethyl-1,3-oxazolin-2-yl)-ethane. *Tetrahedron Lett.* **52**, 3570–3574 (2011).



128. Liu, X., Kilner, C. a. & Halcrow, M. a. Tetrakis(5-tert-butylpyrazole-1κN2)-tetrachloro-1κCl-2κ<sup>3</sup>Cl-μ-oxo-1:2κ<sup>2</sup>-O-diiron(III). *Acta Crystallogr. Sect. C Cryst. Struct. Commun.* **C58**, m290–m291 (2002).
129. Prakash, J. *et al.* Manuscript in preparation. (2015).
130. Decker, A. *et al.* Spectroscopic and quantum chemical studies on low-spin Fe<sup>IV</sup>=O complexes: Fe-O bonding and its contributions to reactivity. *J. Am. Chem. Soc.* **129**, 15983–15996 (2007).
131. Srnec, M., Wong, S. D., England, J., Que, L., Jr. & Solomon, E. I. π-Frontier molecular orbitals in S = 2 ferryl species and elucidation of their contributions to reactivity. *Proc. Natl. Acad. Sci. U. S. A.* **109**, 14326–14331 (2012).
132. Bruker AXS Inc. CELL\_NOW. (2008).
133. Wojdyr, M. Fityk : a general-purpose peak fitting program. *J. Appl. Crystallogr.* **43**, 1126–1128 (2010).
134. Biswas, A. N. *et al.* Modeling TauD-J: A High-Spin Nonheme Oxoiron(IV) Complex with High Reactivity toward C–H Bonds. *J. Am. Chem. Soc.* **137**, 2428–2431 (2015).
135. Seo, M. S. *et al.* A mononuclear nonheme iron(IV)-oxo complex which is more reactive than cytochrome P450 model compound I. *Chem. Sci.* **2**, 1039 (2011).
136. England, J. *et al.* A synthetic high-spin oxoiron(IV) complex: generation, spectroscopic characterization, and reactivity. *Angew. Chemie (Int. ed.)* **48**, 3622–6 (2009).
137. Zhou, Y. *et al.* Contrasting cis and trans effects on the reactivity of nonheme oxoiron(IV) complexes. *Angew. Chemie (Int. ed.)* **47**, 1896–1899 (2008).
138. Sastri, C. V *et al.* Axial ligand tuning of a nonheme iron(IV)-oxo unit for hydrogen atom abstraction. *Proc. Natl. Acad. Sci. U. S. A.* **104**, 19181–19186 (2007).
139. Decker, A. & Solomon, E. I. Comparison of Fe<sup>IV</sup>=O Heme and Non-heme Species: Electronic Structures, Bonding, and Reactivities. *Angew. Chemie (Int. ed.)* **117**, 2292–2295 (2005).
140. Rohde, J. U. *et al.* Nonheme oxoiron(IV) complexes of tris(2-pyridylmethyl)amine with *cis*-Monoanionic Ligands. *Inorg. Chem.* **45**, 6435–6445 (2006).
141. Mayer, J. M. Proton-coupled electron transfer: a reaction chemist's view. *Annu. Rev. Phys. Chem.* **55**, 363–90 (2004).
142. Evans, M. G. & Polanyi, M. Further Considerations on the Thermodynamics of Chemical Equilibria and Reaction Rates. *Transitions Faraday Soc.* **32**, 1333–1360 (1936).
143. Kaizer, J. *et al.* Nonheme Fe<sup>IV</sup>O Complexes That Can Oxidize the C-H Bonds of Cyclohexane at Room Temperature. *J. Am. Chem. Soc.* **126**, 472–473 (2004).

144. Wang, D., Zhang, M., Buhlmann, P. & Que, L., Jr. Redox Potential and C-H Bond Cleaving Properties of a Nonheme Fe<sup>IV</sup>=O Complex in Aqueous Solution. *J. Am. Chem. Soc.* **132**, 7638–7644 (2010).
145. Wilson, S. A. *et al.* [Fe<sup>IV</sup>=O(TBC)(CH<sub>3</sub>CN)]<sup>2+</sup>: Comparative reactivity of iron(IV)-oxo species with constrained equatorial cyclam ligation. *J. Am. Chem. Soc.* **134**, 11791–11806 (2012).